

2011

# Mode I Delamination Fracture Characterization of Polymeric Composites under Elevated Temperature

Wenming Zhao  
*Syracuse University*

Follow this and additional works at: [http://surface.syr.edu/mae\\_etd](http://surface.syr.edu/mae_etd)

 Part of the [Engineering Commons](#)

---

## Recommended Citation

Zhao, Wenming, "Mode I Delamination Fracture Characterization of Polymeric Composites under Elevated Temperature" (2011).  
*Mechanical and Aerospace Engineering - Dissertations*. Paper 59.

This Dissertation is brought to you for free and open access by the College of Engineering and Computer Science at SURFACE. It has been accepted for inclusion in Mechanical and Aerospace Engineering - Dissertations by an authorized administrator of SURFACE. For more information, please contact [surface@syr.edu](mailto:surface@syr.edu).

## ABSTRACT

### Mode I Delamination Fracture Characterization of Polymeric Composites under Elevated Temperature

(May 2011)

Wenming Zhao, M.S., Clarkson University

Delamination is one of the major failure modes seen in the laminated polymeric matrix composite (PMC). Accurate prediction of delamination initiation and propagation is important for the design and analysis of robust composite structures. Existing experimental methodologies that are based on linear elastic fracture mechanics are inadequate to characterize delamination fracture properties under elevated temperature when PMC properties become time-, loading-history, and rate-dependent. A new experimental methodology based on linear viscoelastic fracture theory is developed and verified through finite element analysis and experiments. This new technique determines crack growth curves, such as stress intensity factor vs. crack growth speed and fracture initiation energy vs. crack initiation time, through the experimentally determined J-integral,  $J_s$ , for a linear viscoelastic double cantilever beam (DCB) specimen. Special test setup is designed and validated for determining accurate  $J_s$  using just the applied load and the load end rotation angles. This new methodology is then applied to measure the mode I fracture properties of a highly toughened graphite/epoxy composite under various environmental conditions.

**Mode I Delamination Fracture Characterization of  
Polymeric Composites under Elevated Temperature**

*By*

Wenming Zhao

M.S., Clarkson University, 2003

**DISSERTATION**

Submitted in partial fulfillment of the requirements for the degree of  
**Doctor of Philosophy**  
in Mechanical Engineering in the Graduate School of Syracuse University

May, 2011

Copyright 2011 Wenming Zhao

All rights Reserved

# Table of Contents

<b>List of Tables</b>	<b>vii</b>
<b>List of Figures</b>	<b>viii</b>
<b>Acknowledgement</b>	<b>xii</b>
<b>1. INTRODUCTION</b>	<b>1</b>
1.1.Problem overview	1
1.2.Objectives	3
1.3.Study overview	3
<b>2. USE OF LINEAR ELASTIC FRACTURE MECHANICS IN DELAMINATION GROWTH PREDICTION</b>	<b>5</b>
1.4. Introduction	5
1.5. Fracture parameters in LEFM	6
2.5.1.The mode I energy release rate, $G_I$	6
2.5.2.The mode I stress intensity factor, KI	8
2.5.3.The J-integral	9
2.5.4.Fracture parameters in delamination prediction	10
1.6. The mode I double cantilever beam (DCB) test	11
2.6.1.Introduction	11
2.6.2.LEFM-based data reduction techniques	11
2.6.3.Use of LEFM in delamination toughness measurements	17
1.7. Conclusion	21
<b>3. USE OF VISCOELASTIC FRACTURE MECHANICS IN DELAMINATION GROWTH PREDICTION</b>	<b>23</b>
3.1.Introduction	23
3.2.Linear viscoelastic fracture analysis and characterization	24
3.2.1.Viscoelastic fracture mechanics overview	24
3.2.2.Requirements for application of VEFM to PMCs	25
3.2.3.Previous work	26
3.2.4.Most promising approaches	28
3.3.Schapery's linear viscoelastic fracture theory	29
3.3.1.Fracture energy	29
3.3.2.Stress intensity factor method	30
3.3.3.Generalized J-integral method	39
3.3.4.Summary	46
3.4.Conclusion	46
<b>4. COMPOSITE MATERIAL CONSIDERED</b>	<b>47</b>
4.1.Introduction	47
4.2.Prior work on T800H/3900-2 Laminates	50
4.2.1.Mechanical properties	50

4.2.2. Fracture properties under various environments	51
4.2.3. Summary	52
4.3.Measurement of linear viscoelastic properties	52
4.3.1.Experimental procedures	53
4.3.2.Test results	57
4.4.Conclusion	61
<b>5. FRACTURE CHARACTERIZATION METHODOLOGY</b>	<b>63</b>
5.1. Introduction	63
5.2.Linear viscoelastic DCB specimen	64
5.3.Analysis of crack growth	67
5.3.1.Crack initiation	67
5.3.2.Steady crack propagation	70
5.4.Experimental technique	71
5.5.Roadmap	74
5.6.Conclusion	76
<b>6. MODELING AND VALIDATION</b>	<b>77</b>
6.1.Introduction	77
6.2.Finite element modeling of the DCB test	77
6.2.1.Finite element model	78
6.2.2.Linear elastic analyses	78
6.2.3.Linear viscoelastic analyses	79
6.2.4. $J_s$ from finite element model	81
6.2.5.Mesh refinement study	82
6.3.Results and discussion	82
6.3.1.Linear elastic analyses	82
6.3.2.Linear viscoelastic analyses	87
6.3.3.Specimen dimension	87
6.4.Conclusion	88
<b>7. ROOM TEMPERATURE DELAMINATION TOUGHNESS TESTING</b>	<b>89</b>
7.1.Introduction	89
7.2.Specimen preparation and experimental setup	90
7.3.DCB Data reduction and experimental procedure	92
7.4.Results and discussion	95
7.5.Conclusion	99
<b>8. ELEVATED TEMPERATURE AND MOISTURE TESTING</b>	<b>100</b>
8.1.Introduction	100
8.2.Moisture conditioning chamber and high temperature furnace	100
8.3.DCB testing procedures	102
8.4.Results and discussion	104
8.4.1.Dry DCB tests at 98°C	104
8.4.2.Moisture saturated tests at 98°C	107
8.4.3.Dry DCB tests at 125°C	110

8.4.4.Discussion	112
8.5.Conclusion	118
<b>9. CONCLUSIONS AND RECOMMENDATIONS</b>	<b>120</b>
9.1.Conclusion	120
9.2.Recommendation and future work	123
<b>10. REFERENCES</b>	<b>125</b>
<b>11. APPENDICES</b>	<b>138</b>
<b>TABLES AND FIGURES</b>	<b>149</b>
<b>VITA</b>	<b>229</b>

## **List of Tables**

Table 4.1 Typical elastic properties for unidirectional T800H/3900-2 graphite/epoxy laminate

Table 4.2 Constant load level in creep tests

Table 4.3 Linear viscoelastic properties of T800H/3900-2 at each condition

Table 6.1. Material properties for elastic analyses

Table 6.2. Material properties for viscoelastic analyses

Table 8.1. DCB test matrix under high temperature

Table A.1. Material properties in numerical simulation

Table B.1. Geometries considered



## List of Figures

- Figure 2.1 Basic delamination modes.
- Figure 2.2 Schematic of the double cantilever beam (DCB) test.
- Figure 2.3 Definition of coordinate axes for a unidirectional specimen.
- Figure 3.1 Typical  $K_I$  vs.  $a$  curve from a viscoelastic fracture test.
- Figure 3.2 Schematic of crack geometry and cohesive zone.
- Figure 4.1 Cross-sectional view showing interlayer of a cured composite at (a) low magnification and (b) high magnification.
- Figure 4.2 4-point bending tests schematic drawing and test setup.
- Figure 4.3 Iosipescu in-plane shear test setup.
- Figure 4.4 Verification of linear viscoelasticity from creep-recovery tests.
- Figure 4.5 Storage modulus vs. temperature from DMA tests of dry T800H/3900-2: (a) DMA-dry1; (b) DMA-dry2.
- Figure 4.6 Storage modulus vs. temperature from DMA tests of wet T800H/3900-2: (a) DMA-wet1; (b) DMA-wet2.
- Figure 4.7 Shear strain from two stress levels at  $T=208^\circ\text{F}$  of wet T800H/3900-2 specimen.
- Figure 4.8  $S_{22}(t)$  of T800H/3900-2 at different conditions.
- Figure 4.9  $S_{66}(t)$  of T800H/3900-2 at different conditions.
- Figure 5.1 (a) Experimental indirect angle measurement (b) geometry of “L” shape loading blocks.
- Figure 6.1 Typical FE mesh for DCB analyses.
- Figure 6.2 Percent error of  $J_s$  to  $J$  vs. end rotation angle for the Gr/Ep DCB specimen with various thicknesses and crack lengths.
- Figure 6.3 Percent error of  $J_s$  to  $J$  vs. end rotation angle for the Gl/Ep and the isotropic DCB specimen with various crack lengths and thickness of 4mm.
- Figure 6.4 Evaluation of  $J_s$  for models with adhesive.
- Figure 6.5 Evaluation of  $J_s$  for models with different size of loading blocks.
- Figure 6.6 Comparison of  $J$  between proposed material model and ABAQUS default material model for isotropic materials.

Figure 6.7 Evaluation of  $J_s$  for orthotropic linear viscoelastic materials.

Figure 7.1 Electrical circuits of crack propagation gage.

Figure 7.2 DCB test setup.

Figure 7.3 Typical load-deflection curve for a DCB test of T800H/3900-2 at room temperature.

Figure 7.4 Delamination mechanism of T800H/3900-2 at room temperature (a) fracture surface view; (b) Schematic of crack growth path.

Figure 7.5 Critical  $J_s$  of T800H/3900-2 at room temperature from multiple specimens.

Figure 7.6 Fracture toughness by CC method of T800H/3900-2 at room temperature.

Figure 7.7 Fracture toughness by MWLO method of T800H/3900-2 at room temperature.

Figure 7.8 Comparison of  $J_s$ ,  $G_{IC}^{CC}$  and  $G_{IC}^{MWLO}$  of T800H/3900-2 at room temperature.

Figure 7.9 Percent error of  $G_{IC}^{MWLO}$  to  $G_{IC}^{CC}$  of T800H/3900-2 at room temperature.

Figure 7.10 Percent error of  $J_s$  to  $G_{IC}^{CC}$  of T800H/3900-2 at room temperature.

Figure 7.11 Percent error of  $J_s$  to  $G_{IC}^{MWLO}$  of T800H/3900-2 at room temperature.

Figure 7.12 Typical load-deflection curve of IM7/8551-7 DCB test at room temperature.

Figure 7.13  $J_s$ ,  $G_{IC}^{CC}$ , and  $G_{IC}^{MWLO}$  of IM7/8551-7 DCB specimens.

Figure 7.14 Percent error of fracture toughness from different methods for IM7/8551-7 DCB specimens.

Figure 8.1 Humidity system setup and schematic of flow cycles.

Figure 8.2 Typical moisture content with time for T800H/3900-2 specimens.

Figure 8.3 Typical output from one crack gage: (a) voltage output (b) crack speed.

Figure 8.4 Tele-Microscope System (TMS) and a sample image.

Figure 8.5 Typical load-deflection curve of T800H/3900-2 dry DCB specimen at 98°C.

Figure 8.6 Maximum normal stresses of dry DCB specimens tested at 98°C.

Figure 8.7  $J_s$  vs. crack growth of T800H/3900-2 dry DCB specimens at 98°C.

Figure 8.8 Fracture curve  $t_i(\Gamma_{II})$  of T800H/3900-2 dry DCB specimens at 98°C.

Figure 8.9 Fracture curve  $\dot{a}(K_I)$  for T800H/3900-2 dry DCB specimens at 98°C.

Figure 8.10 Load-deflection curves for T800H/3900-2 wet DCB specimens at 98°C.

Figure 8.11 Percent residual deformation to maximum deformation for T800H/3900-2 wet DCB specimens at 98°C.

Figure 8.12 Maximum normal stresses for wet DCB specimens tested at 98°C.

Figure 8.13  $J_s$  vs. crack growth for T800H/3900-2 wet DCB specimens at 98°C.

Figure 8.14 Fracture curve  $t_i(\Gamma_{II})$  for T800H/3900-2 wet DCB specimens at 98°C.

Figure 8.15 Fracture curve  $\dot{a}(K_I)$  for T800H/3900-2 wet DCB specimens at 98°C.

Figure 8.16 Load-deflection curves for 22-ply dry DCB specimens at 125°C.

Figure 8.17 Load-deflection curves for 32-ply dry DCB specimens at 125°C.

Figure 8.18 Percent residual deformation to maximum deformation for 22-ply dry DCB specimens at 125°C.

Figure 8.19 Percent residual deformation to maximum deformation for 32-ply dry DCB specimens at 125°C.

Figure 8.20 Maximum normal stresses for 22-ply dry DCB specimens tested at 125°C.

Figure 8.21 Maximum normal stresses for 32-ply dry DCB specimens tested at 125°C.

Figure 8.22  $J_s$  vs. crack growth for 22-ply dry DCB specimens at 125°C.

Figure 8.23  $J_s$  vs. crack growth for 32-ply dry DCB specimens at 125°C.

Figure 8.24 Fracture curve  $t_i(\Gamma_{II})$  for T800H/3900-2 dry DCB specimens at 125°C.

Figure 8.25 Fracture curve  $\dot{a}(K_I)$  of T800H/3900-2 dry DCB specimen at 125°C.

Figure 8.26 Pictures of residual deformation after DCB fracture tests.

Figure 8.27 Example crack tip shapes from TMS images.

Figure 8.28 Schematic of specimen cutting sequence.

Figure 8.29 Typical fracture surfaces at initiation next to the delamination insert for specimens at 125°C.

Figure 8.30 Typical fracture surfaces scan during propagation for specimens at 125°C.

Figure 8.31 Comparison of fracture surfaces during propagation for specimens tested at 0.0254mm/sec and 125°C.

Figure 8.32 Typical fracture surfaces of wet specimens at 98°C.

Figure A.1 Evaluation of various data reduction methods for material 1.

Figure B.1. Sketch of 4-point bending test.

Figure B.2. Deformed shape with FE mesh of 4-point bending specimen.

Figure B.3. Loading span ratio effects on the accuracy of the beam theory stress.

Figure B.4. Specimen thickness effects.

Figure B.5. Roller diameter effects with (a) specimen thickness 4mm and (b) specimen thickness 2mm.

Figure B.6. Stress level effects on prediction of stresses for various geometries.

## **Acknowledgement**

I would like to show my greatest appreciation from my heart to Dr. Barry D. Davidson, my advisor, who taught me the knowledge, guided my study, helped me to develop the skills, and especially trained me to be a better professional in thinking, executing, writing, and presenting. His consistent and warmhearted support is the key to the success of this work.

I would like to thank NASA Glen Research Center and the Department of Mechanical and Aerospace Engineering for funding. I would like to thank all the members of my committee as well as all the professors helping me in accomplishing the study at Syracuse University. I would also like to thank my colleague friends for the productive discussion and information.

I would like to express my endless thanks to my wife, Ping, and my Son, Evan, for their patient love and persistent supports.

# **CHAPTER 1.**

## **INTRODUCTION**

### **1.1. Problem overview**

Fiber reinforced polymeric matrix composites (PMCs) can be found in structures from sporting goods, automotive, industrial, and residential to aerospace and aircraft applications. Typically, PMCs are replacing conventional metals and unreinforced polymers because of their superior stiffness-to-weight and strength-to-weight ratios. Lamination is one of the major configurations in these PMCs. Continuous fiber reinforced composite laminates are made up of two or more laminas, or plies, stacked together at various orientations depending on the required stiffness and strength along certain directions. Individual plies are generally unidirectional or bi-directional (woven). For these composites, interlaminar delamination is a common failure mode. Here, delamination refers to cracking or debonding of the interface between plies. Delamination is a critical failure mode, as it typically leads to other structural problems such as premature buckling of the laminate, excessive vibration, intrusion of moisture, strength and/or stiffness degradation, and/or loss of fatigue life. Accurate prediction of delamination initiation and propagation is therefore necessary for the design and analysis of robust composite structures.

Delamination analysis of composites is typically carried out with the use of linear elastic fracture mechanics (LEFM), a theory originally developed for brittle fracture

analysis of glasses and metals. According to linear elastic fracture mechanics, delamination growth is predicted when the available surface energy exceeds the fracture toughness. The fracture toughness is defined as the energy required to create a new unit of surface area, commonly regarded to as the critical strain energy release rate. This is assumed to be a material property and is determined experimentally. For composite materials, experimental techniques and associated data reduction methodologies are mature for the determination of delamination toughness under those conditions where the matrix exhibits linear elastic behavior. This includes behaviors of most PMCs at low temperature and room temperature dry conditions. However, with increasing temperature and moisture, especially at temperatures approaching the material's glass transition temperature, PMC properties may become time-, loading-history, and rate-dependent. That is, the matrix begins to exhibit viscoelastic behaviors. Existing experimental methodologies that are based on LEFM are inadequate to characterize delamination fracture properties under these conditions. This is important, as PMCs are now being considered for use at higher operating temperatures; in some instances, these may approach the material's glass transition temperature. Research work is therefore necessary to better understand delamination failure and to make accurate measurements of delamination toughness under these conditions. Specifically, a new methodology is required that accounts for the viscoelastic nature of PMCs under these conditions, and can therefore be used in these cases to accurately characterize PMC delamination.

## **1.2. Objectives**

The objective of this study is to develop and verify an experimental methodology, based on linear viscoelastic fracture theory, for characterizing the delamination fracture of PMCs under conditions where viscoelastic effects are important. The study is limited to mode I (opening) delamination growth, and the focus is on the use of unidirectional lay-ups for toughness characterization. The result consists of the development and validation of an experimental approach and associated data reduction method. This new methodology is then applied to measure the mode I fracture properties of a highly toughened graphite/epoxy composite under various environmental conditions.

## **1.3. Study overview**

Chapter 2 of this dissertation presents the background on the use of linear elastic fracture mechanics in delamination prediction, and points out the deficiencies in these approaches for use under conditions where viscoelastic behaviors are present. Chapter 3 discusses viscoelastic fracture theory, reviews previous studies utilizing viscoelastic fracture mechanics in fracture prediction, and addresses both the promising aspects and the shortcomings of these approaches. Chapter 4 introduces the specific composite material used in this work. Chapter 5 develops the new fracture characterization methodology. Validation of the new methodology is performed through finite element simulation and experiments in chapters 6 and 7, respectively. In chapter 8, the approach is then applied to characterize the fracture behavior of T800H/3900-2 graphite/epoxy under temperatures approaching the material's glass transition temperature,  $T_g$ , for both



dry and moisture-saturated specimens. Conclusions from this study are summarized in chapter 9, and recommendations for future work are also given.

## **CHAPTER 2.**

# **USE OF LINEAR ELASTIC FRACTURE MECHANICS IN DELAMINATION GROWTH PREDICTION**

### **2.1. Introduction**

Delamination fracture may occur under three different loadings, referred to as opening or peel mode (mode I), forward sliding shear mode (mode II), and tearing mode (mode III). These modes are based on the relative displacements of the crack faces, as shown in Figure 2.1. The resistance to delamination growth is expressed in terms of delamination fracture toughness, which is generally measured experimentally. Numerous studies have attempted to determine delamination criterion based on the resistance to delamination due to mixed-loadings by combination of pure modes (Davidson and Zhao 2007). This study is focused on characterizing mode I delamination only.

In this chapter, the application of linear elastic fracture mechanics (LEFM) in the prediction and characterization of delamination growth is reviewed. The primary focus is the review of typical experimental approaches for the determination of the mode I toughness. The limitations of these approaches for characterizing delamination growth when viscoelasticity becomes important are also addressed.

## 2.2. Fracture parameters in LEFM

Fracture parameters are defined here as those used for fracture prediction and toughness characterization. For mode I fracture of elastic media, the three most commonly used parameters are the mode I energy release rate,  $G_I$ , the mode I stress intensity factor,  $K_I$ , and the path-independent J-integral (Broek, 1986). The critical value of these parameters, i.e., their values at the instant that crack growth initiates, is called the fracture toughness and is generally assumed to be an intrinsic material property. Additional details are presented in the following sections.

### 2.2.1 The mode I energy release rate, $G_I$

Griffith's work (1921) introduced the energy release rate to describe fracture based on an energy conservation principle. The energy release rate is defined as the decrease in total potential energy per unit area of crack extension. For pure mode I loading, the mode I energy release rate,  $G_I$ , is therefore given by

$$G_I = -\frac{\partial \Pi}{\partial A} \quad (2.1)$$

where  $A$  is the new surface area and  $\Pi$  is the potential energy. The potential energy relates to the external work done,  $W$ , on the structure and the strain energy,  $U$ , through

$$\Pi = U - W \quad (2.2)$$

For a cracked body of uniform thickness,  $B$ , under a single load input,  $G_I$  can be determined using the compliance of the body. The compliance  $C$  is defined as

$$C = \frac{\delta}{P} \quad (2.3)$$

where P is the magnitude of the applied load and  $\delta$  is the associated displacement. Using equations (2.1) – (2.3),  $G_I$  can be shown to be (Broek, 1986),

$$G_I = \frac{P^2}{2} \frac{\partial C}{\partial A} = \frac{P^2}{2B} \frac{\partial C}{\partial a} \quad (2.4)$$

where a is the crack length. Equation (2-4) is valid if crack advances along the full width of the specimen and self-similar crack growth happens. The compliance in terms of crack length is either calculated from analysis of the geometry and material properties or determined experimentally from measured load and displacement for the specimen. The derivative of compliance is then calculated or found graphically to give an expression for  $G_I$ .

A basic assumption concerning the applicability of  $G_I$  as determined from equations (2.1)-(2.4) is that the crack growth is the only process in the body that dissipates energy. If other processes not associated with crack advance occur, such as plasticity, viscoelasticity, or distributed micro cracking, then the energy release rate needs to be determined from a local analysis around the crack tip.

The critical value of the energy release rate is called the fracture toughness,  $G_{Ic}$ , which is the material's resistance to crack growth and is determined by experiments. For crack initiation and propagation to occur, the fracture criterion is

$$G_I \geq G_{Ic} \quad (2.5)$$

### 2.2.2. The mode I stress intensity factor, $K_I$

Irwin (1948) extended the Griffith theory to a crack-tip parameter for linear elastic materials. Irwin showed that there is a singular stress field around the crack tip that, for pure mode I conditions, can be expressed in terms of the mode I stress intensity factor,  $K_I$ . Crack propagation is predicted when the stress intensity factor exceeds a critical value of the material,  $K_{Ic}$ , i.e., when

$$K_I \geq K_{Ic} \quad (2.6)$$

where  $K_I$  is the stress intensity factor calculated from the geometry and loading and  $K_{Ic}$  is the critical stress intensity factor, or fracture toughness. In terms of linear elasticity,  $K_I$  is related to the mode I energy release rate for homogeneous isotropic materials through

$$G_I = K_I^2 / E' \quad (2.7)$$

For plane stress conditions,  $E' = E$ , for plane strain conditions,  $E' = E/(1-\nu^2)$ , where  $E$  is the material's Young's modulus and  $\nu$  is the Poisson's ratio. Sih et al (1965) derived a generalized relationship between the mode I energy release rate,  $G_I$ , and the mode I stress intensity factor,  $K_I$ , for homogeneous orthotropic materials when the crack plane is parallel to a plane of symmetry as

$$G_I = \left( \frac{1}{\sqrt{2E_1E_3}} \sqrt{\frac{E_1}{E_3} - \nu_{13} + \frac{E_1}{2G_{13}}} \right) K_I^2 \quad (2.8)$$

where  $E_1$  and  $E_3$  are the Young's moduli in the fiber and transverse directions respectively,  $\nu_{13}$  is the corresponding Poisson's ratio, and  $G_{13}$  is the in-plane shear modulus (Daniel and Ishai, 2001). For isotropic materials, equation (2.8) reduces to equation (2.7).

### 2.2.3. The J-integral

The J-integral as originally defined by Rice (1968) is a contour integral and for a two-dimensioned problem is given by

$$J = \int_{\partial S} \Phi dy - T_i \frac{\partial u_i}{\partial x_1} ds \quad i,j=1,2 \quad (2.9)$$

where  $\partial S$  is an arbitrary enclosed contour path around the crack tip,  $T_i$  are traction elements on the contour,  $u_i$  are displacement components of the displacement vector on the path,  $\Phi$  is the stress potential function,  $\Phi = \int_A \sigma d\varepsilon$ , and  $ds$  is the line segment along the path  $\partial S$ . The integral exists if the potential function exists and is independent of the coordinate axis along the crack propagation direction.

The J-integral is a path-independent contour integral. Thus, the path can be taken close to the crack tip, where the integral depends on the local crack tip fields, or the path can be taken along external boundaries for convenient calculation of the integral where the tractions and displacements are known.

Under mode I loading, J is equivalent to the mode I energy release rate,  $G_I$ . Prediction of crack growth using J is similar to equation (2.5), i.e.

$$J \geq J_c \quad (2.10)$$

where  $J_c$  is the critical value of  $J$ , or the fracture toughness.

#### **2.2.4. Fracture parameters in delamination prediction**

In terms of linear elastic material response, the three parameters above,  $G_I$ ,  $K_I$  and  $J$ -integral are equivalent and interchangeable. The critical values of these parameters or the fracture toughnesses are measured experimentally. In order to measure the accurate fracture toughness in terms of the stress intensity factor,  $K_I$ , the small scale yielding condition has to be satisfied. That is, the process zone ahead of the crack tip, defined here as the near-tip region where inelastic processes predominate, must be smaller than the singular zone or zone of  $K_I$ -dominance, and the zone of  $K_I$ -dominance is scaled by the characteristic dimension of the problem. In a thin unidirectional composite, the characteristic dimension is on the order of several ply thickness. The process zone, however, may be quite large compared to the thickness (Dubois and Keunings 1997; Jordan et al, 1987 and 1989). When this occurs, a zone of  $K_I$ -dominance does not exist and the small scale yielding condition breaks down. The energy release rate,  $G_I$ , and  $J$ -integral are defined based on the energy balance approach and are typically used in measurement of the delamination fracture toughness of laminates because use of area in these methods is natural for describing delamination growth, and also the experimental approaches generally don't need measurement of material properties. The next section reviews mainly experimental methods for measuring the mode I delamination toughness in terms of the energy release rate and  $J$ -integral.

## **2.3. The mode I double cantilever beam (DCB) test**

### **2.3.1 Introduction**

The mode I delamination toughness is usually measured using the double cantilever beam (DCB) test, which was standardized for fiber reinforced composites by ASTM D-5228 (1994). A schematic of the DCB test is shown in Figure 2.2, where the specimen thickness is given by  $t$ , the crack length is given by  $a$ , and the applied load is given by  $P$ . The single point loading condition of the DCB provides the ability to use a compliance calibration based data reduction procedure, which is preferred because the only assumptions that must be made are of linear elastic behavior and of self-similar crack advance. Stable crack advance occurs under displacement-controlled loading (Broek, 1986), which makes continuous measurement of fracture toughness with crack growth feasible.

### **2.3.2. LEFM-based data reduction techniques**

For the linear elastic case under consideration, a variety of data reduction methods are available for DCB tests to determine the fracture toughness. One group of data reduction method calculates the compliance from the experiments. This is referred to as the compliance calibration approach. The compliance calibration approach uses a compliance versus crack length relationship which is determined in the experiments by loading and unloading the specimen at various crack lengths. The compliance at each crack length is determined from the slope of the load versus displacement data. A least-



squares curve fit is performed on points in the plot of compliances versus crack lengths using an empirical power law form (Berry, 1963),

$$C = Ra^n \quad (2.11)$$

where R and n are constants. Substitution of equation (2-11) into equation (2-4) gives an expression for calculation of the fracture toughness (Sainath 1999; Soffa et al 2006; Davidson et al 2009a and 2009b) as

$$G_{Ic}^{CC} = \frac{nP_c^2 Ra^{n-1}}{2B} \quad (2.12)$$

where  $P_c$  is the critical load used for the toughness definition. This equation is a little different from the one used in other literature (ASTM D5228-94; Rhee et al 2000; de Chaentenay et al 1984), in which the relation  $C = \delta_c / P_c$  was substituted into equation (2-12) to define  $G_{Ic}$ ,

$$G_{Ic} = \frac{nP_c \delta_c}{2Ba} \quad (2.13)$$

Here  $\delta_c$  is the crack opening displacement at the onset of fracture. Davidson et al (2006) showed that for certain materials that showed nonlinearities prior to crack advance, the use of equation of (2-13) was somewhat problematic due to the error in measuring  $\delta_c$  and recommended the use of equation (2-12).

The second group of data reduction methods for the DCB derives the compliance in equation (2-4) using classical beam theory or modified beam theory. The classical

beam theory approach calculates the compliance from a cantilever beam rigidly fixed at the crack tip (ASTM D5228-94; Hashemi et al, 1990b). Later analyses account for the non-rigid constraint of the DCB legs at the crack tip as well as shear deformation (ASTM D5228-94; Crews et al 1986; Kanninen 1974; Aliyu and Daniel, 1985; Williams 1988, 1989a; Song and Waas 1994). Some analyses (Whitcomb 1985; Wang et al 1984; Devitt et al, 1980; Williams 1987; Kageyama 1995; Matsuda et al 1999; Hojo et al 1995) also addressed geometrical nonlinearities, that is, when the deflections of the legs of DCB specimens are large and the load-displacement relationship becomes nonlinear. This situation happens for linear elastic material response when the laminates are thin or the material has a high toughness which requires high loads for crack propagation. Williams' works (1987, 1988, 1989a, 1989b) are perhaps the most representative that consider end rotation effects at the crack tip, transverse shear effects, possible large deformations, and effects due to the finite size of the DCB's loading blocks. For the DCB setup as in Figure 2.2, the two promising expressions from Williams' work are the WLO (Williams Load only) and WLD (Williams Load & Displacement) methods, given by

$$\text{WLO:} \quad G_{Ic} = F \frac{12P_c^2 (a + \chi h)^2}{B^2 E_{11} h^3} \quad (2.14)$$

$$\text{WLD:} \quad G_{Ic} = \frac{F}{N} \frac{3P_c \delta_c}{2B(a + \chi h)} \quad (2.15)$$

In the above,  $P_c$  and  $\delta_c$  are the critical load and deflection at the crack initiation.  $F$  and  $N$  are large deformation parameters. Loading block effects include local stiffening and

moment arm shortening, which are considered in the factors F and N by the dimensions of the loading block. F and N are expressed as

$$F = 1 - \frac{3}{10} \left(\frac{\delta}{a}\right)^2 - \frac{3}{2} \left(\frac{\delta l_1}{a^2}\right) \quad (2.16)$$

$$N = 1 - \left(\frac{l_2}{a}\right)^3 - \frac{9}{8} [1 - (l_2/a)^2] \left(\frac{\delta l_1}{a^2}\right) - \frac{9}{35} \left(\frac{\delta}{a}\right)^2 \quad (2.17)$$

The factor  $\chi h$  used in equation (2.14) and (2.15) is a crack length correction that is added to the crack length in order to compensate for the crack tip rotation and traverse shear effects.  $\chi$  can be calculated from the composite orthotropic moduli  $E_{11}$ ,  $E_{22}$ , and  $G_{12}$  with the material properties directions defined in Figure 2.3,

$$\chi = \sqrt{\frac{E_{11}}{11G_{12}} \left[ 3 - 2 \left( \frac{\Gamma}{1+\Gamma} \right)^2 \right]^{1/2}} \quad (2.18)$$

$$\Gamma = 1.18 \frac{\sqrt{E_{11}E_{22}}}{G_{12}}$$

One drawback of the above approaches is that they require material properties to be determined prior to the fracture test. The accuracy of the measured toughness depends on the accuracy of these properties. Hashemi et al (1990a, 1990b) developed an experimental approach that addressed this issue.  $E_{11}$  and  $\chi$  in equations (2.14) and (2.15) are determined based on the compliance and crack length relationship from a single specimen fracture test. The compliance was derived from analysis of DCB specimen (Hashemi 1990b) and expressed as a function of crack length,

$$C = N \frac{8(a + \chi h)^3}{E_{11}^{DCB} B h^3} \quad (2.19)$$

Rearranging equation (2.19), a linear relationship between  $(C/N)^{1/3}$  and  $a$  is found as

$$(C/N)^{1/3} = k_1 a + k_2 \quad (2.20)$$

where

$$k_1 = \left( \frac{8}{E_{11}^{DCB} B h^3} \right)^{1/3} \quad (2.21)$$

$$k_2 = k_1 \chi h$$

The slope,  $k_1$ , in equation (2.20), obtained from the linear fit of  $(C/N)^{1/3}$  versus  $a$  is used to calculate the modulus  $E_{11}$  from experiments, and the slope  $k_1$  and the intercept  $k_2$  together are used to calculate the correction factor  $\chi$ . In order to apply this approach, the specimen is tested using a load-unload-reload process for propagating the crack as in the compliance calibration approach. The compliance at each crack length is determined from the slope of the load versus displacement data.

A third approach is called the area method (Hashemi et al 1990b; Charalambides and Williams, 1994). This approach determines the energy release rate from the ratio of change in strain energy to the change in crack area, i.e., from a finite approximation of equation (2.1). The basic assumption in the area method is that all of the strain energy released during crack extension goes into the fracture process. However, this is not the case when other energy consuming processes occur such as viscoelastic deformation or distributed damage (micro-cracks) away from the crack tip. Typically these processes are

not significant for unidirectional composites tested under room temperature; however, they are more likely to happen under elevated temperature conditions. Another disadvantage of the area method is that the average toughness is determined over some values of crack growth increment, and is therefore imprecise and leads to scattered results (Hashemi et al 1990b).

The last group of LEFM based data reduction methods use the value of the J-integral as a fracture parameter. A  $J_c$ -estimation procedure was developed during the early 1970s (Landes and Begley 1972, Bucci et al 1972, Rice et al 1973) using multiple specimens. Fracture toughness  $J_c$  was determined from the relationship of the J-integral versus the displacements from testing multiple specimens, as well as the critical displacement at the fracture in the fracture test. This procedure is time-consuming and costly. In addition, a large amount of curve-fitting processes are involved and there are inherent errors in this process. Based on the definition of the integral, a closed-form solution in terms of the DCB geometry was derived for a composite material without the assistance of computational simulation. Yamada (1988) developed an explicit expression of J for a DCB specimen by analyzing a cantilever beam on an elastic-plastic foundation. The complexity of the expression caused difficulties in experiments for determining all the parameters accurately. Anthony and Paris (1988) developed a simple expression for a double cantilever beam along the path of the boundary of the specimen.  $J_c$  was calculated as a function of the critical force,  $P_c$ , and the end rotation angle,  $\theta_c$ , at the delamination initiation instant as,

$$J_c = \frac{2P_c\theta_c}{B} \quad (2.22)$$

Anderson and Stigh (2004) derived the same expression. Williams (1987) presented a different expression that accounted for large deflection in an elastic DCB specimen as

$$J_c = \frac{2P_c \sin(\theta_c)}{B} \quad (2-23)$$

Williams' analysis was based on nonlinear beam theory for a linear elastic material. Goetz (1988) developed a more general expression of J-integral along the path through any cross sections of the DCB beam. He obtained the same expression as in equation (2-23) based on analysis of a general beam with mid-plane straining when the integral path was chosen along the DCB boundary surfaces. Goetz applied the expression of J-integral in DCB fracture tests to determine mode I delamination toughness of multidirectional composite laminates. The equation (2.23) can be approximated by equation (2.22) when DCB specimens have small end rotation angle at the critical load  $P_c$ , that is,  $\sin(\theta_c) \approx \theta_c$  when  $\theta_c$  is small. Equation (2.23) is more accurate to determine J from DCB specimens, especially when large deflection occurs.

### **2.3.3. Use of LEFM in delamination toughness measurements**

In this subsection, results in the literature from DCB tests that are relevant to the present study are reviewed. LEFM based data reduction methods reviewed in the preceding section were used in these works to determine the mode I delamination toughness.

The interlaminar delamination toughness has been shown to be dependent on the toughness of the matrix material (Hunston 1984; Hunston et al 1987). Mechanisms

involving the fibers increase the resistance to the delamination growth in the composite, but the properties variation of the polymeric matrix with temperature and moisture content is an important source of the variation of the composite toughness. A number of works evaluated environmental effects like temperature and moisture effects on the composite toughness variation (de Charentenay et al. 1984; Davies and de Charentenay 1987; Garg and Ishai 1985; Cowley and Beaumont 1997; Russell and Street 1985; Asp 1998; Soffa et al 2006). A general trend was found that the mode I toughness increased with increasing temperature and moisture content. This trend was commonly explained by the increasing matrix plasticization and ductility in the polymeric matrix.

Aside with above works, some researchers conducted experiments at different displacement rates. Gillespie et al (1987) and Smiley and Pipes (1987), studied graphite fiber reinforced poly (ether ether ketone) thermoplastic composite, AS4/PEEK, and a graphite/epoxy composite, AS4/3501-6, over a range of displacement loading rates at room temperature. Results showed a loading rate dependence of the toughness of AS4/PEEK while the toughness of AS4/3501-6 composites was found to be insensitive to the loading rate. The authors concluded that the graphite/epoxy composite behaved in a linear elastic manner until fracture, but the rate dependent toughness of graphite/PEEK was ascribed to plastic and viscoelastic effects in the process zone around the crack tip. Aliyu and Daniel (1985) found out that mode I toughness of AS4/3501-6 composite showed fracture toughness increased with increasing crack growth rate. If the proportional relationship between crack growth rate and loading rate is applied, then the results from Aliyu and Daniel (1985) contradict the results by Gillespie et al (1987) and Smiley and Pipes (1987). The different trends are possibly due to the different test

procedures occupied in different works. Both Gillespie et al (1987) and Smiley and Pipes (1987) conducted the tests with traditional load-unload-reload procedure at each loading rate while Aliyu and Daniel (1985) performed the test using continuously loading process. The rate-dependent toughness as found from the work (Aliyu and Daniel 1985) indicated that inelastic fracture process occurred in the AS4/3501-6 composite, however, the traditional load-unload-reload procedure neglects the potential time-history effect and might cause questionable results.

Kusaka and coworkers (1998) conducted fracture tests using a continuously loading procedure, which eliminated the concerns of unloading effects of inelastic material response. They observed that the fracture toughness  $G_{Ic}$  of a carbon fiber/epoxy composite, T300/2500, at room temperature decreased stepwise with increasing loading rate. This work incorporated the kinetic energy during crack propagation in the energy release rate calculation to explain the rate dependence of the fracture toughness.

Rate effects on fracture toughness were also evaluated over a large range of temperatures (from room temperature to a temperature approaching the material's  $T_g$ ) so that a master curve could be created using the time-temperature equivalence postulate (Frassine and Pavan 1995; Frassine et al 1996a; Fracasso et al 2000). The work from Frassine and Pavan (1995a) showed the fracture toughness of a carbon fiber reinforced polyetherimide (PEI) thermoplastic composite increased with increasing crack growth rate, but the reverse result was noticed by the work from Fracasso et al (2000), in which the fracture toughness of a carbon fiber reinforced poly (ether ether ketone) CF/PEEK laminate decreased with increasing crack growth speed. Frassine et al (1996a) also found



the toughness of the carbon/PEEK decreased with increasing crack growth rate. The mode I toughness on CF/PEEK as a function of the displacement rate from Fracasso et al (2000) showed the similar trends as previous works (Gillespie et al 1987; Smiley and Pipes 1987). There are different trends for two thermoplastic composites. The hypothesis for different trends of rate dependency of two thermoplastic composites was that the delamination of PEI-based composite might involve a diffuse far-field viscoelastic behavior of the material, especially at the temperature approaching material  $T_g$ , while the rate dependency of PEEK composite was due to the local material effects within the process zone around the crack tip. Besides this hypothesis, the rate-dependent results can be questionable because all these works used a load-unload-reload procedure that ignored the time-dependent nature of the system.

Wang et al (1998b) studied the rate and temperature effects on the fracture toughness of a high temperature polymer composite material, carbon/polyamide, IM7/LaRC-RP46. Fracture toughness increased with increasing temperature below  $T_g$ , but dropped greatly when temperature was beyond  $T_g$ . The authors noticed the fracture toughness decreased with increasing crack growth-rate, but no distinct trend could be quantified from that work when the proportional effect of loading rate on the crack growth rate was removed out.

Ashcroft et al (2000) evaluated the mode I fracture of epoxy adhesive bonded composite joints at low, room and high temperatures. At low and room temperatures, linear elastic response was noticed and no rate-dependency was found. At higher test temperatures where nonlinearity was observed, the fracture tests exceeded the limits of

linear elastic fracture mechanics. So the delamination toughness determined from LEFM-based data reduction methods was questionable.

## **2.4. Conclusion**

Traditional data reduction methods for the double cantilever beam test are derived using linear elastic fracture mechanics principles. The energy release rate is the most commonly accepted parameter for characterizing delamination toughness. Under conditions of linear elastic material response, LEFM-based data reduction procedures may be used to determine a composite's fracture toughness with high confidence. However, with changes in environmental (elevated temperature and/or moisture) loads or loading conditions (particularly loading rate), the fracture toughness shows dependencies on the loading rate and crack growth rate. Previous test results have indicated inelastic material responses such as viscoelasticity or plasticity are likely involved in the PMC delamination fracture process. However, LEFM-based delamination growth analyses and data reduction procedure usually neglect these effects.

Thus, in summary, the above studies show that inelastic fracture phenomena are often involved in PMC delamination growth, but approaches other than LEFM are seldom used. When inelastic response is observed, especially when the viscous nature of the matrix dominates the crack propagation, the time- and rate- factors should be accounted for in the fracture characterization. Therefore, in order to fully characterize delamination properties, a more general methodology with consideration of viscoelastic nature of the fracture process needs be developed. In the next chapter, the available viscoelastic theory from the literature is reviewed, with the goal of obtaining an

appropriate viscoelastic theory for use in explaining the rate dependencies that are observed.

## **CHAPTER 3.**

# **USE OF VISCOELASTIC FRACTURE MECHANICS IN DELAMINATION GROWTH PREDICTION**

### **3.1. Introduction**

Polymeric materials generally exhibit time- and temperature-dependent behaviors (Ferry 1961). The stress-strain relationship follows neither Hooke's law for elastic solids nor Newton's law for viscous liquids. Stress is proportional to both rate of strain and the strain itself. Viscoelastic constitutive laws have been developed and are applicable to these materials for representing the stress dependence on both strain and rate of strain (Christensen 1971). Linear viscoelastic behaviors are applicable when the ratio of stress to strain is a function of time only, and not of stress magnitude. This is generally the case when the strain and rate of strain are infinitesimal. If the ratio also depends on stress level, then a nonlinear viscoelastic constitutive law is required. In terms of polymeric matrix composites (PMCs) under static loading conditions, due to the reinforcing effects from the high stiffness elastic continuous fibers, the strain and rate of strain in the composite structure are typically within the infinitesimal assumption. Therefore, linear viscoelastic theory is focused on in this work. The focus of this chapter is to find a linear viscoelastic theory that can be applied to experimentally characterize delamination growth in PMCs. To this end, the available viscoelastic fracture theories and their

application in characterizing linear viscoelastic fracture properties are reviewed and the most promising approach is identified.

## **3.2. Linear viscoelastic fracture analysis and characterization**

### **3.2.1. Viscoelastic fracture mechanics overview**

Fracture prediction is done by comparing the stress intensity factor  $K_I$ , energy release rate  $G_I$  or path-integral  $J$ , to the fracture toughness for linear elastic materials; however, for viscoelastic materials, crack growth prediction has to account for the materials' time- and rate-dependent properties. The fracture parameters like  $K_I$ ,  $G_I$  and  $J$  are possibly dependent on the rate and time-history. Early works discovered some important aspects of fracture of viscoelastic media. For example, that the crack initiation depended on loading history (Williams 1965) and that the work of fracture was a function of crack growth speed (Vincent and Gotham, 1966). Kostrov and Nikitin (1970), following the lead of Dugdale (1960) and Barenblatt (1962) for time-independent materials, indicated that a process zone needed to be introduced ahead of the crack if the time dependence of the fracture process was to be properly modeled. Based on these works, crack growth equations were developed to relate the fracture parameters to the fracture energy,  $\Gamma_I$ , which is the driving force dominating the crack growth in a viscoelastic material, and the crack growth rate  $\dot{a}$  (Knauss 1970; Schapery 1975a, 1975b, and 1975c; Christensen 1979 and 1981). It was found (Schapery 1975) that for a stress intensity factor  $K_I$  below some critical value,  $K_{Ie}$ , crack growth will not occur. When  $K_I$  is above some critical value,  $K_{Ig}$ , crack growth will proceed at a very rapid speed, under which failure will generally occur. For  $K_{Ie} < K_I < K_{Ig}$ , crack growth will occur at some finite

speed. In this case, a crack growth equation (Schapery 1975) is applied for predicting crack initiation time and crack speed. Initiation time is generally defined as the time required from the point of load application until the material at the crack tip just begins to fail. Figure 3.1 illustrates the crack growth rate dependency of the stress intensity factor  $K_I$  (Schapery 1975). For many materials, the fracture energy may also depend on the crack growth speed (Swanson 1976). This implies for general viscoelastic fracture mechanics (VEFM) problems, it is necessary to have an experimentally derived curve relating the fracture energy to crack speed, or else relating the critical stress intensity factor to crack speed such as presented in Figure 3.1 (i.e., if the  $K_I$  vs.  $\dot{a}$  relation is known, then the  $\Gamma_I$  vs.  $\dot{a}$  relation may be derived from the crack growth equation). Also note that these curves are temperature dependent, i.e., it is often necessary to develop curves such as that presented in Figure 3.1 over a range of temperatures.

### **3.2.2. Requirements for application of VEFM to PMCs**

Application of VEFM in characterizing fracture of viscoelastic PMCs requires the experimental crack growth curves such as  $K_I$  vs.  $\dot{a}$  as described above. This requires a knowledge of  $K_I$  for the experimental configuration. If an analytical or experimental solution for  $K_I$  is unavailable for the test configuration, one can compute  $K_I$  using the finite element method (Liang and Zhou, 1997; Wang et al, 1998a; Dubois and Petit, 1999 and 2005; Park, 2004). This procedure, however, is impractical for the purpose of determining PMC VEFM crack growth curves because, for viscoelastic problems, the reliability of the finite element results depends on the level of agreement between the assumed material properties for the simulation and the real structural properties. It might

be acceptable for isotropic materials, but difficulty is generally encountered due to the variation of material properties when working on composites, especially under harsh environments like elevated temperatures. Thus, it is preferable if the fracture parameter such as  $K_I$  can be determined from experiments. One can select a test configuration that has a closed-form solution of the fracture parameter in linear elastic material. Additional analysis work is then required to develop the solution for evaluating linear viscoelastic material fracture. Different approaches for doing this are described in the literature are reviewed in the following subsection.

### **3.2.3. Previous work**

The test configuration for Griffith's problem is an infinite strip with a center crack subjected to far field constant stress. It was used in early works (Knauss 1970; Christensen 1979 and 1981) to illustrate the dependency of fracture parameters on crack speed using experimental data. Knauss (1970) performed the tests under various temperatures that were all above the glass transition temperature so that the material far from the crack tip was always in the rubbery regime. Christensen (1979 and 1981) solved the Griffith problem at two extreme cases of high- and low-rate conditions so that he could determine the global energy directly from experiments. Thus, these works chose certain conditions in order to simplify the calculation of the fracture parameters. However, the application of this test configuration under more general conditions is still not clear, and the geometry is very difficult to use for delamination characterization in laminated composites.

The SE(T) test, consisting of single edge notched specimens loaded in tension, has a closed-form solution and allows the direct computation of the history and instantaneous value of  $K_I$  from experiments. Crack growth curves following the theory of Schapery (1975) and Christensen (1981) were determined for isotropic polymers using experimental data (Frassine et al 1990; Frassine et al 1996b). Gamby and Delaunay (1997) applied Schapery's extended theory (Brockway and Schapery 1978) for composite materials to study the steady-state crack propagation in a continuous carbon-fiber/epoxy-matrix composite using a tapered double cantilever beam (TDCB) specimen under a constant-velocity opening. Here, the energy release rate is constant during crack propagation if the height of the specimen and the crack length keep a constant relationship. Then the stress intensity factor can be determined based on the energy release rate with measured material properties. However, both SE(T) and TDCB tests are inapplicable to characterize delamination growth in composites.

Besides the above works that utilized test configurations with known closed-form solutions, some works applied the Laplace transform in a linear viscoelastic medium to analyze the stationary crack problem in the linear elastic domain (Lee et al. 1996, 2005; Linkov 1994; Arai et al, 2007). Complex solutions were achieved from advanced mathematical derivations for simple geometries. Comparisons between the analytical solution and numerical simulation results were performed for stationary cracks in simple specimen geometries. However, these works do not consider crack growth.

The double cantilever beam (DCB) test configuration that is widely used to determine mode I delamination toughness of linear elastic PMCs has been used to



determine the rate dependency of delamination growth (Plausinis and Spelt 1995; Devitt et al 1980). Crack growth curves following Schapery's linear viscoelastic fracture theory (Schapery 1975) were generated. These works assumed globally elastic material response outside the delamination tip region so that the LEFM-based approaches could be used to determine the fracture parameters. However, these works lacked verification from associated experiments on material properties to determine whether the assumption that the viscoelastic response was fully constrained within the process zone was valid.

### **3.2.4. Most promising approaches**

As reviewed above, crack growth curves based on Schapery's theory (Schapery 1975) and Christensen's theory (Christensen 1979 and 1981) have been determined experimentally using various assumptions in the material's response. The application of Christensen's theory, however, is strictly limited to a particular test configuration (Gamby and Chaoufi 1999), while fracture curves based on Schapery's viscoelastic fracture theory can be established for different test configurations, especially for experimental tests to determine delamination growth curves in PMCs. Therefore, the following sections review Schapery's linear viscoelastic fracture theory and investigate the necessary information needed in our study in order to develop an experimental approach *without* using the assumption of globally linear elastic material response.

### 3.3. Schapery's linear viscoelastic fracture theory

In this section, Schapery's linear viscoelastic theory is reviewed in detail. The fracture energy is defined first, and then the focus is on introducing the crack growth equations developed from the theory.

#### 3.3.1 Fracture energy

Schapery (1975) defined the fracture energy in a linear viscoelastic medium based on a local stress analysis. For mode I, Schapery's criterion takes the form

$$2\Gamma_I = \int_0^\alpha \sigma_i(\xi) \frac{\partial \Delta u_i(x, \xi)}{\partial \xi} d\xi \quad (3.1)$$

In the above, a Barenblatt-type cohesive zone is assumed as shown in Figure 3.2,  $\alpha$  is the cohesive zone length,  $\sigma_i(\xi) = \sigma_{yy}(x, y=0, t)$  along the crack faces within the cohesive zone,  $\Delta u_i(x, \xi)$  is the crack separation displacement, and  $\Gamma_I$  is the fracture energy. If a Dugdale cohesive zone is assumed, i.e., constant stress within the cohesive zone, the fracture energy takes the form

$$2\Gamma_I = \sigma_f \Delta u_f \quad (3.2)$$

where  $\sigma_f$  is the failure stress in the Dugdale cohesive zone and  $\Delta u_f$  corresponds to the crack separation displacement at the tip,  $\xi = \alpha$ . With the variable transformation,  $\xi = \xi(x, t) = a(t) - x$  for the crack tip region as in Figure 3.2, the fracture energy may be transformed from equation (3.1) to the time domain as

$$2\Gamma_I = \int_{t_1}^{t_2} \frac{\partial \Delta u_i(\tau)}{\partial \xi} \sigma_i(\tau) d\tau \quad (3.3)$$

where  $t_1$  and  $t_2$  give the time period when the crack grows the length of the cohesive zone, i.e.,  $t_1$  is the time when the crack tip arrived the element, and  $t_2$  is the time the right end of the process zone is arrived.  $a(t)$  is the crack length at the time  $t$ . This is the same expression that Schapery (1984) proposed for a general viscoelastic material based on the work input to the process zone,  $W_f$ , where  $W_f=2\Gamma_I$ .

Schapery proposed two methods in developing the crack growth equations. One is based on the instantaneous stress intensity factor,  $K_I$ , (Schapery 1975), and the other is based on a generalized J-integral,  $J_v^R$ , (Schapery 1984). The following subsections review these two methods separately for the analysis of crack initiation and crack propagation.

### 3.3.2 Stress intensity factor method

Derivation of the crack growth curves from the stress intensity factor,  $K_I$ , was firstly introduced for isotropic materials (Schapery 1975a, 1975b, 1975c). Later, with the use of the results by Biot (1972) on the equivalent response between an orthotropic and isotropic structure, the  $K_I$ -method was extended to composite materials (Brockway and Schapery, 1978).

#### 3.3.2.1 Crack initiation criterion

From the fracture energy definition in equation (3.2), Schapery (1975b) obtained an implicit equation to predict crack initiation as

$$2\Gamma_{ii} = (1/4)C_v^{(2)}(t_i)K_I^2 \quad (3.4)$$

where  $\Gamma_{ii}$  is fracture initiation energy, and  $t_i$  is the crack initiation time when the crack starts propagating.  $K_I$  is the instantaneous stress intensity factor;  $C_v^{(2)}(t)$  is called the secant creep compliance and is defined from the history of the stress intensity factor as

$$C_v^{(2)}(t) = \frac{1}{K_I^2(t)} \int_0^t C_v(t-\tau) \frac{dK_I^2(\tau)}{d\tau} d\tau \quad (3.5)$$

where  $C_v(t) = 4(1-\nu^2)D(t)$ ,  $\nu$  is the Poisson's ratio and  $D(t)$  is the creep compliance from uniaxial tensile loading. The crack initiation time,  $t_i$ , is implicitly included in the equation (3.4). Based on the form of creep compliance, an explicit expression of crack initiation time may be determined if the stress intensity factor can be expressed in an analytical form. The fracture initiation energy can be constant or time-dependent.

### 3.3.2.2 Crack growth criterion

In equation (3.1), the fracture energy is defined within the cohesive zone in Figure 3.2. The cohesive zone length,  $\alpha$ , is calculated using the mode I stress intensity factor,  $K_I$ , as

$$\alpha = (\pi/2)(K_I / \sigma_m I_1)^2 \quad (3.6)$$

where  $\sigma_m I_1$  is the integral of the failure stress distribution over the failure zone. For a steady-state crack propagation problem, when the slope of logarithmic plot of creep compliance and time is small, Schapery (1975b) derived the crack growth equation as

$$\Gamma_I = (1/8)C_v(t_\alpha)K_I^2 \quad (3.7)$$

where  $t_\alpha = \alpha/3\dot{a}$  is called the effective time and  $\dot{a}$  is the crack growth speed. Equation (3.7) is an implicit function of crack speed. For a specific form of  $C_v(t)$ , equation (3.7) may be used to obtain  $\dot{a}$  explicitly as a function of the instantaneous stress intensity factor  $K_I$  and fracture energy,  $\Gamma_I$ . For example, for a power law material where  $C_v(t)=C_1t^n$ , Schapery (1975b) derived an explicit relationship of the stress intensity factor and the crack speed as

$$\dot{a} = AK_I^{2(1+1/n)} \quad (3.8)$$

where

$$A = \frac{\pi}{6} \left[ \frac{C_1}{8\Gamma_I (\sigma_m I_1)^{2n}} \right]^{1/n} \quad (3.9)$$

Accordingly, if the creep compliance takes other forms, then other expressions for crack speed may be derived (Schapery, 1975).

In the above derivation of equations (3.8) and (3.9), the fracture energy,  $\Gamma_I$ , the quantity  $\sigma_m I_1$ , and the crack speed,  $\dot{a}$ , are assumed to be constant during the time in which the crack grows the length of the cohesive zone,  $\alpha$ . However,  $\Gamma_I$  and  $\sigma_m I_1$  are not necessarily constant during all growth histories and may be dependent on the time and crack speed (Swanson, 1976).  $\Gamma_I$  and  $\sigma_m I_1$  in the cohesive zone are also functions of

environmental conditions such as temperature and moisture. They are, however, independent of geometry and loading.

For the case where  $\Gamma_I$  and  $\sigma_m I_1$  are not functions of crack speed, the coefficient A in equation (3.9) is independent of crack speed. In this case, equation (3.8) may be used to predict crack speed from the instantaneous value of  $K_I$  for different geometries. Here, the crack growth curve,  $\dot{a}(K_I)$ , is established experimentally. When  $\Gamma_I$  is not constant and can be expressed as a function of crack speed, expressions similar to (3.8) can be derived (Swanson 1976; Davidson 1990).

Brockway and Schapery (1976) extended the stress intensity factor method from isotropic to orthotropic media. Biot (1972) showed an equivalent displacement response on a half space subjected to the same sinusoidal surface traction for an orthotropic material and an equivalent isotropic material. Brockway and Schapery (1976) utilized this relationship in linear viscoelastic orthotropic materials based on p-multiplied Laplace transform of material properties. Equivalent linear viscoelastic properties or equivalent compliance,  $\kappa_{\alpha\beta}$ , are determined by inverting its p-multiplied Laplace transform

$\tilde{\kappa}_{\alpha\beta} = p \int_0^{\infty} e^{-pt} \kappa_{\alpha\beta}(t) dt$ . Under the Laplace domain,  $\tilde{\kappa}_{\alpha\beta}$  is derived as

$$\tilde{\kappa}_{\alpha\beta} = \frac{\delta B_{\alpha\beta}}{B \tilde{C}_{66}}, \quad B = \det(B_{\alpha\beta})$$

(3.10)

with

$$\delta = \tilde{C}_{11} + \tilde{C}_{66}\lambda_1\lambda_2, \quad B_{11} = \tilde{C}_{22}(\lambda_1 + \lambda_2)\lambda_1\lambda_2$$

$$B_{12} = \tilde{C}_{12}\lambda_1\lambda_2 - \tilde{C}_{11}, \quad B_{22} = \tilde{C}_{11}(\lambda_1 + \lambda_2)$$

where  $\lambda_1$  and  $\lambda_2$  are given by

$$\lambda_1 = [q + (q^2 - r^2)^{1/2}]^{1/2}, \quad \lambda_2 = [q - (q^2 - r^2)^{1/2}]^{1/2}$$

$$2q = [\tilde{C}_{11}\tilde{C}_{22} - 2\tilde{C}_{66}\tilde{C}_{12} - \tilde{C}_{12}^2]/(\tilde{C}_{66}\tilde{C}_{22}), \quad r = (\tilde{C}_{11}/\tilde{C}_{22})^{1/2}$$

In the above,  $\tilde{C}_{ij}$  ( $i,j=1,2,\dots,6$ ) are the terms in the stiffness matrix that relate elastic stress and strain in the Laplace domain and which follows the orthotropic constitutive law for a composite (Daniel and Ishai, 1994). For a plane problem with compliance matrix  $\tilde{S}_{ij}$  ( $i,j=1,2,\dots,6$ ),

$$\tilde{C}_{11} = \tilde{S}_{22}/\tilde{D}, \quad \tilde{C}_{22} = \tilde{S}_{11}/\tilde{D}, \quad \tilde{C}_{12} = -\tilde{S}_{12}/\tilde{D}, \quad \tilde{C}_{66} = 1/\tilde{S}_{66}$$

where

$$\tilde{D} = \tilde{S}_{11}\tilde{S}_{22} - \tilde{S}_{12}^2$$

For plane stress problems,

$$\tilde{S}_{11} = 1/\tilde{E}_{11}, \quad \tilde{S}_{22} = 1/\tilde{E}_{22}, \quad \tilde{S}_{12} = -\nu_{12}/\tilde{E}_{11}, \quad \tilde{S}_{66} = 1/\tilde{G}_{12}$$

For plane strain problems,

$$\tilde{S}_{11} = \frac{1}{\tilde{E}_{11}}(1 - \nu_{12}^2 \frac{\tilde{E}_{22}}{\tilde{E}_{11}}), \quad \tilde{S}_{22} = \frac{1}{\tilde{E}_{22}}(1 - \nu_t^2), \quad \tilde{S}_{12} = -\frac{\nu_{12}}{\tilde{E}_{11}}(1 + \nu_t), \quad \tilde{S}_{66} = \frac{1}{\tilde{G}_{12}}$$

where  $\tilde{E}_{11}, \tilde{E}_{22}, \tilde{G}_{12}, \tilde{\nu}_{12}$  are the p-multiplied Laplace transforms of viscoelastic relaxation properties,  $E_{11}(t), E_{22}(t), G_{12}(t)$  and  $\nu_{12}(t)$ .  $\nu_t$  is the so-called “transverse Poisson’s ratio” that relates  $S_{23}(t)$  to  $S_{22}(t)$  (Brockway and Schapery, 1978).

For mode I crack growth problems, Brockway and Schapery (1978) derived the simple expression for mode I fracture in general linear viscoelastic polymeric composites as

$$\Gamma_I = (1/4)\kappa_{22}(3\alpha/\dot{a})K_I^2 \quad (3.11)$$

This is a similar result as in equation (3.7) for isotropic materials except that the creep compliance is replaced by equivalent viscoelastic properties. Equation (3.11) is an implicit function of crack growth speed  $\dot{a}$  and the discussion of equation (3.7) for isotropic materials can be used to guide the use of the method to predict crack growth speed in composites.

### 3.3.2.3. Application of the $K_I$ -method

The  $K_I$ -method, i.e., directly obtaining  $\dot{a}(K_I)$  through a knowledge of  $K_I$ , has been applied in determining crack growth curves in the literature. This was introduced in section 3.2.3, but additional details of these works are discussed here in order to extract information that is key to this study, such as the procedure to determine the crack growth curves, the evaluation of the results, and the feasibility of the  $K_I$ -method in composites.



The works from Frassine et al (1990, 1996b) present a typical procedure to determine the crack growth curves for isotropic materials using the  $K_I$ -method. A series of tests were performed in characterizing linear viscoelastic fracture in isotropic polymers, such as creep tests and SE(T) tests at different loading rates, different temperatures and different loading histories. The SE(T) specimen was used in these studies which enabled the determination of  $K_I$  from the far field loading and crack geometry using a closed-form solution. Therefore, the difficulty of differentiation of the stress intensity factor with respect to time was avoided. The explicit expressions of equations (3.4) and (3.8) were determined from the measured creep compliances, and then were compared to the experimentally determined crack growth curves,  $t_i(\Gamma_{II})$  and  $\dot{a}(K_I)$ . In both works, a time-temperature superposition principle (Ferry 1961) was used to create a master curve for the measured creep compliance over the range of temperatures covering the material glass-rubbery transition. This technique allows the material properties to be determined over the long period of time at one temperature based on the time-temperature equivalence. The same technique was applied to create the master curve as in Figure 3.1 using the measured fracture curve at each temperature (Frassine et al 1990, 1996b).

Use of the above procedure resulted in just qualitative agreement between the measured fracture curve,  $\dot{a}(K_I)$ , and theoretical prediction in the work of Frassine et al (1990). The slope of the measured curve from the log-log plot of  $\dot{a}(K_I)$  was almost double the prediction from the theory. No explicit explanation was provided by Frassine et al (1990) about this disagreement. Actually, the material used in that study (Frassine et al 1990) was a “flexible” thermosetting epoxy with the measured exponent of the creep

compliance in the range of 0.38~0.5. This is a comparable large slope for Schapery's linear viscoelastic theory to be applicable. The explicit expression in equation (3.8) requires that the creep compliance slope in a power law polymer should be at the lower end of the range 0~0.5 (Schapery 1975b). In addition, the authors (Frassine et al 1990) lacked the verification if the measured creep compliances were within the scope of linear viscoelasticity (at least not described in the paper). It is highly possible that the response of that material already stepped into the nonlinear viscoelastic field and a different method such as the generalized J-integral (Schapery 1984) should be used.

On the other hand, use of the above procedure resulted in good correlation between the experiments and the Schapery's theoretic prediction in the work by Frassine and coworkers (1996b). In that study, two other thermosetting polymers were used. Although limited information about the material properties was discussed in the paper (linearity check of viscoelasticity was not available), Frassine and coworkers (1996b) did some very important explorations to show that the Schapery's linear viscoelastic theory could be applicable. They investigated the time-dependence, loading history dependence and temperature-dependence in the application of both the crack initiation criterion and crack growth criterion, which are important aspects for a theory to be transferable from the test loading condition to the physical structural and thermal loadings. Provided that work also included a different test configuration and reproduced the fracture curve, that work would have experimentally shown the measured fracture curves could be transferred from a test configuration to physical structures.

The key requirement of the above procedure is that the  $K_I$  needs be determined for the test geometry from a closed-form solution. This requirement is hard to meet for composites due to the complexity of the orthotropic experiments and the dependency of  $K_I$  on material properties. For a linear elastic composite,  $K_I$  is usually determined from the relationship to the energy release rate (equation 2.8). For linear viscoelastic composites, the determination of  $K_I$  is rarely found in the literature and the method needs further investigation. Gamby and Delaumenie (1997) determined  $K_I$  of a tapered DCB specimen for a linear viscoelastic carbon fiber/epoxy composite using equation (2.8). Then, equation (3.11) was used to find the fracture energy during crack propagation. Equivalent creep compliance in equation (3.10) was derived from the measured orthotropic linear viscoelastic properties. Different from the works of Frassine et al (1990, 1996b), Gamby and Delaumenie (1997) did verify the material's linear viscoelastic response by performing creep tests at different loading levels. In order to obtain the explicit fracture energy during crack propagation, which is not needed when only prediction of the crack growth speed is required (Schapery 1975), the cohesive zone length was calculated using the measured failure strength from testing  $90^\circ$  specimens. Gamby and Delaumenie (1997) obtained a decreasing fracture energy with increasing crack growth speed, which could be described by Schapery's theory. However, two things might weaken the conclusion stated by the authors (Gamby and Delaumenie 1997). One is that the calculation of the stress intensity factor used the linear elastic modulus even though the material had been shown to be viscoelastic. The modulus relaxation effects during the fracture tests were ignored. The other is a constant cohesive zone length assumed in deriving the fracture energy. No physical evidence or test

monitoring results were provided that could ensure the constant cohesive zone length during crack propagation. Actually, Schapery's linear viscoelastic theory removed this assumption (Schapery 1975). Therefore, Schapery (1975) suggested that fracture curve  $\dot{a}(K_I)$  could be used in the structural analysis, which avoided the difficulties in measuring the intrinsic material properties of the cohesive zone (such as fracture energy, stress distribution in the zone, and cohesive zone length).

The  $K_I$ -method was successfully applied in isotropic materials such as in the work by Frassine et al (1996b), but encountered problems in characterizing linear viscoelastic delamination growth in composites because of the difficulty to determine  $K_I$  from experiments. Therefore, the other method, the generalized J-integral (Schapery, 1984, 1989, 1990) is introduced in the following section.

### **3.3.3 Generalized J-integral method**

The generalized J-integral method was initially developed for nonlinear viscoelastic fracture analysis (Schapery, 1984, 1989, 1990), but it is also applicable to the linear viscoelastic problem. In what follows, correspondence principles are first introduced. This is followed by introduction of the generalized J-integral and a discussion of how the method is used to predict crack initiation time and growth rate.

#### **3.3.3.1 Correspondence principles**

Schapery (1984) developed the correspondence principles with use of the heredity integrals. The stress ( $\sigma_{ij}$ ) and displacement ( $u_i$ ) in a viscoelastic problem are related to the corresponding terms in an elastic problem, which are called pseudo parameters, such as

“pseudo stress”,  $\sigma_{ij}^R$ , and “pseudo displacement”,  $u_i^R$ , respectively through the following equations

$$u_i^R = \{Edu_i\}, u_i = \{Ddu_i^R\} \quad (3.12)$$

$$\sigma_{ij}^R = \{D_1d\sigma_{ij}\}, \sigma_{ij} = \{E_1d\sigma_{ij}^R\} \quad (3.13)$$

where

$$\{Edf\} = E_R^{-1} \int_0^t E(t-\tau, t) \frac{\partial f}{\partial \tau} d\tau \quad (3.14)$$

$$\{Ddf\} = E_R \int_0^t D(t-\tau, t) \frac{\partial f}{\partial \tau} d\tau \quad (3.15)$$

In the above,  $f=f(t,x)$  is a time-dependent function, and  $E_R$  is a free constant which has the same units as modulus.  $E(t)$  and  $D(t)$  are the material's relaxation modulus and creep compliance, respectively.

Three correspondence principles were introduced for different problems (Schapery, 1984). They are based on different boundary conditions to solve the governing equations. For our crack growth problem in a viscoelastic medium, the surfaces with traction boundary increase with time. The correspondence principle II gives the solution as

$$u_i = \{Ddu_i^R\}, \text{ and } \sigma_{ij} = \sigma_{ij}^R \quad (3.16)$$

Where  $u_i^R$  and  $\sigma_{ij}^R$  satisfy the elastic problem on the same geometrical model with boundary conditions as

$$T_i^R = T_i \quad \text{on traction boundaries} \quad (3.17)$$

$$U_i^R = \{EdU_i\} \quad \text{on displacement boundaries} \quad (3.18)$$

Here  $T_i$  and  $U_i$  are the specified traction and displacement boundary conditions on the viscoelastic problem and  $T_i^R$  and  $U_i^R$  are the transformed boundary conditions in the reference elastic problem. The elastic problem usually has no physical meaning and is only referenced for solving the viscoelastic problem. It may be a nonlinear elastic problem corresponding to the nonlinear viscoelastic problem (Park, 2004) or be a linear elastic problem if the body of interest has its response within the linear viscoelastic regime.

### 3.3.3.2 Generalized J-integral

In the pseudo elastic problem, Schapery (1984) defined a path independent integral, the generalized J-integral,  $J_v^R$ , as the line integral outside the process zone for a plane problem as

$$J_v^R = \int_l \Phi^R dx_2 - T_i^R \frac{\partial u_i^R}{\partial x_1} dl \quad (3.19)$$

where  $\Phi^R$  is the stress potential function in the pseudo elastic problem,  $\Phi^R = \int_A \sigma^R d\varepsilon^R$ .

The pseudo elastic problem has the same geometry as the physical (viscoelastic) problem

and the pseudo parameters satisfy correspondence principle II. From the original conservation integral

$$J_v^R = J_f^R \quad (3.20)$$

where  $J_f^R$  is the integral along the interface of the cohesive zone and outside of the continuum.  $J_f^R$  is defined as

$$J_f^R = \int_0^\alpha \sigma_i^R \frac{\partial \Delta u_i^R}{\partial \xi} d\xi \quad (3.21)$$

where  $\sigma_i^R$  and  $\Delta u_i^R$  are the stress and crack separation displacement in the pseudo elastic problem. In an elastic problem,  $J_f^R$  is the work input into the process zone and the driving force dominating crack propagation (Rice 1968; Broek 1986). Work input or fracture energy defined in equations (3.1) - (3.3) in a viscoelastic problem is related to the  $J_f^R$  in a pseudo elastic problem through correspondence principle II. Thereafter the generalized J-integral,  $J_v^R$  can be related to the fracture energy according to equation (3.20). The following subsections describe the analysis of the crack initiation and propagation problem using the generalized J-integral.

### 3.3.3.3 Crack initiation criterion

Schaperly (1984) considered the case where  $\sigma_i$  on the interface is independent of time and distance from the crack tip (using a local coordinate system,  $\xi$ , as shown in Figure 3.2). These are similar assumptions to those used in  $K_I$ -method. Equation (3.3) reduces to

$$W_f = \sigma_i \Delta u_i \quad (3.22)$$

With the same assumptions, equation (3.21) becomes

$$J_f^R = \sigma_i \Delta u_{i\alpha}^R \quad (3.23)$$

For the crack initiation problem with correspondence principle II applied, combine equations (3.22) and (3.23),

$$W_f = \sigma_i \Delta u_i = \sigma_i \{Dd\Delta u_i^R\} = \{Dd(\sigma_i \Delta u_i^R)\} = \{DdJ_f^R\} = \{DdJ_v^R\} \quad (3.24)$$

Expanding the abbreviation above,

$$W_f = E_R \int_0^{t_i} D(t-\tau) \frac{\partial J_v^R}{\partial \tau} d\tau \quad (3.25)$$

Schapery (1984) defined the term “fracture initiation energy”,  $\Gamma_{ii}$ , to be the energy consumed at each crack surface when crack propagated, which is the same as in the  $K_I$ -method, so that

$$2\Gamma_{ii} = \{DdJ_v^R\} = E_R \int_0^{t_i} D(t-\tau) \frac{\partial J_v^R}{\partial \tau} d\tau \quad (3.26)$$

Taking the similitude to the  $K_I$ -method above, crack initiation time may be predicted using the implicit equation (3.26) in terms of history of  $J_v^R$  regardless of whether  $\Gamma_{ii}$  is constant or if it depends on the time.



### 3.3.3.4 Crack growth criterion

For the crack problem in Figure 3.2, since  $W_f = 2\Gamma_I$ , equation (3.1) can be written as

$$W_f = \int_0^\alpha \sigma_i \frac{\partial \Delta u_i}{\partial \xi} d\xi \quad (3.27)$$

The assumptions in the above equation include that the crack speed,  $\dot{a}$ , and the cohesive zone length,  $\alpha$ , are independent of time during the short time interval  $\alpha/\dot{a}$ . Also, the stress and the crack opening displacement are assumed independent of  $x_1$ , i.e.,  $\sigma_i(x_1, t) = \sigma_i(\xi)$ ,  $\Delta u_i(x_1, t) = \Delta u_i(\xi)$ . For most polymeric materials having small slope in the creep compliance, Schapery (1984) simplified the equation (3.16) to the following equation

$$\Delta u_i = E_R D(t_\alpha) \Delta u_i^R \quad (3.28)$$

where  $t_\alpha = \frac{1}{3} \frac{\alpha}{\dot{a}}$  and  $D(t_\alpha)$  is the creep compliance evaluated at time  $t_\alpha$ . Substituting equation (3.28) into (3.27) and using equation (3.20) yields

$$W_f = E_R D(t_\alpha) J_v^R \quad (3.29)$$

Or, in terms of fracture energy,

$$2\Gamma_I = E_R D(t_\alpha) J_v^R \quad (3.30)$$

$W_f$  or  $\Gamma_I$  are expressed in terms of the instantaneous value of  $J_v^R$  for steady crack propagation. Equations (3.29) and (3.30) implicitly include the relationship between

crack speed and  $J_v^R$ . An explicit relationship of crack speed and  $J_v^R$  can be derived if the creep compliance is defined in a known form, which follows the same discussion as crack speed expressed in terms of the  $K_I$ -method. For orthotropic materials, an equivalent compliance from Brockway and Schapery (1978) is used to replace  $D(t)$  in equation (3.30).

The generalized J-integral method described above reduces to the  $K_I$ -method when the material response is within the linear viscoelastic domain. For the linear viscoelastic problem, the reference elastic problem is linear elastic so that the linear elastic theory applies. Further, for the reference elastic problem, equation (2.7) may be used for these cases where  $J$  and  $G$  are equivalent. In this case, substituting equation (2.7) into (3.30) results in equation (3.7).

### **3.3.3.5 Application of the $J_v^R$ -method**

Crack growth curves such as  $\Gamma_{II}$  vs.  $t_i$  and  $J_v^R$  vs.  $\dot{a}$  are used to characterize crack growth using the  $J_v^R$ -method. The fracture parameter,  $J_v^R$  is defined in the pseudo-elastic problem and can be determined from the finite element method with calibrated pseudo elastic properties and measured material failure strength (Park 2006). Use of computational simulation to determine the fracture parameter always has shortcomings. For example, finite element models require highly accurate material properties that are usually difficult to obtain for composites due to the complex manufacturing process, batch differences, specimen-to-specimen variations and especially simulation-to-test differences. Direct use of  $J_v^R$ -method is not preferred in characterizing delamination growth if  $J_v^R$  needs be determined from finite element modeling.

### 3.3.4 Summary

Schapery's work (1975 and 1984) provided two methods to determine the crack growth curves, but neither of them is ready to be used in characterizing delamination propagation from the above review of the existing applications. Rather, a new experimental methodology for delamination testing needs to be developed. Some useful information from Schapery's analysis (1975 and 1984) provides the possibility. The pseudo problem of the linear viscoelastic problem is a linear elastic problem so that there exist closed-form solutions for  $J_v^R$  in the delamination test such as DCB as reviewed in chapter 2. Then,  $K_I$  can be determined from  $J_v^R$  using the pseudo linear elastic properties. This procedure avoids using finite element analysis. Consequently, the instantaneous values and history of  $J_v^R$  or  $K_I$  can be determined in the pseudo problem. However, crack growth curves need to be determined from experiments, which requires  $J_v^R$  or  $K_I$  being determined using experimental data from the linear viscoelastic test. The focus of our new experimental methodology is on establishing the relationship between the closed-form solution of  $J_v^R$  and the experimental parameters. This will be discussed in the following chapters.

### 3.4. Conclusion

In this chapter, we reviewed available linear viscoelastic theories related to our work on characterizing PMC delamination and their application. Schapery's viscoelastic fracture theory was selected in our work because this method allows fracture curves to be directly determined from a delamination fracture test. Fracture energy is defined in viscoelastic media taking into account of time, loading history and rate effects. Two

methods are available to calculate the fracture energy, stress intensity factor and generalized J-integral from a pseudo elastic model. Both methods are equivalent in case of the analysis in linear viscoelastic materials, but neither of them can readily be used to determine delamination growth curves. Therefore, a new experimental methodology needs to be developed. This approach, and the specific material used for its implementation and validation, is described in the following chapters.

## **CHAPTER 4.**

# **COMPOSITE MATERIAL CONSIDERED**

### **4.1. Introduction**

The material used in this study is Torayca T800H/3900-2 graphite/epoxy manufactured by Toray Industries, Inc. It is a carbon fiber reinforced polymeric matrix composite with particulate interlayers and was qualified as the first composite material for primary structures of Boeing's civil transport and applied to its 777 aircraft. T800H/3900-2 utilizes both the good processability of thermoset resins and high fracture toughness of thermoplastics. The base prepreg tape is coated with amorphous polyamide (a thermoplastic polymer) particles on both sides. The composite laminate is manufactured from multiple prepreg layers and is cured in an autoclave. Figure 4.1 shows backscatter scanning electron microscope (SEM) images of the interfacial region after curing from a previous colleague's work (Kumar 2004), which are similar to the results for this material in another work (Matsuda et al, 1997). The images present the cross-sectional view of a unidirectional T800H/3900-2 laminate at two different magnifications. Figure 4.1(a) clearly display two interlayers, the dark regions. Figure 4.1(b) amplifies the interfacial region between two plies so that the composite phases are distinguishable from the shade colors. The lightest circular shades represent the fibers, the intermediate shade represents the epoxy resin, and the darkest shade is the polyamide particles. The SEM pictures illustrate that the thermoplastic polymer particles are

embedded in the base epoxy resin in the interface between layers. Delamination initiation and growth may have to pass through or around the thermoplastic particles so that high thermoplastic material toughness contributes to the delamination toughness of the laminate, but on the other hand, this particulate interface makes the delamination fracture characterization more complicated.

Odagiri et al (1991) found out that T800H/3900-2 exhibited improved toughness than the base composite. Hojo et al (2006) compared mode I delamination toughness of T800H/3900-2 and base material T800H/3631 without polyamide particles and showed that the initiation toughness of T800H/3900-2 was about 4 times higher than the base material while the propagation toughness was almost identical at room temperature. This was attributed to a change of the delamination growth path. In T800H/3900-2 laminates, delamination initiation occurred within the interlayer, where the polyamide particles contribute to the delamination toughness. However, as the delamination propagated, it grew to the interface between interlayer and the adjacent ply, where there are no polyamide particles.

In this chapter, the mechanical and fracture properties of the T800H/3900-2 material from the literature are reviewed first. This survey is to find out the material responses of T800H/3900-2 under different environmental conditions including temperature and moisture content. Based on the review in chapter 3, the linear viscoelastic properties need be determined experimentally in order to apply the Schapery's linear viscoelastic theory. The rest part of this chapter describes new experiments to measure the viscoelastic properties of T800H/3900-2 and their results.

## **4.2. Prior work on T800H/3900-2 laminates**

### **4.2.1. Mechanical properties**

Basic elastic properties for T800H/3900-2 laminate at room temperature are given in table 4.1 (Davidson et al 2006) for a unidirectional laminate with coordinate axes as in Figure 2.3. Nielsen (1962) showed the polymeric material increased ductility and time-dependency with increase of temperature and decrease of loading rate. It is expected that properties of T800H/3900-2 change with presence of different moisture content under various temperature conditions. Woo (1994) did a series of creep tests and revealed that the T800H/3900-2 showed obvious viscoelastic response. The increase of slopes in the curves of compliance versus time at different temperatures illustrated more viscous effects under higher temperature and higher moisture content. Nearly constant compliance at room temperature implied negligible viscous effects. From Woo's work (1994), a master curve of T800H/3900-2 was determined using the compliances measured at different temperatures up to 132°C under moisture-free conditions using the time-temperature superposition technique (Williams, Landel, and Ferry, 1955). In addition to this, temperature-moisture equivalency was also applied to find the master curve of the results from moisture-saturated T800H/3900-2 specimens at different temperature levels.

The material properties are usually different below and above the glass transition temperature,  $T_g$ . The glass transition temperature,  $T_g$ , refers to the temperature where the phases change from glassy state to rubbery state for polymeric material.  $T_g$  of T800H/3900-2 in dry state was reported to be 189°C (Matsuda, Hojo, and Ochiai 1992)

and 140.5°C (Davidson, Soffa, and Kumar, 2009a).  $T_g$  was also measured on moisture-saturated specimens (Davidson, Soffa, and Kumar, 2009a) to be 114.4°C.

#### **4.2.2. Fracture properties under various environments**

A series of fracture tests on T800H/3900-2 laminates were performed at the Syracuse University Composite Material Lab (SUCML) across a large range of environmental conditions, from low temperature (-45°C) to elevated temperature at a large percentage of  $T_g$ : 98°C for moisture-saturated specimens and 125°C for dry specimens (Soffa et al 2006, Davidson et al 2009). The purpose of the work was to investigate the dependence of fracture toughness on temperature and moisture content. From these tests, noticeable differences in load-deflection responses were observed under different environmental conditions. With an increase in temperature or moisture content, the nonlinearity of the load versus deflection relationship increased and permanent deformation was observed at temperatures close to  $T_g$ . Among various data reduction methods considered for the double cantilever beam (DCB) test, the load based compliance calibration method and a modified beam theory method that utilized only the load and the material's elastic modulus were concluded to produce the most accurate results under all test conditions. The toughness variations with the temperatures and moisture content were related to the amount of matrix plasticization that occurred. All the tests were performed at the same displacement rate.



### **4.2.3. Summary**

In this section, fundamental material properties of T800H/3900-2 were reviewed. With increasing temperature and moisture content, the material exhibits more viscoelastic effects. The mechanical properties of dry T800H/3900-2 appear to be linear viscoelastic at temperature up to approximately 130°C. The perceived fracture toughness of T800H/3900-2 is influenced by the environmental conditions (both temperature and moisture). The linear viscoelastic properties of unidirectional laminate T800H/3900-2 are measured using laboratory tests for our work. The following sections describe the experimental procedure and results.

### **4.3. Measurement of linear viscoelastic properties**

Unidirectional 22-ply laminates from Toray T800H/3900-2 prepreg were fabricated by hand lay-up and cured in autoclave following the manufacturer's recommended vacuum, pressure and temperature cycles. The specimens were carefully cut from the plate using a diamond saw. There are total 4 groups of the specimens prepared for the material properties determination. The first group of specimens are  $[0]_{22}$  specimens used for the glass transition temperature measurement. Since the current study uses prepreg that has been stored in the freezer for several more years than the previous work at the SUCML (Soffa, Davidson and Kumar, 2006), the  $T_g$  may be different than that previously obtained and reevaluation is necessary. The second group of specimens are  $[0]_{22}$  unidirectional specimens for measurement of the longitudinal viscoelastic creep compliance. The third group of the specimens are  $[90]_{22}$  transverse specimens, which are used to measure the transverse viscoelastic creep compliance. The fourth group of

specimens are  $[90]_{22}$ , used for measuring the in-plane shear viscoelastic creep compliance. The following section discusses details of each experiment.

### **4.3.1 Experimental procedures**

#### **4.3.1.1 Tg measurement**

Tg of T800H/3900-2 was measured using a Dynamic Mechanical Analyzer (DMA Q800) following ASTM E1640-04. This test configuration uses a beam in three-point bending beam with a 50mm span. Cyclic loading is applied at a frequency of 1 Hz under a heating rate of 5°C/min (9°F/min) up to 350°F. Tg is then determined from a logarithmic plot of dynamic storage modulus versus temperature.

#### **4.3.1.2. Longitudinal and transverse creep tests**

Uniaxial tensile tests are widely used in the literature for measuring axial material properties including elastic modulus and creep compliance. However, the tensile specimen requires the use of loading tabs on the end of the specimen, which may cause debonding problems at elevated temperatures. In view of this, a few works (Ha and Springer, 1989; Guedes, et al, 1999; Pramanick and Sain 2006) used 4-point bending tests to measure viscoelastic properties of composites. This approach was followed in this study. There are always concerns about direct application of beam theory for stress prediction in the orthotropic composite beam. To ensure an accurate stress prediction by beam theory in the middle span of the 4-point bending composite beam, stress analysis of an orthotropic composite beam is performed in our study using the finite element method with consideration of geometrical nonlinearity and contact. This model accounts for all

roller effects, including possible changes of reaction force direction and moment arm lengths. Appendix B presents the details of this study. The result was a series of 4-point bending geometries for which the beam theory prediction for stress within the center span is accurate to 1.5% or better.

Figure 4.2 presents the test setup for 4-point bending test of unidirectional T800H/3900-2 composites.  $[0]_{22}$  and  $[90]_{22}$  specimens were tested for longitudinal and transverse viscoelastic properties, respectively. Vishay Micro-measurement EA-06-240LZ-120/E strain gages were glued on the top and bottom surfaces of the specimen following the strain gage preparation guidelines from Vishay. The strain averaged from the top and bottom surface eliminates the thermal strain and any possible non-symmetric effects. The gages were centered across the width of the specimen in the middle of the loading span. Both longitudinal and transverse gages were used, allowing the calculation of Poisson's ratio.

#### **4.3.1.3. In-plane shear tests**

In-plane shear properties are believed to play very important roles in analysis of laminated composite due to the shear coupling effects, especially under bending loads. A number of test configurations are available in the literature for measuring in-plane shear properties of composites, such as  $[\pm 45]_{ns}$  tension,  $[10]_n$  off-axis tension and Iosipescu shear tests, all of which are commonly accepted as accurate.

Rosen (1972) derived the expressions for obtaining the in-plane shear stress-strain curve using a uniaxial tension test of the  $[\pm 45]_{ns}$  off-axis composite laminates. The

method was later accepted as an ASTM test standard (ASTM D-3518) for measuring in-plane shear modulus of polymeric matrix composites. This configuration can provide a highly uniform strain field. However, the stress along the  $\pm 45^\circ$  principal direction is not pure shear because of the effects by the stresses normal to the fiber direction in each layer. In addition to above, the specimen is usually tested with loading tabs on the ends. The potential problem of loading tab debonding due to the shear stress in adhesive prevents the adaptation of this method at elevated temperatures.

Chamis and Sinclair (1976) were perhaps the first to theoretically and experimentally investigate the  $10^\circ$  off-axis tensile specimen for measuring in-plane shear stress-strain of unidirectional composites. This method is usually occupied to measure the in-plane critical stress and strain. However, care must be taken for the relative orientation between fiber and strain gage since the in-plane shear stress is very sensitive to small mis-orientation errors. In addition, the  $10^\circ$  off-axis tensile specimen also has the same loading tab debonding concerns as the  $[\pm 45]_{ns}$  off-axis tensile specimen.

The Iosipescu shear test (Iosipescu 1967) is used in composite materials to measure the in-plane shear modulus, critical stress and strain. This test was also standardized by ASTM (ASTM D-5379). Recently, this test was used to determine the viscoelastic shear modulus of a composite (Chan et al 2006). It is preferable to the  $[\pm 45]_{ns}$  off-axis tension and  $10^\circ$  off-axis tension tests, since it provides a uniform shear stress state at the middle section of the specimen that can be directly calculated from the applied load and the test geometry. In our work, in consideration of testing under elevated temperature with and without moisture, the Iosipescu shear test was selected because it is

able to measure the in-plane shear creep compliance and eliminates the potential tab-debonding problem that exists with the other two tests.

Figure 4.3 presents photographs of the Iosipescu shear tests. A modified Wyoming Iosipescu fixture was manufactured at Syracuse University. The  $[90]_{22}$  specimens were prepared following the ASTM D-5379. The  $\pm 45^\circ$  strains were measured by Vishay micro-measurements EA-06-062TH-120/E shear strain gages. Strain gages were glued on both surfaces of the specimens in order to account for effects of possible non-symmetric stress-strain due to out-of-plane twisting, as well as to eliminate thermal strains. The strain output from strain gages were conditioned by a Micro-measurement Vishay 2100 strain gage conditioner. A data acquisition program written with Labview software through a personal computer was used to record all test data.

#### **4.3.1.4. Creep test procedure and linearity check**

Creep-recovery tests were performed under various loading levels to verify the linearity of the viscoelasticity by checking superposition and proportionality. The creep test procedure included a fast loading step within 1 minute and a hold step under the constant target stress level for one hour. Target constant stresses were calculated from the constant load applied on the specimen based on specimen geometries and loads. Constant stress levels used in the creep tests were chosen to be above the maximum stress seen in the fracture test specimen (other than in the crack tip region). The maximum stress was predicted according to the previous fracture tests on the similar material and a finite element simulation. The constant load level for different tests are shown in table 4.2. The recovery procedure included a fast unloading step at the same rate as loading step,

followed by a 60-minute hold period under zero stress. The strain data and time were recorded continuously during the whole process. All tests were performed on a MTS 810 frame with a 1000 lb load cell.

The characteristics of the linear viscoelastic response include that the creep strain can be fully recovered and the creep compliance is independent of the stress level. The verification of these factors was performed following the procedure shown in Figure 4.4. The Boltzmann superposition principle for linearity check was first used as shown in Figure 4.4(a) by evaluating the creep-recovery test results. Proportionality was then verified from creep tests under different stress level following the procedure shown in Figure 4.4(b).

### **4.3.2 Test results**

#### **4.3.2.1. Tg of T800H/3900-2**

Four [0]<sub>22</sub> coupons of T800H/3900-2 were measured using the DMA equipments. Two of them were dry, and the other two were moisture saturated. Figure 4.5 depicts the storage modulus as a function of temperature for the two dry specimens. The value of Tg was obtained as the temperature corresponding to the intersection points from the two dashed lines, one line fits the linear portion of the curve before storage modulus drop and the other fits the decreasing portion of the storage modulus. The average dry Tg of T800H/3900-2 was found to be 141.9°C (287.4°F). Figure 4.6 plots the results for two wet specimens. The average wet Tg of T800H/3900-2 was found to be 112.5°C (234.5°F). There are no significant differences from previous results of the same material

T800H/3900-2 from the same batch (Soffa, Davidson and Kumar, 2006), in which dry  $T_g$  is  $140.6^\circ\text{C}$  ( $285^\circ\text{F}$ ) and wet  $T_g$  is  $114.4^\circ\text{C}$  ( $238^\circ\text{F}$ ). According to these results, the test temperatures,  $T=98^\circ\text{C}$  ( $208^\circ\text{F}$ ) and  $T=125^\circ\text{C}$  ( $257^\circ\text{F}$ ), are used for our study which are about 89% of  $T_g$  for wet and dry specimens, respectively. The test temperatures are consistent with the previous work (Soffa et al 2006), who chose them according to the highest usage temperature of T800H/3900-2 based on FAA recommendations.

#### **4.3.2.2. Linear viscoelastic properties**

Viscoelastic creep compliances were measured using 4-point bending and Iosipescu shear configurations. Dry specimens were tested at  $T=98^\circ\text{C}$  ( $208^\circ\text{F}$ ) and  $T=125^\circ\text{C}$  ( $257^\circ\text{F}$ ), and wet specimens were tested at  $98^\circ\text{C}$  ( $208^\circ\text{F}$ ) only. A simple power law form was used to express the time dependence of the creep compliance. The exponents of orthotropic creep compliances at each condition are presented in table 4.3. Whether or not linear viscoelastic response occurs was evaluated for the individual orthotropic creep compliances following the procedure of Figure 4.4. Figure 4.7 shows an example experiment for shear strain as a function of time during creep-recovery tests at two stress levels for wet specimens at  $98^\circ\text{C}$ . The shear creep strain of T800H/3900-2 is observed to be independent of stress magnitude within the stress range of interest, and the creep strain is fully recovered. A similar check was also performed in all other creep tests. Linear viscoelastic response was observed in all the specimens. These results indicate that T800H/3900-2 laminates under these conditions behave within the linear viscoelastic scope.

The longitudinal creep compliance in table 4.3,  $S_{11}(t)$ , shows negligible time dependence under all three conditions because the longitudinal properties are dominated by the elastic graphite fibers. Therefore, viscoelastic response is negligible in longitudinal direction and elastic modulus can be used in the analyses of orthotropic polymeric composites (Brockway and Schapery 1978; Gamby and Chaoufi 1999). In contrast, noticeable time-dependence is observed in the transverse directions, as reflected  $S_{22}(t)$ , and along shear directions, as indicated by  $S_{66}(t)$ . Here, the polymeric matrix dominates the composite behaviors.  $S_{22}(t)$  and  $S_{66}(t)$  at different conditions are plotted in Figures 4.8 and 4.9, respectively as a function of relative time,  $t/t_0$ . Here, the time  $t$  is in minutes and  $t_0 = 1.0$  minute. The solid lines are linear fits of the log-log plot of creep compliance versus time. The slopes of these linear curve fits give the exponents in the simple power law expressions of table 4.3. The slopes at different stresses under the same environmental condition are nearly identical, which also verifies the compliance of the composite is independent of stress level. The intercepts of the linear fit line to the ordinate give the constant multiplier, which is the inverse of the initial elastic modulus of the material at that temperature. Some of these curves under the same environmental condition are not coincident for different stress levels. But the differences of the magnitude between stress levels under the same condition are very small (less than 1%). The Poisson's ratios  $\nu_{12}$  were also found from 4-point bending tests of  $[0]_{22}$  and  $[90]_{22}$  laminates, respectively. Poisson's ratios show negligible time dependence and are shown in table 4.3.

The exponents in table 4.3 measured from our tests show the similar trends as the work by Woo (1994) on T800H/3900-2. That is, the exponents increase with increasing



temperature and moisture content, which illustrates that the viscoelastic properties of T800H/3900-2 are more time-dependent at higher temperature with and without moisture. Woo (1994) measured the viscoelastic properties of T800H/3900-2 using a  $[\pm 45]_{2s}$  tension configuration from temperatures of 26°C to 160°C. A complete power law expression,  $S(t) = S_0 + S_1 t^n$  was employed to represent the time dependence of creep compliance. From his work, the shear creep compliance was found from the uniaxial creep data following ASTM D-3518. Then, the complete power law form of creep compliance was replaced by a simple power law format containing one constant multiplier. After these transformations, we notice the compliances of  $S_{66}(t)$  from our results at 98°C and 125°C have smaller time exponents than Woo's results at close temperatures, 104°C and 132°C. Possible reasons are ascribed to different batches and the manufacturing procedure used in two studies, as well as different specimen configurations. In our test, 22-ply unidirectional specimens were tested, but Woo tested angle-ply laminates with only 8 layers. One-ply thickness calculated from Woo's specimen is much thicker than that of our 22-ply specimen. Therefore, our specimens may have higher fiber volume contents. In accordance, higher fiber volume content decreases viscoelastic effects due to better reinforcing effects on the matrix. In addition to possible fiber content difference, Woo performed the creep tests with the initial strain at 0.5~0.55%, which is much higher than measured in our work (0.2~0.28%). The higher strain level may have exceeded the linear viscoelastic range and nonlinear viscoelastic or viscoplastic responses may have occurred in Woo's work. This would result in larger exponents in the creep compliances.

Orthotropic relaxation moduli  $E_{ij}(t)$  are obtained by converting creep compliances using interconversion relationship for viscoelastic solids (Park and Kim, 1999). Following the work by Brockway and Schapery (1976), equations (4.1) to (4.3) give the equivalent viscoelastic compliances calculated from test results in table 4.3 for dry specimen at 98°C, wet specimens at 98°C and dry specimens at 125°C, respectively.

$$\text{Dry } 98^{\circ}\text{C:} \quad \kappa_{22}(t) = 9485.2 \times \left(\frac{t}{t_0}\right)^{0.0086} \text{ MPa}^{-1} \quad (4.1)$$

$$\text{Wet } 98^{\circ}\text{C:} \quad \kappa_{22}(t) = 8451.1 \times \left(\frac{t}{t_0}\right)^{0.0221} \text{ MPa}^{-1} \quad (4.2)$$

$$\text{Dry } 125^{\circ}\text{C:} \quad \kappa_{22}(t) = 9178.4 \times \left(\frac{t}{t_0}\right)^{0.0109} \text{ MPa}^{-1} \quad (4.3)$$

These results will be used in the determination of the fracture initiation energy and the instantaneous stress intensity factor during the steady crack propagation of T800H/3900-2 laminates that are presented in subsequent chapters.

#### 4.4. Conclusion

In this chapter, the T800H/3900-2 material was introduced. A literature survey showed that T800H/3900-2 composites exhibit viscoelastic behaviors in the mechanical and fracture properties. The viscoelastic properties at three environmental conditions of interest in our work were measured. The linearity of the viscoelastic response under three conditions was verified. From these results, fracture characterization of T800H/3900-2 at elevated temperatures should utilize a linear viscoelastic fracture theory that accounts for

the material's time-dependent response. Continuing the idea from chapter 3, we see that the material in consideration meets the basic requirements for the application of Schapery's linear viscoelastic theory (1985, 1984). In the next chapter, we develop the experimental approach in order to make the linear viscoelastic delamination characterization feasible under the environmental conditions of interest.

## CHAPTER 5.

# FRACTURE CHARACTERIZATION METHODOLOGY

### 5.1. Introduction

As described in chapter 3, material characterization curves such as  $\dot{a}(K_I)$  and  $t_i(\Gamma_{II})$  are necessary to predict crack initiation and growth in viscoelastic materials. These curves must be obtained experimentally. In chapter 4, it was shown that the composite material considered in this work, T800H/3900-2, shows linear viscoelastic behaviors under three conditions of interest, dry 98°C, wet 98°C and dry 125°C. In this chapter, an approach is developed that is based on Schapery's linear viscoelastic theory that can be used to characterize delamination initiation and growth of T800H/3900-2 under these three environmental conditions.

In what follows, the double cantilever beam (DCB) test configuration is used to characterize mode I delamination initiation and growth. This test is simple and has been used extensively for polymeric matrix composites (PMCs). The task in this chapter is to develop an approach to determine the linear viscoelastic fracture parameters such as  $K_{Ic}$  and  $\Gamma_{IIc}$  and the characterization curves such as  $\dot{a}(K_I)$  and  $t_i(\Gamma_{II})$  from DCB test data. The first part of this chapter focuses on an analysis of a linear viscoelastic DCB specimen. It

is used to establish a relationship between the measurable experimental parameters and the desired fracture parameters. Following this, the experimental setup is proposed and a roadmap of this study is described.

## **5.2. Linear viscoelastic DCB specimen**

The DCB test has been widely accepted in delamination toughness measurement for linear elastic composite. Experimental parameters, such as load, displacement, crack lengths, and material modulus are typically used to determine the critical energy release rate or critical J-integral in a linear elastic material. In case of linear viscoelastic materials, we still want to use these experimental parameters, and also need to consider the time-history of these parameters and the time-dependent material properties so that a time-dependent fracture criterion can be established.

A number of data reduction approaches are available for linear elastic media as presented in chapter 2. All these approaches capture the strain energy released during crack propagation. The energy release rate definition for linear elastic materials assumes all energy dissipated during the crack growth process contributes to forming the new crack surface, but in linear viscoelastic materials, the energy released during crack propagation also includes the viscous energy dissipation. Therefore, the data reduction technique based on energy release rate as derived for linear elastic materials can't be used directly for a linear viscoelastic material. However, J-integral might be a valid parameter because it is defined based on the instantaneous stress, strain and displacement state without considering the energy dissipation. Thus, we introduce the J-integral for a linear viscoelastic DCB test.

For a linear viscoelastic DCB specimen tested under a constant displacement rate, the strain rate is constant at each location. Application of the convolution integral form of the viscoelastic constitutive law gives the linear viscoelastic stress-strain relationship as

$$\sigma_{(t)} = \int_0^t E_{(t-\tau)} \frac{\partial \varepsilon}{\partial \tau} d\tau = \dot{\varepsilon} \int_0^t E_{(t-\tau)} d\tau \quad (5.1)$$

With the assumption of a power law material  $E(t)=E_0t^n$ , which is good for most polymeric materials, and for initial strain-free conditions,  $\varepsilon = \dot{\varepsilon}t$ , expression (5.1) becomes

$$\sigma_{(t)} = E_0 \dot{\varepsilon} \frac{t^{n+1}}{n+1} = \frac{E_0 t^n}{n+1} \varepsilon \quad (5.2)$$

Equation (5.2) is very similar to a linear elastic constitutive relationship except the equivalent secant modulus,  $\frac{E_0 t^n}{n+1}$ , is time-dependent. At any time,  $t$ , equation (5.2) represents a linear elastic relationship. So the J-integral exists at any instant in a linear viscoelastic problem.

We have shown that an instantaneous J-integral exists in the linear viscoelastic DCB specimen under constant displacement rate. Data reduction technique for determining J-integral for a linear elastic DCB specimen presented in chapter 2 needs be reevaluated for a linear viscoelastic DCB specimen. Equation (2.23) in chapter 2 presents a method to find the critical J-integral with use of the critical applied load and critical load point slope accounting for possible large deformation in the DCB legs. Rewrite that equation to a general form for J-integral evaluated at any instantaneous moment as

$$J_s = \frac{2P \sin(\theta)}{B} \quad (5.3)$$

$J_s$  is given as the instantaneous J-integral in a linear viscoelastic material to avoid confusion with the linear elastic J-integral.  $P$  and  $\theta$  are the instantaneous load and end rotation angle, respectively, in a test at constant displacement rate. These parameters are measured experimentally. In this manner,  $J_s$  accounts for the time-dependent material properties. In chapter 6, the path independence for  $J_s$  in equation (5.3) is further verified through finite element modeling.

The instantaneous linear elastic problem described above enables the relationship of the J-integral and stress intensity factor  $K_I$  to be evaluated in a linear viscoelastic material as,

$$J_s = K_I^2 / E^{LVE} \quad (5.4)$$

where  $E^{LVE}$  is equivalent modulus for composite material. Equation (5.4) is similar to equation (2.8) in chapter 2. Therefore,  $E^{LVE}$  is determined using the instantaneous moduli  $E_{ij}$  having the form of the instantaneous secant modulus in equation (5.2). According to Schapery's correspondence principle II (Schapery 1984), the same stress distributions are defined for both the linear viscoelastic problem and the pseudo linear elastic problem, which indicates the same value of stress intensity factor,  $K_I$ , in both problems at any instantaneous time. Therefore,  $J_v^R$  as defined in a pseudo elastic problem and  $J_s$  as defined at the instantaneous moment,  $t$ , in a linear viscoelastic problem are related through the stress intensity factor,

$$K_I^2 = E^{LVE} J_s = E_R J_v^R \quad (5.5)$$

where  $E_R$  is a free constant and may be selected as desired (Schapery 1984), but usually need be calibrated from experiments and simulation (Park et al 2006).

Equation (5.5) relates the experimentally measured parameter  $J_s$  to the fracture parameters needed in Schapery's linear viscoelastic theory. The next section describes the explicit usage of  $J_s$  in determining the fracture curves for crack initiation and crack growth problem.

### 5.3. Analysis of crack growth

#### 5.3.1. Crack initiation

The material characterization curve,  $t_i(\Gamma_{li})$ , was defined by Schapery (1984) to predict crack initiation time. In order to get this curve, the first requirement is to find the explicit relationship between the fracture initiation energy  $\Gamma_{li}$  and  $J_v^R$  at the crack initiation time,  $t_i$ . Then, the relationship in equation (5.5) makes the determination of  $\Gamma_{li}$  feasible from  $J_s$ . Considering a DCB specimen under constant displacement rate,  $\delta = \dot{\delta}t$ , according to Schapery's correspondence principle II, there exists a pseudo elastic DCB problem with displacement  $\delta^R$  defined as

$$\delta^R = \{Ed \delta\} = \frac{1}{E_R} \int_0^t E(t - \tau, t) \frac{\partial \delta}{\partial \tau} d\tau \quad (5.6)$$



For many polymeric materials in consideration, the creep compliance and relaxation modulus can be expressed as a simple power law form,

$$D(t) = D_0 t^n \text{ and } E(t) = E_0 t^{-n} \quad (5.7)$$

and  $D_0 E_0 = \sin(n\pi)/n$  (Park and Kim, 1999). For isotropic materials,  $D(t)$  is the creep compliance, and for orthotropic materials,  $D(t)$  refers to the equivalent compliance,  $\kappa_{22}$  (equation, 3.10 in chapter 3), for the mode I conditions considered here.

Substituting equation (5.7) into (5.6), and accounting for the constant displacement rate in the physical specimen, we obtain

$$\delta^R = \frac{E_0}{E_R} \frac{t^{1-n}}{1-n} \dot{\delta} \quad (5.8)$$

In the pseudo linear elastic DCB problem, the generalized J-integral,  $J_v^R$  can be evaluated based on the equivalence to energy release rate. Using modified beam theory after (Williams, 1989),

$$J_v^R = \frac{F}{N} \frac{3P^R \delta^R}{2B(a + \chi h)} \quad (5.9)$$

If the problem has small displacement,  $F/N \approx 1.0$ . The crack length correction factor  $\chi$  is only function of geometry and material elastic properties, and independent of time. Therefore, for clarity in the derivation of the explicit expression between  $\Gamma_{li}$  and the  $J_v^R$ , we use the classical beam theory solution,

$$J_v^R = \frac{3P^R \delta^R}{2Ba} = \frac{3E_R h^3}{16a^4} (\delta^R)^2 \quad (5.10)$$

where the corrected crack length  $a+\chi h$  can be substituted for  $a$ . Substituting equation (5.8) into equation (5.10) gives

$$J_v^R = k \left( \frac{t^{1-n}}{1-n} \right)^2 \quad (5.11)$$

where

$$k = \frac{3E_R h^3}{16a^4} \left( \frac{E_0}{E_R} \right)^2 \dot{\delta}^2 \quad (5.12)$$

A closed form solution for  $J_v^R$  in the pseudo-elastic DCB problem is explicitly described in equation (5.11) as a function of loading time, displacement rate, and the reference elastic property  $E_R$ . By substituting equation (5.11) into equation (3.26) in chapter 3, an explicit relationship of  $\Gamma_{II}$  and  $J_v^R$  for a stationary crack is obtained as

$$2\Gamma_{II}(t_i) = E_R D(t_i) g(n) J_v^R(t_i) \quad (5.13)$$

where  $J_v^R$  is given in equation (5.11), and  $g(n)$  is a function of the exponent of the equivalent creep compliance of the linear viscoelastic material,

$$g(n) = \frac{4^{(1-n)} \times \text{Gamma}(1.5 - n) \times \text{Gamma}(n + 1)}{\sqrt{\pi}(2 - n)} \quad (5.14)$$

where  $\Gamma(n)$  is the Gamma function.  $n$  is the exponent of the viscoelastic compliance function for a power law linear viscoelastic material.

With the relationship established in equation (5.5), equation (5.13) becomes

$$2\Gamma_{ii}(t_i) = g(n)D(t_i)E^{LVE}(t_i)J_s(t_i) \quad (5.15)$$

Following the work by Brockway and Schapery (1978), for a power law composite material tested under constant displacement rate,  $D(t_i)E^{LVE}(t_i) = 1.0$ . Therefore, equation (5.15) becomes

$$2\Gamma_{ii}(t_i) = g(n)J_s(t_i) \quad (5.16)$$

The fracture initiation energy,  $\Gamma_{ii}$ , can be directly obtained from  $J_s$  at the instant of crack initiation as a function of the exponent of the equivalent viscoelastic compliance. Under each environmental condition,  $n$  is a material property and independent of test geometry and loading-history. For a linear elastic material,  $n=0.0$ ,  $g(n)=1.0$ , equation (5.16) reduces to the linear elastic crack propagation solution, i.e.,  $2\Gamma=J_s$ . For a linear viscoelastic material with known  $n$ , when  $J_s$  vs.  $t_i$  is determined experimentally from DCB tests, we can obtain the fracture curve  $\Gamma_i$  vs.  $t_i$  for the material through equation (5.16).

### 5.3.2. Steady crack propagation

For crack propagation, equation (3.8) shows the explicit relationship of stress intensity factor,  $K_I$ , and crack speed,  $\dot{a}$ , for a power law material in mode I crack propagation (Schapery 1975, Brockway and Schapery, 1976).

$$\dot{a} = AK_I^{2(1+1/n)} \quad (5.17)$$

where

$$A = \frac{\pi}{6} \left[ \frac{C_1}{8\Gamma(\sigma_m I_1)^{2n}} \right]^{1/n} \quad (5.18)$$

At any instantaneous moment during crack propagation,  $K_I$  can be determined from the measured  $J_s$  using equation (5.5). The relationship of  $K_I$  and  $\dot{a}$  can be found from measured  $J_s$  and crack speed  $\dot{a}$ . In equation (5.17),  $n$  is the exponent of the viscoelastic creep compliance at each environmental condition. The material property term,  $A$ , defined in equation (5.18) can be obtained from the curve fitting using equation (5.17) on the experimentally determined relationship of  $K_I$  versus  $\dot{a}$ .

#### 5.4. Experimental technique

For linear viscoelastic materials,  $J_s$  must be measured so that fracture characterization using Schapery's linear viscoelastic theory can be applied. In this section, experimental techniques measuring  $J_s$  are discussed for a DCB specimen.

Measurement of  $J_s$  using equation (5.3) has not been widely adopted in the literature. One reason is that there are other data reduction techniques to determine fracture toughness from energy release rate. The other reason is due to the difficulty in direct measurement of the load-point rotation angle. Goetz (1988) measured the load-point angle by a protractor and manually recorded the slope change during the tests. The method requires direct view on the protractor, good illumination, and free of disturbance.

The accuracy of the method also depends on the observer. It may work well for tests under room temperature under slow loading rates; however, the method cannot precisely record simultaneous the time-history of the applied load and the load point rotation angle, which are required in determining the fracture curves in linear viscoelastic material. Bazhenov (1995) measured the angles after tests using a set of photographs taken periodically with a Zenith TTL camera focused on the cantilever ends. The accuracy of the angle measurement is affected by the quality of the pictures and the relative position of the camera and the specimen. Anderson and Stigh (2004) occupied a shaft encoder to measure the load point rotation angle. This method obviates the disadvantages in using a protractor. Data recording is also automated through a computer program and results are highly accurate. However, the installation of the encoder results in a complicated experimental setup that prevents common use in the DCB test. Our test needs to be performed at room temperature and also at elevated temperatures in an oven. Therefore, the experimental setup needs be small enough to fit in the oven and the equipment is required to have a working temperature higher than our test temperature. None of these existing methods meet our requirements.

Due to the difficulty of the direct angle measurement, an indirect angle measurement method is developed. Usually, a DCB specimen is loaded through loading blocks. The rotation angle of the loading block is equal to the slope of the DCB leg at the loading point. Figure 5.1(a) shows the updated DCB test setup with specially designed “L” shape loading blocks made of stainless steel in Figure 5.1(b). The rotation angle of the loading block is calculated with measured displacements from two displacement transducers and the constant distance from the transducer to the actuator. In Figure 5.1(a),

both the initial and deformed shapes of the DCB specimen are schematically plotted. The center of the top block allows the free rotation. The center of the bottom block allows free rotation and moves with the displacement actuator. The displacement transducers are mounted on the DCB loading fixture at a constant distance,  $L_0$ , to the actuator. The top transducer measures the displacement,  $\delta_1$ , along the loading direction due to the rotation of the top block. *The bottom transducer is mounted so that it moves together with the hydraulic actuator.* It also measures the displacement,  $\delta_2$ , on the leg of the bottom block due to the rotation of the bottom block. The rotation angles of the loading blocks then can be calculated from the displacements  $\delta_1$ ,  $\delta_2$  and the constant distance  $L_0$  as

$$\begin{aligned}\theta_1 &= \arctan\left(\frac{\delta_1}{L_0}\right) \\ \theta_2 &= \arctan\left(\frac{\delta_2}{L_0}\right)\end{aligned}\tag{5.19}$$

where  $\theta_1$  and  $\theta_2$  are end rotation angles of DCB legs as shown in Figure 5.1(a). This technique utilizing “L” blocks and displacement transducers avoids the use of the load-point displacement from the hydraulic actuator, which always has lower accuracy than measured load in reducing fracture toughness (Soffa et al 2006). Details of the experimental setup will be described in chapter 7.

Equation (5.3) is derived for symmetric DCB legs under symmetric loading. A more general form would be

$$J_s = \frac{P}{B} [\sin(\theta_1) + \sin(\theta_2)]\tag{5.20}$$

which takes into account possible unsymmetric deformation due to possible unsymmetric specimen configuration or an unsymmetric system, for example, an unsymmetric DCB test, an unsymmetric lay-up, an angle-ply specimen, or face sheet splitting in sandwich structure. Substituting equation (5.19) into (5.20), the experimental expression for  $J_s$  becomes

$$J_s = \frac{P}{B} \left[ \sin\left(\arctan\left(\frac{\delta_1}{L_0}\right)\right) + \sin\left(\arctan\left(\frac{\delta_2}{L_0}\right)\right) \right] \quad (5.21)$$

Equation (5.21) allows  $J_s$  to be determined directly from the experimentally measured data.

## 5.5. Roadmap

General application of the approach to DCB specimens requires the measurement of the parameters in equation (5.21) at the critical moment of crack initiation and continuous measurement during crack propagation. The critical load is measured from the load cell output. The relative displacements of the top and bottom legs on “L” shape blocks are measured using the displacement transducers. From the review of the derivation of equation (5.3) in the literature, the load is assumed to act on a single point on the DCB leg. However, the load is generally applied on the DCB legs on a finite area, as the practical implementation of DCB loading requires loading blocks or hinges to be employed. The effects on the accuracy of equation (5.3) induced by the loading blocks can be reduced by careful specimen geometry design. Therefore, the first stage of the work is to perform a series of finite element analyses in order to design appropriate

specimen geometries. This is described in chapter 6. Typical linear elastic orthotropic materials are used for the evaluation of loading blocks effects and to choose the specimen geometry. Power-law linear viscoelastic orthotropic composites are also simulated to verify the existence of  $J_s$  in a linear viscoelastic DCB specimen. Based on these results, unidirectional composite specimens are found to be appropriate, and T800H/3900-2 specimens are manufactured and prepared.

The experimental setup and data acquisition system used in this work are different from common DCB tests because we need the synchronized time history of both load and rotation angles. This setup is discussed in chapters 7 and 8 for testing at room temperature and elevated temperatures, respectively. Before applying the technique for fracture characterization under elevated temperatures, the experimental system is calibrated under room temperature in chapter 7. That is, under room temperature, T800H/3900-2 exhibits linear elastic response (Davidson et al 2009) and LEFM-based data reduction methods generally determine accurate fracture toughness. Thus, as an initial verification, the critical value of  $J_s$ , as obtained from equation (5.21) at the onset of crack advance, is compared to the critical energy release rate as obtained using a compliance calibration approach.

Following the above, DCB fracture tests under elevated temperatures with and without moisture saturation are then performed. Constant rate, displacement controlled test are used. Thus, equation (5.16) may be used to derive the fracture initiation energy. The instantaneous  $J_s$  during the steady-state crack propagation is used to determine the  $\dot{a}(K_I)$  curve. The details will be covered in chapter 8.



## 5.5. Conclusion

An experimental approach was developed based on the analysis of a linear viscoelastic DCB specimen. This approach establishes a method to determine a path-integral parameter,  $J_s$  in a linear viscoelastic DCB specimen from the experimentally measured data. The resulting  $J_s$  then can be used to derive the fracture parameters  $K_{Ic}$  and  $\Gamma_{Ic}$ . The following chapters discuss verification of this approach and its use to determine the fracture properties of T800H/3900-2 graphite/epoxy composite specimens.

# **CHAPTER 6.**

## **MODELING AND VALIDATION**

### **6.1. Introduction**

Chapter 5 developed an experimental technique that may be used to apply Schapery's linear viscoelastic fracture theory to characterize the delamination behavior of linear viscoelastic polymeric matrix composites. An analytical expression for  $J_s$  was derived for a DCB specimen that utilizes specially designed loading blocks. The accuracy of  $J_s$  needs be evaluated. In this chapter, finite element method is used to investigate the accuracy of  $J_s$  for linear elastic and linear viscoelastic materials. From this study, it is intended to find the appropriate DCB test geometries including crack length, specimen thickness and block size that can give accurate  $J_s$ .

### **6.2. Finite element modeling of the DCB test**

This section describes the details of the finite element analysis of a DCB specimen with L-shape loading blocks as shown in Figure 5.1. The details of the finite element mesh and material models are introduced. Determination of the  $J_s$  from the finite element model is described. The mesh convergence is then studied for getting the correct result.

### **6.2.1 Finite element model**

A two-dimensional finite element mesh of a DCB specimen was established using ABAQUS. Eight-noded quadratic quadrilateral plane stress elements were used to better account for the parabolic shear stress distribution across the section in a bending specimen. Figure 6.1 presents a typical finite element mesh used for this portion of the study. The mesh is refined around the crack tip using square shaped elements. The boundary conditions and loading were chosen to reflect the physical situation. The center node of the bottom block (node B) is restrained from both horizontal and vertical translations. The horizontal translation of the center node on the top block (node A) is also restrained. The top and bottom block can freely rotate about their center nodes. A constant increment of displacement in the vertical direction was applied to node A to represent the constant rate, displacement controlled loading in the test. Geometrical nonlinearity option in the ABAQUS analysis is turned on to account for possible large deformations in DCB test.

Two types of materials are used in the analyses. One is linear elastic, and the other is linear viscoelastic. The following subsections introduce the details of the analyses in terms of these two materials.

### **6.2.2. Linear elastic analyses**

The purpose of this analysis is to investigate the applicability of the  $J_s$  method in different material systems and to find an appropriate specimen geometry for accurate use of  $J_s$  in linear elastic DCB tests. These results are then used for the linear viscoelastic

analyses. Table 6.1 presents the linear elastic material properties that are considered. The first two rows represent two types of orthotropic composites, a typical graphite reinforced epoxy with a high  $E_{11}/G_{12}$  ratio and a typical glass reinforced epoxy with a low  $E_{11}/G_{12}$  ratio. The third row is an isotropic material with properties of typical a Aluminum. The geometries of DCB specimens studied include crack lengths,  $a$ , of 25, 37, 50, and 75mm, and uncracked specimen thicknesses,  $t$ , of 2, 4 and 6mm, which are generally used in the experiments.

### **6.2.3. Linear viscoelastic analyses**

#### **6.2.3.1 Background**

Finite element analysis of linear viscoelastic material is available recently with the development of the linear viscoelastic theory and advanced computational techniques. Many finite element packages integrate a linear viscoelastic material model. However, none of these provide a default option to simulate orthotropic linear viscoelastic material response. Rather, users develop their own approximation method. Often, a linear viscoelastic problem is simplified to a linear elastic problem with appropriate assumptions of loading rate or test condition. For example, the constant strain rate assumption simplifies the linear viscoelastic constitutive law to a linear elastic stress-strain relationship. For the assumption of the extreme test conditions, such as initial short-term loading and long-term loading, the relaxation modulus can be considered constant. The constant strain rate was applicable in our work.

### 6.2.3.2 Objective and approach

In this subsection, the approximation method of orthotropic linear viscoelastic material model is developed in terms of the DCB specimen. Then, the same FE model as in the linear elastic analyses was used to evaluate  $J_s$  for a range of orthotropic linear viscoelastic materials.

For a linear viscoelastic material loaded under constant strain rate, an instantaneous elastic stress-strain relationship at any instant has been introduced in chapter 5. In terms of a constant rate displacement controlled DCB specimen, the values of the constant strain rate are location-dependent, but the time-dependent secant moduli are the same. Therefore, the time-dependent equivalent secant moduli are used as material properties input in the ABAQUS model. The equivalent secant moduli are determined from the relaxation moduli. For an orthotropic material with time-independent Poisson's ratios,  $\nu_{ij}$ , three relaxation functions need be provided in order to fully describe the material response in a plane problem. These functions might be in simple power law forms as

$$E_{11}(t) = E_{11}(t/t_0)^s, E_{22}(t) = E_{33}(t) = E_{22}(t/t_0)^m, G_{12}(t) = G_{12}(t/t_0)^k \quad (6.1)$$

where  $t_0 = 1\text{min}$ , and  $E_{11}$ ,  $E_{22}$  and  $G_{12}$  are modulus at time  $t = 1\text{min}$  at certain temperature and moisture content. Orthotropic linear viscoelastic materials with a range of exponents,  $s$ ,  $m$ , and  $k$ , in table 6.2 are considered. These exponents cover the time-dependent response of T800H/3900-2 at three conditions of interest.  $E_{11}$ ,  $E_{22}$  and  $G_{12}$  use the elastic moduli of a typical graphite reinforced epoxy in table 6.1.

Isotropic linear viscoelastic materials are also simulated using the ABAQUS default option with varied exponents,  $p$ , of  $-0.01$ ,  $-0.03$  and  $-0.05$  in the relaxation modulus,  $E(t) = E_0(t/t_0)^p$ . For a special case,  $E_0=E_{11}=E_{22}$ ,  $G_{12}=E_0/(1+\nu)/2$ , and  $s = m = k = p$ , the orthotropic model becomes an isotropic model.

#### 6.2.4. $J_s$ from finite element model

$J_s$  has been defined in equation (5.3) using the rotation angles of loading blocks and the applied force. In terms of the test setup proposed in chapter 5, the rotation angle can be calculated from the measured deformations and the constant distance “ $L_0$ ” shown in Figure 5.1 using equation (5.19). However, in the finite element model, it is inconvenient to determine “ $L_0$ ”, while the distance “ $L$ ” between two nodes A and C, or B and D in Figure 6.1 is constant. Rather, the block rotation angles can be calculated using vertical displacements at those nodes and the constant distance “ $L$ ” as

$$\begin{aligned}\theta_1 &= \arcsin\left(\frac{|\delta_A - \delta_C|}{L}\right) \\ \theta_2 &= \arcsin\left(\frac{|\delta_B - \delta_D|}{L}\right)\end{aligned}\tag{6.2}$$

where  $\delta$  represents the displacement measured at nodes A,B,C and D. It is noted that equation (6.2) is different from the experimental expression in equation (5.19), but both of them calculate the rotation angles of loading blocks that are used to determine  $J_s$ . For the symmetric DCB configuration in FE model,  $\theta_1 = \theta_2$  and  $|\delta_A - \delta_C| = |\delta_B - \delta_D|$ . Therefore,  $J_s$  defined in equation (5.3) becomes

$$J_s = \frac{2P}{w} \left[ \frac{|\delta_B - \delta_D|}{L} \right] \quad (6.3)$$

Here,  $w$  is the specimen width and  $P = P(t)$  is the reaction force (at node B, Figure 6.1) from the simulation. Further, since the displacement load is applied at point A,  $\delta_B = 0$ .  $J_s$  calculated from equation (6.3) was determined for both linear elastic and linear viscoelastic models and was compared to the J-integral from ABAQUS output.

### 6.2.5. Mesh refinement study

$J_s$  in expression (6.3) and  $J$  from ABAQUS output are evaluated for different refined meshes near the crack tip. The meshes studied include the tip element size of  $h/8$ ,  $h/16$ ,  $h/32$ ,  $h/48$ ,  $h/64$ , and  $h/96$ .  $h$  is the thickness of one DCB leg. The mesh elements far from the tip always have aspect ratio of less than 3 in the stressed region and 6 in the free end far from the tip. The aspect ratio of the quadrilateral element in the model refers to the length ratio of its second longest edge to its second shortest edge. Simulation results showed that the  $J_s$  and  $J$  were within 0.5% between different mesh sizes when the tip element size was equal to or greater than  $h/32$ . So the FE mesh with tip element size of  $h/32$  was used in the analysis for comparing  $J_s$  and  $J$ .

## 6.3. Results and discussion

### 6.3.1 Linear elastic analyses

Figure 6.2 depicts the percent error of the  $J_s$  to  $J$  versus the end rotation angle for the graphite epoxy composite of table 6.1 from DCB specimens with various thicknesses,

t, and crack lengths, a. The  $J_s$  is computed using equation (6.3). Percent error is determined as  $(J_s - J)/J * 100$ . The abscissa is the end rotation angle at the loading point from simulation, which is calculated using equation (6.2). End rotation angles between  $0^\circ$  and  $20^\circ$  are what are generally obtained in DCB experiments, and the range used in the figure is slightly larger than this. In Figure 6.2, open symbols represent the simulation results of DCB specimens with  $t = 4\text{mm}$  and  $a = 25, 37, 50$  and  $75\text{mm}$ ; closed symbols show the results of DCB specimens with  $t = 2\text{mm}$  and  $a = 25$  and  $37\text{mm}$ ; and other symbols represent the results of DCB specimens with  $t = 6\text{mm}$  and  $a = 25, 50$  and  $75\text{mm}$ . Except for the results from the DCB specimen with  $t = 2\text{mm}$  and  $a = 25\text{mm}$ , the percent errors from all specimens are less than 1.5% for the end rotation angles less than or equal to  $20^\circ$ . Generally, with increasing end rotation angle, the accuracy of  $J_s$  increases. This is true except for the specimen with  $t = 6\text{mm}$  and  $a = 25\text{mm}$ , which shows when the angle is larger than  $20^\circ$ , the errors somewhat increase. In Figure 6.2, specimens with longer crack lengths give better accuracy of  $J_s$  for a given thickness. Also, thicker specimens show smaller errors than thinner specimens at the same crack length. However, the  $a/t$  ratio does not scale the accuracy of  $J_s$ . For example, in Figure 6.2, for specimens with the same ratio of  $a/t = 12.5$ , the data with open square symbols for  $a = 50\text{mm}$  and  $t = 4\text{mm}$ , and solid square symbols for  $a = 25\text{mm}$  and  $t = 2\text{mm}$ , show different magnitudes of errors of  $J_s$  to  $J$ . The thicker specimen ( $t = 4\text{mm}$ ) gives better agreement between  $J_s$  and  $J$ .

Figure 6.3 shows similar results for the glass epoxy composite and the isotropic material of table 6.1. All specimens have the same thickness of  $4\text{mm}$ , but with different crack lengths. From Figures 6.2 and 6.3, the four observations that follow can be made. First,  $a/t$  does not directly scale the accuracy of  $J_s$ . Second, for a given specimen



thickness, the accuracy of  $J_s$  improves with increasing crack length. Third, for a given crack length, accuracy increases with increasing thickness. Fourth, for a given crack length and thickness, the accuracy of  $J_s$  improves with increasing  $E_{11}/G_{12}$  and  $E_{11}/E_{22}$ .

Figures 6.2 and 6.3 show that  $J_s$  has larger errors at lower loads when the end rotation angle is small and becomes more accurate when the deformation of specimen increases. This is the opposite of the trend observed from other data reduction methods based on beam theory. This is more favorable since we measure fracture toughness at higher loads, i.e., when growth occurs. By comparing to literature test results, the end rotation angle at fracture usually falls in the range of 5-20 degrees. Within this range,  $J_s$  can be determined with high accuracy for Gr/Ep specimens having an initial crack length longer than 37mm for specimen thicknesses of 2-6mm, here, errors in  $J_s$  to  $J$  are less than 1.5%. For the GI/Ep and the isotropic material of table 6.1, errors in  $J_s$  are also less than 1.5% for specimens with crack lengths longer than 37mm and a thickness of 4mm. Here, results show that the  $J_s$  method will be highly accurate for geometries that are generally used in linear elastic DCB fracture tests of composite material.

Recall that the derivation of the  $J_s$  expression is based on a point load on the specimen boundaries. But in the practical testing and FE modeling, we introduce loading blocks for the purpose of load application and angle measurement in the  $J_s$  method. Williams (1987, 1988, 1989a, 1989b) developed modified beam theory based data reduction methods accounting for possible large deformations and loading block effects. This was done through the use of a crack length correction to classical beam theory, which accounted for end rotation effects at the crack tip and transverse shear effects, plus

the application of nonlinear corrections for large deformation and loading block effects. The crack length correction and possible large deformation are implicitly included in the  $J_s$  method with the use of the end rotation angle. The effects of loading blocks from Williams' work, however, cannot be directly applied in  $J_s$  because the moment arm change due to the loading blocks is implicitly contained in the  $J_s$  expression. The other effects of the loading blocks, local stiffening, is not considered in the expression of the  $J_s$ .

Results in Figures 6.2 and 6.3 are obtained from FE models with loading blocks directly connected to the specimen legs, which creates a stiffer connection between them than the practical application. To eliminate or reduce this effect in the FE model, a thin layer of material with adhesive properties is added between the block and the specimen. Figure 6.4 compares the percentage errors of  $J_s$  in comparison to  $J$  between models with and without adhesive for the three materials in table 6.1. Symbols only without lines denote results from the graphite/epoxy composite. Symbols with solid lines represent results from glass/epoxy composite. Symbols with dashed lines are for the isotropic material. In this figure, filled symbols are from the models with adhesive and the open symbols represent results from the models without adhesive. Specimen geometries selected for the comparison are the ones that showed large deviations between  $J_s$  and  $J$  in Figures 6.2 and 6.3. For all materials and geometries, the models with adhesive give better agreement between  $J_s$  and  $J$ . Therefore, the results in Figure 6.2 and 6.3 from models without adhesive are conservative compared to the physical test setup, i.e., the true error is less than that in these figures.

Different sizes of loading blocks may be selected in DCB tests. All of the previous results are from models using a block size of  $j = 0.5''$  and  $k = 0.5''$  in Figure 5.1(b). Figure 6.5 presents the percent error in  $J_s$  versus end rotation angle for specimens with different block sizes. The specimen has the same geometry of  $a = 25\text{mm}$  and  $t = 2\text{mm}$  and the material uses the  $G_r/E_p$  in table 6.1. The chosen geometry in the simulation is rarely adopted in the fracture test. However, for this geometry, we see large errors between  $J_s$  and  $J$ , and this specimen geometry therefore can more clearly show the effects of loading block size. In Figure 6.5, filled symbols without lines represent results for specimens with square loading blocks, i.e.,  $j = k = 0.25''$ ,  $0.375''$  and  $0.5''$ . It is observed that smaller-sized blocks give better accuracy for  $J_s$ , which indicates smaller stiffening effects. The triangular symbols with or without lines in Figure 6.5 present the results for given the same loading block width  $j = 0.25''$ . For rotation angles up to  $20^\circ$ , the errors are similar for different block heights,  $k$ , of  $0.25''$ ,  $0.375''$  and  $0.5''$ . However, the percent errors are different due to the different block height  $k$  for a given block width  $j$  of  $0.375''$  or  $0.5''$ , i.e., a taller block improves the accuracy of  $J_s$ . The square symbols with solid and dashed lines represent the results from block width  $j$  of  $0.375''$  and  $0.5''$ , respectively for the given block height  $k = 0.25''$ . Considering also the results from the square block  $0.25'' \times 0.25''$ , it is observed that with a wider block, the accuracy of the  $J_s$  is lower. The same trend is seen for the given height  $0.375''$  and  $0.5''$ . In summary, the accuracy of  $J_s$  improves by reducing block width and increasing the block height.

### 6.3.2 Linear viscoelastic analyses

Linear viscoelastic material model as proposed in section 6.2.3 needs be validated before being used in evaluation of  $J_s$ . Figure 6.6 shows the percent difference of  $J$  from the proposed material model in comparison to the value of  $J$  from the ABAQUS default isotropic linear viscoelastic model. The materials shown in the above section 6.2.3.2 were used. Good agreement (less than 1% difference) was obtained for the end rotation angles in the range of  $3^\circ \sim 20^\circ$  that are generally obtained in DCB experiments. Therefore, the proposed orthotropic material model was utilized for evaluating  $J_s$  for the orthotropic linear viscoelastic materials in table 6.2. The specimens used the dimensions of  $a=50\text{mm}$  and  $t=4\text{mm}/6\text{mm}$  because good agreement between  $J_s$  and  $J$  was obtained for linear elastic material. Loading block of  $0.5'' \times 0.5''$  was utilized. Figure 6.7 presents the percent difference of  $J_s$  in comparison to  $J$  from ABAQUS output. Up to an end rotation angle of  $20^\circ$ , good agreement between  $J_s$  and  $J$  were achieved. The error is always less than 0.5%.

### 6.3.3. Specimen dimension

The simulation results in linear elastic and linear viscoelastic materials indicate that a DCB specimen with thicknesses of 4-6mm and crack length of equal to or more than 50mm can determine  $J_s$  with high accuracy. As a result, DCB specimens with starting crack lengths of 50mm are manufactured for fracture tests. Simulation results suggest using smaller loading blocks. However, considering the manufacturing requirements for the size of the hole and the associated pin stiffness,  $0.5'' \times 0.5''$  loading blocks were selected. With this block size, for the initial crack length of 50mm, the accuracy of  $J_s$  is still good as shown in Figures 6.2, 6.3 and 6.7.

## 6.4. Conclusion

Finite element analyses were performed to evaluate the accuracy of the  $J_s$  method with loading blocks. For specimens with crack lengths larger than 37mm and thicknesses of 2-6mm, the error between  $J_s$  and  $J$  was less than 1.5% in linear elastic DCB specimens. The specimen dimensions of  $a = 50\text{mm}$  and  $t = 4\text{mm}$  and  $6\text{mm}$  gave high accuracy of  $J_s$  for orthotropic linear viscoelastic materials. No efforts were contributed in this study to find a closed-form expression to account for loading block effects because these effects can be avoided by a careful design of specimen geometries. Especially, this work showed that effects of loading blocks were very small for practical DCB specimen geometries. The accuracy of  $J_s$  improves with smaller loading blocks, but for the specimen dimension of  $a = 50\text{mm}$  and  $t = 4-6\text{mm}$ , using the block size of  $0.5'' \times 0.5''$  provided good results of  $J_s$ . Therefore, in our tests, the specimen dimension of  $a = 50\text{mm}$  and  $t = 4-6\text{mm}$ , and the loading block of  $0.5'' \times 0.5''$  were used. Detailed results are discussed in the following chapters.

## CHAPTER 7

# ROOM TEMPERATURE DELAMINATION TOUGHNESS TESTING

### 7.1. Introduction

In chapter 6, an experimental technique to measure  $J_s$  was validated through finite element analyses of double cantilever beam (DCB) specimens for both linear elastic and linear viscoelastic materials. This was done by comparing  $J_s$  as found by the proposed technique to  $J$  as evaluated from the contour integral using results from the local stress analysis. It was shown that  $J_s$  can be determined accurately from DCB specimens with initial crack lengths of 50mm and thicknesses of 4-6mm with use of the 0.5”X0.5” loading blocks. However, the experimental setup for measuring  $J_s$  still needs validation before it is ready to be employed in DCB experiments under environments such as elevated temperature with or without moisture. Two carbon fiber-reinforced polymeric composites, T800H/3900-2 and IM7/8551-7, are available in our lab. These two composites were tested previously using the DCB configuration in our lab and exhibited linear elastic response at room temperature. Traditional data reduction methods such as the compliance calibration (CC) method and modified beam theory (MBT) were used and resulted in accurate delamination toughnesses for these two materials at room temperature. Therefore,  $J_s$  as found using the newly proposed technique can be validated

by comparing it to the delamination toughness as found by traditional methods for these two materials.

In this chapter, the DCB experimental setup is first described. The data reduction method and experimental procedure are then introduced. Then, results are compared between  $J_s$  and fracture toughnesses as found from CC and MBT methods in order to validate the approach to determine  $J_s$ .

## **7.2. Specimen preparation and experimental setup**

Unidirectional 22-ply laminates from Toray T800H/3900-2 prepreg were manufactured. The average thickness of the specimens was 3.98 mm. Two 32-ply specimens were also available which were made by other colleagues in the SUCML lab and the thickness was 6.03 mm. Another material system, IM7/8551-7, is also used in the verification, which is a carbon fiber-reinforced rubber toughened epoxy. 32-ply specimens of IM7/8551-7 laminate were made by previous students in the SUCML lab. The thickness was 4.52 mm.

The initial delamination was created by embedding a 13  $\mu\text{m}$  thick Teflon film between two central plies (11/12 for  $[0]_{22}$  and 16/17 for  $[0]_{32}$ ) during lay-up. The insert is about 2.5" long and creates an initial delamination. The laminates are cut into 1" wide specimens by a diamond saw. The specimens have a total length of about 5"- 6" with a 2" initial delamination on one of the ends. Specimen edges are coated with Aluminum DH1606 silver spray paint for clearer observation of crack propagation. One edge of the specimen is marked with pencils following the DCB test standard ASTM D5228 (1994).

The other edge is either covered by paint with pencil marks or glued with Vishay Micro-Measurement TK-09-CPB02-005/DP crack gages by Vishay M-Bond 200 adhesive following the general gage installation guidelines. Each TK-09-CPB02-005/DP crack gage has 10 resistance grid lines uniformly distributed within 2.5mm. 4 crack gages are glued in a series on the edge of the specimen to cover up to about 55 mm crack growth. The first grid of the first gage is aligned with the insert front. The second gage is 25 mm away from the first gage to accommodate the crack jump as observed from previous work on this material (Davidson et al, 2009b). Other two gages are about 5mm apart. Electrical circuits, shown in Figure 7.1, are used to measure the voltage change when the gage grid line breaks. The primary reasons for using the crack gages at room temperature are to practice installation procedure, address the use of crack gages for determining both crack length and critical load. Loading blocks are glued on the specimen using 3M Scotch-weld DP-420 epoxy adhesive. The dimensions of the block are as shown in Figure 5.1(b).

Figure 7.2 presents the experimental setup for determining  $J_s$  through the angle measurement approach described in chapter 5. The displacements on the loading blocks legs are measured using Differential Variable Reluctance Transducers (DVRTs) from Microstrain, Inc. Two-piece C-clamp mounting blocks secure the DVRTs in place. Based on the results from previous fracture tests of similar materials, an 8mm stroke length, spring-loaded subminiature SG-DVRT-8 linear transducer was selected. The maximum operating temperature of this DVRT is 175°C. A Microstrain MB-SMT-D conditioner transforms the DVRT displacement to a voltage and transfers the voltage output to the data acquisition system on a personal computer. A linear relationship between voltage



output and relative displacement from the DVRT from the company calibration sheet was used.

All DCB tests were performed on a MTS 810 load frame equipped with a +/- 4” stroke length actuator, a 1000 lb load cell and an MTS TestStar II controller. However, for these tests a 100 lb load range and a +/-1” displacement range were used. Displacement control with a rate of 0.0008 inch/sec was used. A new data acquisition program based on Labview software was developed that allows all the data from the load cell, actuator, crack gages and DVRTs to be recorded synchronously through a desktop computer.

### **7.3. DCB Data reduction and experimental procedure**

Fracture toughness from the load-based compliance calibration (CC) approach is defined in chapter 2 and repeated here as

$$G_{Ic}^{CC} = \frac{nP_c^2 Ra^{n-1}}{2B} \quad (7.1)$$

Application of a compliance calibration procedure to determine delamination toughness in a DCB test exhibits advantages over other approaches. The first is that there are no requirements for accurate material properties. This is needed in many other approaches. This can be a drawback, because inaccurate knowledge of material properties could cause erroneous results in the perceived toughness. Secondly, the CC approach is a single specimen data reduction method that avoids possible effects due to specimen-to-specimen variations in properties. Thirdly, the accuracy of the perceived toughness from

the CC approach shows less dependency on the measuring method of crack length. The compliance function,  $C(a)$ , in the CC approach is obtained through curve fitting of the results from several crack lengths during growth, which could reduce the effects from errors in a single crack length measurement. For crack initiation from the insert, accurate crack length can be made from post-test assessments (i.e., by splitting the specimen and noting the location of the end of the Teflon insert.)

Another LEFM-based data reduction from Williams (1987, 1988, 1989a, 1989b) is also explored. Chapter 2 shows the WLO and WLD equations that are generally used in the literature. However, in these two expressions, the correction factors  $F$  and  $N$  neglect the crack length correction. In our work, we evaluate the effects of the crack length correction in the factors  $F$  and  $N$  on the accuracy of the energy release rate by utilizing a nonlinear finite element model of a linear elastic DCB specimen with loading blocks. Based on these results (presented in Appendix A), the modified Williams' load only (MWLO) approach is shown to give energy release rates that agree closely with the value from an established energy balance approach. Thus, the MWLO data reduction approach is used in our work for reducing test data, and is expressed as

$$G_{Ic}^{MWLO} = F_e \frac{P_c^2 (a + \chi h)^2}{BE_{11}I_1} \quad (7.2)$$

Where  $P_c$  is the critical load when fracture toughness is calculated,  $a$  is the crack length,  $h$  is the thickness of one DCB leg,  $B$  is the width of the specimen, and  $I_1$  is the second moment of inertia of one DCB leg. The correction factor  $\chi$  is a function of the orthotropic material properties and is defined in equation (2.18).  $F_e$  is the correction factor for

consideration of large deformation and effects of loading blocks and uses the corrected crack length  $a_e$ . It is given by

$$F_e = 1 - \frac{3}{10} \left( \frac{\delta}{a_e} \right)^2 - \frac{3}{2} \left( \frac{\delta l_1}{a_e^2} \right) \quad (7.3)$$

where  $a_e = a + \chi h$ . In the above,  $\delta$  is the actuator displacement,  $l_1$  is the distance between the centerline of the loading pin and the end of the loading block, which yields  $l_1 = j/2$ , as shown in figure 5.1.  $E_{11}^{\text{DCB}}$  and  $\chi$  are determined following the works by Hashemi et al (1990a, 1990b) following the procedure described in chapter 2.

A “load-unload-reload” procedure is used in DCB tests in order to obtain the relationship of compliance and crack length that is used in both the CC and MWLO approaches. Usually, the specimen is unloaded when approximately 0.1”-0.2” of crack propagation occurs. The new crack length is taken as the average from the observation of both edges of the specimen. A total of 6 additional increments of growth are then obtained from each specimen. The compliance at any crack length is calculated based on the slope of a linear fit of the applied load versus actuator displacement data. The critical load in calculating fracture toughness usually uses either the nonlinear load point, the 5% offset point, or the maximum load point during each loading cycle (Hashemi et al, 1990b). In this work, the maximum load is used to calculate the fracture toughness because the load-deflection curve always showed negligible nonlinearity before crack growth. In addition, from those specimens with crack gages, we find that the crack initiation always happens at the maximum load point.

Delamination toughness is calculated by the CC method using equations (7.1) and the MWLO method in equation (7.2).  $J_s$  is determined from the expression of (5.21) using the same critical load that is used in the other two approaches.

#### **7.4. Results and discussion**

Figure 7.3 presents a typical load-deflection curve recorded for one of the T800H/3900-2 specimens. The specimen was loaded and unloaded several times to obtain multiple crack growths. The figure shows multiple load-deflection curves. Each of those curves corresponds to loading the specimen until fracture at one crack length. After about 0.1”~0.2” propagation occurred, the specimen was unloaded to less than 5N, then the specimen was reloaded. Figure 7.3 shows that the unloading and reloading curves are almost identical. The crack initiation occurs when the load reaches the maximum in each loading cycle for all specimens. A sudden load drop is usually seen after the first several growths as shown in Figure 7.3, which corresponds to the delamination path change. Figure 7.4(a) shows the typical fracture surface morphology for three stages during crack growth, i.e., delamination initiation, crack jump and steady state growth. For the delamination initiation stage (usually the first several increments), honey-comb shapes are seen on the fracture surface and fibers are barely seen. This indicates that the delamination happens between the interlayer. The fracture surface of crack jump and steady growth show clearly fibers on the surface. This indicates that crack growth path changes from inside the interlaminar resin to the interface between interlayer and lamina layer as illustrated in Figure 7.4(b). All T800H/3900-2 specimens tested at room temperature showed the similar load-deflection curves and fracture surface morphology.

Figures 7.5, 7.6 and 7.7 show  $J_s$  and  $G_{IC}$  as determined from CC and MWLO methods from 22-ply and 32-ply T800H/3900-2 DCB specimens tested at room temperature. Filled symbols represent the critical  $J_s$  or  $G_{IC}$  of 22-ply specimens calculated using the maximum load from each loading cycle. Open symbols represent the critical  $J_s$  or  $G_{IC}$  of 22-ply specimens determined using the instantaneous load at the moment when each crack gage line broke. Tests of two 32-ply specimens are also plotted in these figures. No crack gages are attached on these two 32-ply specimens so that the fracture toughness is only determined from maximum load point in each loading cycle. All 6 specimens show consistent results that are independent of the specimen thicknesses and crack length measurement methods, either from crack gage or from the side marks. Fracture toughnesses from 22-ply and 32-ply specimens at room temperature are believed to represent the same population of the laminates as shown here. The average initiation value of  $J_s$  from insert is  $792.6 \text{ J/m}^2$ , with a standard deviation of  $51.9 \text{ J/m}^2$  and Coefficient of Variance (C.V.) of 6.5, which is the percentage of standard deviation over the mean. The average  $J_s$  during steady crack propagation is  $284.6 \text{ J/m}^2$ , with a standard deviation of  $12.5 \text{ J/m}^2$  and C.V. of 4.4. Fracture toughnesses  $G_{IC}$  from CC and MWLO approaches were determined using equations 7.1 and 7.2. The average value of  $n$  is about 2.8 with C.V. of 2.5, which is very close to the results from previous work (Kumar 2004). In this work, the average initiation toughness from CC approach is  $816.3 \text{ J/m}^2$  with a standard deviation of  $58.0 \text{ J/m}^2$  and C.V. of 7.1. The fracture toughness during steady crack propagation is  $290.2 \text{ J/m}^2$  with a standard deviation of  $12.1 \text{ J/m}^2$  and C.V. of 4.2 using CC approach.  $E_{11}$  and  $\chi$  from different specimens are calculated from equation (2.21) with coefficients  $k_1$  and  $k_2$  determined from the least square fit of the curve

$(C/N)^{1/3}$  versus crack lengths,  $a$ . The average  $E_{11}$  is 145.0 GPa with C.V. of 4.1. The average  $\chi$  is 2.64 with C.V. of 13.1. The toughness value from the insert using the MWLO method is  $786.7 \text{ J/m}^2$  with a standard deviation of  $47.2 \text{ J/m}^2$  and C.V. of 6.0. The fracture toughness during steady crack propagation using MWLO method is  $288.9 \text{ J/m}^2$  with a standard deviation of  $9.5 \text{ J/m}^2$  and C.V. of 3.3. A comparison of the average magnitudes, along with +/-1 standard deviation data for  $J_s$ ,  $G_{IC}^{CC}$  and  $G_{IC}^{MWLO}$  is shown in Figure 7.8. The average magnitudes of  $J_s$  and  $G_{IC}$  from CC and MWLO agree with each other and are also close to the previous results of the same material at room temperature (Davidson et al 2009).

In Figures 7.5, 7.6 and 7.7,  $J_s$ ,  $G_{IC}^{CC}$  and  $G_{IC}^{MWLO}$  drop from a high initiation value to a lower propagation value. This may happen immediately after the first crack increment or after several increments of growth. The sudden drop of delamination toughness induces unstable crack growth because the energy available to propagate the crack is suddenly much larger than the toughness of the material to resist the growth. Crack jumps about 25mm for T800H/3900-2 specimens at room temperature. This is accompanied by a sudden load drop as shown in Figure 7.3. The similar results are found by the previous work (Kumar 2004). The different values of toughnesses between initiation and steady propagation stage are associated with the crack growth mechanism as shown in Figure 7.4. Some broken fibers shown in the microscopic view of fracture surface in Figure 7.4(a) indicate possible fiber bridging in the steady growth stage. The cumulative effects of fiber bridging may explain the slightly increasing curve observed in Figures 7.5, 7.6 and 7.7.

Figures 7.9, 7.10, and 7.11 show the percent error of  $G_{IC}^{MWLO}/G_{IC}^{CC}$ ,  $J_s/G_{IC}^{CC}$ , and  $J_s/G_{IC}^{MWLO}$  versus crack growth for T800H/3900-2 specimens, respectively. Filled symbols represent the difference from the results of 22-ply T800H/3900-2 specimens using the maximum load from each loading cycle. Open symbols represent the difference from the results of 22-ply specimens using the instantaneous load at the moment when each crack gage line broke. Figure 7.9 indicates very close results are found from CC and MWLO approach. Most of errors are within 5%. Except the results from specimen TH32-2, the perceived toughness from MWLO method is consistently smaller than those from CC method. In Figures 7.10 and 7.11, dashed lines represent the difference of +/-5%.  $J_s$  is comparable to  $G_{IC}$  from CC and MWLO methods. Most of the differences are within 5%. There are different patterns in Figures 7.10 and 7.11 compared to Figure 7.9. The reason is that  $J_s$  is not a direct function of the crack length, but other two parameters,  $G_{IC}^{CC}$  and  $G_{IC}^{MWLO}$  are dependent on the crack length explicitly.

Figures 7.5, and 7.9-7.11 show close results of  $J_s$  to  $G_{IC}^{CC}$  and  $G_{IC}^{MWLO}$  of T800H/3900-2 at room temperature. Therefore,  $J_s$  as determined using the critical load is an equivalent fracture toughness of the material. This validates that the approach and test setup of determining  $J_s$  as described in section 7.2 can be used to determine the delamination toughness of T800H/3900-2 with acceptable accuracy. The test setup is also used to determine the toughness of another material, IM7/8551-7.

Figure 7.12 presents a typical load-deflection curve from an IM7/8551-7 DCB specimen. Crack initiation occurs at the maximum load in each loading cycle. A sudden load drop is also seen after the first loading cycle which is accompanied by a crack jump.

$J_s$ ,  $G_{IC}^{CC}$  and  $G_{IC}^{MWLO}$  are determined similarly as was done for the T800H/3900-2 specimens. Figure 7.13 shows the results of these three parameters versus the crack growth for each specimen. The filled symbols represent the results of  $J_s$ , and the open symbols represent the results of  $G_{IC}^{CC}$ . The rest of the symbols represent the results of  $G_{IC}^{MWLO}$ . The fracture toughnesses drop from initiation toughness of 677.1 J/m<sup>2</sup> to steady growth toughness of 460.0 J/m<sup>2</sup>. The smaller difference between initiation toughness and steady stage toughness leads to smaller crack jump length, about 8 mm for IM7/8551-7 comparing to over 25 mm for T800H/3900-2. Figure 7.14 plots the percent error of  $G_{IC}^{MWLO}/G_{IC}^{CC}$ ,  $J_s/G_{IC}^{CC}$ , and  $J_s/G_{IC}^{MWLO}$  versus crack growth for IM7/8551-7 specimens. All three errors are within 5%. The good agreement of  $J_s$  to other two parameters,  $G_{IC}^{CC}$  and  $G_{IC}^{MWLO}$ , indicates the appropriate use of the test setup in determining  $J_s$ .

## 7.5. Conclusion

The approach of determining  $J_s$  by the newly proposed technique was validated using two unidirectional graphite/epoxy composite systems, T800H/3900-2 and IM7/8551-7, at room temperature. The percent difference between  $J_s$ ,  $G_{IC}^{CC}$  and  $G_{IC}^{MWLO}$  are similar to those obtained between generally accepted conventional data reduction methods from the DCB test. This validates that the test setup can be used to determine  $J_s$  with acceptable accuracy. Therefore, the test setup may be used for high temperature tests of T800H/3900-2. This work is described in chapter 8.



## **CHAPTER 8.**

# **ELEVATED TEMPERATURE AND MOISTURE TESTING**

### **8.1. Introduction**

In chapter 4, the linear viscoelastic properties of T800H/3900-2 were measured. In chapter 5, the proposed experimental approach to determine  $J_s$  using DCB tests was developed. This approach was validated in chapters 6 and 7. In this chapter, the  $J_s$ -approach is used to characterize the delamination growth behavior of T800H/3900-2 at temperatures and moisture conditions that are a significant percentage of the material's glass transition temperature.

### **8.2. Moisture conditioning chamber and high temperature furnace**

Moisture conditioning system was achieved by upgrading an existing humidity chamber. The system is shown in Figure 8.1(a). It integrates a number of components, all which are placed on a movable cart. Figure 8.1(b) presents a schematic of the circulation system. It includes two flowing cycles, wet air and water, and two electrical circuits, control of temperature and relative humidity. The major cycle of wet air starts from the Atomizing water tank. Distilled water in the Atomizing water tank is sprayed into the same tank (top vacant space) through one of two atomizing nozzles that are driven by the compressor. The wet air is forced by the blower to flow through the conditioning loop in

the sequence of atomizing water tank, chamber, water drain tank, blower, heater, and back to the atomizing tank. The water flow loop includes the atomizing water tank, chamber and water drain tank. The wet air condenses in the chamber and water drain tank, and water flows back to the atomizing tank. A proportional–integral–derivative (P.I.D.) controller controls the temperature and relative humidity (R.H.) inside the chamber. Thermocouples and a humidity transducer inside the humidity chamber measure the temperature and relative humidity (R.H.), respectively. When the temperature is lower than the set point from the P.I.D. controller, the heater is triggered to start heating the air. When the R.H. is lower than the set point, the compressor starts working to force the nozzles to spray more water into the air flowing cycle. The system ran continuously for more than 4 years.

The system described above was used to condition T800H/3900-2 specimens to a moisture-saturated condition. The specimens were placed in the chamber at 49°C and 95% relative humidity air following the suggestion from Soffa (2003). The initial dry mass of each specimen was measured before putting in the chamber. The mass gain of each specimen due to moisture absorption was recorded until saturated. Figure 8.2 shows a typical plot of moisture mass gain versus the square root of days for conditioning T800H/3900-2 specimens. The open symbols represent the results from Soffa (2003). The solid symbols represent the results using the new system. The T800H/3900-2 specimens reached saturation condition after about three months in both chamber.

A high temperature furnace was designed and built at the Syracuse University Composite Materials Lab. This furnace produces temperature control through a JUMO

iTRON 16 digital P.I.D. controller. The P.I.D. parameters were programmed based on heating rate requirements for different tests. Sensitivity studies of the combination of all parameters were performed in order to achieve fast heating requirements. Two glass windows on both sides of the furnace allow the observation of crack initiation and propagation during fracture tests. The forced convection air by a rotating fan inside the furnace ensures a uniform temperature profile of the specimen during elevated temperature tests.

### **8.3. DCB testing procedures**

The DCB tests performed at temperatures of 98°C and 125°C used the same experimental setup as described in chapter 7. Additional items, specific to the elevated temperature tests, are described below.

Multiple crack gages were glued on the edge of the DCB specimen. There are two purposes of crack propagation gages in the DCB tests under elevated temperatures. The first is to indicate the crack initiation time that is used in the derivation of the fracture initiation curve. The first grid line on the first gage was carefully aligned with the initial delamination tip. Any small mismatch of the position for the first grid line can be identified after the tests. The breakage time of the first grid line indicates the delamination initiation time, which is more accurate than any estimation technique of initiation time from the load-deflection curve. The second is to determine the crack growth speed. The crack gages gave the crack lengths as a function of the load and time. Figure 8.3(a) is an example of the crack gage voltage output versus test time. The time when each step change in voltage occurs indicates crack propagation through the

corresponding crack gage grid line. Crack growth speed can be obtained with crack lengths and grid line breakage time as shown in figure 8.3 (b). The sampling rate of data acquisition was 500Hz.

A tele-microscope system (TMS) was built to observe the crack tip region during the fracture tests conducted in the furnace. T800H/3900-2 at elevated temperatures may exhibit inelastic responses as shown in the previous work (Soffa et al 2006). The crack growth history recorded through the TMS system helps us better understand crack propagation. Figure 8.4 shows the TMS experimental setup, which integrates a K2/S<sup>TM</sup> tele-microscope, a Leica EC3 digital imaging camera and a personal computer. The system allows a working distance of 10” - 12”. This distance gives an optical magnification of 4.5X-8.6X. Figure 8.3(b) is an example image taken during a test. The Leica EC3 digital imaging camera only allows taking still pictures. In order to record the crack growth history, a personal Sony digital camcorder is used to record the computer screen during crack propagation. A traveling stage supporting the TMS allows for vertical and horizontal motion to track crack propagation. The clock on the image acquisition computer is adjusted to show the same time as the clock on the data acquisition computer. The specimen edge is painted for marking with 1 mm-spaced marks drawn on the edge surface.

3M Scotch-weld DP-420 epoxy adhesive was initially used to glue the loading tabs for tests under elevated temperatures. Some of the tabs debonded during the tests. Therefore, AREMCO-bond 570 from AREMCO Products Inc., a high temperature adhesive, was used to glue the loading tabs for the remainders of the specimens.

DCB tests were performed under three environmental conditions: at 98°C with dry and wet specimens, and at 125°C with dry specimens. Under each condition, three displacement rates, 0.005mm/sec, 0.0254mm/sec, and 0.254mm/sec were used. These loading rates allowed for the evaluation of delamination growth over several decades of crack speed. Continuous loading was used until the crack grew by approximately 20mm, which extended the crack over all the crack gages. Unloading was then performed at the same displacement rate as the loading step to recover the viscoelastic deformation during the fracture test.

## **8.4. Results and discussion**

In this section, the test results of the DCB specimens are presented. Due to the quantity limitation of T800H/3900-2 prepreg left in our lab for this work, the number of specimens for tests at different conditions was used differently according to the test data variation. Under conditions showing consistent results, a small number of specimens were used. On the other hand, more specimens were used under conditions where large variations in the data were observed.

### **8.4.1. Dry DCB tests at 98°C**

Six dry 22 ply DCB specimens were tested at 98°C. Three constant displacement rates were used, with two specimens tested at each rate. As shown in the following, very consistent and reproducible results were obtained from the two specimens at each loading rate. The specimen dimensions are shown in the test matrix of table 8.1. The thickness of each specimen was obtained by averaging 6 measurements along each specimen at both

sides of three locations. The width of each specimen was obtained by averaging three measurements along the specimen. The initial crack length is measured from the center of the loading block to the insert tip as shown in Figure 6.1.

Figure 8.5 presents a typical plot of the load-deflection curve from one of the dry DCB specimens tested at 98°C. The loading curve shows a very linear relationship between the load and the deflection up to the crack initiation point. There was no residual deformation (crack opening displacement at the loading point) in any of the 6 specimens after testing.

Figure 8.6 shows the maximum normal stress calculated using beam theory for a cantilever beam with fixed root at the crack tip. Each data point in the plot represents the maximum normal stress calculated using the crack length at each gage grid line at the undeformed specimen shape and the measured load when the grid line breaks. The longitudinal maximum stress at the root of the cracked leg shows a small dependence on crack length. The average stress is about 200MPa, which is lower than the target stress level used in the creep-recovery tests. This indicates that the material response in the fracture specimens at 98°C was within the assumption of the linear viscoelasticity.

$J_s$  was obtained using equation (5.21) following the procedure described in chapter 5. Figure 8.7 presents  $J_s$  as a function of crack growth length. Here, crack growth length was measured at each crack gage grid line. Fracture initiation energy,  $\Gamma_{li}$ , at the instant of delamination initiation was determined using equation (5.16). In this equation,  $J_s$  at the instant of crack initiation was used.  $g(n)$  was determined using equation (5.14) through the analysis of the linear viscoelastic DCB specimen in chapter 5. The exponent

of the equivalent viscoelastic compliance,  $n$ , was determined from material properties tests as described in chapter 4. For the dry specimens at 98°C,  $n=0.0086$  as shown in equation (4.1).

Figure 8.8 presents the results of fracture initiation energy versus delamination initiation time. Each open symbol represents the fracture initiation energy from each specimen with respect to the crack initiation time. The fracture initiation energy shows negligible dependence on the crack initiation time over a range of 10 - 1000 seconds. The dashed line in the figure is the average value of the fracture initiation energy from 6 specimens, which is  $426.9 \text{ J/m}^2$  with a standard deviation of  $27.0 \text{ J/m}^2$ . The constant fracture initiation energy indicates that the initiation of crack growth happens when the fracture energy in the structure is above the curve. If the fracture energy is below this curve, the crack will not propagate.

Figure 8.9 presents results for the instantaneous stress intensity factor,  $K_I$ , versus crack growth speed for all 6 specimens. Each individual symbol represents the average result of  $K_I$  from each crack gage.  $K_I$  was calculated from instantaneous  $J_s$  using equation (5.4) at each crack gage grid line. The average value of  $K_I$  for each gage is shown in Figure 8.9. The crack speed was obtained from the relationship of crack length and loading time for each gage following the same method as the example in Figure 8.2. In Figure 8.7, all the data points follow the trend of a power law fitting curve (the dashed line). The slope of the dashed line is the inverse of the exponent of crack growth equation (5.17), i.e.,  $1/(2(1+1/n))$ , in which  $n=0.0086$ , the exponent of the equivalent viscoelastic compliance from equation (4.1). Based on equation (5.17) and (5.18) from the Schapery's

linear viscoelastic theory, the constant multiplier of the curve fitting equation in Figure 8.9 indicates that the fracture energy and the stress distribution inside the failure zone are independent of crack speed for dry T800H/3900-2 specimens at 98°C. It is unnecessary to derive the explicit fracture energy with further assumption of the stress distribution inside the failure zone because the fracture curve can be used to predict crack growth speed at an instantaneous moment (Schapery 1975). The  $\dot{a}(K_I)$  curve represents the fracture behavior of the material under this condition and may be used for fracture prediction in other structures.

#### **8.4.2. Moisture saturated tests at 98°C**

DCB tests were performed on twelve moisture saturated (“wet”) T800H/3900-2 specimens at 98°C: nine 22-ply, two 32-ply and one 24-ply unidirectional specimens of T800H/3900-2. The dimensions of the specimens are shown in table 8.1. The 22-ply specimens were manufactured specifically for this study. The 24-ply specimen and 32-ply specimens were left from a previous study (stored in a sealed bag with desiccant for one year). Based on the results from the room temperature tests, these three thicknesses should belong to the same population for perceived toughness. All these specimens had been conditioned in the humidity chamber as described above for more than 3 months before fracture tests were performed.

Figure 8.10 displays the load-deflection curves of DCB specimens at each displacement rate. Some of the curves show that the load suddenly drops to zero instead of a continuous unloading curve because the tab debonding happened in these specimens.



Some specimens had residual deformation, i.e., there existed crack opening displacement at the loading point after unloading the specimen. For example, the 24-ply specimen tested at 0.0254mm/sec had residual deformation of 0.95mm. All the 22-ply specimens had residual deformations, but with different magnitudes from 0.25mm to 2.1mm. Two 32-ply specimens had nearly zero residual deformation. Figure 8.11 shows the percent of the residual deformation in comparison to the maximum deformation for each specimen.

Figure 8.12 shows the maximum normal stresses versus the crack growth length for all the wet specimens tested at 98°C. All the stresses are below the target stresses used in the creep tests. Large variations are seen between different specimens, especially, the 32-ply specimen shows much smaller normal stress. The calculation of the normal stress was based on the undeformed specimen shape, which ignored the change of moment arm during the tests. As shown in Figure 8.10, the crack opening displacement at the loading point in the 32-ply specimens is almost half of the displacement in 22-ply specimens at the similar amount of crack growth. This indicates smaller effects of the moment arm shortening in calculating the normal stress for 32-ply specimens than for 22-ply specimens.

Figure 8.13 presents the results of  $J_s$  versus the amount of crack growth for all twelve wet specimens tested at 98°C. A large variation of  $J_s$  is seen between specimens. Larger  $J_s$  was determined for the specimens having a higher percent residual deformation (Figure 8.11). These specimens (one 24-ply specimen and three 22-ply specimens) have residual deformations that were more than 5% of the maximum deflection in the test and show  $J_s$  larger than 1500 J/m<sup>2</sup> during the steady-state crack propagation.

Fracture initiation energy was determined from equation (5.16) using the measured  $J_s$  at the initiation of the delamination growth and the exponent of the equivalent viscoelastic compliance in equation (4.2). Figure 8.14 presents the results of fracture initiation energy as a function of the crack initiation time for all the wet specimens tested at 98°C. Individual symbols represent the result from each specimen at each loading rate. A solid line in the figure represents the average magnitude of fracture initiation energy from all twelve specimens, which is 406.4 J/m<sup>2</sup> with a standard deviation of 59.1 J/m<sup>2</sup>. Two dashed lines represent +/-1 standard deviation from the mean. Most of the data are bounded by the +/-1 standard deviation except the specimens of Z2-T22-11B and Z2-T22-3B.

In Figure 8.15, the instantaneous stress intensity factor is plotted against crack growth speed. The symbols represent the average result of stress intensity factor from each gage for all wet specimens tested at 98°C. The filled symbols represent the results of the 22-ply specimens at each displacement rate. The open symbols represent one 24-ply specimen and two 32-ply specimens. A dashed line in Figure 8.18 is a power law curve fitting on the test data except those data that are circled representing specimens with residual deformation larger than 5% of the maximum deformation in Figure 8.11. The exponent of the curve fitting expression in Figure 8.15 is equal to the inverse of the exponent of the crack growth curve (5.17), i.e.,  $1/(2(1+1/n))$ , in which  $n=0.0221$ , the exponent of the equivalent viscoelastic compliance from equation (4.2). Based on the good match of the exponent in the crack growth curve between the test data and Schapery's linear viscoelastic theory, the constant multiplier in the curve fitting equation indicates that the fracture energy and the stress distribution inside the failure zone are

independent of crack speed for wet T800H/3900-2 specimens at 98°C. The test data that are circled in Figure 8.18 (one 24-ply specimens and three 22-ply specimens) deviating from the theory are explored in the discussion section later based on the investigation of the specimens.

#### **8.4.3. Dry DCB tests at 125°C**

Fourteen 22-ply and eleven 32-ply specimens were tested at 125°C. More specimens were tested under this condition because larger scatter in results occurred under this condition as compared to other conditions. The specimen dimensions are shown in table 8.1. The number of specimens tested at each displacement rate varied according to the amount of scatter in the data. For example, at the medium displacement rate of 0.0254mm/sec, eight [0]<sub>22</sub> and four [0]<sub>32</sub> specimens were tested as this rate showed the largest variation in results.

Figures 8.16 and 8.17 depict the load-displacement relationship of 22-ply specimens and 32-ply specimens tested at 125°C, respectively. Different magnitudes of residual deformations are observed. Figures 8.18 and 8.19 present the percent residual deflection in comparison to the maximum deflection for 22-ply specimens and 32-ply specimens. In Figure 8.18, some 22-ply specimens show residual deformations larger than 5%, but the results for all 32-ply specimens are less than 5%.

Figures 8.20 and 8.21 present the maximum normal stress versus crack growth length for 22-ply and 32-ply dry specimens tested at 125°C, respectively. All the stresses are below the target stresses used in the creep tests. The 32-ply specimens show smaller

maximum normal stress than the 22-ply specimens. Larger variation is seen in 22-ply specimens with a stress difference of 150MPa compared to 32-ply specimens with a stress difference of 20MPa.

Figure 8.22 presents  $J_s$  versus the crack growth length for all 22-ply dry specimens tested at 125°C. Large variation is seen in the  $J_s$  at the same crack growth length. Very high  $J_s$  always occurred in the specimens with large residual deformations (Figure 8.18). The specimen in the box in this figure all had residual deformation below 5%. Figure 8.23 presents  $J_s$  versus crack growth length for all 32-ply specimens. The variation of  $J_s$  at the same crack length is small and the magnitudes of  $J_s$  are close to the magnitudes of  $J_s$  for the 22-ply specimens in the box in Figure 8.22, i.e., for those that have residual deflections less than 5% of the maximum deflection.

Fracture initiation energy for each specimen was determined using equation (5.16) with the  $J_s$  at the initiation of delamination growth and the exponent of equivalent viscoelastic compliance in equation (4.3). Figure 8.24 presents the fracture initiation energy as a function of crack initiation time. The discrete symbol represents data from each specimen. The closed symbols represent 22-ply specimens and the open symbols represent 32-ply specimens. The dashed line in the figure is the curve fit of all the data. The fracture initiation energy is not constant any more, but time-dependent. From both 22-ply and 32-ply specimens, the results indicate that higher fracture energies cause more rapid crack initiation for T800H/3900-2 dry specimens at 125°C.

Figure 8.25 presents the relationship between instantaneous stress intensity factor,  $K_I$ , and crack growth speed for all 22-ply and 32-ply dry specimens at 125°C. Each

discrete symbol represents the mean value of  $K_I$  from each crack gage. The crack growth speed was calculated from each gage as in Figure 8.3. Filled symbols represent data from 22-ply specimens while open symbols represent data from 32-ply specimens at three loading rates. The dashed line in Figure 8.25 is a power law curve fitting with equation shown in the figure. This fitting curve uses the data from the specimens with residual deflections lower than 5% of their maximum deflections. The exponent of the fitting curve matches the exponent of Schapery's linear viscoelastic crack growth function. It is the inverse of the exponent of equation (5.17), i.e.,  $1/(2(1+1/n))$ , in which  $n=0.0109$ , the exponent of the equivalent viscoelastic compliance from equation (4.3). As has been seen in the other two conditions, the good match of the exponents between the theory and the measured crack growth curve indicates that the fracture energy and the stress distribution inside the failure zone are independent of crack speed for dry T800H/3900-2 specimens at 125°C. The outliers from the curve fitting (some data from 22-ply specimens circled in Figure 8.25) are discussed in the following section.

#### 8.4.4. Discussion

The crack growth curves such as fracture initiation energy versus crack initiation time,  $t_i(\Gamma_{II})$ , and instantaneous stress intensity factor versus crack growth speed,  $\dot{a}(K_I)$ , were determined for T800H/3900-2 DCB specimens under three environmental conditions using the linear viscoelastic experimental model introduced in chapter 5. The indirect angle measurement technique determined  $J_s$  under these three conditions. The fracture initiation energy and instantaneous stress intensity factor were obtained from  $J_s$  using the methods as described in chapter 5. The experimental parameters such as crack

initiation time and crack growth speed were measured using the validated experimental setup. The following discussion is specifically focused on the evaluation on T800H/3900-2 specimen results under three conditions.

Good agreement was achieved for all dry specimens at 98°C between the measured crack growth curves and the prediction of the crack growth function from Schapery's linear viscoelastic theory. The crack initiation curve was determined based on the linear viscoelastic theory. The fracture initiation energy is constant so that crack initiation happens when the fracture energy determined based on the crack geometry and load history in the structure is above the curve in Figure 8.8. Crack growth speed in the structure may be predicted by the instantaneous stress intensity factor using the crack growth curve in Figure 8.9. However, as discussed in chapter 3 (Figure 3.1), the crack growth curve should be bounded by the limited stress intensity factors, which were not determined in this work. Additional fracture tests with different loading rates at one temperature or application of the time-temperature superposition method (William et al, 1955) should be used in order to fully determine the master crack growth curve.

Under other two conditions, wet 98°C and dry 125°C, large variations in the test results were obtained for 22-ply specimens, for example, the curves for  $J_s$  vs. crack growth lengths during the crack propagation in Figures 8.13 and 8.22. Larger  $J_s$  during crack growth was always obtained for the specimens with larger residual deflections. For the clarity of discussion below, the specimens with residual deflections larger than 5% of the maximum deflection are categorized as “problematic specimens”, and all other specimens with less residual deformation are called “regular specimens.” The results

from problematic specimens were circled in Figures 8.15 and 8.25. Without the results from problematic specimens, the curve fitting from the regular specimens (including part of 22-ply specimens and all 32-ply specimens) matched the crack growth curves derived from Schapery's linear viscoelastic theory. Different techniques were used to investigate the specimens in order to find the different behaviors between problematic and regular specimens in DCB tests.

First of all, large residual deflections (greater than 5% of maximum deflection) in the problematic specimens indicates these specimens behaved other than linear viscoelastic or linear elastic response, which violated the requirements of the  $J_s$ -method developed in chapter 5, i.e.,  $J_s$  could be determined with acceptable accuracy for linear elastic and linear viscoelastic material. The indirect angle measurement technique in determining  $J_s$  from the test may include the dissipated energy due to the plastic/viscoplastic/nonlinear viscoelastic deformation in these problematic specimens. Figure 8.26 show the pictures taken after fracture tests on some of the problematic specimens. The specimen legs (initially cracked/delamination insert region) are not flat anymore, but are permanently curved. This phenomenon in 22-ply specimens after the fracture tests was not noticed from the creep tests as presented in chapter 4. One of possible reasons is due to difference of the thickness used in fracture tests and creep tests. 22-ply specimens were used in the creep tests, but one leg of 22-ply DCB specimen was only half of the thickness. However, not all the 22-ply DCB specimens resulted in large residual deformations. Therefore, other reasons specific to the problematic specimens existed. As shown in Figure 4.1, the polyamide particles are randomly distributed in the interlayers of T800H/3900-2 composite to improve the fracture toughness of the base

composite material, but the inclusion of polyamide particles on the delamination path increases the complexity of the delamination growth characterization. The delamination may go through the particles or it may grow around the particles. In addition, depending on the specific environmental conditions and size of the polyamide particles at the delamination front, the response of the polyamide particles may behave differently under loading. Consequently, the measured toughness may vary from specimen to specimen. In creep tests for specimens without an embedded delamination, the global structural response was determined while the effects of the polyamide particle were small. However, in DCB tests, the local effects of polyamide particles on the delamination front became important, and therefore affected the measured  $J_s$ . This effect could be different from specimen to specimen because of the different distribution of the polyamide particles in the interlayer. Depending on the amount of the local effects, the global response of the specimen might be different as seen in this work. Different techniques were utilized to investigate the specimens in the following for better understanding the effects of polyamide particles.

The tele-microscope system that was used during the tests provided information about the crack growth mechanisms. The recorded crack growth history under temperatures of 98°C and 125°C showed that the problematic specimens had a more blunt crack tip than others prior to the crack initiation. Sample pictures in Figure 8.27 were extracted from the recorded video at the moment of crack initiation from the insert. The first picture is from one of the problematic specimens at 125°C, the other two are regular specimens from dry 125°C and wet 98°C. The actual crack tip contour cannot be correctly measured from the images because there is a layer of silver paint covering the



specimen edge surface. The amount of opening deformation at the tip may be larger or smaller than the size in the image. However, under the same surface painting condition, the scale bar on the pictures can indicate the relative sizes between specimens for comparison. Crack tip blunting is usually found in elastic-plastic fracture (Broek 1986) and indicates non-viscoelastic behaviors in the problematic specimens. The plasticization of the polyamide particles next to the Teflon insert might be the reason, which is supported by the fracture surface morphology as discussed below.

Further investigations of specimens after the tests were performed for the problematic specimens having large residual deformations and blunt crack tips. DCB Specimens were cut into halves after the fracture tests by a diamond saw at constant speed. Following the process shown in Figure 8.28, the first cut was several millimeters ahead of the crack tip. This cut was to aid in splitting specimens. The second cut was along the fiber direction in the middle of the specimen before splitting the specimen. The second cut was to create a clear edge for observation under a microscope. The cut edge surface for observation was cleaned by compressed air to remove the debris before the examination under a three-dimensional microscope. The delamination propagation was observed always within the interlayer, which agreed with the observation through TMS during tests. However, no obvious differences were seen between problematic and regular specimens.

After the cutting edge observation under a 3D microscope, the specimens were split into halves for observation of the fracture surface morphology. Typical fracture surface morphologies are shown in Figure 8.29. These images represent the delamination

next to the insert for specimens tested at 125°C at different displacement loading rates. Similar surface morphologies are observed for both 22-ply specimens and 32-ply specimens. In these images, dark holes are possibly due to pullout of the base resin. The bright, colloidal lumps are plasticized polyamide particles.

Figure 8.30 presents photomicrographs of typical fracture surfaces during delamination propagation for specimens tested at 125°C at different displacement loading rates. Similar surface morphologies are observed for all 32-ply specimens at all displacement rates. The 22-ply specimens tested at 0.005mm/sec have different surface features than the specimens tested at the other two loading rates. There are “honeycomb”-shaped walls at displacement rates of 0.0254mm/sec and 0.254mm/sec, but almost no honeycomb shape on the surface of specimens at the rate of 0.005mm/sec. Instead, the surface of the 22-ply specimens at 0.005mm/sec shows polyamide lumps sticking together. Figure 8.31 shows the comparison between fracture surfaces of 22-ply specimens tested at 0.0254 mm/sec at 125°C in the delamination propagation stage. The fracture surfaces of problematic 22-ply specimens show sticking lumps of polyamide material, but regular specimens show honeycomb shapes on the fracture surfaces.

Typical fracture surfaces of wet specimens tested at 98°C are shown in Figure 8.32. Figure 8.32(a) presents the fracture surfaces at delamination initiation next to the insert. Surface morphologies of problematic specimens at 0.005mm/sec are different from the ones at other two displacement rates. There are largely lumped polyamide materials sticking together. While in Figure 8.32(b), fracture surfaces of regular specimens have clearly honeycomb shapes.

## 8.5. Conclusion

The experimental technique developed using linear viscoelastic theory in chapter 5 was applied in characterizing fracture behaviors of unidirectional T800H/3900-2 composites under temperatures close to  $T_g$  for dry and moisture saturated specimens. The general procedure applying the method was summarized here. Firstly, orthotropic linear viscoelastic properties within stress range of interests were determined as described in chapter 4. This step was necessary to validate the basic requirement of application of linear viscoelastic theory. Equivalent viscoelastic properties then were derived. Secondly, DCB fracture tests were performed under each environmental condition utilizing the validated test setup. Experimental parameters such as load history, crack growth-time history, crack initiation time, relative displacements at loading points were recorded synchronously. Thirdly, fracture parameters such as fracture initiation energy,  $\Gamma_{II}$ , and instantaneous stress intensity factor,  $K_I$ , were derived from the measured  $J_s$ . Fourthly, fracture curves, such as  $t_i(\Gamma_{II})$  and  $\dot{a}(K_I)$ , were constructed from curve fitting of the test data. Last, test data were evaluated and compared to the theoretical prediction. Following this procedure, the fracture curves of a linear viscoelastic composite can be obtained.

The following conclusions are specific for the test results of T800H/3900-2 composites. For dry specimens of T800H/3900-2 at 98°C, crack growth curves determined from the test using the developed method agreed with the prediction from the linear viscoelastic theory. However, for dry specimens at 125°C and moisture saturated specimens at 98°C, only part of test data showed the similar trends as the theoretical prediction. Additional investigations of the DCB specimens during tests and after tests

indicated that the complexity of the interlayer due to the distributed polyamide particles caused the large variation in the measured  $J_s$ . The variation of distribution and amount of plasticization of polyamide particles between specimens caused different behaviors of the specimens in DCB tests. Large residual deformations, crack tip blunting and lumped plasticized polyamide particles on the fracture surface morphology in some specimens are behaviors other than linear viscoelastic response. The developed method determining fracture parameters from measured  $J_s$  was inappropriate for these specimens. The plasticization effects of polyamide particles on global behaviors of some DCB specimens were not captured in the creep tests as described in chapter 4, but plastic/nonlinear viscoelastic behaviors were seen for some DCB specimens. Other than the possible influences due to the thickness difference, the amount of effects of polyamide particles in the delamination layer for creep tests and DCB tests is different. DCB specimens are more sensitive to the distribution of polyamide particles than creep tests. A method that can account for the effects of different distribution and amount of the plasticization of the polyamide particles are needed for fully characterizing the fracture behaviors of T800H/3900-2. Nevertheless, the results of the study do confirm the validity of the approach for materials that exhibit a linear viscoelastic response.

## CHAPTER 9.

# CONCLUSIONS AND RECOMMENDATIONS

### 9.1. Conclusion

The results of this work developed an experimental technique that directly determined the J-integral,  $J_s$ , for the linear viscoelastic DCB test. The linear viscoelastic fracture parameters were able to be found from the  $J_s$ . This method avoided the utility of numerical simulation in determining linear viscoelastic fracture properties and eliminated potential errors induced by discrepancies of material properties between simulation and physical specimens.

The  $J_s$  as measured using the applied load and the slope of the DCB legs at the loaded ends was equivalent to the path-independent J-integral when there were no distributed damage in the laminate legs. A simple experimental expression of  $J_s$  was developed based on an indirect angle measurement technique. The accuracy of  $J_s$  method was validated through finite element modeling of linear elastic and linear viscoelastic DCB specimen and the loading block stiffening effects were assessed.

Experimental results including  $J_s$ , crack initiation time, crack length and crack speed can be used to determine the experimental relationship such as  $t_i(\Gamma_{II})$  and  $\dot{a}(K_I)$  for

a linear viscoelastic material. If the results agree with the crack growth curves derived from the linear viscoelastic theory, the material delamination in other structures under different loading can be predicted using the linear viscoelastic theory. So the  $J_s$ -method developed here can characterize the crack growth curves. In this case, when the values of  $\Gamma_{II}$  and  $K_I$  are found for a given structure under known loading history, these values are used to find the status of the crack using the crack growth curves. For example, if the values are below the curves, no crack initiation occurs. If the values are on the curves, the corresponding crack initiation time and crack speed are found. If the values are above the curves, structural failure is predicted. On the other hand, if the experimental relationship such as  $t_i(\Gamma_{II})$  and  $\dot{a}(K_I)$  determined from  $J_s$ -method don't agree with the crack growth curves derived from the linear viscoelastic theory, the linear viscoelastic theory may not be able to characterize the material delamination properties and  $J_s$ -method breaks down. Additional investigation of the material is needed and other methods such as nonlinear viscoelastic theory or viscoplastic theory need be explored, which are out of the scope of this study.

DCB test results from two graphite fiber reinforced polymers at room temperature with the suggested specimen dimensions validated the proposed DCB experimental setup and angle measurement technique. The accuracy of  $J_s$  was acceptable comparing to the fracture toughness as found from LEFM-based data reduction methods such as the compliance calibration method and modified beam theory method.

The developed technique was applied to characterize the mode I delamination of unidirectional T800H/3900-2 DCB specimens under high temperature and moisture

saturated conditions. The general procedure for applying the  $J_s$ -method was illustrated. The following conclusions are only for T800H/3900-2 specimens tested in this study. For other materials, results may be different according to specimen configurations, range of loading rates and hygrothermal conditions.

Creep tests utilizing 4-point bending and Iosipescu test configurations were used to measure orthotropic linear viscoelastic properties on dry specimens at 98°C and 125°C and moisture saturated specimens at 98°C. Equivalent viscoelastic properties were found. DCB tests were then performed under these conditions at three displacement rates for determining the crack growth curves covering several decades of delamination initiation time and growth speed.  $J_s$  was determined from the developed indirect angle measurement setup. Fracture parameters such as  $\Gamma_{II}$ , and  $K_I$  were found using the relationship to the measured  $J_s$ . Experimental curves of  $t_i(\Gamma_{II})$  and  $\dot{a}(K_I)$  were determined from the  $J_s$  and experimental parameters such as time history, crack length and crack speed. Good agreement was achieved between test data and theoretical crack growth curves for all dry T800H/3900-2 specimens at 98°C, and a subset of the dry specimens at 125°C and moisture saturated specimens at 98°C. Observations of crack growth mechanisms during the tests and investigation after the tests on crack tip blunting, residual deformations, edge delamination paths, and fracture surface morphologies indicated behaviors other than linear viscoelastic response for specimens with results away from the theoretical curves. The variation of distribution and amount of plasticization of polyamide particles caused different behaviors of DCB specimens. The  $J_s$ -method developed in this study was inappropriate for these specimens. Another

method that can account for the effects of different distribution and amount of the plasticization of the polyamide particles are needed for fully characterizing the delamination behaviors of T800H/3900-2 when these effects occur. However, this study did validate that the new method are accurate and appropriate for specimen exhibiting either linear elastic or linear viscoelastic responses.

## **9.2. Recommendation and future work**

The  $J_s$ -method developed in this study is to characterize the mode I delamination behaviors of the composite when the DCB specimens show linear elastic and linear viscoelastic behavior. It is appropriate for the composites showing consistent global responses that are independent of the test configuration. That is, creep tests are used beforehand to determine the material viscoelastic properties and the DCB specimens should behave in the similar way as in the creep test. However, the behavior of DCB specimen may be affected by the local response at the delamination front, which cannot be captured from a global creep test. For example, T800H/3900-2 laminate in this study has randomly distributed polyamide particles along the delamination path. The responses of some DCB specimens were affected by the local material response and were different from the creep test. Therefore, use of  $J_s$ -method is not enough. Other methods that can take into account the non-uniformity of the polyamide particles are needed.

Schapery's linear viscoelastic fracture theory (Schapery, 1975) indicates that the crack growth curve of  $\dot{a}(K)$  bounded by short-term creep (elastic) and long-term creep. Our current work only characterized the fracture properties of T800H/3900-2 at the transition crack growth speed, where linear proportional relationship is found based on



the log-log plot of stress intensity factor and crack growth speed. Additional tests with wider range of crack growth speed need be performed to measure the full fracture curves. This may be done through testing the materials at a larger range of temperature by utilizing the time-temperature superposition (Williams et. al., 1955)/moisture-temperature superposition (Woo 1994, Park 2004) technique developed for linear viscoelastic materials.

Mode I fracture curves are ready to be determined from the laboratory tests based on the developed experimental technique with use of the linear viscoelastic fracture model. However, composite laminate delamination is commonly initiated and propagated by mixed-mode loading condition in the structure. It is necessary to measure the fracture curves of the material under different mode ratios. Mode I  $J_s$  is the parameter determined from the DCB test that accounts for the loading and time history. Similar  $J_s$  can also be derived for mode II test, end flexure beam test (ENF) and mixed mode I/II test, single-leg bending test (SLB), which are used for establishing the failure locus curves in linear elastic composite (Davidson and Zhao, 2007).

## CHAPTER 10.

## REFERENCES

### A

- Aliyu, A.A. and Daniel, I.M., 1985, "Effects of strain rate on delamination fracture toughness of Graphite/Epoxy," ASTM STP 876, *American Society for Testing and Materials*, Philadelphia, pp.336-348
- Anderson, T.L., 1995, *Fracture Mechanics-Fundamentals and Applications*, 2nd edition, CRC Press
- Anderson, T. and Stigh, U., 2004, "The stress-elongation relation for an adhesive layer loaded in peel using equilibrium of energetic forces," *International Journal of Solids and Structures*, v.41, pp.413-434
- Anthony, J. and Paris, P.C., 1988, "Instantaneous evaluation of J and C\*," *International Journal of Fracture*, v.38, R19-R21
- Arai, M., Sumida, T., and Shimizu, M., 2007, "Effect of Residual Stress on Interlaminar Fracture Toughness of CFRP Laminates," *Journal of Thermal Stresses*, v.30, pp.1099-1116
- Ashcroft, I.A., Hughes, D.J., and Shaw, S.J., 2001, "Mode I fracture of epoxy bonded composite joints: 1. Quasi-static loading," *International Journal of Adhesion & Adhesives*, v.21, pp.87-99
- Asp, L.E., 1998, "The Effects of Moisture and Temperature on the Interlaminar Delamination Toughness of a Carbon/Epoxy Composite," *Composite Science and Technology*, Vol. 58, pp. 967-977.
- ASTM D-3518 (1994), "Standard test method for in-plane shear response of polymeric matrix composite materials by tensile test of a  $\pm 45^\circ$  laminate," *American Society for Testing and Materials*

ASTM Standard D5228-94, 1994, "Standard test method for mode I interlaminar toughness of unidirectional reinforced polymeric matrix composites," *American Society for Testing and Materials*, West Conshohocken, PA

ASTM D-5379 (1998), "Standard test method for shear properties of composite materials by the V-notched beam method," *American Society for Testing and Materials*

ASTM E1640-04, "Standard Test Method for Assignment of the Glass Transition Temperature By Dynamic Mechanical Analysis," *ASTM International*

## **B**

Barber, J.R., 1999, *Elasticity*, Kluwer Academic Publishers

Barenblatt, G.I., 1962, "The mathematical theory of equilibrium cracks in brittle fracture," *Advances in Applied Mechanics*. v7, pp.56–125

Bazhenov, S.L. 1995, "Interlaminar and intralaminar fracture modes in 0/90 cross-ply glass/epoxy laminate," *Composites*, v26, pp. 125-133

Berry, J.P., 1963, "Determination of Fracture Energies by the Cleavage Technique," *Journal of Applied Physics*, Vol. 34, pp. 62-66.

Biot, M.A. (1972), "Nonlinear effect of initial stress on crack propagation between similar and dissimilar orthotropic media," *Quarterly of Applied Mathematics*, No.3, pp.379-406

Brockway, G.S. and Schapery, R.A., 1978, "Some viscoelastic crack growth relations for orthotropic and prestrained media," *Engineering Fracture Mechanics*, v.10, pp.453-468

Broek, D. 1986, *Elementary Engineering Fracture Mechanics*, 4th edition, Kluwer Academic Publishers, Dordrecht

Bucci, R.J., Paris, P.C., Landes, J.D. and Rice, R.J. 1972, "J-integral estimation procedure," ASTM STP 514, 1972, pp. 40-69

## **C**

Chamis, C.C. and Sinclair, J.H. (1976), "10 off-axis tensile test for intralaminar shear characterization of fiber composites," *NASA technical note D-8215*

- Chan, A., Liu, X.L. and Chiu, W.K. (2006), "Viscoelastic interlaminar shear modulus of fiber reinforced composites," *Composite Structures*, v.75, pp.185-191
- Charalambides, M.N. and Williams, J.G., 1994, "Mode I delamination of angle-ply epoxy/glass-fiber laminates exhibiting permanent deformation during fracture," *Composite Science and Technology*, v.50, pp.187-196
- Christensen, R.M., 1971, *Theory of Viscoelasticity, An Introduction*, Academic Press, INC, New York and London
- Christensen, R.M., 1979, "a rate-dependent criterion for crack growth," *International Journal of Fracture*, vol.15, No.1, pp.3-21
- Christensen, R.M. and Wu, E.M., 1981, "A Theory of Crack Growth in Viscoelastic Materials," *Engineering Fracture Mechanics*, v.14, pp.215-225.
- Cowley, K. D. and Beaumont, P. W. R., 1997, "The interlaminar and intralaminar fracture toughness of carbon-fibre/polymer composites: the effect of temperature," *Composite Science and Technology*, v.57, pp. 1433-1444.
- Crews, J.H., Jr. K.N. Shivakumar and I.S. Raju, 1986, "Factors influencing elastic stresses in double cantilever beam specimens," *NASA TM-89033*

## **D**

- Daniel, I.M. and Ishai, O., 2001, *Engineering Mechanics of Composite Materials*, Oxford University Press, Inc.
- Davidson, B.D., 1990, "An analysis to predict failure in solid rocket motors by case liner debonding," *JPL (Jet Propulsion Laboratory) Document D-7145*
- Davidson, B.D., Bialaszewski, R.D. and Sainath, S.S., 2006, "A non-classical, energy release rate based approach for predicting delamination growth in graphite reinforced laminated polymeric composites," *Composites Science and Technology*, v.66, pp.1479-1496.
- Davidson, B.D., Sun, X. and Vinciquerra, A.J., 2007, "Influences of friction, geometric nonlinearities, and fixture compliance on experimentally observed toughnesses from three and four point bend end notched flexure tests," *Journal of Composite Materials*, v.41, pp. 1177-1196

- Davidson, B.D., Soffa, M.A., and Kumar, M., 2009a, "Temperature and moisture effects in a particulate interlayered composite: mode I data reduction and toughness," *Journal Of Reinforced Plastics And Composites*, v.28, pp. 2049-2068
- Davidson, B.D., Kumar, M., and Soffa, M.A., 2009b, "Influence of mode ratio and hygrothermal condition on the delamination toughness of a thermoplastic particulate interlayered carbon/epoxy composite," *Composites: Part A*, v.40, pp.67-79
- Davidson, B.D., and Zhao, W., 2007, "An accurate mixed-mode delamination failure criterion for laminated fibrous composites requiring limited experimental input," *Journal of Composites Materials*, Vol.41, No.6, pp. 679-702
- Davies, P. and de Charentenay, F.X., 1987, "Effect of temperature on the interlaminar fracture of tough composites," *Deformation and Fracture of Laminated Composites*, Proceedings of the 6th International Conference on Composite Materials.
- Devitt, D.F., Schapery, R.A., and Bradley, W.L. 1980, "A method for determining the mode I delamination fracture toughness of elastic and viscoelastic composite materials," *Journal of Composite Materials*, v.14, pp.1270-285
- de Chaentenay, F.X., Harry, J.M., Prel, Y.J., 1984, and Benzeggagh, M.L., "Characterizing the effect of delamination defect by mode I delamination Test," *Effect of Defects in Composite Materials, ASTM STP 836*, American Society for Testing and Materials, pp. 84-103.
- Dubois F, and Keunings R., 1997, "DCB testing of thermoplastic composites: a non-linear micro - macro numerical analysis," *Composites Science and Technology*, v.57 pp.437-450
- Dubois, F., Chazal, C., and C. Petit, 1999, "A finite element analysis of creep-crack growth in viscoelastic media," *Mechanics of Time-Dependent Materials*, v.2, pp. 186-269.
- Dubois, F. and Petit, C., 2005, "Modeling of the crack growth initiation in viscoelastic media by the  $G_v^0$ -integral," *Engineering Fracture Mechanics*, V.72, pp. 2821-2836
- Dugdale, D.S., 1960, "Yielding of steel sheets containing slits," *Journal of the Mechanics and Physics of Solids*, v8, pp.100-104

## **F**

- Ferry, J.D., 1961, *Viscoelastic Properties of Polymers*, John Wiley & Sons, inc
- Fracasso, R., Rink, M., Pavan, A., Frassine, R., 2001, "The effects of strain-rate and temperature on the interlaminar fracture toughness of interleaved PEEK/CF composites," *Composites Science and Technology*, v.61, pp.57-63
- Frassine, R., and Pavan, A. 1990, "An application of viscoelastic fracture criteria to steady crack propagation in a polymeric material under fixed deformation," *International Journal of Fracture*, v. 43, pp. 303-317
- Frassine R., and Pavan, A. 1995, "Viscoelastic effects on the interlaminar fracture behavior of thermoplastic matrix composites: I. rate and temperature dependence in unidirectional PEI/carbon-fiber laminates," *Composites Science and Technology*, v54, pp193-200
- Frassine, R., Rink, M. and Pavan, A. 1996a, "Viscoelastic effects on the interlaminar fracture behavior of thermoplastic matrix composites: II. rate and temperature dependence in unidirectional PEEK/carbon-fiber laminates," *Composites Science and Technology*, v.56, pp1253-1260
- Frassine, R., and Rink, M., and Pavan, A. 1996b, "Experimental analysis of viscoelastic criteria for crack initiation and growth in polymers," *International Journal of Fracture*, v.81, pp.55-75

## **G**

- Gamby, D. and Delaumenie, V., 1997, "Measurement and modeling of crack propagation velocity in a viscoelastic matrix composite," *Composites Part A*, v.28, pp.875-881
- Gamby, D. and Chaoufi, J. 1999, "Application of viscoelastic fracture criteria to progressive crack propagation in polymer matrix composites," *International Journal of Fracture*, v.100, pp. 379-399
- Garg, A. and Ishai, O., 1985, "Hygrothermal Influence on Delamination Behavior of Graphite/Epoxy Laminates," *Engineering Fracture Mechanics*, v.22, no.3, pp. 413-427.

- Gillespie, J.W., Carlson, L.A., and Smiley, A.J., 1987, "Rate-dependent mode I interlaminar crack growth mechanism in graphite/epoxy and graphite peek," *Composites Science and Technology*, v28, no.1, pp.1-15
- Goetz, D.P., 1988, "Determination of the mode I delamination fracture toughness of multidirectional composites laminates," Ph.D dissertation, Texas A&M University
- Graham, G.A.C., 1968, "The correspondence principle of linear viscoelasticity theory for mixed boundary value problems involving time-dependent boundary regions," *Quarterly Applied Mathematics*, v26, pp.167-74
- Griffith, A.A., 1921, "The phenomenon of rupture and flow in solids," *Philosophical Transactions of the Royal Society of London*, A221, pp.163-197
- Guedes, R.M., Marques, A.T., and Cardon, A. (1999), "Creep/creep-recovery response of fibredux 920C-TS-5-42 composite under flexural loading," *Applied Composite Materials*, v6, pp.71-86

## **H**

- Ha, S.K., Springer, G.S. (1989), "Time dependent behavior of laminated composites at elevated temperature," *Journal of Composite Materials*, v.23, pp.1159-1197
- Hashemi, S., Kinloch, A.J. and Williams, J.G. 1990a, "The analysis of interlaminar fracture in uniaxial fiber-polymer composites," *Proc. R. Soc. Lond*, A427, pp.173-199
- Hashemi, S., Kinloch, A.J. and Williams, J.G. 1990b, "Mechanics and mechanism of delamination in a poly(ether sulphone)-fiber composite," *Composites Science and Technology*, v.37, pp.429-462
- Hojo, M., Kageyama, K., and Tanaka, K., 1995, "Prestandardization study on mode I interlaminar fracture toughness test for CFRP in Japan," *Composites*, v.26, pp.243-255
- Hojo, M., Matsuda, S., Tanaka, M., Ochiai, S., and Murakami, A., 2006, "Mode I delamination fatigue properties of interlayer-toughened CF/epoxy laminates," *Composites Science and Technology*, v.66, pp.665-675

Hunston, D.L., 1984, "Composite interlaminar fracture: effect of matrix fracture energy," *Composites technology review*, v.6, n.4, pp.176-180

Hunston, D.L., Moulton, R.J., Johnston, N.J., and Bascom, W.D., 1987, "Matrix resin effects in composite delamination: mode I fracture aspects," *ASTM Special Technical Publication 937*, pp.74-94

## **I**

Iosipescu, N. (1967), "New accurate procedure for single shear testing of metals," *Journal of Materials*, September 1967

Irwin, G.R., 1948, "Fracture dynamics," *Fracturing of Metals*, American Society for Metals, Cleveland, pp.147-166

## **J**

Jordan WM, and Bradley WL., 1987, "Micromechanisms of fracture in toughened graphite-epoxy laminates," In: Johnston NJ, editor. Toughened composites. *ASTM STP 937. American Society for Testing and Materials*, pp. 95-114.

Jordan WM, Bradley WL, Moulton RJ., 1989, "Relating resin mechanical properties to composite delamination toughness," *Journal of Composite Materials*, v.23, pp.923-942.

## **K**

Kageyama, K., Kimpara, I., Ohsawa, I., Hojo, M., and Kabashima, S., 1995, "Mode I and mode II delamination growth of interlayer toughened carbon/epoxy (T800H/3900-2) composite system," *Composite Materials: Fatigue and Fracture- fifth volume*, ASTM STP 1230, R.H. Martin, Ed., Philadelphia, pp.19-37

Kanninen, M.F. 1973. "An augmented double cantilever beam model for studying crack propagation and arrest," *International Journal of Fracture*, v.9, n.1, pp.83-92

Knauss, W.G., 1970, "Delayed failure – the Griffith problem for linearly viscoelastic materials," *International Journal of Fracture*, v6, 7–20.



- Knauss, W.G. and Losi, G.U., 1993, "Crack propagation in a nonlinear viscoelastic solid with relevance to adhesive bond failure," *Journal of Applied Mechanics*, v.60, pp.793–801.
- Kostrov, B.V., and Nikitin, L.V., 1970, "Some general problems of mechanics of brittle fracture," *Archiwum Mechaniki Strosowanej*, v 22, n 6, pp. 749-76
- Kumar, M. 2004, "Influence of hygrothermal condition on delamination toughness at different mode-mixities for T800H/3900-2 graphite/epoxy," M.S. thesis, Syracuse University
- Kusaka, T., Hojo, M., Mai Y.-W., Kurokawa, T., Nojima, T., and Ochiai, S., 1998, "Rate dependence of mode I fracture behaviour in carbon-fibre/epoxy composite laminates," *Composites Science and Technology*, v.58, pp.591-602

## L

- Landes, J.D. and Begley, J.A., 1972, "The effect of specimen geometry on JIC," ASTM STP 514, pp.24-39
- Lee, Sang Soon, 1996, "Time-dependent boundary element analysis for an interface crack in a two-dimensional unidirectional viscoelastic model composite," *International Journal of Fracture*, v 77, n 1, pp. 15-28
- Lee, S.S. and Kim, N.H., 2005, "Boundary element analysis of viscoelastic fracture," *Key Engineering Materials*, v 297-300, pp. 2240-2246
- Liang, R.Y., and Zhou, J., 1997, "Energy based approach for crack initiation and propagation in viscoelastic solid," *Engineering Fracture Mechanics*, v.58, pp.71-85
- Linkov, A.M.,1994, "Boundary value problem for crack growth in viscoelastic media," *International Journal of Fracture*, v 65, n 3, pp. 197-218

## M

- Matsuda, S., Hojo, M. and Ochiai, S., "Mesoscopic Fracture Mechanism of Mode II Delamination Fatigue Crack Propagation in Interlayer-Toughened CFRP," *Transactions of the Japan Society of Mechanical Engineers*, 1997, pp. 39-45.

Matsuda, S., Hojo, M. and Ochiai, S., "Effect of Water Environment on Mode II Delamination Fatigue in Interlayer-toughened CFRP," *Transactions of the Japan Society of Mechanical Engineers, Series A*, Vol. 64, No. 622, 1998, pp. 1639-1645.

Matsuda, S., Hojo, M. and Ochiai, S., Murakami, A., Akimoto, H., and Ando, M., 1999, "effect of ionomer thickness on mode I interlaminar fracture toughness for ionomer toughened CFRP," *Composites, Part A*, v.30, pp.1311-1319

## **N**

Nielsen, L.E., 1962, *Mechanical Properties of Polymers*, Reinholdt, New York, pp.108-112

## **O**

Odagiri, N., Kishi, H. and Nakae, T., "T800H/3900-2 Toughened Epoxy Prepreg System: Toughening Concept and Mechanism," Proc. of the 6th Conf. of the American Society for Composites, 43, 1991, pp. 43-52

## **P**

Pagano, N.J. and Schoeppner, G.A., 2001, "Delamination of polymer matrix composites: problems and assessment," *Polymer Matrix Composites*, pp.434-525

Park, S.W. and Kim, Y.R. 1999, "Interconversion between relaxation modulus and creep compliance for viscoelastic solids," *Journal of Materials in Civil Engineering*, vol.11, pp.76-82

Park, S., Liechti, K.M., and Roy, S., 2006, "A nonlinear viscoelastic fracture analysis of concrete/FRP delamination in aggressive environments," *International Journal of Fracture*, v.142, pp.9-27

Plausinis, D. and Spelt, J.K., 1995, "Designing for time-dependent crack growth in adhesive joints," *International Journal of Adhesion and Adhesive*, v. 15, pp.143-154

Pramanick, A. and Sain, M. (2006), "Temperature-stress equivalency in nonlinear viscoelastic creep characterization of thermoplastic/Agro-fiber composites," *Journal of Thermoplastic Composite Materials*, v.19, pp.35-60

## R

- Rhee, K.Y., Koh, S.K., and Lee, J.H., 2000, "Mode I fracture resistance characteristics of graphite/epoxy laminated composites," *Polymer Composites*, v.21, n.2, pp.155-164
- Rice, J.R., 1968, "A path independent integral and the approximate analysis of strain concentration by notches and cracks," *Journal of Applied Mechanics*, v.35, pp.379-386
- Rice, J.R., Paris, P.C., and Merkle, J.G., 1973, "Some further results of J-integral analysis and estimates," ASTM STP 536, pp. 231-245
- Rosen, B.W. (1972), "A simple procedure for experimental determination of the longitudinal shear modulus of unidirectional composites," *Journal of Composites*, v.6, pp.552-554
- Russell, A.J. and Street, K.N., 1985, "Moisture and Temperature Effects on the Mixed-Mode Delamination Fracture of Unidirectional Graphite/Epoxy," *Delamination and Debonding of Materials*, ASTM STP 876, W.S. Johnson, Ed., American Society for Testing and Materials, Philadelphia, pp. 349-370.

## S

- Schapery, R.A., 1975a, "A theory of crack initiation and growth in viscoelastic media, I. theory development" *International Journal of Fracture*, v.11, pp. 141–159
- Schapery, R.A., 1975b, "A theory of crack initiation and growth in viscoelastic media, II. Approximate methods of analysis," *International Journal of Fracture*, v.11, pp. 369-388
- Schapery, R.A., 1975c, "A theory of crack initiation and growth in viscoelastic media, III. Analysis of continuous growth," *International Journal of Fracture*, v.11, pp. 549-562
- Schapery, R.A., 1984, "Correspondence principles and a generalized J integral for large deformation and fracture analysis of viscoelastic media," *International Journal of Fracture*, v25, pp.195–223.
- Schapery, R.A., 1989, "On the mechanics of crack closing and bonding in linear viscoelastic media," *International Journal of Fracture*, v39, 163–189

- Schapery, R.A., 1990, "On some path independent integrals and their use in fracture of nonlinear viscoelastic media," *International Journal of Fracture*, v.42, pp.189-207.
- Sih, G.C., Paris, P.C. and Irwin, G.R., 1965, "On cracks in rectilinearly anisotropic bodies," *International Journal of Fracture Mechanics*, v.1, pp.189-203
- Smiley, A.J. and Pipes, R.B., 1987, "Rate effects on mode I interlaminar fracture toughness in composite materials," *Journal of composite materials*, v.21, pp.670- 687
- Soffa, M.A. (2003), "Effects of moisture and temperature on the delamination toughness of an interlayer-toughened Graphite/Epoxy," *Thesis for Master of Science at Syracuse University*
- Soffa, M.A., Davidson, B.D. and Kumar, M. 2006, "Mode I Toughness of a Particulate Interlayered Composite as a Function of Moisture and Temperature," *Proceedings of the 21st Annual American Society for Composites Technical Conference*, Dearborn, MI
- Song, S.J., and Waas, A.M., 1994, "Mode I failure of laminated polymeric composites," *Engineering Fracture Mechanics*, v.49, pp.17-27
- Swanson, S.R., 1976, "Application of Schapery's theory of viscoelastic fracture to solid propellant," *Journal of Spacecraft*, v.13, n.9, pp.528-533

## U

- Uematsu, Y., Kitamura, T., and Ohtani, R., 1995, "Delamination behavior of a carbon-fiber-reinforced thermoplastic polymer at high temperatures," *Composites Science and Technology*, v.53, pp.333-341

## V

- Vincent, P.I. and Gotham, K.V., 1966, "Effect of crack propagation velocity on the fracture surface energy of PMMA," *Nature*, v.210, 1966, 1254–1255

## W

- Wang, B., Yuen, M.F., and Xiao, Z., 1998a, "On the calculation of energy release rate for viscoelastic cracked laminates," *International Conference on Solid-State and Integrated Circuit Technology Proceedings*, pp. 564-567
- Wang, S.S., Suemasu, H., and Zahlan, N.M., 1984, "Interlaminar fracture of random short-fiber SMC composite," *Journal of composite materials*, v.18, pp574-594
- Wang, W.X., Takao, Y., Yuan, F.G., Potter, B.D., and Pater, R.H., 1998b, "The interlaminar mode I fracture of IM7/LaRC-RP46 composites at high temperatures," *Journal of Composite Materials*, v.32, N.16, pp.1508-1526
- Williams, J.G., 1987, "large displacement and end block effects in the DCB interlaminar test in Mode I and II," *Journal of Composite Materials*, v.21, pp. 330-347
- Williams, J.G. 1988, "On the calculation of energy release rate for cracked laminates" *International Journal of Fracture*, v.36, pp.101-119
- Williams, J.G. 1989a, "End correction for orthotropic DCB specimens," *Composite Science and Technology*, v.35, pp.367-376
- Williams, J.G. 1989b, "The fracture mechanics of delamination tests," *Journal of Strain Analysis*, v.24, pp.207-214
- Williams, M.L., Landel, R.F., and Ferry, J.D., 1955, "The temperature dependence of relaxation mechanisms in amorphous polymers and other glass forming liquids," *Journal of American Chemistry Society*, v.77, pp.3701-3707
- Williams, M.L. , 1965, "Initiation and growth of viscoelastic fracture," *International Journal of Fracture Mechanics*, v 1, n 4, pp. 292-310
- Whitcomb, J.D., 1985, "a simple calculation of strain-energy release rate for a nonlinear double cantilever beam," *Composites of Technology and Research*, v.7, n.2, pp.64-66
- Woo, E.M. (1994), "Moisture-temperature equivalency in creep analysis of a heterogeneous-matrix carbon fibre/epoxy composite," *Composites*, v 25, n 6, pp. 425-430

## Y

- Yamada, S., 1988, "The J-integral for augmented double cantilever beams and its application to bonded joints," *Engineering Fracture Mechanics*, v.29, n.6, pp. 673-682
- Ye, L., 1992, "Evaluation of Mode-I interlaminar fracture toughness for fiber-reinforced composite materials," *Composites Science and Technology*, v.43, pp.49-54

# **APPENDICES**

**Appendix A. Numerical Evaluation of DCB Data Reduction Approaches for Linear Elastic Materials**

**Appendix B. Geometry evaluation of 4-point bending tests for accurate stresses from BT solution**

## **APPENDIX A.**

# **NUMERICAL EVALUATION OF DCB DATA REDUCTION APPROACHES FOR LINEAR ELASTIC MATERIALS**

### ***A.1 Introduction***

Finite element analysis of double cantilever beam (DCB) specimens was used in this work to evaluate the accuracy of a modified beam theory based data reduction methods when geometrical nonlinearities are considered. The finite element models used are as described in the Chapter 6. The reason for considering geometrical nonlinearity is that, when the specimen is relatively thin and the fracture toughness of the material is relatively high, a DCB specimen may experience large displacements before the crack initiation. This may invalidate data reduction methods derived from the assumptions of linear beam theory. Williams et al (1987, 1988, 1989a, 1989b) developed analytical solutions for DCB specimens taking into account large displacements in the test, as well as the effects of loading blocks. To this end, we will evaluate these expressions for various materials and also propose a modified Williams's MBT method.

### **A.2. Numerical fracture parameters**

Energy release rate from an energy balance approach (EBA) was used (Davidson et al 2007). Energy release rate was also calculated based on Williams' closed-form solution with use of the model parameters such as geometry, loads and material



properties. Different expressions from Williams' work include the WLO (Williams Load only) and WLD (Williams Load & Displacement) methods:

$$\text{WLO:} \quad G_I = F \frac{P^2 (a + \chi h)^2}{BE_{11}I_1}$$

$$\text{WLD:} \quad G_I = \frac{F}{N} \frac{3P\delta}{2B(a + \chi h)}$$

Where

$$F = 1 - \frac{3}{10} \left(\frac{\delta}{a}\right)^2 - \frac{3}{2} \left(\frac{\delta l_1}{a^2}\right)$$

$$N = 1 - \left(\frac{l_2}{a}\right)^3 - \frac{9}{8} [1 - (l_2/a)^2] \left(\frac{\delta l_1}{a^2}\right) - \frac{9}{35} \left(\frac{\delta}{a}\right)^2$$

$$\chi = \sqrt{\frac{E_{11}}{11G_{13}}} \left[ 3 - 2 \left( \frac{\Gamma}{1 + \Gamma} \right)^2 \right]^{1/2}$$

$$\Gamma = 1.18 \frac{\sqrt{E_{11}E_{22}}}{G_{13}}$$

It is noted that, in Williams' original work, the correction factors F and N were calculated using the specimen original crack length without accounting for the crack length correction. However, according to the various effects including end rotation at the crack tip and transverse shear effects in orthotropic composites, it might be better to use the effective crack length in the calculation of correction factors F and N. Therefore, we proposed the modified Williams' solution as,

$$\text{MWLO:} \quad G_I = F_e \frac{P^2(a + \chi h)^2}{BE_{11}I_1}$$

$$\text{MWLD1:} \quad G_I = \frac{F_e}{N_e} \frac{3P\delta}{2B(a + \chi h)}$$

$$\text{MWLD2:} \quad G_I = \frac{F_e}{N} \frac{3P\delta}{2B(a + \chi h)}$$

where

$$F_e = 1 - \frac{3}{10} \left(\frac{\delta}{a_e}\right)^2 - \frac{3}{2} \left(\frac{\delta l_1}{a_e^2}\right)$$

$$a_e = a + \chi h$$

$$N = 1 - \left(\frac{l_2}{a}\right)^3 - \frac{9}{8} [1 - (l_2/a)^2] \left(\frac{\delta l_1}{a^2}\right) - \frac{9}{35} \left(\frac{\delta}{a}\right)^2$$

$$N_e = 1 - \left(\frac{l_2}{a_e}\right)^3 - \frac{9}{8} [1 - (l_2/a_e)^2] \left(\frac{\delta l_1}{a_e^2}\right) - \frac{9}{35} \left(\frac{\delta}{a_e}\right)^2$$

Evaluation of the above data reduction methods was performed using the finite element model of unidirectional orthotropic DCB specimens.

### A.3. Simulation results

Comparisons were performed between the EBA and the energy release rate reduced from modified beam theory expressions. The composite material properties of table A.1 were used. The specimen geometry was taken as crack length  $a = 50\text{mm}$  and thickness  $t = 2h = 4\text{mm}$ . Figure A.1 shows the calculated percent errors, in comparison to

the EBA, for  $G_I$ \_WLO,  $G_I$ \_WLD,  $G_I$ \_MWLO,  $G_I$ \_MWLD1 and  $G_I$ \_MWLD2 as functions of end rotation angle for Mat.1, which represent a typical graphite fiber reinforced epoxy. Energy release rates from WLO, WLD, and MWLD1 methods were only good at small end rotation angle. A little better agreement was found for  $G_I$ \_MWLD2. The energy release rate from MWLO method agrees very well with EBA results for end rotation angles up to 29 degree (the difference was less than 1.0%). Similar results were also found in other materials in table A.1.

## **Appendix B.**

# **Evaluation of beam theory for predicting stresses in 4-point bending tests**

### ***B.1 Introduction***

Closed-form solutions of the simple bending specimens (3-point bending or 4-point bending) are available, which were derived based on beam theory. These expressions are usually used in experimental tests for establishing stress-strain relationship of the testing materials. However, direct use of these equations might be limited for composite laminates due to the shear coupling effects. Also, the “ideal” simply supported condition was hard to meet since finite-diameter loading pin/roller are typically used to load the specimen (even a wedge has finite radius). Therefore, it is necessary to evaluate the dependency of predicted stresses from beam theory on the specimen geometry and test setup.

In this work, we use finite element (FE) analysis to evaluate the 4-point bending tests that were used to measure material properties. The goal is to investigate if the stress from the simple beam theory solution using the initially measured specimen geometries and loading could give accurate inner-span stresses for various geometries that are commonly used in experiments. In this work, only roller-loaded conditions are

considered in order to avoid potential local compression failure on composite surface when the wedge is used.

## ***B.2 Finite element model and numerical parameters***

The FE model was developed using ANSYS. Plane stress elements, PLANE42, were used. At the regions with loading rollers, meshes were refined accounting for the large local stress gradient. The model geometries were based on the 4-point bending configuration shown in Figure B.1. The normal stress in the middle region of the beam is derived from beam theory solution as

$$\sigma_{11}^{BT} = \frac{(P/2)d}{I} \frac{t}{2}$$

The stresses from the beam theory solution were compared to the FE model stress output  $\sigma_{11}^{FEM}$  for different geometries in table B.1. All these geometries are selected for the availability in our lab. The percent error in the beam theory expression was calculated as

$$\%Error = \frac{\sigma_{11}^{BT} - \sigma_{11}^{FEM}}{\sigma_{11}^{FEM}} \times 100$$

Nonlinear contact model was established within the FE model to account for the shift of loading point, directional change of loading and reaction forces, and effective loading span changes due to the potential finite displacement in the test. Figure B.2 is the example FE model from this study.

This analysis work was to assist the overall study. The typical properties of T800H/3900-2 in table 4.1 were used in the analysis. The maximum stress level was determined from the fracture tests of T800H/3900-2 from previous work in our lab. The maximum normal stresses in DCB or ENF specimen all fell in the range of 300~400MPa. Therefore, in the current simulations, this stress level was used for comparison of all different geometries. Also, stress level effects on the error of predicted stress by beam solution were also evaluated.

### ***B.3 Simulation results and discussion***

In this section, we evaluate the effects of specimen geometry (thickness and span ratio), test setup geometry (loading roller effects) and stress level on the accuracy of the beam theory solution.

#### ***B.3.1. Loading span ratio effects***

According to table B.1, there are 4 major dimensions for the 4-point bending specimen. The loading span ratio effects study was based on a specimen with  $t = 4\text{mm}$  thick and roller diameter  $D = 12.7\text{mm}$ . The target stress is 314MPa. Figure B.3 shows the different combinations of the outer and total loading spans that were considered and the associated percent errors. The ratio  $d/t$  primarily controls the accuracy of the beam theory solution, where larger  $d/t$  ratios result in smaller errors. For  $d/t \geq 12.7$ , the error from beam theory solution is equal to or less than 1%. For  $d/t = 9.525$ , the error was about 1.22%, which is also very small.

### **B.3.2. Specimen thickness effects**

Different specimen thicknesses were simulated to cover a range of test specimens. According to above results, the evaluation of thickness effects were based on constant span ratio  $d/t = 12.7$ , a stress level of 314MPa and roller diameters  $D = 12.7\text{mm}$  and  $6.35\text{mm}$ . Figure B.4 plots the results. Thinner laminates result in larger errors. In addition to the thickness effect, we also see that thicker specimens ( $t = 3\text{mm}$  and  $4\text{mm}$ ) had small dependency on the roller diameter, but the thin specimen ( $t = 2\text{mm}$ ) had significant dependency on the roller diameter. This is also seen in the next section.

### ***B.3.3. Loading roller diameter effects***

For the constant span to thickness ratio  $d/t = 12.7$  and half inner span length  $L = 12.7\text{mm}$ , Figure B.5 show the effects of roller diameter on two thicknesses of specimen. For  $t = 4\text{mm}$  in Figure B.5(a), there are negligible effects of roller diameters from  $3.175\text{mm}$  to  $12.7\text{mm}$  for stress level up to 314MPa. However, increasing roller diameter will increase the error when  $t=2\text{mm}$ , as shown in Figure B.5(b).

### **B.3.4. Stress level effects**

The above evaluation shows the geometrical effects on the accuracy of the beam theory solution of inner span stresses. However, as we mentioned before, all these evaluations were based on the target stress level from the previous fracture tested specimen. The accuracy of the beam theory solution may also be affected by the magnitude of the load. That is, with increasing load, nonlinear effects will change the accuracy of the linear beam solution. Therefore, the percent error of the beam theory

solution was evaluated against the stress level. In this analysis, the test setup used the constant span lengths  $d = 38.1\text{mm}$  and  $L = 12.7\text{mm}$ . Figure B.6 shows the results for different roller diameters and two thicknesses of specimens ( $t = 2\text{mm}$  and  $t = 4\text{mm}$ ). The beam theory solution over-predicts the stress when the magnitude of mid-span stress is low. With an increase of the external load, the beam solution begins under-predicting the stress. However, the percent error is small (less than 1.5%) within the stress range of 300~400MPa, which is the range of interest in our work. Roller diameter has no significant effect on these results for both specimen thicknesses of  $t = 2\text{mm}$  and  $t = 4\text{mm}$ .

#### ***B.4 Summary***

The error of the linear beam solution in expression B.1 was evaluated by comparing to the nonlinear contact FE model results. The comparison study is summarized in the following.

1. The span-to-thickness ratio,  $d/t$ , has significant effects on the accuracy of calculated stress from linear beam solution. Larger values of  $d/t$  produce more accurate results.
2. Specimen thickness,  $t$ , is a very important parameter that affect the accuracy of the beam solution, which is independent of the span-to-thickness ratio,  $d/t$ . Thicker specimen produces more accurate results.
3. Smaller roller diameters result in smaller errors, but for larger  $d/t$  ratios at certain thickness (like  $t = 4\text{mm}$ ), roller diameter shows negligible effects within stress range (300~400MPa) of interest.



4. With increasing stress level, the error changes due to the shift of relative positions of the loading rollers, rotation of force direction and change of moment arm.

Based on above simulation summary, we chose our experimental setup such that the linear beam theory solution would be accurate to better than 1.5%. The ranges considered were  $d \geq 38.1\text{mm}$  (1.5"),  $L = 12.7\text{mm}$  (0.5"),  $t = 2\sim 4\text{mm}$ , and  $D \leq 6.35\text{mm}$  (0.25").

**Table 4.1 Typical elastic properties for unidirectional T800H/3900-2 graphite/epoxy laminate**

<b>E<sub>11</sub></b> <b>(GPa)</b>	<b>E<sub>22</sub></b> <b>(GPa)</b>	<b>E<sub>33</sub></b> <b>(GPa)</b>	<b>G<sub>12</sub></b> <b>(GPa)</b>	<b>G<sub>13</sub></b> <b>(GPa)</b>	<b>G<sub>23</sub></b> <b>(GPa)</b>	<b>v<sub>12</sub>, v<sub>13</sub>, v<sub>23</sub></b>
143.13	7.58	7.58	4.27	4.27	2.88	0.32

**Table 4.2 Constant load level in creep tests**

<i>Test configuration</i>	<i>Longitudinal bend</i>	<i>Transverse bend</i>	<i>Shear test</i>
<b>Load</b>	200lb/889.7N; 400lb/1779.4N	10lb/44.8N; 15lb/66.7N	75lb/333.6N; 100lb/448.3N

**Table 4.3 Linear viscoelastic properties of T800H/3900-2 at each condition**

	<i>98 °C Dry</i>	<i>98 °C Wet</i>	<i>125 °C Dry</i>
<b>s</b>	0.000	0.0007	0.0009
<b>m</b>	0.0073	0.0120	0.0100
<b>k</b>	0.0112	0.0372	0.0131
<b>S<sub>1</sub> (10<sup>-6</sup>/MPa)</b>	6.6	6.7	6.6
<b>S<sub>2</sub> (10<sup>-6</sup>/MPa)</b>	135.1	156.3	138.9
<b>S<sub>6</sub> (10<sup>-6</sup>/MPa)</b>	277.8	312.5	291.8
<b>v<sub>12</sub></b>	0.202	0.160	0.192

Note:  $S_{11}(t) = S_1 t^s$ ,  $S_{22}(t) = S_{33}(t) = S_2 t^m$ ,  $S_{66}(t) = S_6 t^k$

**Table 6.1. Material properties for elastic analyses**

	$E_{11}$ (MPa)	$E_{22}$ (MPa)	$E_{33}$ (MPa)	$\nu_{12}$	$\nu_{13}$	$\nu_{23}$	$G_{12}$ (MPa)	$G_{13}$ (MPa)	$G_{23}$ (MPa)	$E_{11}/G_{12}$	$E_{11}/E_{22}$
<b>Gr/Ep</b>	143000	7580	7580	0.33	0.33	0.33	4280	4280	2880	33.41	18.87
<b>Gl/Ep</b>	47500	7580	7580	0.33	0.33	0.33	4800	4800	2850	9.90	6.27
<b>Iso</b>	70000	70000	70000	0.33	0.33	0.33	26923	26923	26923	2.66	1.00

**Table 6.2. Material properties for viscoelastic analyses**

Exponents	$s$	$m$	$k$
Mat. 1	-0.01	-0.02	-0.02
Mat. 2	-0.01	-0.02	-0.03
Mat. 3	-0.01	-0.03	-0.03
Mat. 4	-0.01	-0.02	-0.04

Note:  $E_{11}(t) = E_{11}t^s$ ,  $E_{22}(t) = E_{33}(t) = E_{22}t^m$ ,  $G_{12}(t) = G_{12}t^k$

Table 8.1. DCB test matrix under high temperature

Test condition	Loading rate	Specimen name	Width	Thickness	Initial crack length
	mm/sec		mm	mm	mm
Dry, 98°C, 22-ply	0.005	Z1-TH22-5	25.5	4.0	53.7
		Z1-TH22-9	25.7	4.0	53.8
	0.0254	Z1-TH22-7	25.5	4.1	54.5
		Z1-TH22-8	25.6	4.0	53.2
	0.254	Z1-TH22-6	25.4	4.1	54.1
		Z1-TH22-10	25.7	3.9	54.0
Wet, 98°C, 22-ply	0.005	Z2-TH22-3B	23.5	3.9	53.5
		Z2-TH22-6A	23.4	4.0	54.8
		Z2-TH22-9B	23.5	4.0	51.3
	0.0254	Z2-TH22-2A	23.4	3.9	53.3
		Z2-TH22-2B	23.5	3.9	51.5
		Z2-TH22-3A	23.5	3.9	53.6
		Z2-TH22-11B	23.6	4.0	51.5
	0.254	Z2-TH22-6B	23.4	4.0	50.7
		Z2-TH22-11A	23.3	4.0	54.9
Wet, 98°C, 24-ply	0.0254	T24-2-2A	23.3	4.4	49.1
Wet, 98°C, 32-ply	0.005	T32-1-11A	21.8	5.9	53.0
	0.254	T32-1-11B	21.9	5.9	50.0
Dry, 125°C, 22-ply	0.005	Z2-TH22-7A	23.1	4.1	56.8
		Z2-TH22-7B	23.4	4.0	51.1
		Z2-TH22-10A	23.6	4.1	54.6
	0.0254	Z2-TH22-1A	23.3	3.8	52.3
		Z2-TH22-1B	23.0	3.9	53.3
		Z2-TH22-5A	23.3	4.0	55.1
		Z2-TH22-5B	23.4	4.0	51.3
		Z2-TH22-8A	23.5	4.1	50.8
		Z2-TH22-8B	23.5	4.0	53.0
		Z2-TH22-9A	23.5	4.0	54.9
		Z2-TH22-10B	23.6	4.1	51.4
	0.254	Z2-TH22-4A	23.5	4.0	54.8
		Z2-TH22-4B	23.4	4.0	53.9
Z1-TH22-11		25.6	3.9	53.8	
Dry, 125°C, 32-ply	0.005	Z3-TH32-1	22.6	5.9	54.0
		Z3-TH32-5	22.5	5.9	53.7
		Z3-TH32-7	22.5	5.9	53.9
		Z3-TH32-8	22.8	5.9	54.1
	0.0254	Z3-TH32-3	22.7	5.9	54.0
		Z3-TH32-4	22.7	5.9	54.9
		Z3-TH32-9	22.8	5.9	54.7
		Z3-TH32-10	22.8	5.8	54.2
	0.254	Z3-TH32-2	22.7	5.9	54.9
		Z3-TH32-6	22.7	5.9	54.0
		Z3-TH32-11	22.8	5.8	54.8

**Table A.1. Material properties in numerical simulation**

<b>Materials</b>	<b>E11 (MPa)</b>	<b>E22 (MPa)</b>	<b>E33 (MPa)</b>	<b>Nu12</b>	<b>Nu13</b>	<b>Nu23</b>	<b>G12 (MPa)</b>	<b>G13 (MPa)</b>	<b>G23 (MPa)</b>	<b>E11/G12</b>	<b>E11/E22</b>
<b>Mat. 1</b>	143000	7580	7580	0.33	0.33	0.33	4280	4280	2880	33.4	18.9
<b>Mat. 2</b>	47500	7580	7580	0.33	0.33	0.33	4800	4800	2850	9.9	6.3
<b>Mat. 3</b>	47500	2518	2518	0.33	0.33	0.33	4800	4800	947	9.9	18.9
<b>Mat. 4</b>	12768	7580	7580	0.33	0.33	0.33	4800	4800	2850	2.7	1.7
<b>Mat. 5</b>	12768	12768	12768	0.33	0.33	0.33	4800	4800	4800	2.7	1.0
<b>Mat. 6</b>	88000	4665	4665	0.33	0.33	0.33	4280	4280	1754	20.6	18.9
<b>Mat. 7</b>	47500	4800	4800	0.33	0.33	0.33	4800	4800	1805	9.9	9.9

**Table B.1. Geometries considered**

D [mm]	d [mm]	L [mm]	t [mm]	d/t
3.175;	25.4;	12.7;	2;	6.35;
6.350;	38.1;	25.4	3;	9.525;
9.525;	50.8		4	12.7;
12.700				15.875

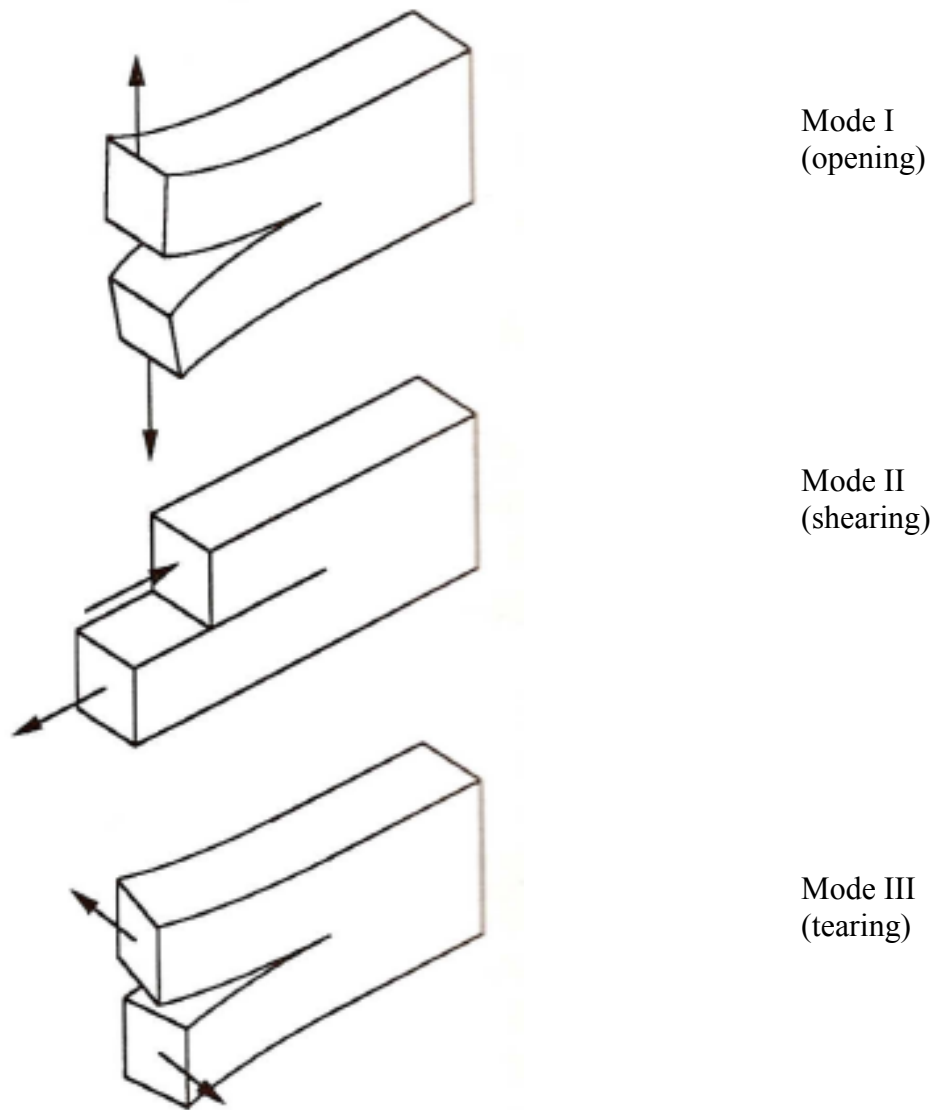


**Figure 2.1 Basic delamination modes.**

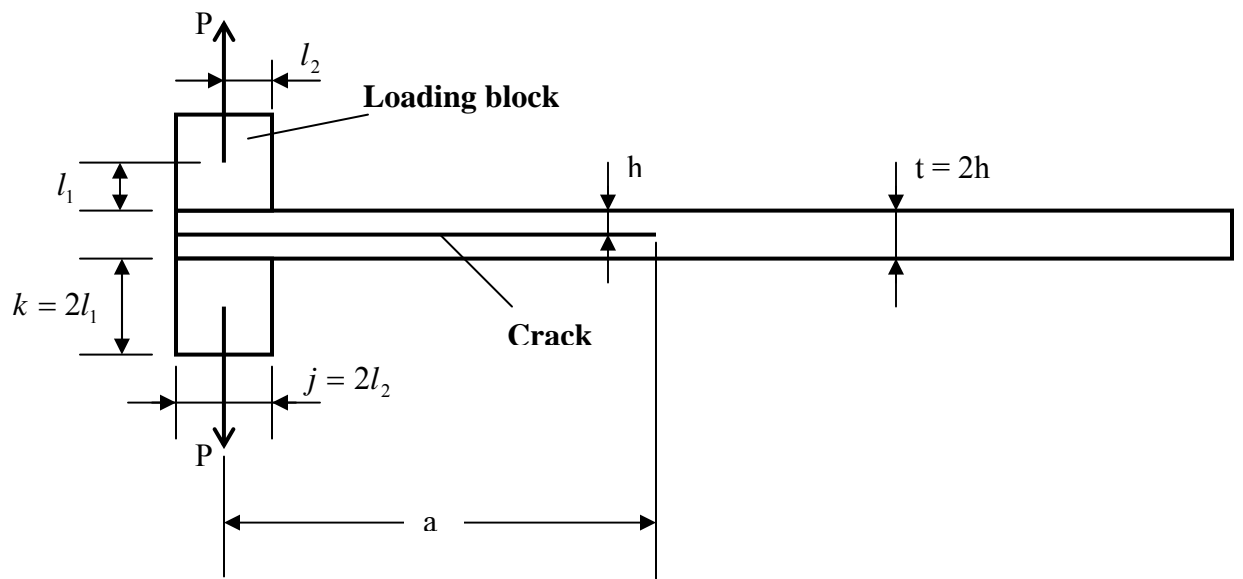
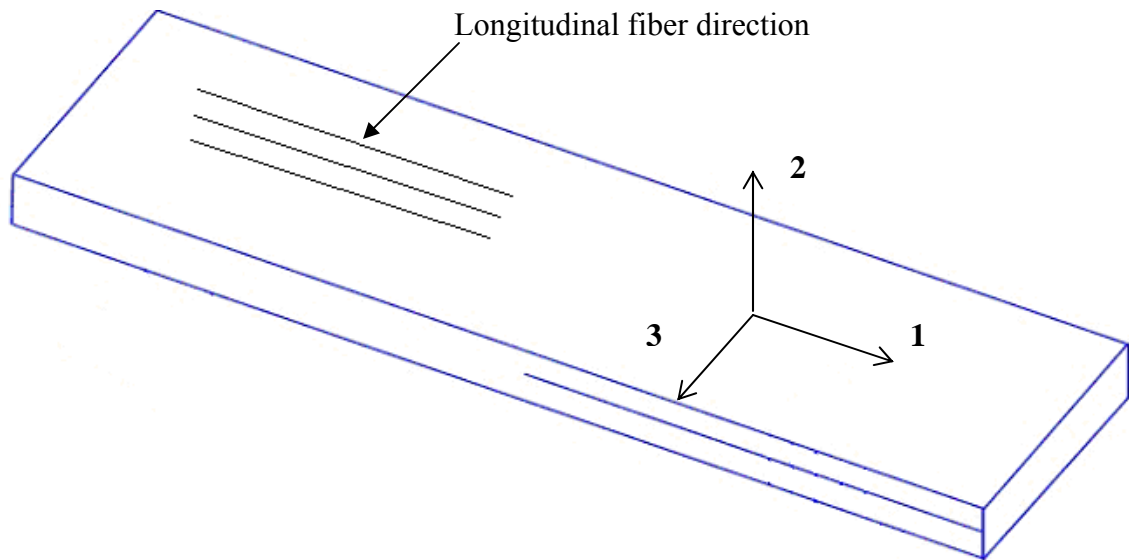
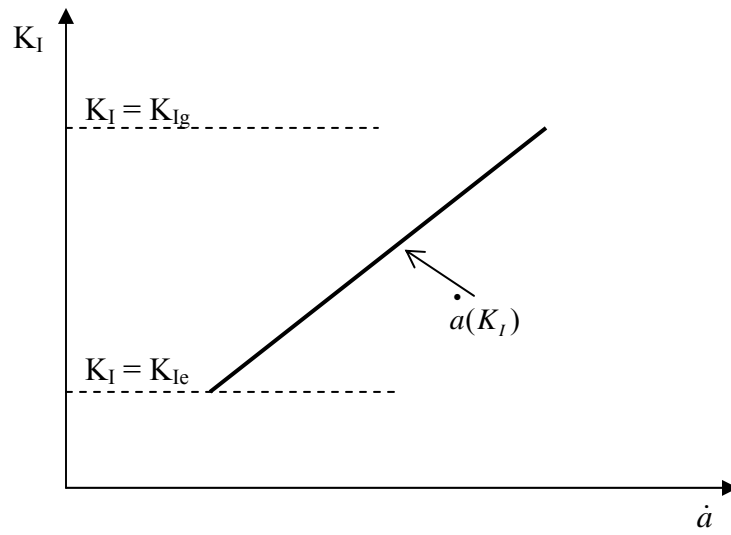


Figure 2.2 Schematic of the double cantilever beam (DCB) test.





**Figure 2.3 Definition of coordinate axes for a unidirectional specimen.**



**Figure 3.1 Typical  $K_I$  vs.  $\dot{a}$  curve from a viscoelastic fracture test.**

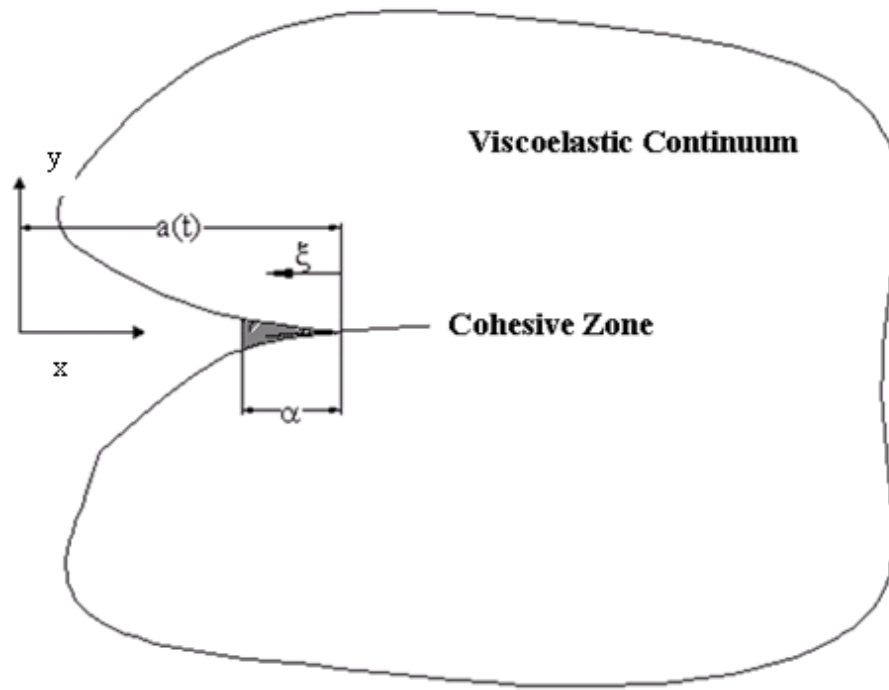
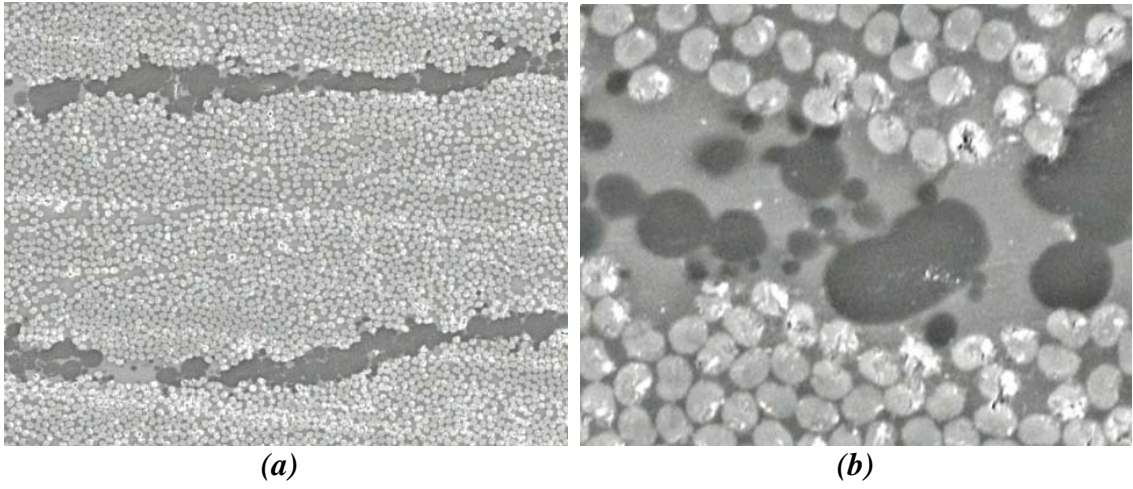
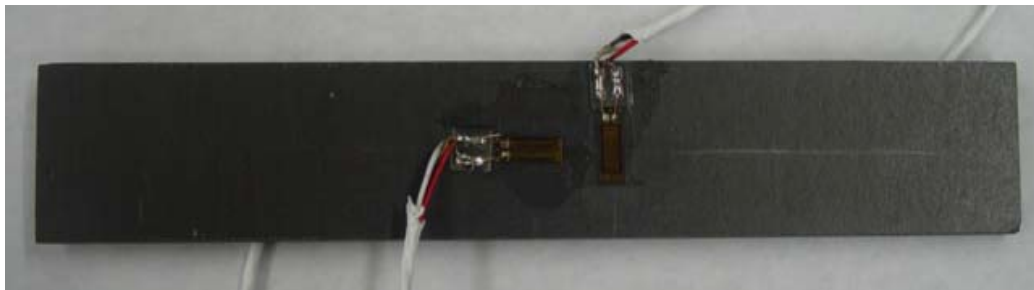
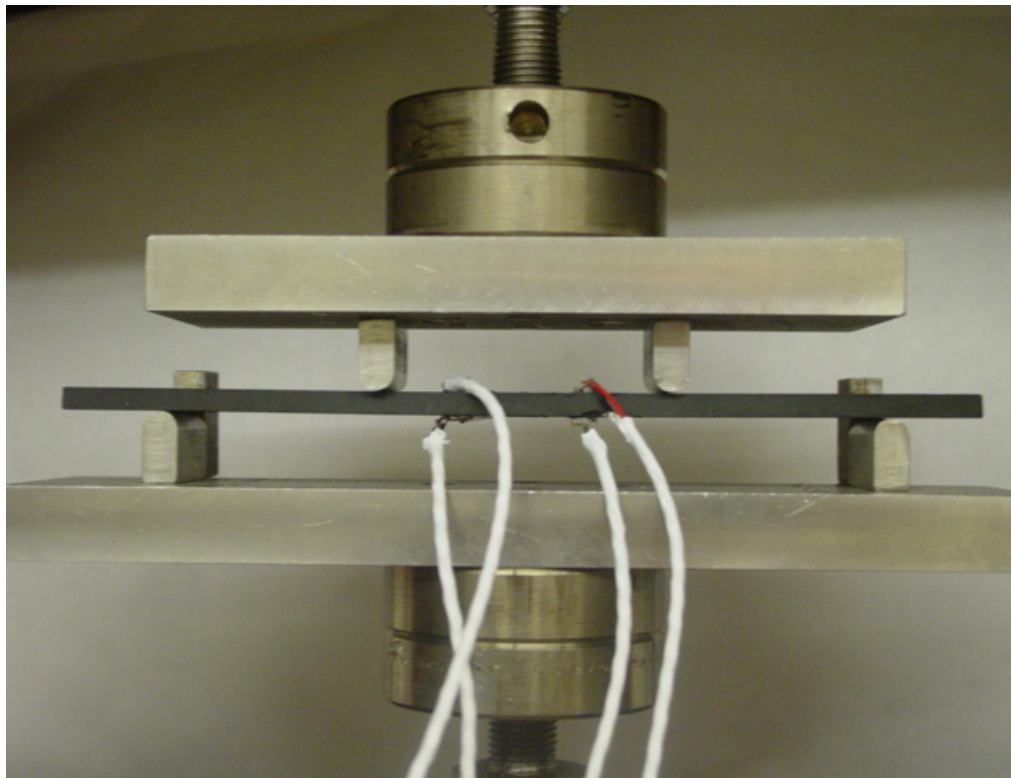
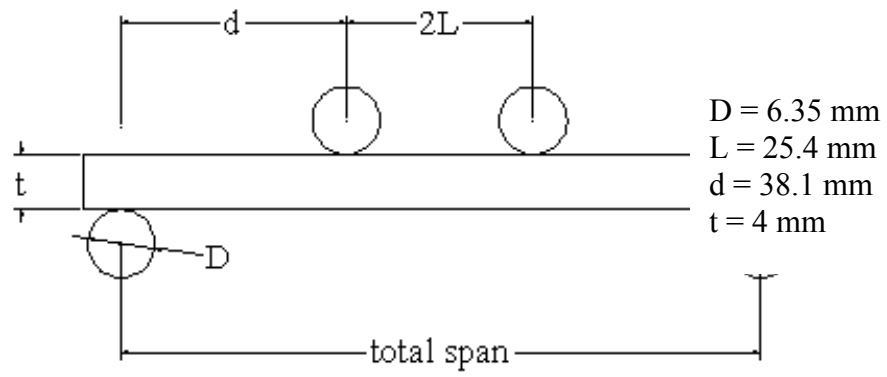


Figure 3.2 Schematic of crack geometry and cohesive zone.



**Figure 4.1 Cross-sectional view showing interlayer of a cured composite at (a) low magnification and (b) high magnification.**



**Figure 4.2 4-point bending tests schematic drawing and test setup.**

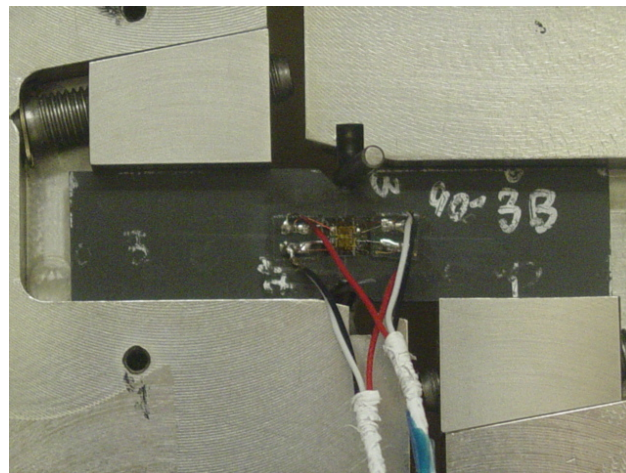
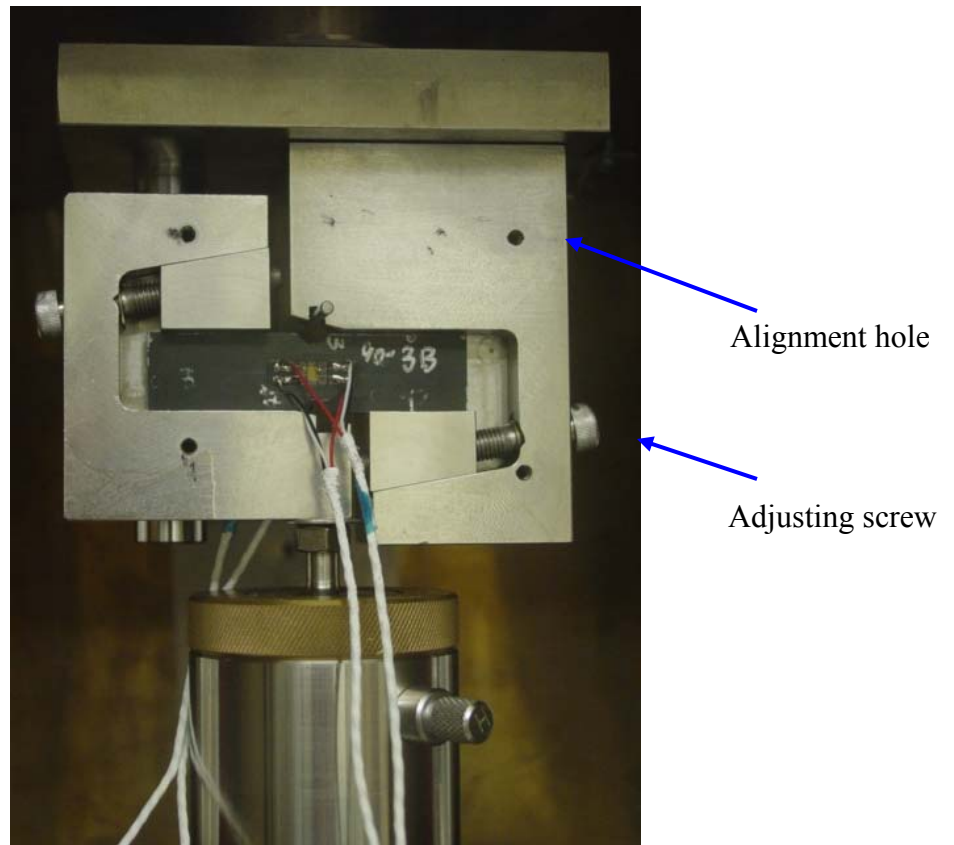
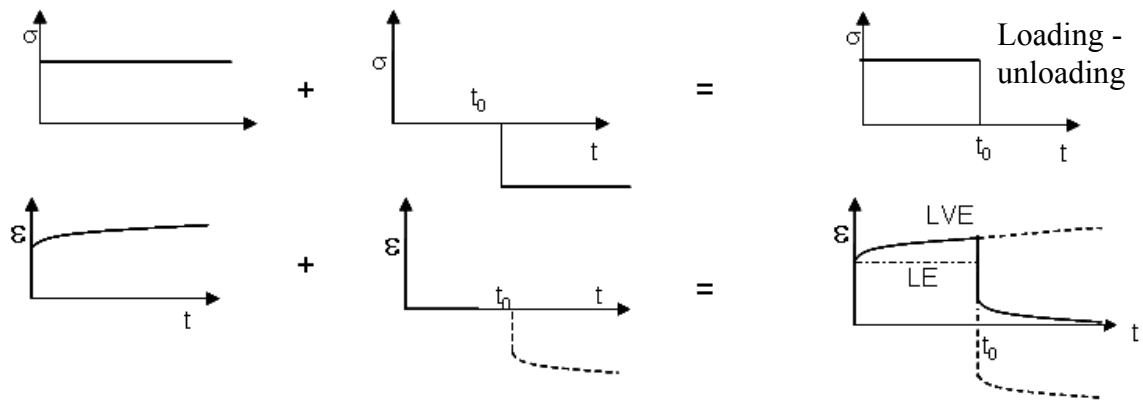
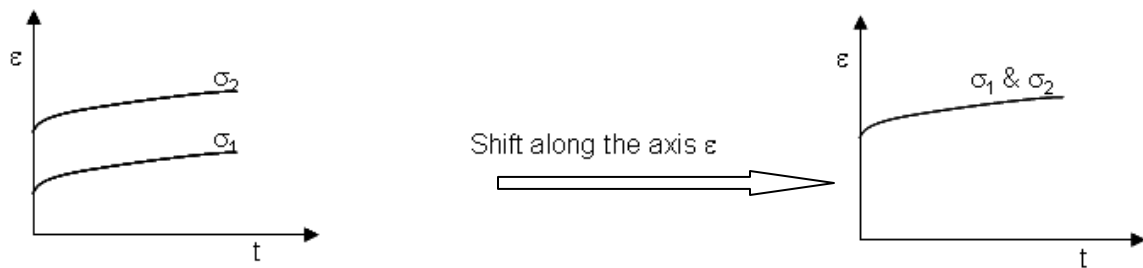


**Figure 4.3 Iosipescu in-plane shear test setup.**

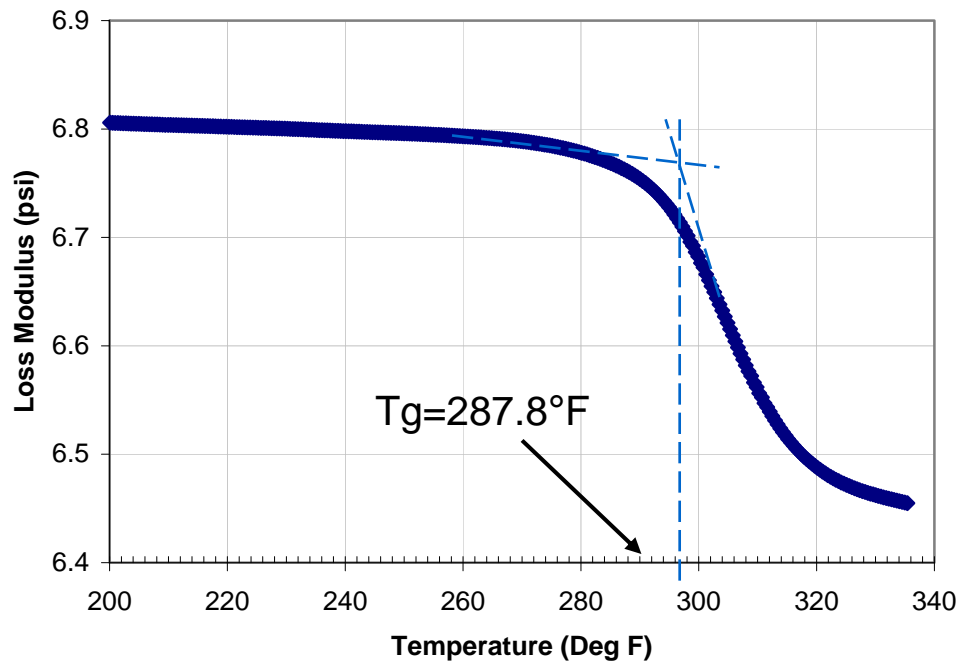


Superposition check procedure

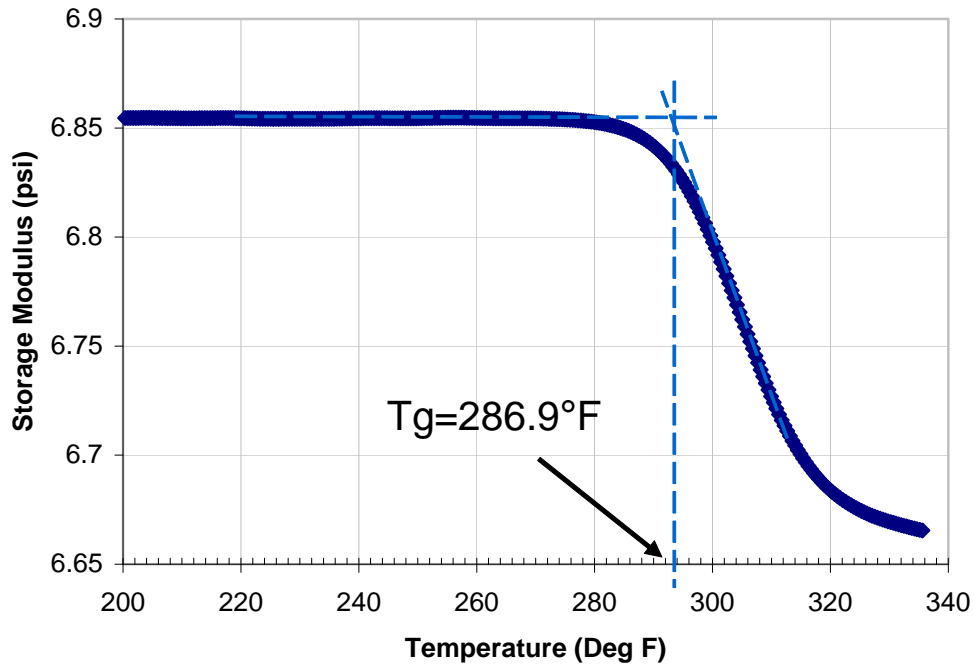


(b) Proportionality check procedure

**Figure 4.4 Verification of linear viscoelasticity from creep-recovery tests.**



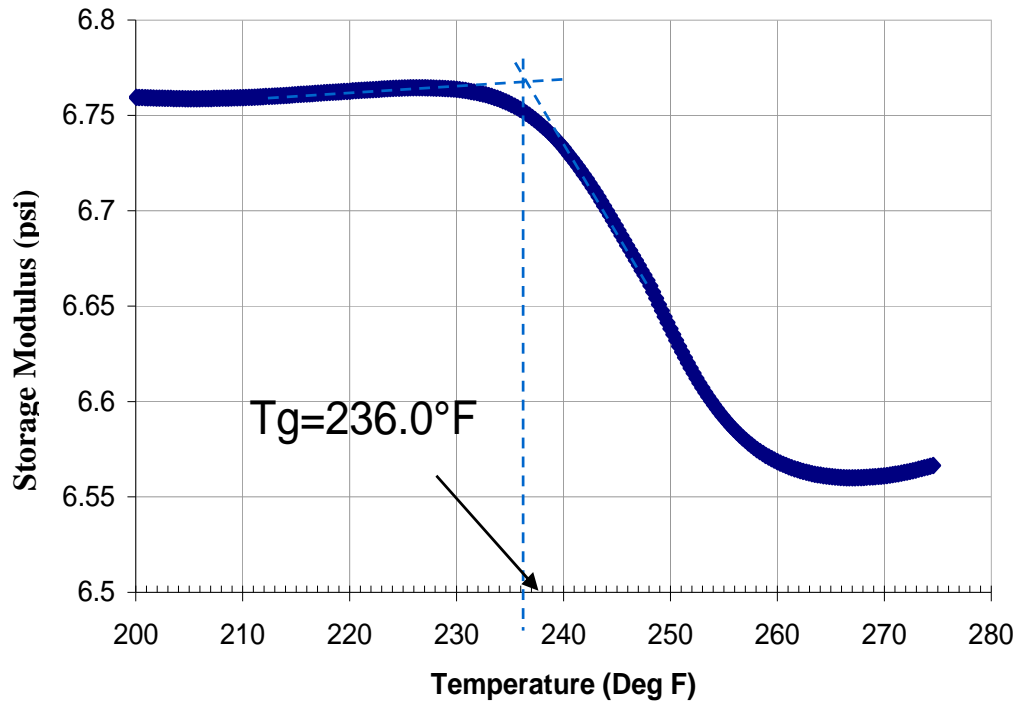
(a)



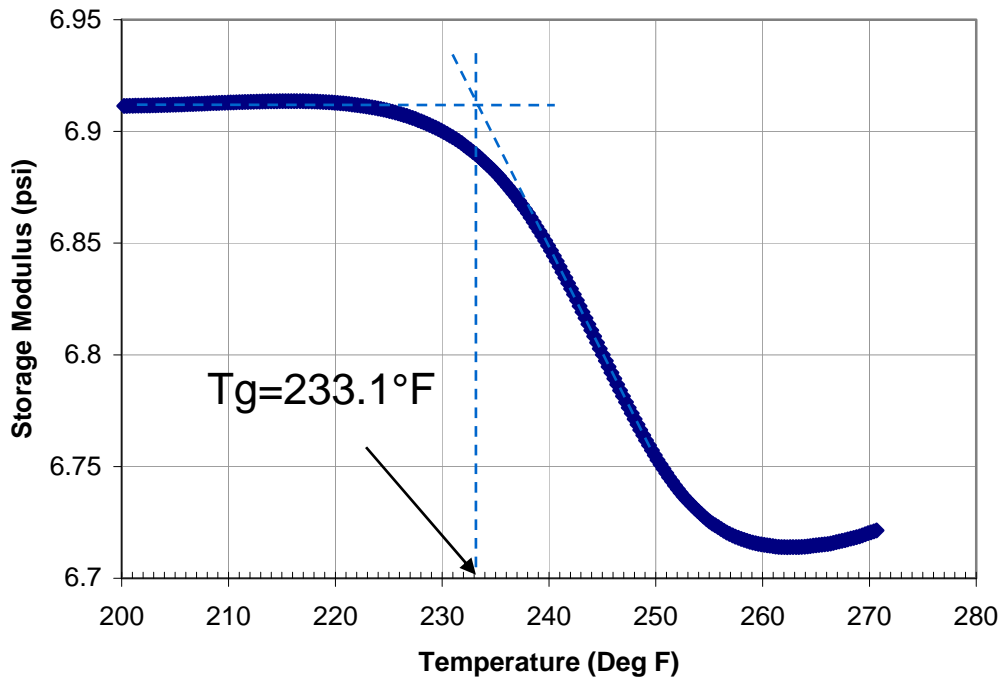
(b)

Figure 4.5 Storage modulus vs. temperature from DMA tests of dry T800H/3900-2:  
 (a) DMA-dry1; (b) DMA-dry2.





(a)



(b)

Figure 4.6 Storage modulus vs. temperature from DMA tests of wet T800H/3900-2:  
 (a) DMA-wet1; (b) DMA-wet2.

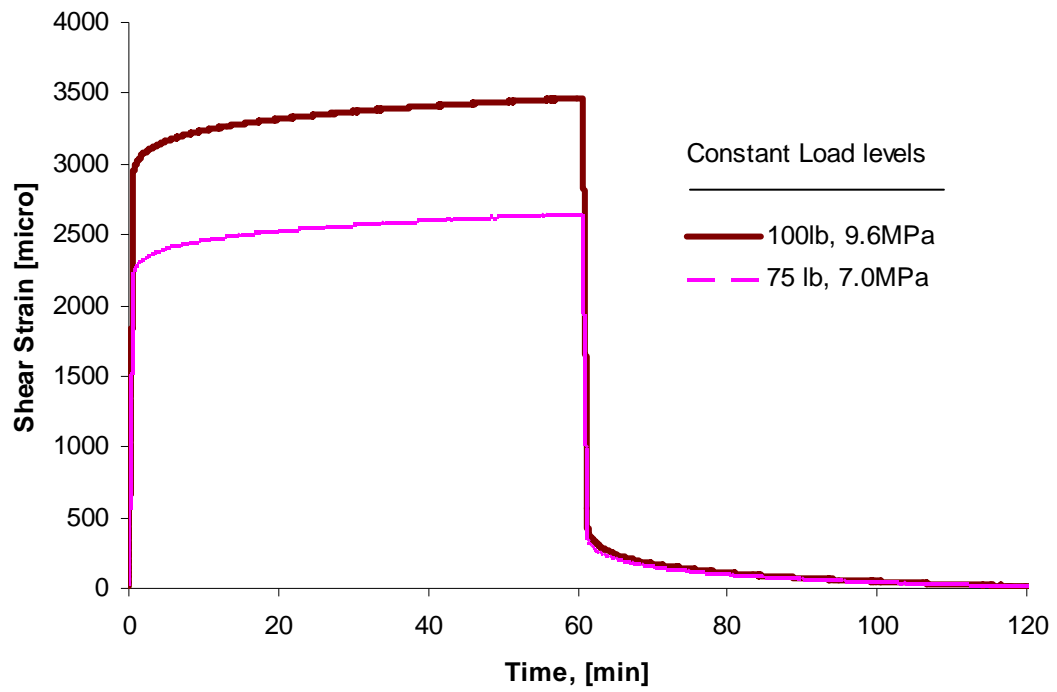


**Figure 4.7 Shear strain from two stress levels at T=208°F of wet T800H/3900-2 specimen.**

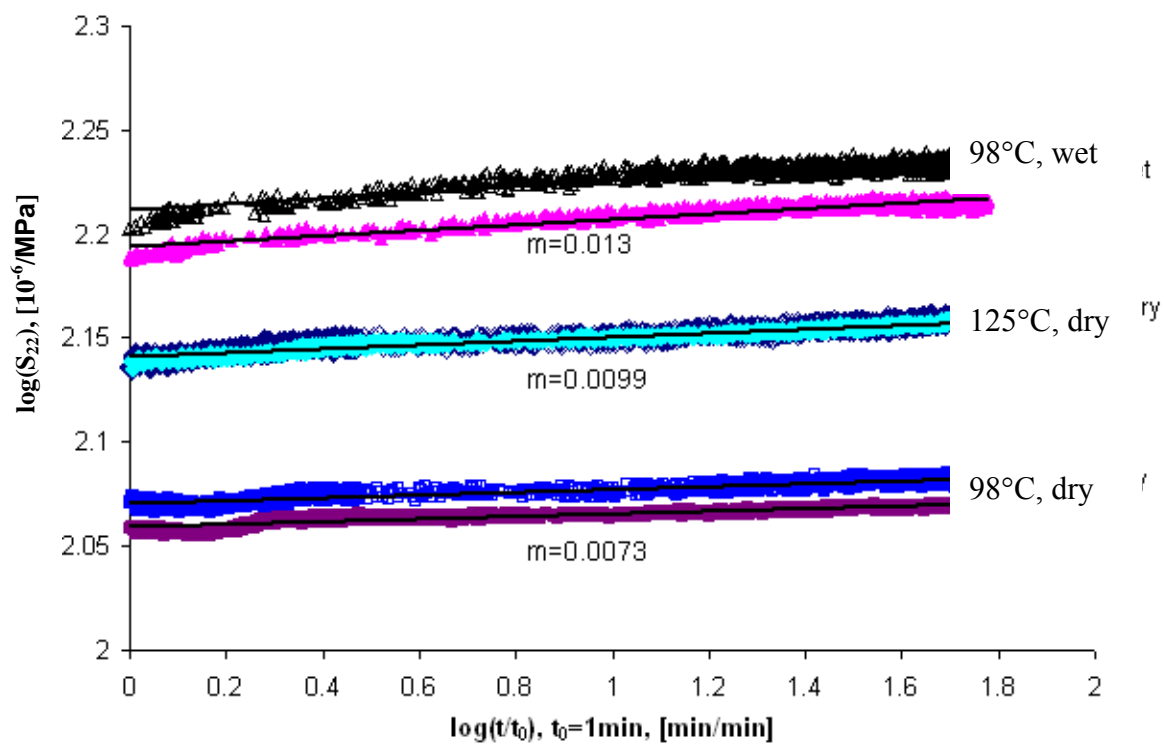


Figure 4.8  $S_{22}(t)$  of T800H/3900-2 at different conditions.

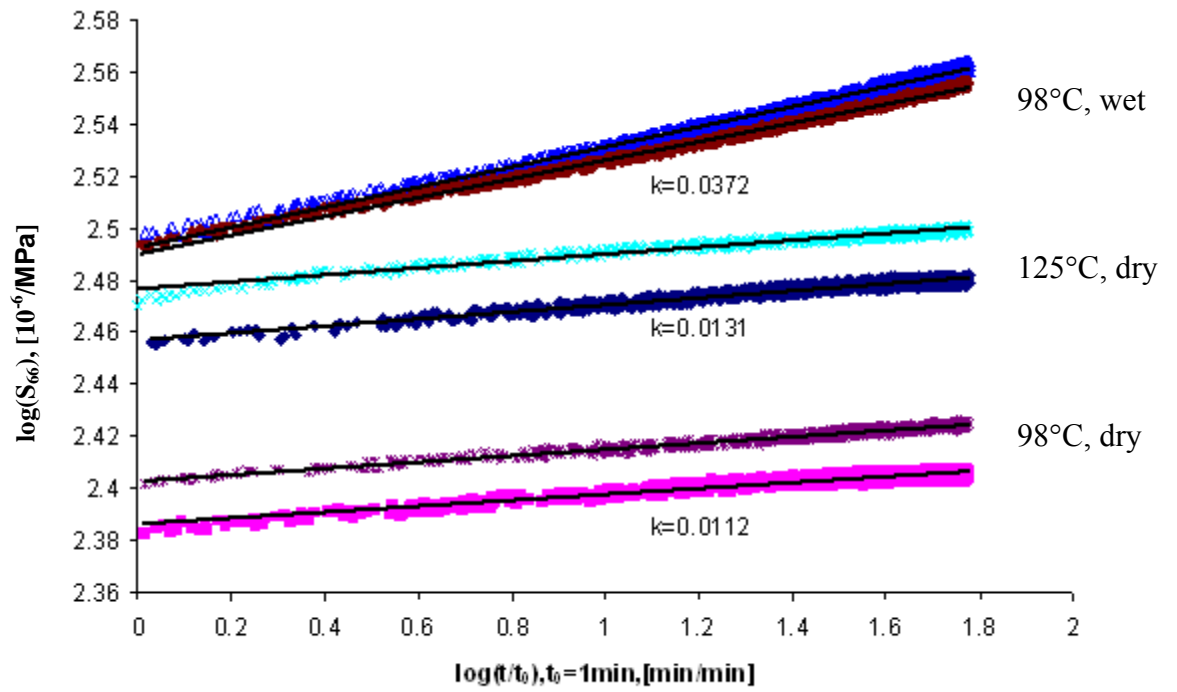
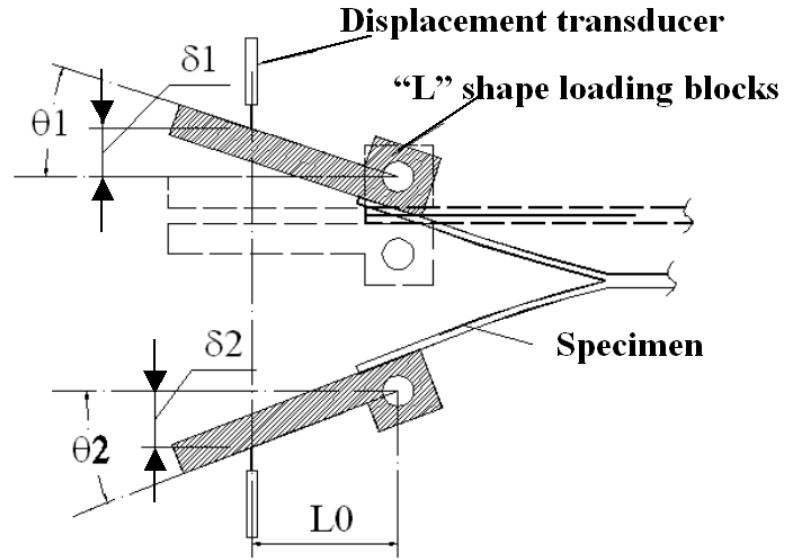
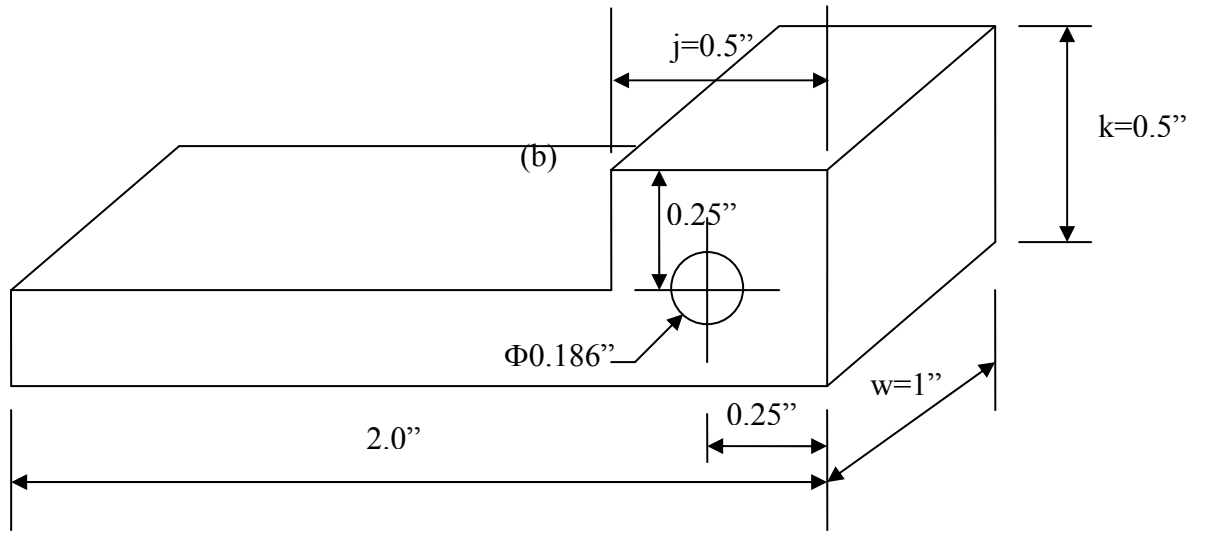


Figure 4.9  $S_{66}(t)$  of T800H/3900-2 at different conditions.



(a)



(b)

**Figure 5.1 (a) Experimental indirect angle measurement (b) geometry of "L" shape loading blocks.**

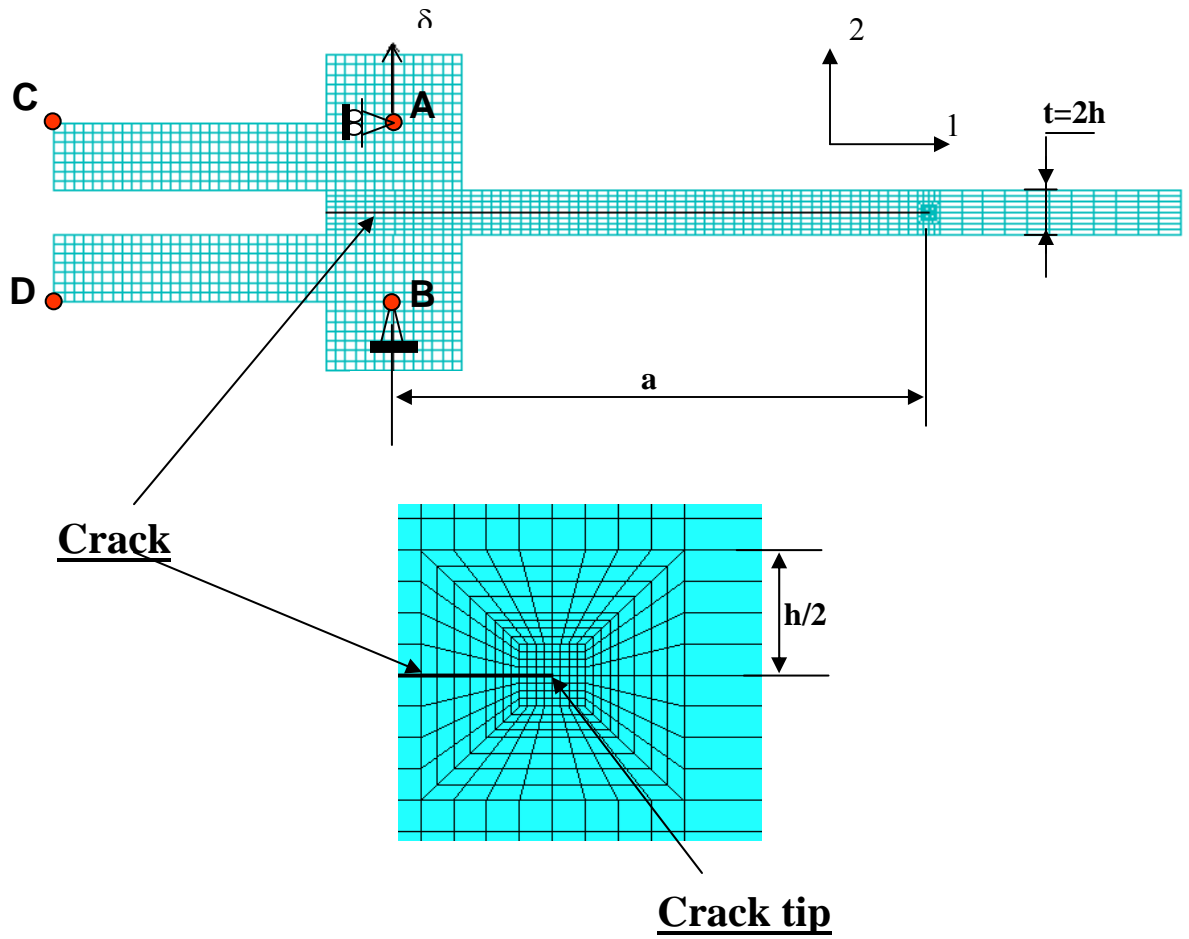
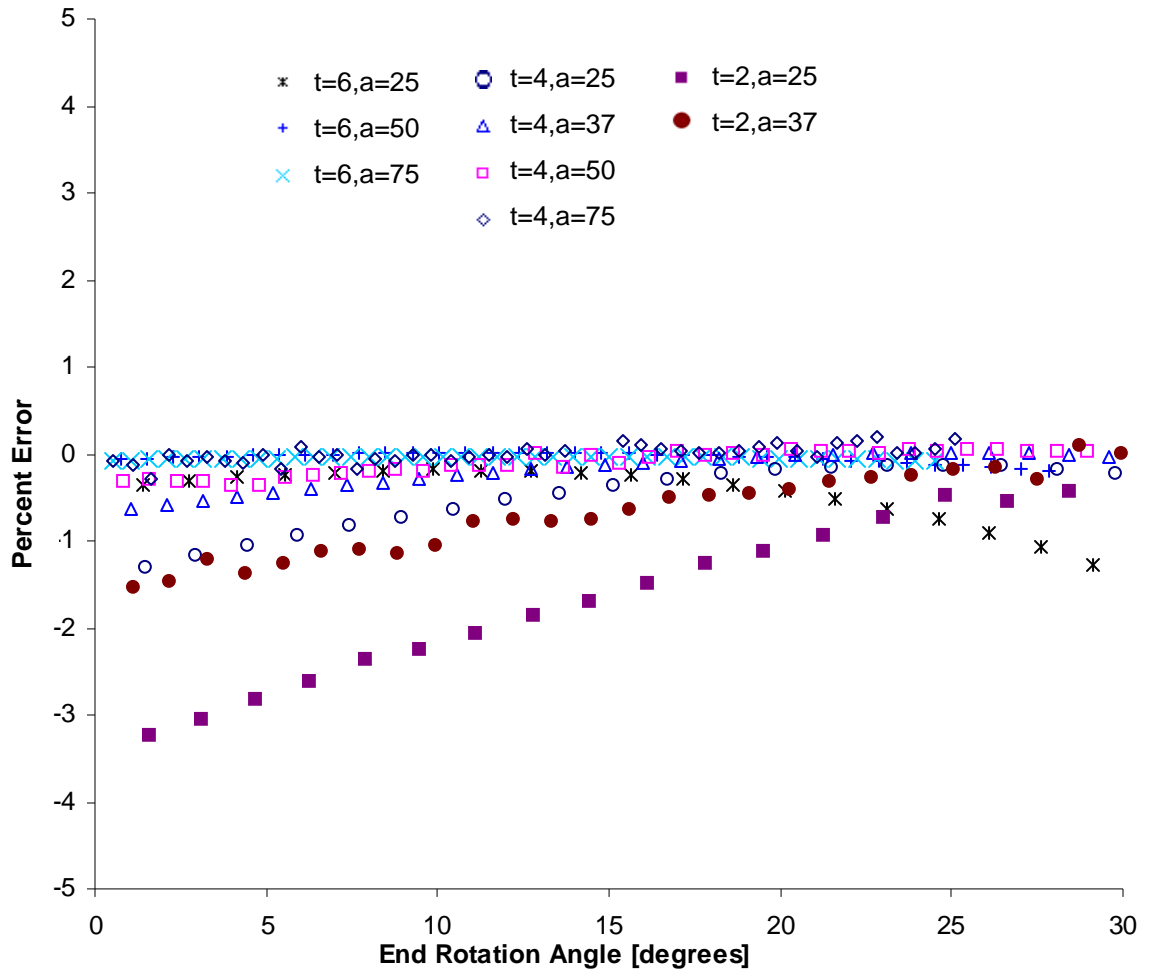
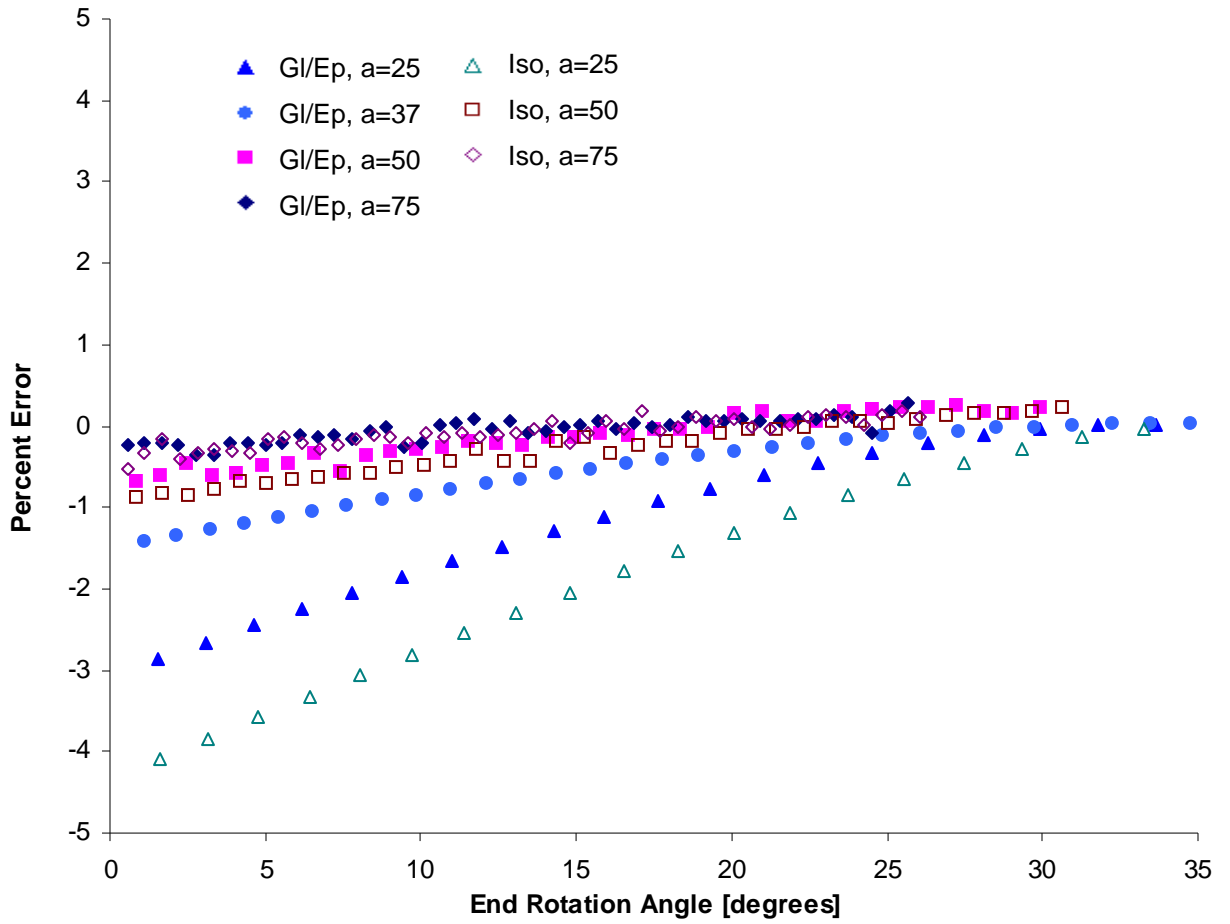


Figure 6.1 Typical FE mesh for DCB analyses.



**Figure 6.2 Percent error of  $J_s$  to  $J$  vs. end rotation angle for the Gr/Ep DCB specimen with various thicknesses and crack lengths.**



**Figure 6.3 Percent error of  $J_s$  to  $J$  vs. end rotation angle for the GI/Ep and the isotropic DCB specimen with various crack lengths and thickness of 4mm.**



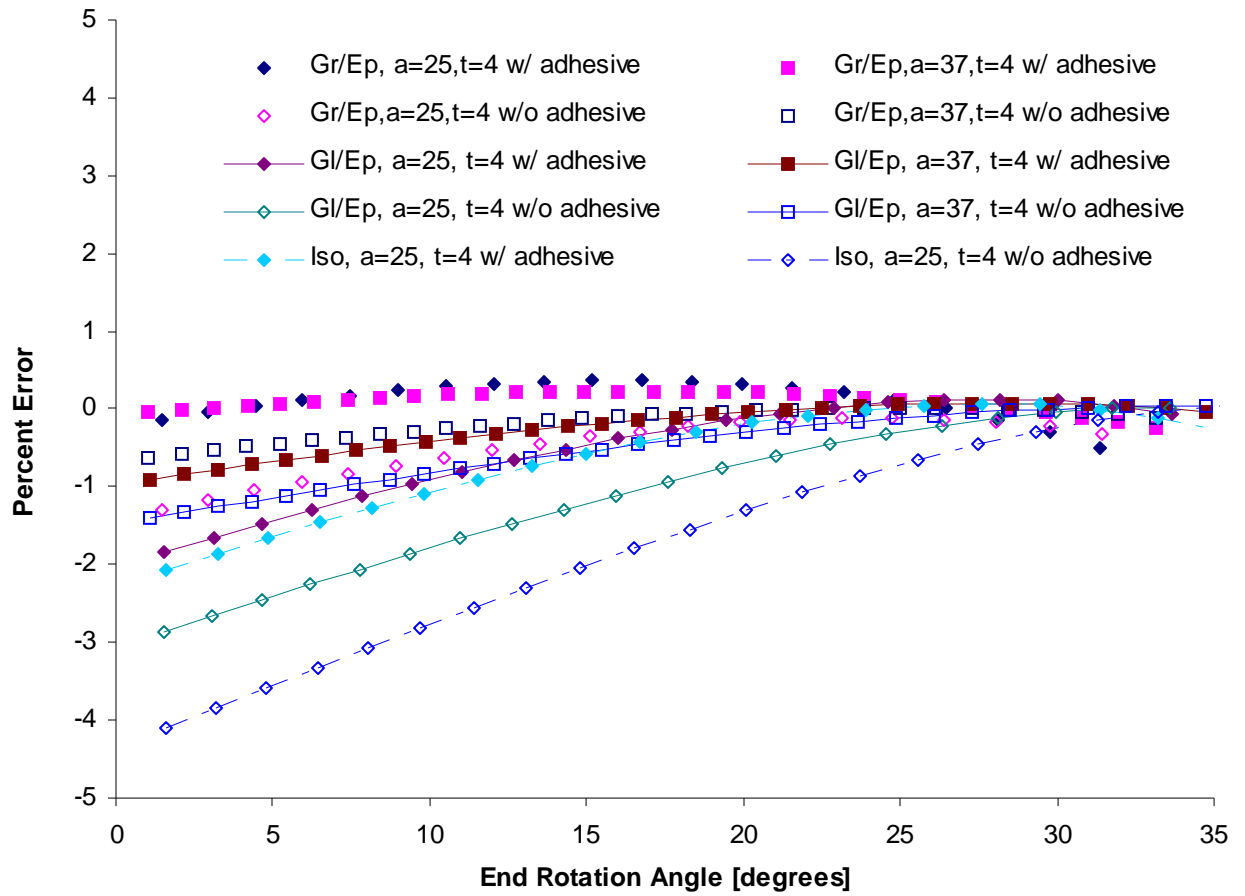


**Figure 6.4 Evaluation of  $J_s$  for models with adhesive.**

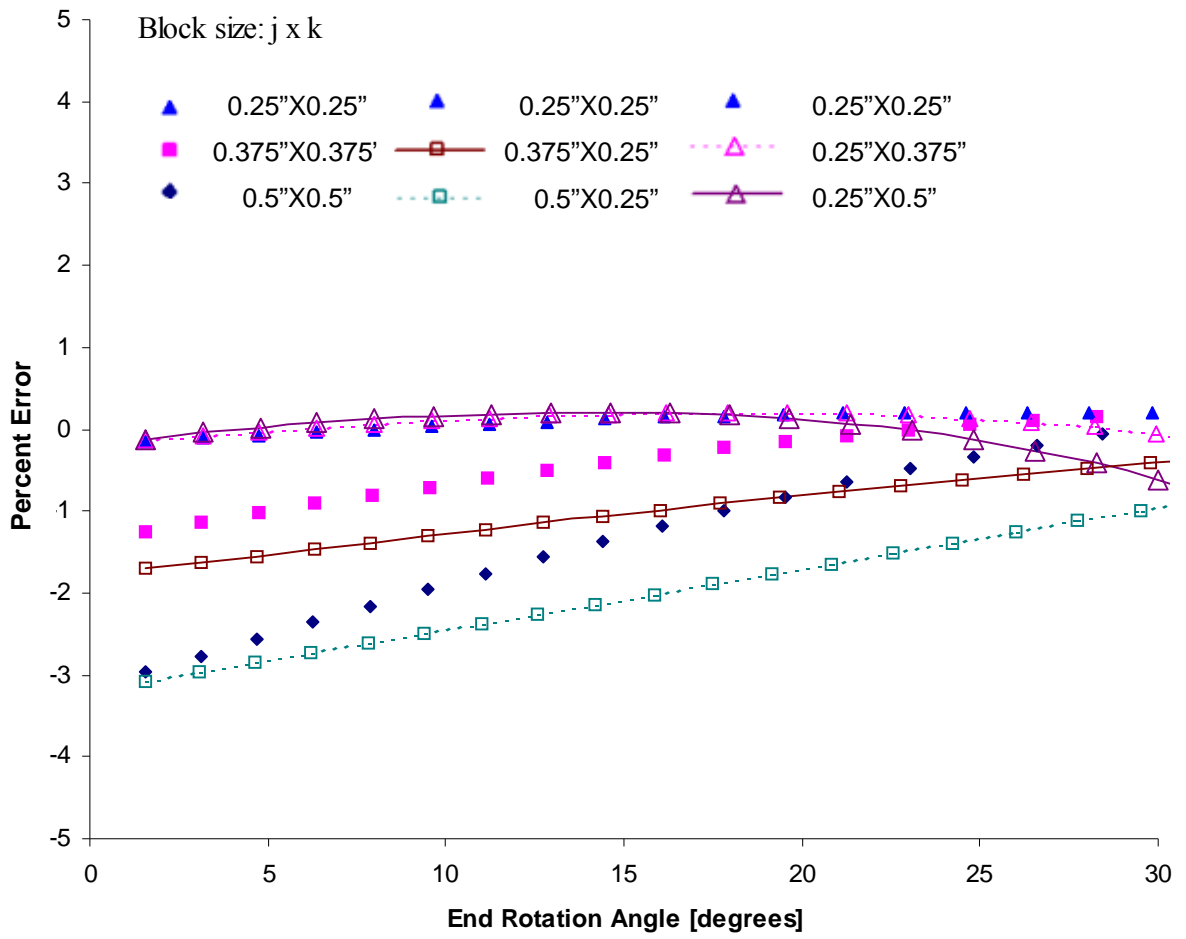
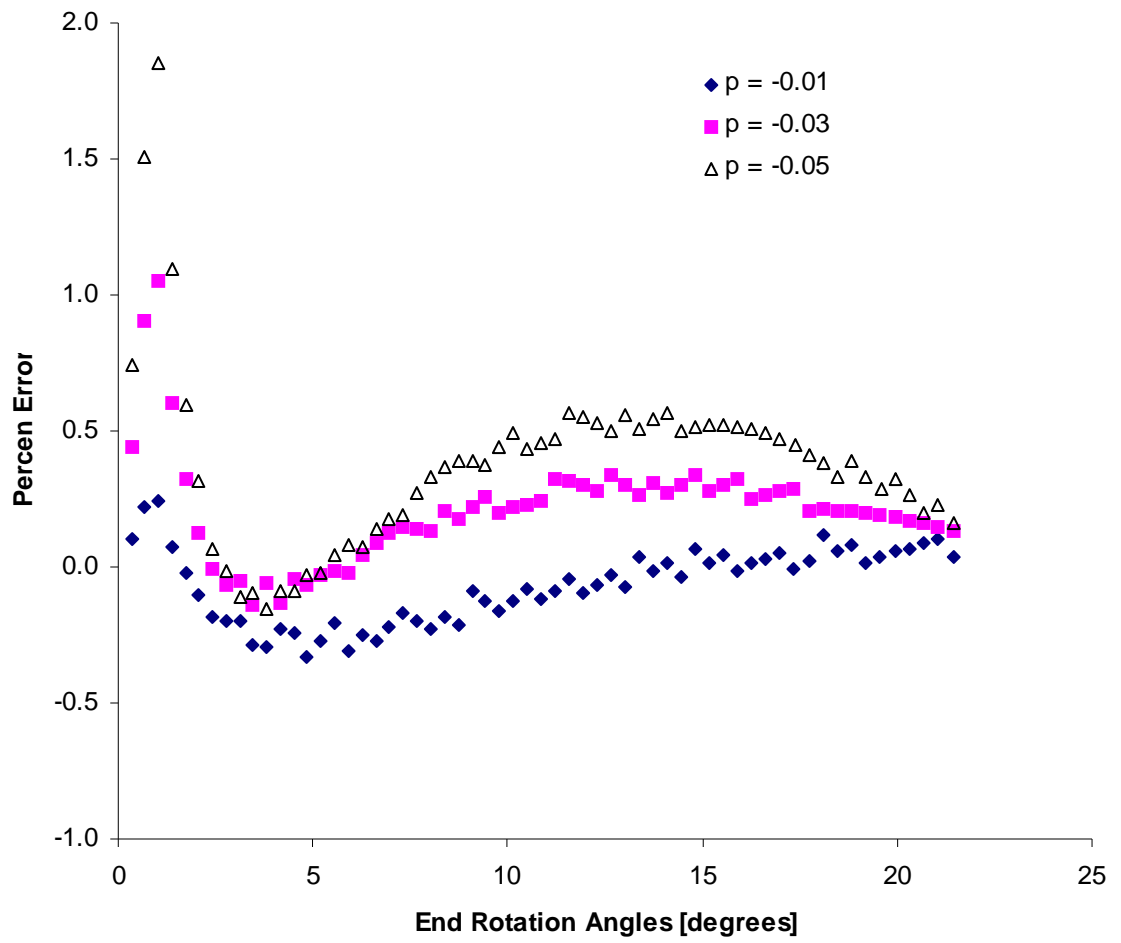
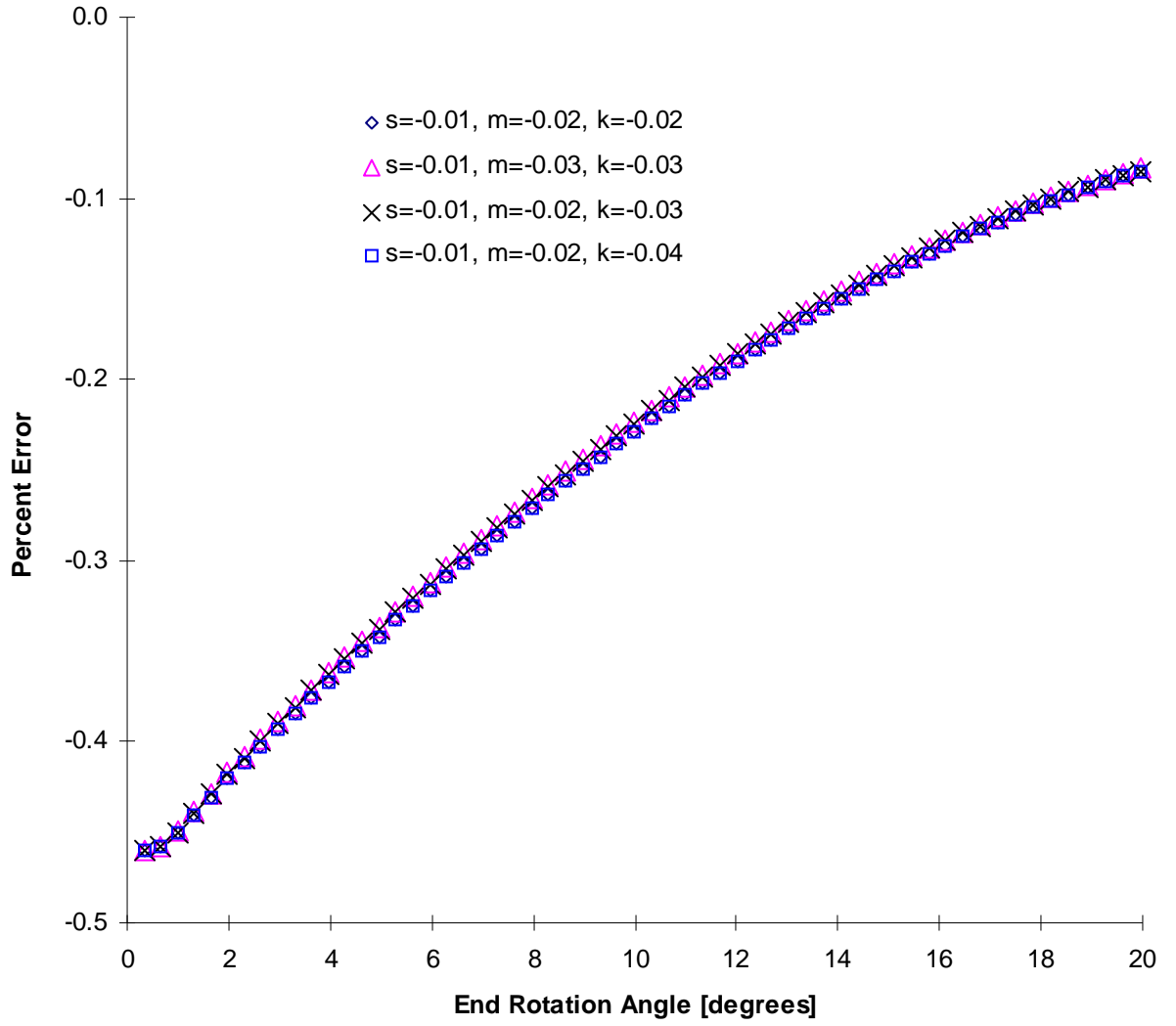


Figure 6.5 Evaluation of  $J_s$  for models with different size of loading blocks.



**Figure 6.6 Comparison of J between proposed material model and ABAQUS default material model for isotropic materials.**



**Figure 6.7 Evaluation of  $J_s$  for orthotropic linear viscoelastic materials.**

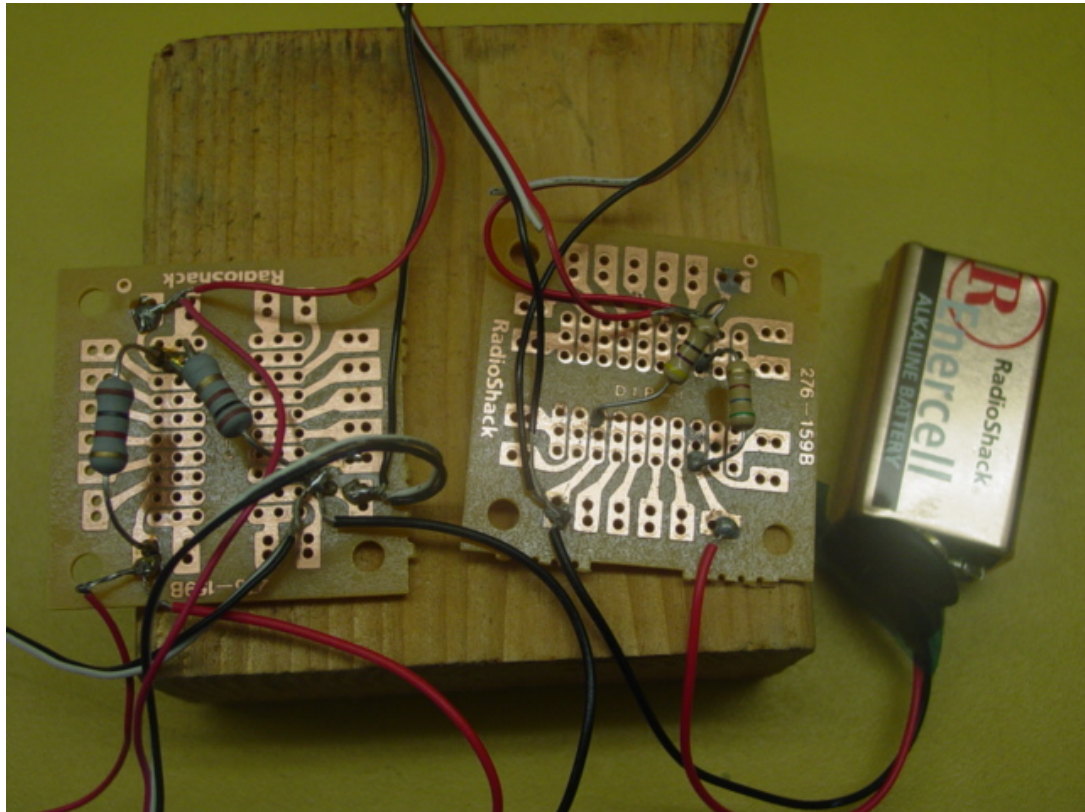
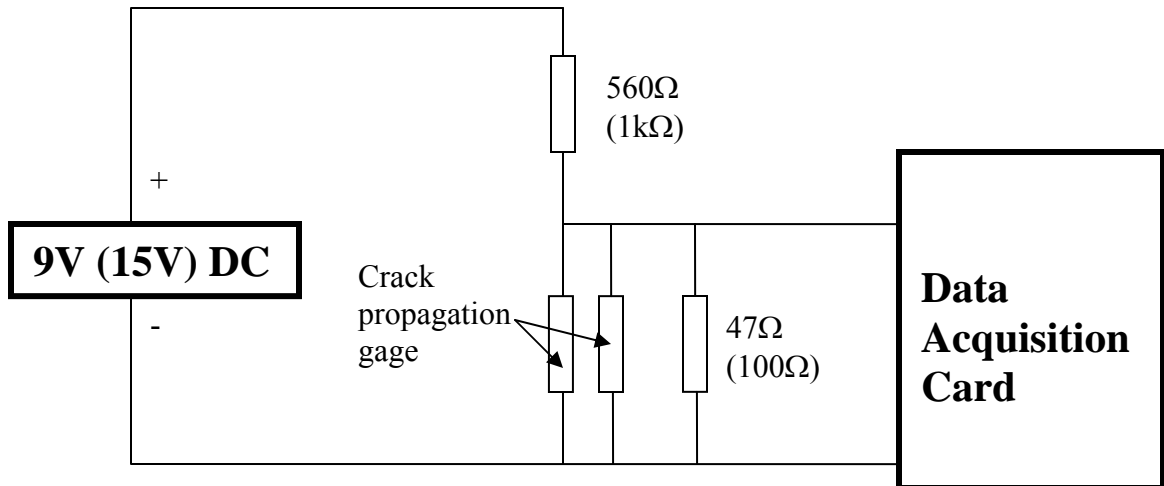


**Figure 7.1 Electrical circuits of crack propagation gage.**

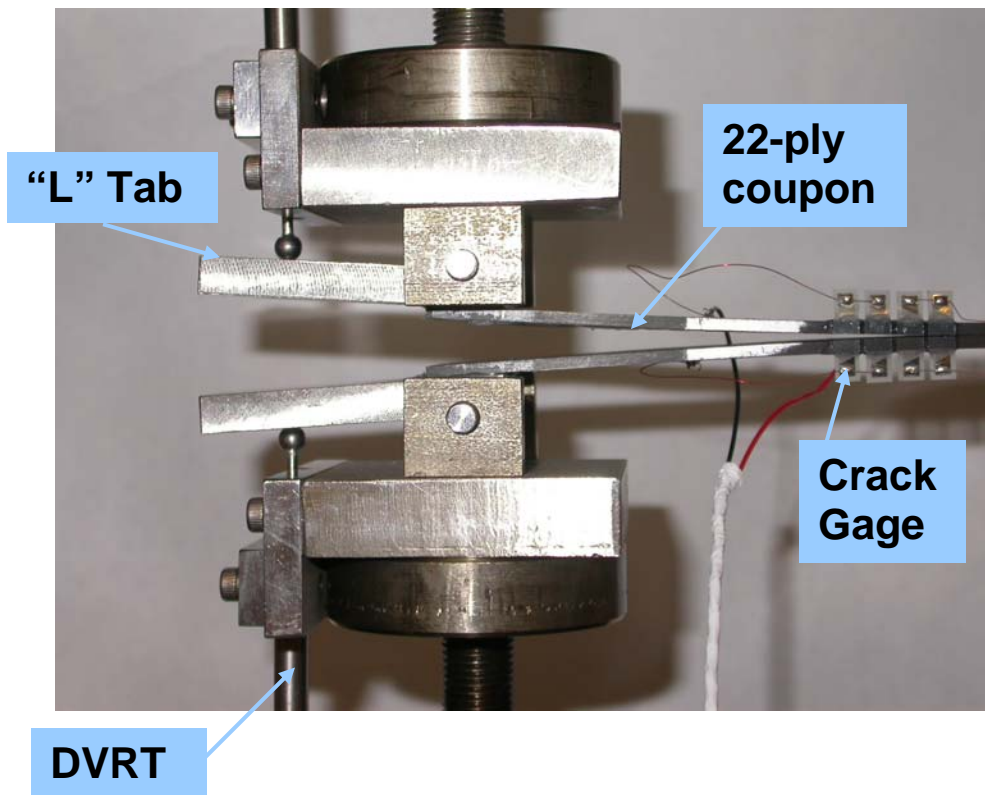
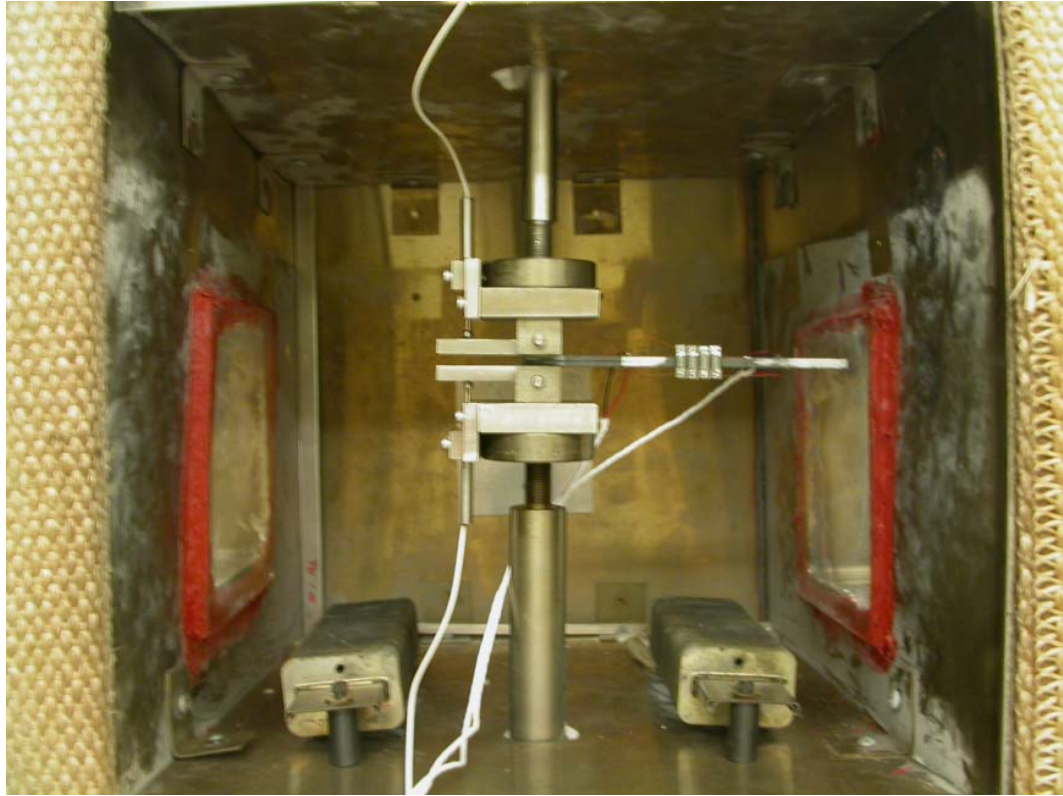


**Figure 7.2 DCB test setup.**

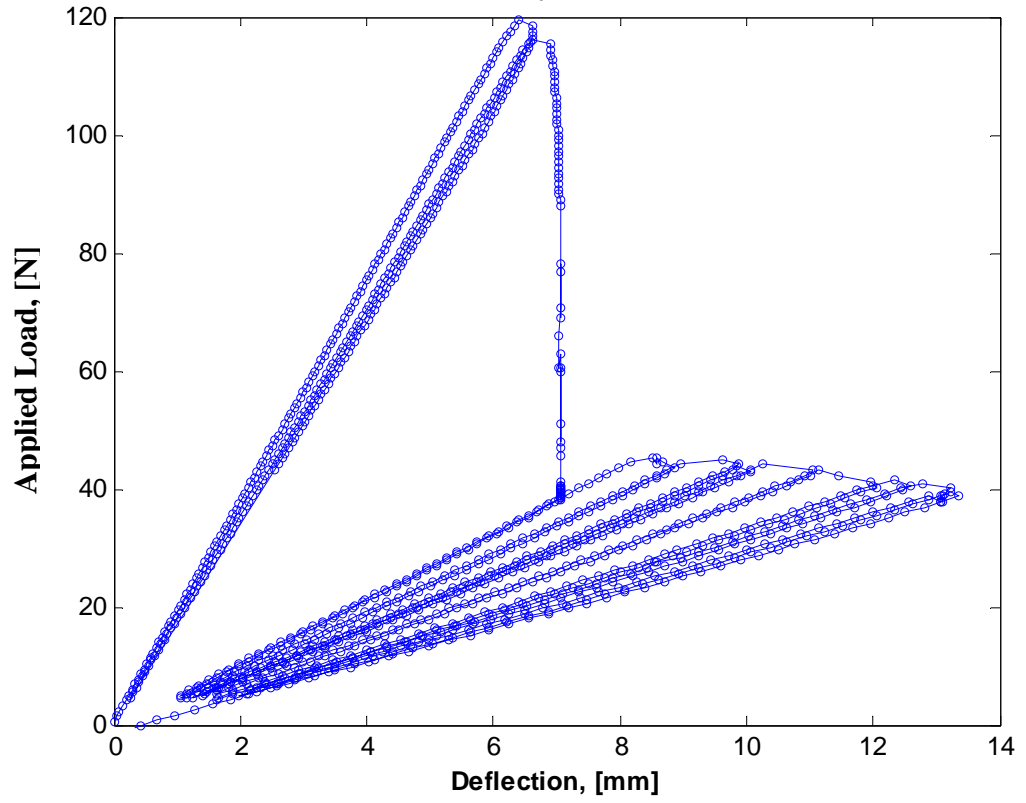
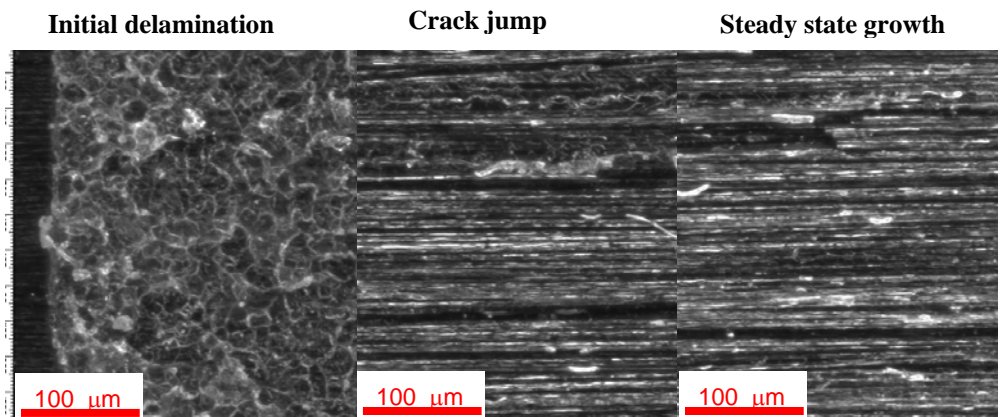
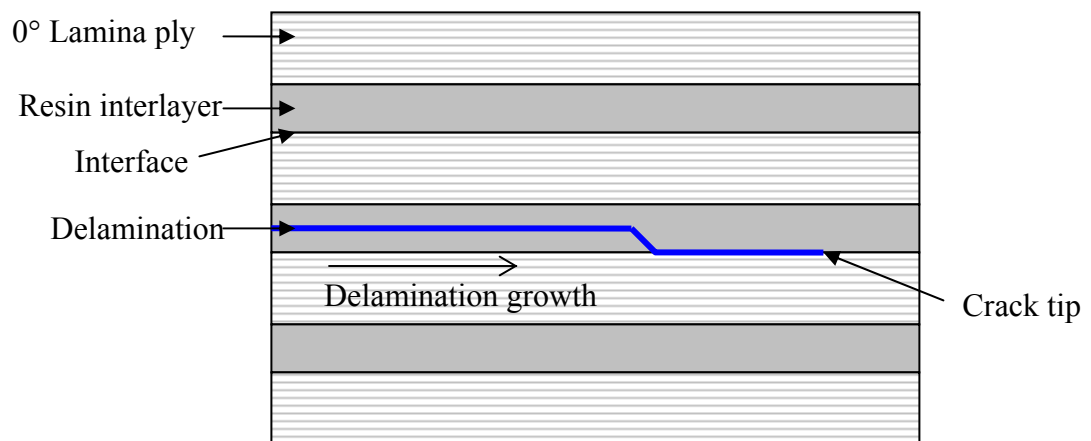


**Figure 7.3 Typical load-deflection curve for a DCB test of T800H/3900-2 at room temperature.**



(a)



(b)

**Figure 7.4 Delamination mechanism of T800H/3900-2 at room temperature (a) fracture surface view; (b) Schematic of crack growth path.**



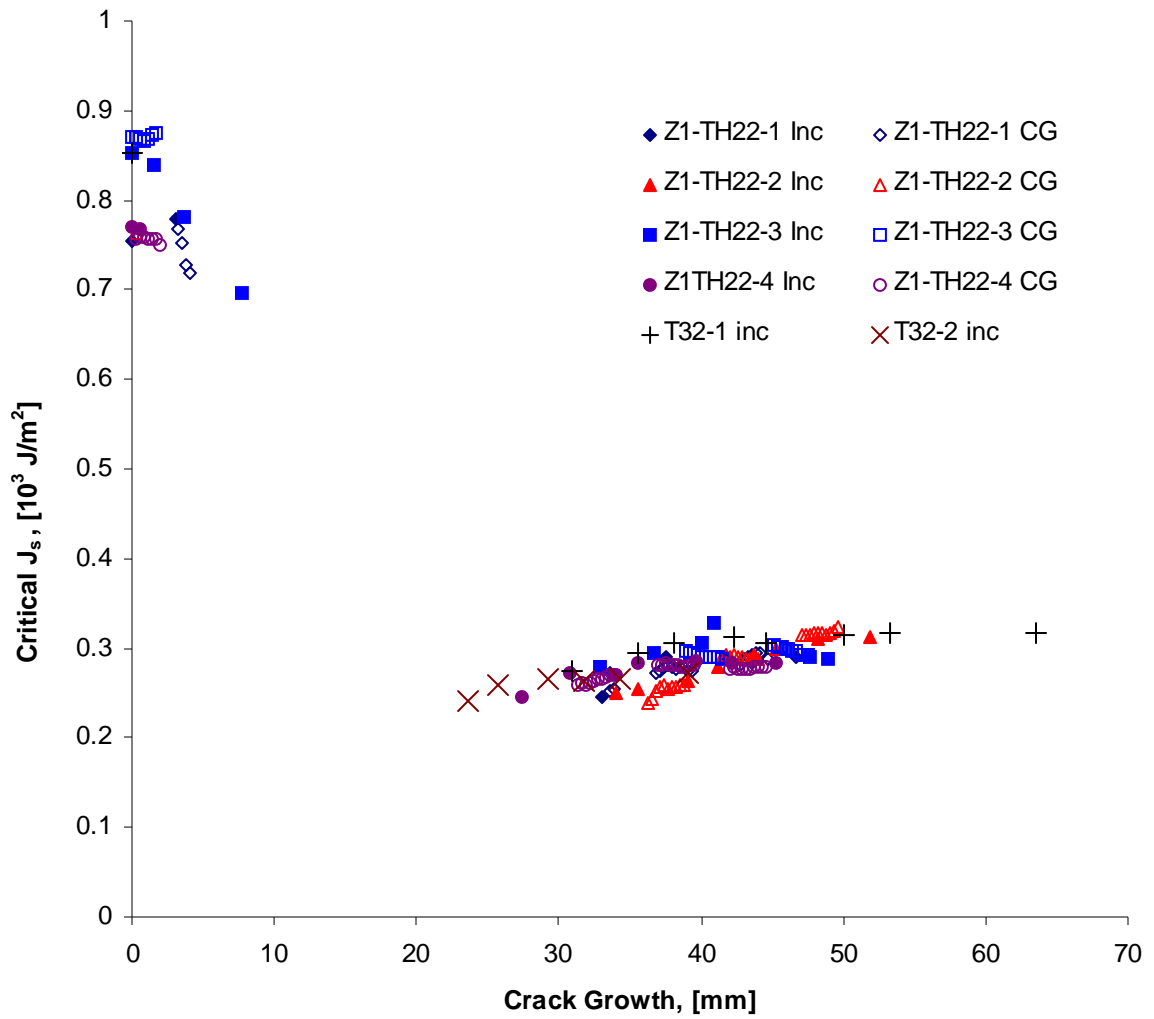


**Figure 7.5 Critical  $J_s$  of T800H/3900-2 at room temperature from multiple specimens.**

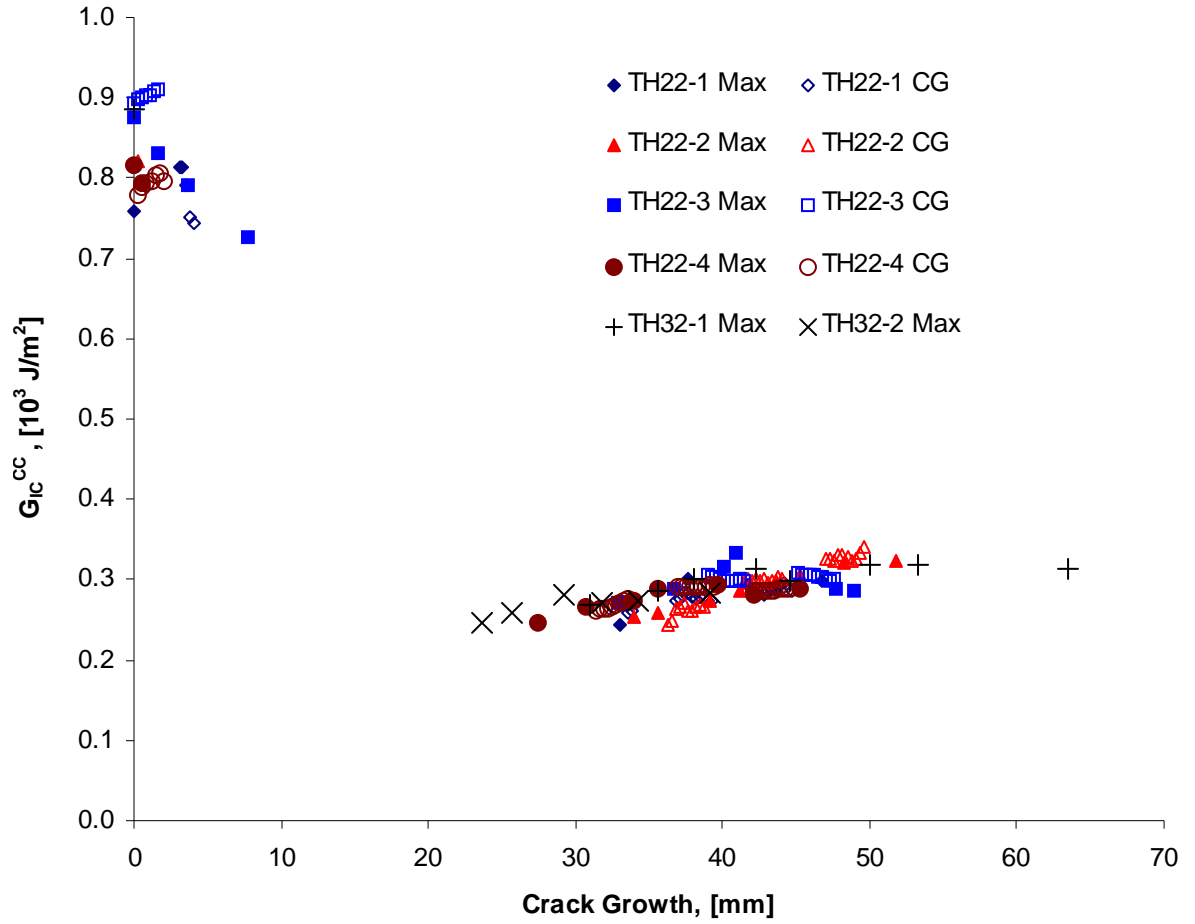


**Figure 7.6 Fracture toughness by CC method of T800H/3900-2 at room temperature.**

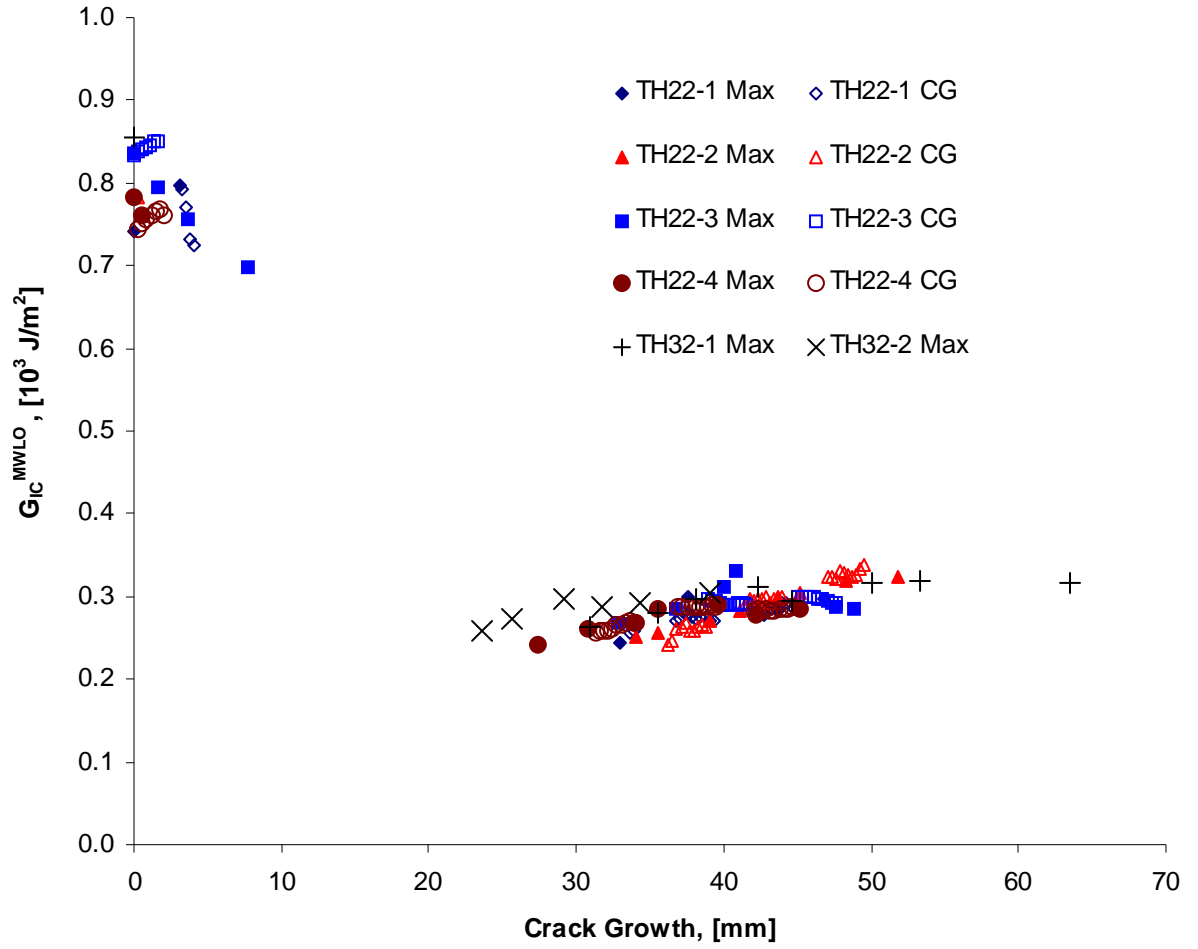


**Figure 7.7 Fracture toughness by MWLO method of T800H/3900-2 at room temperature.**

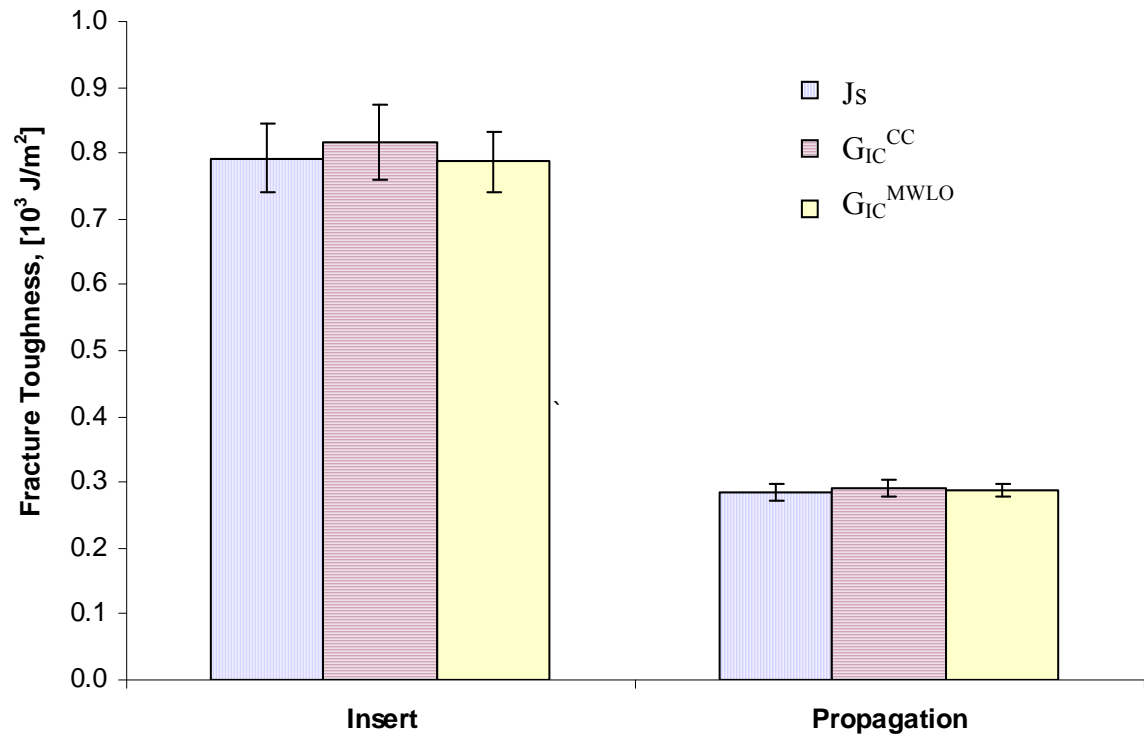


**Figure 7.8 Comparison of  $J_s$ ,  $G_{IC}^{CC}$  and  $G_{IC}^{MWLO}$  of T800H/3900-2 at room temperature.**

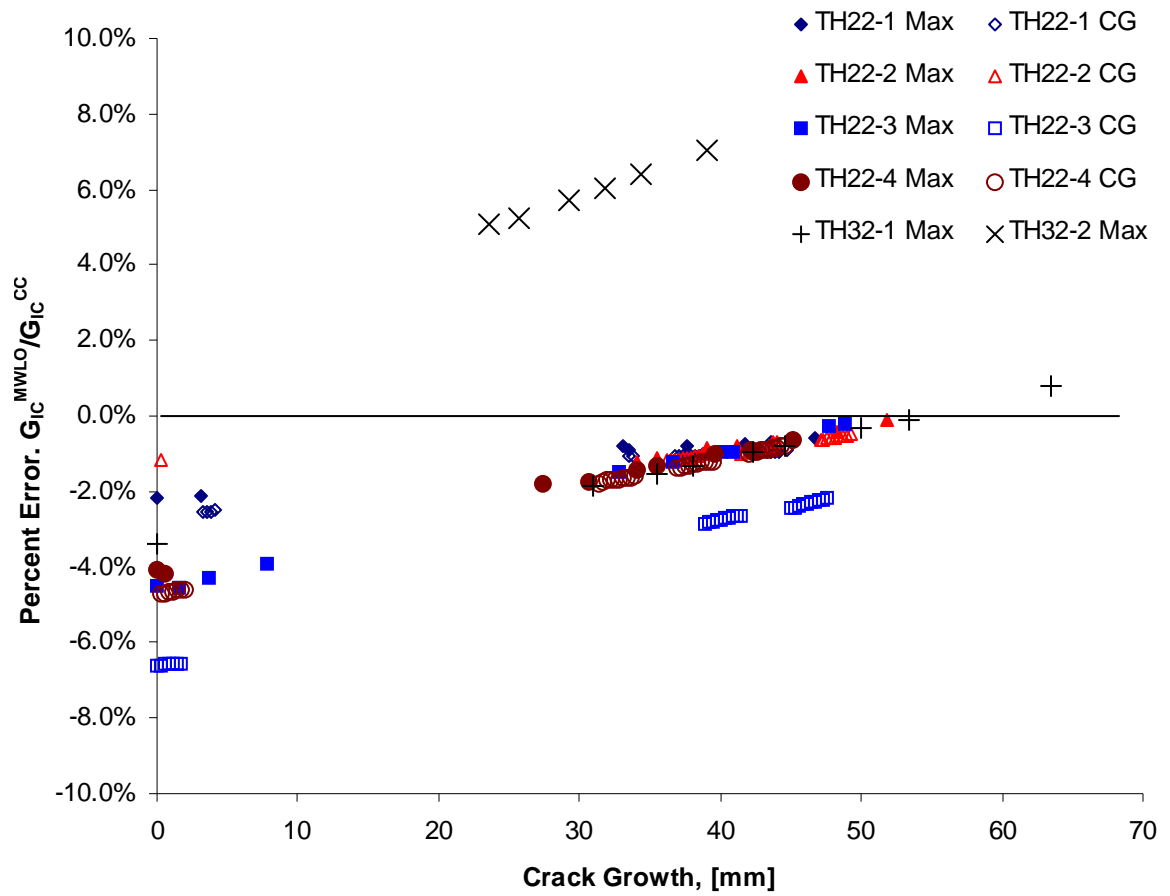


Figure 7.9 Percent error of  $G_{IC}^{MWLO}$  to  $G_{IC}^{CC}$  of T800H/3900-2 at room temperature.

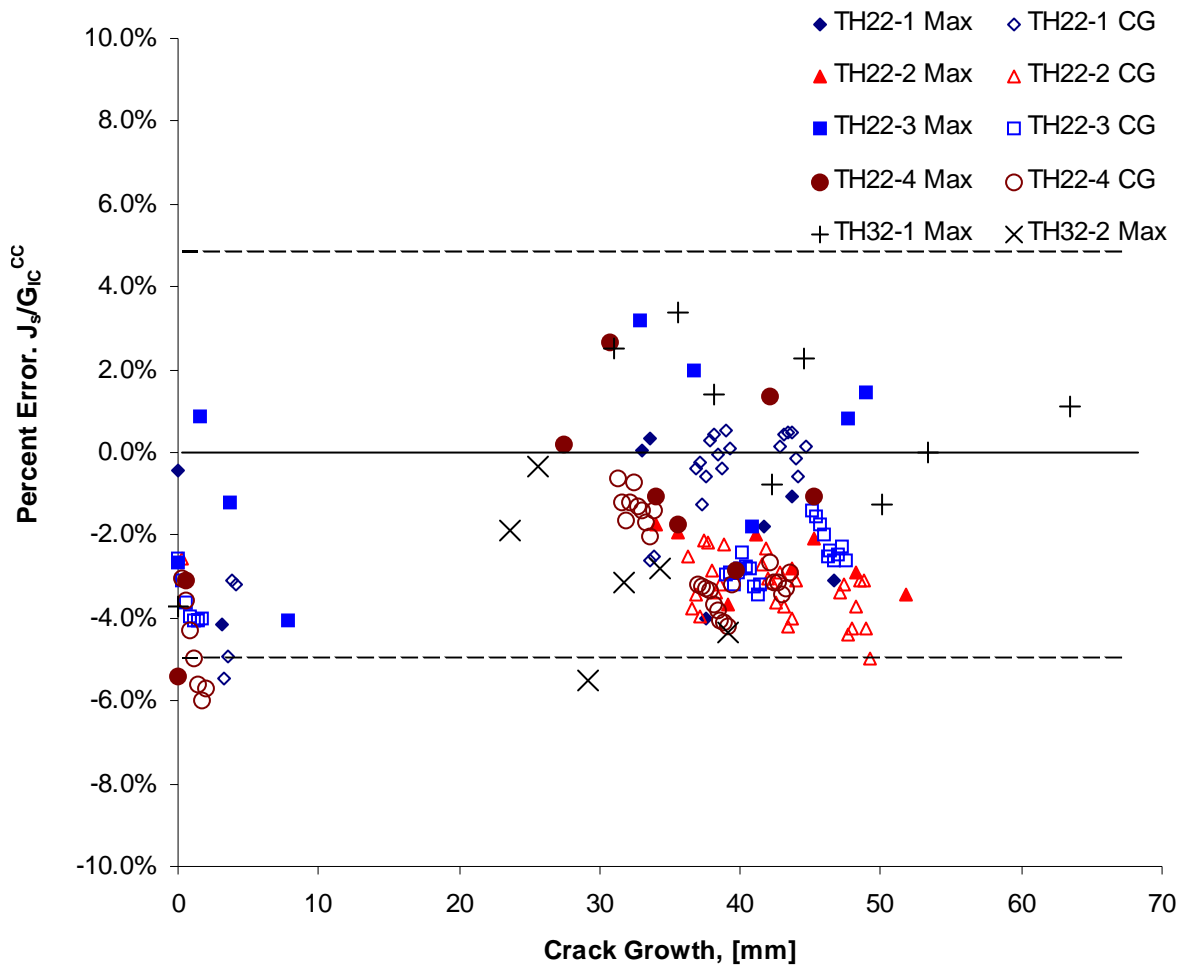


Figure 7.10 Percent error of  $J_s$  to  $G_{IC}^{CC}$  of T800H/3900-2 at room temperature.

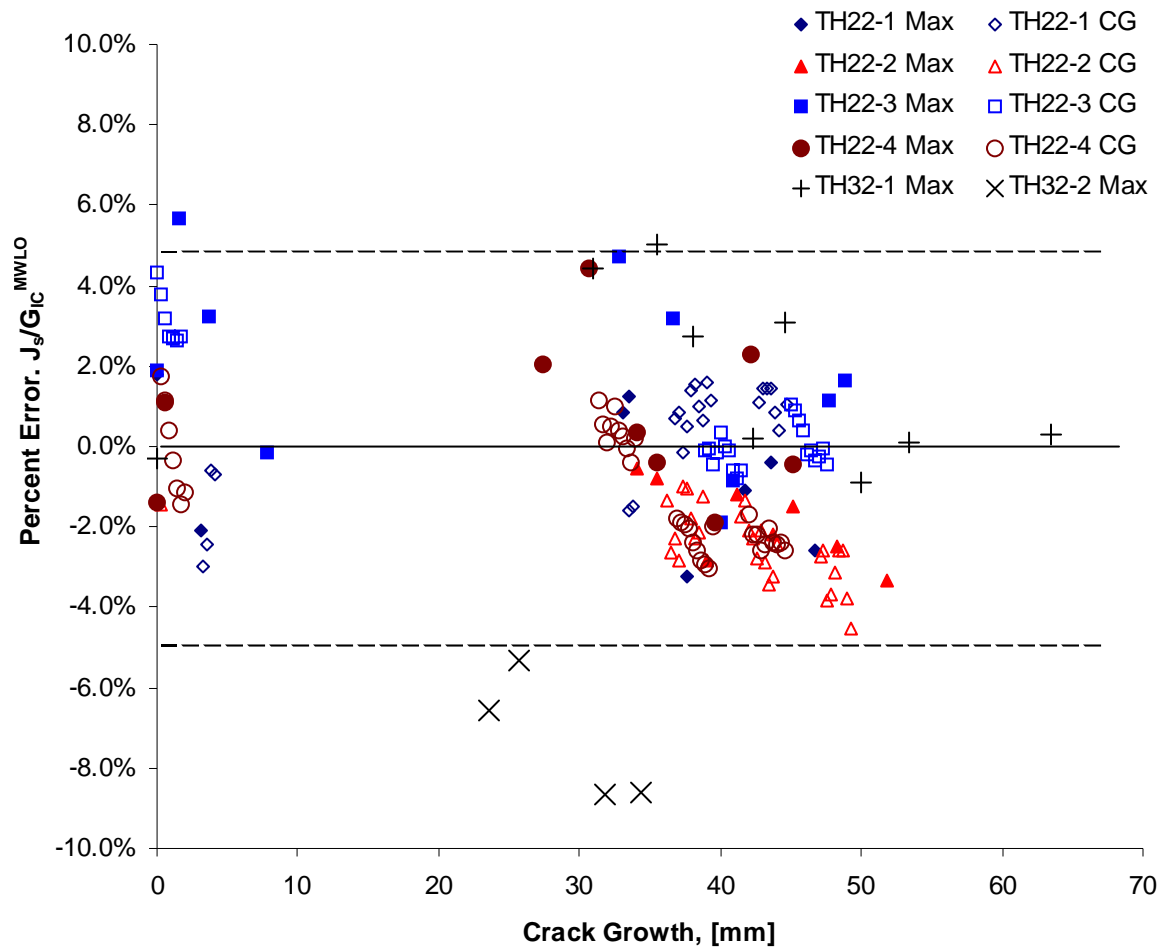
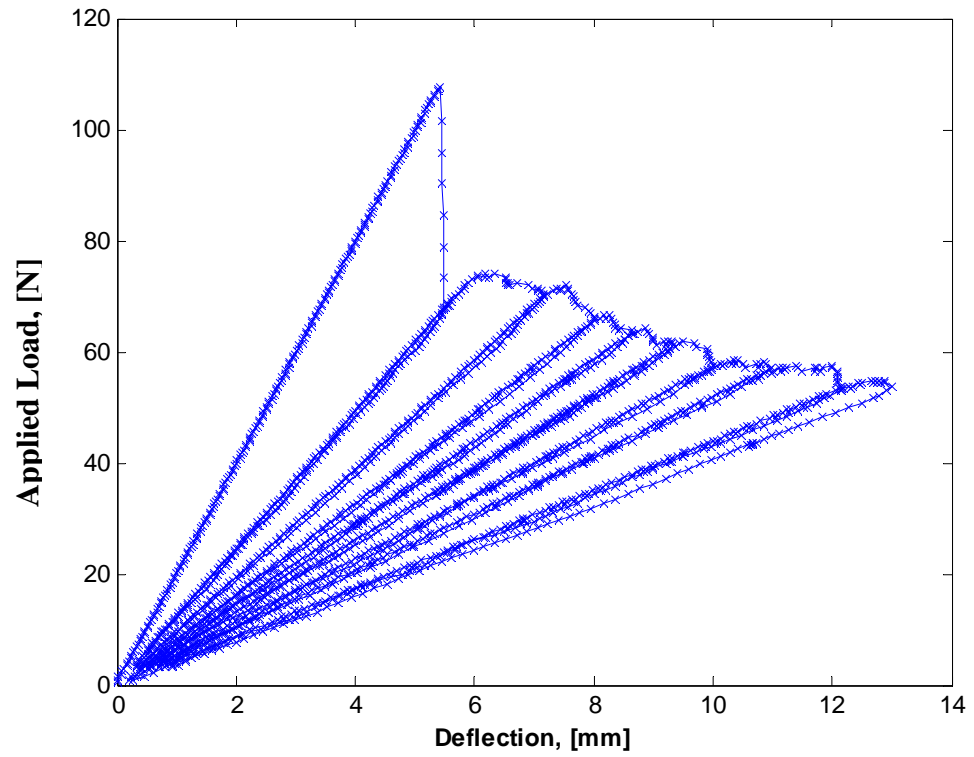


Figure 7.11 Percent error of  $J_s$  to  $G_{IC}^{MWLO}$  of T800H/3900-2 at room temperature.



**Figure 7.12 Typical load-deflection curve of IM7/8551-7 DCB test at room temperature.**



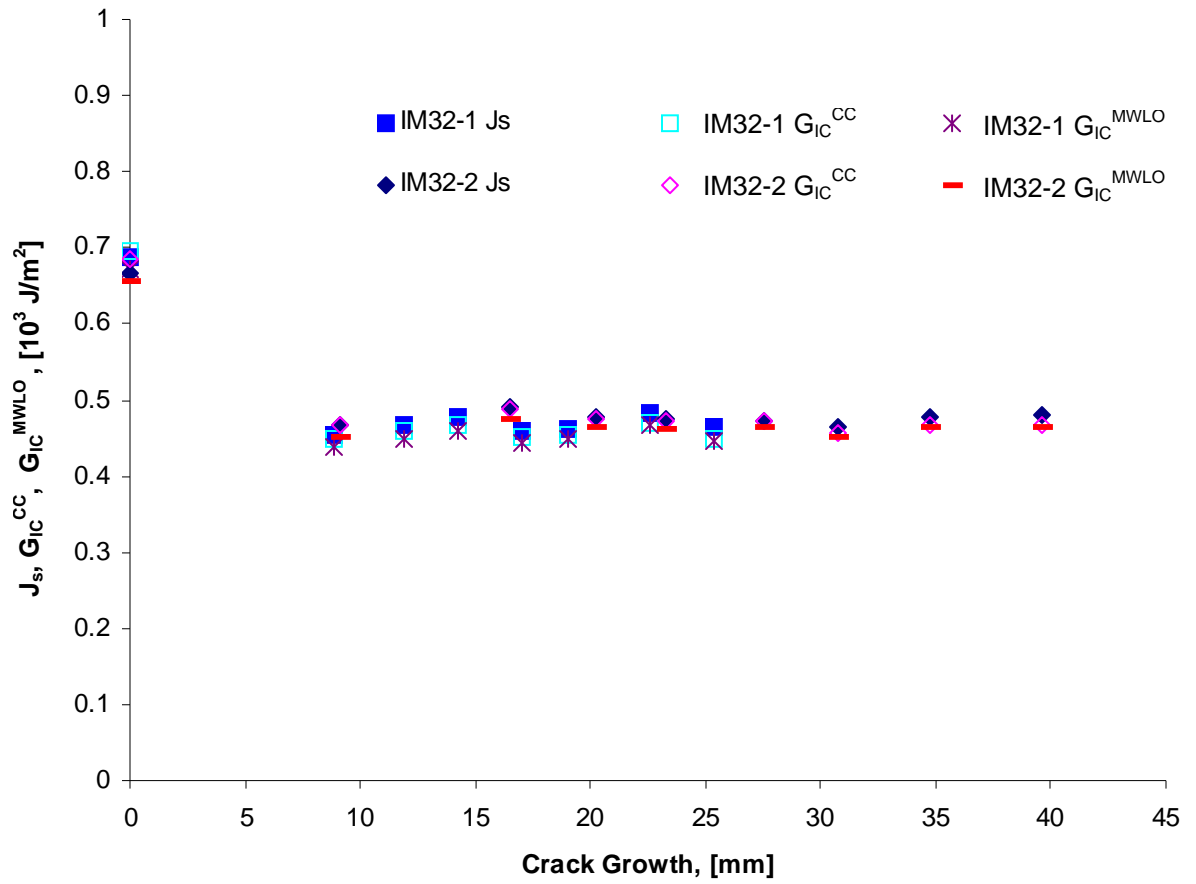
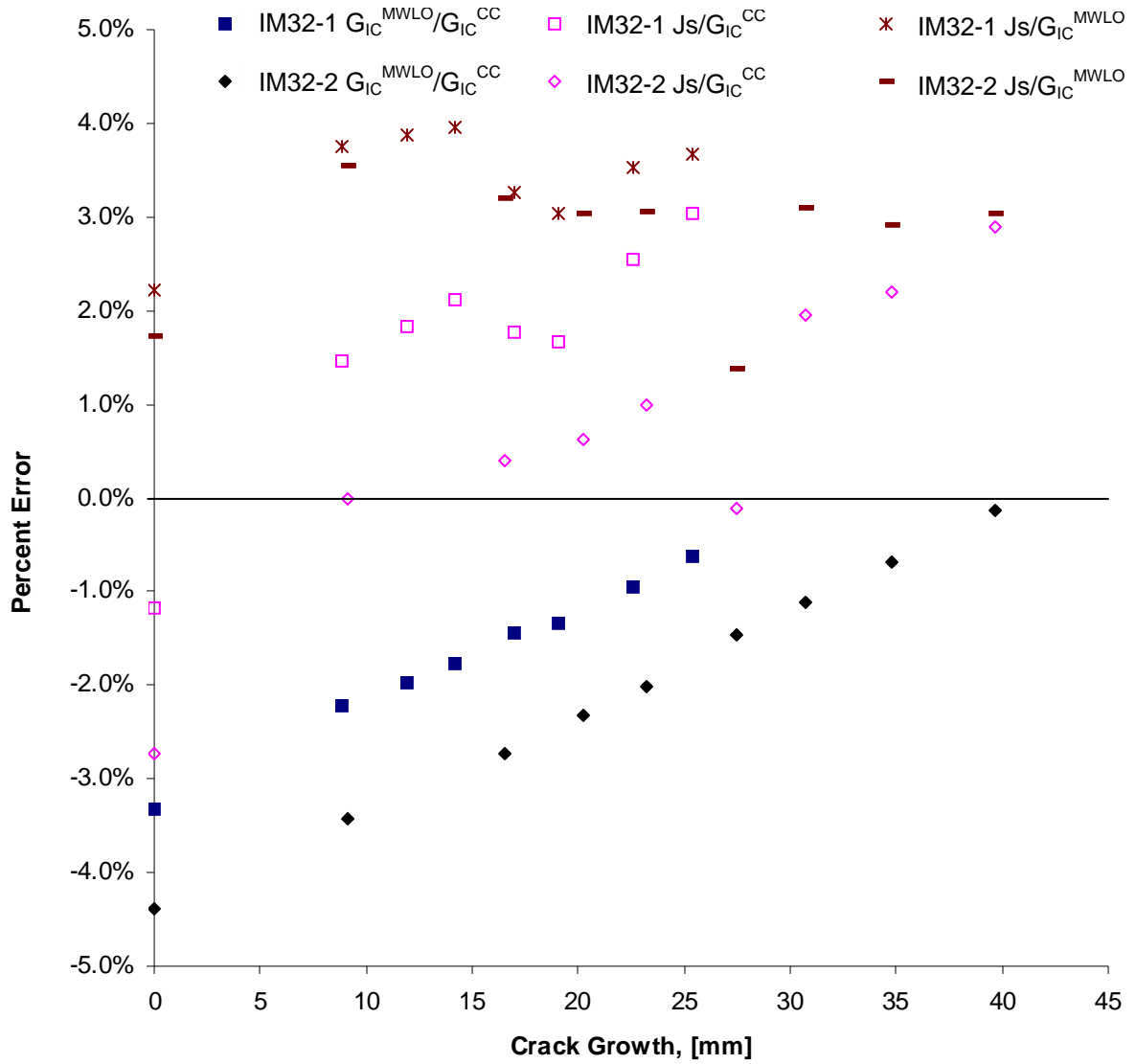
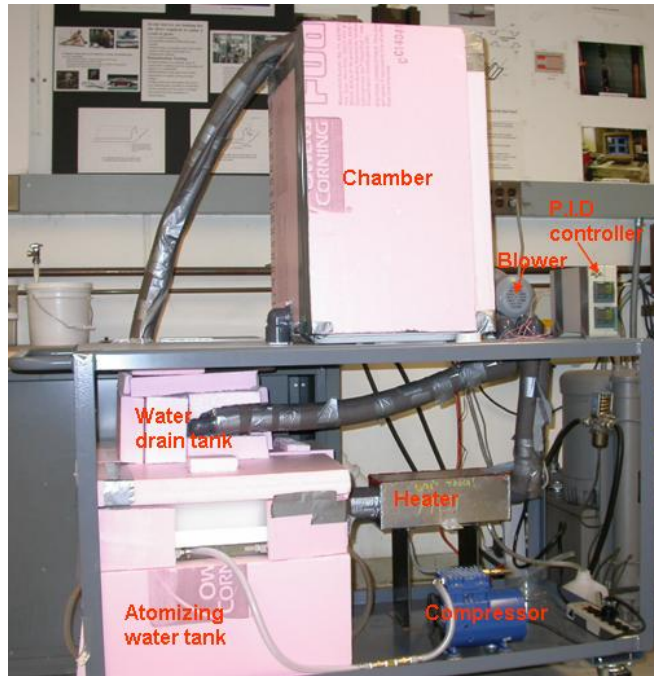


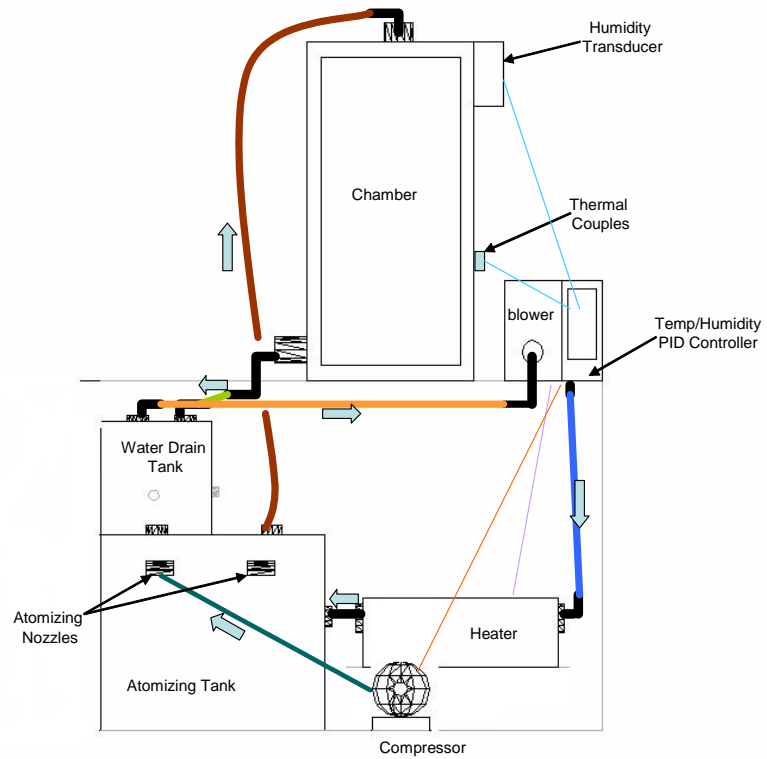
Figure 7.13  $J_s$ ,  $G_{IC}^{CC}$ , and  $G_{IC}^{MWLO}$  of IM7/8551-7 DCB specimens.



**Figure 7.14 Percent error of fracture toughness from different methods for IM7/8551-7 DCB specimens.**



(a)



(b)

**Figure 8.1 Humidity system setup and schematic of flow cycles.**

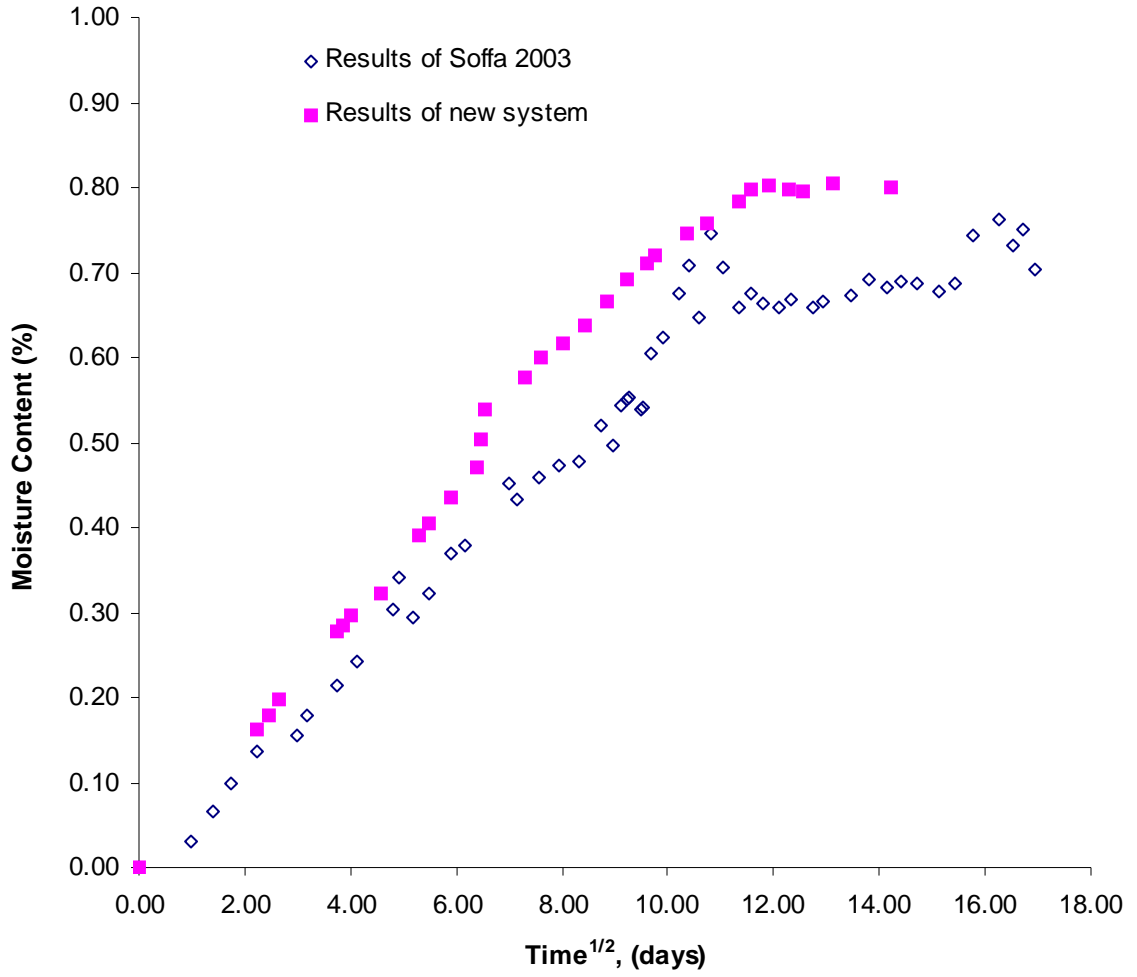
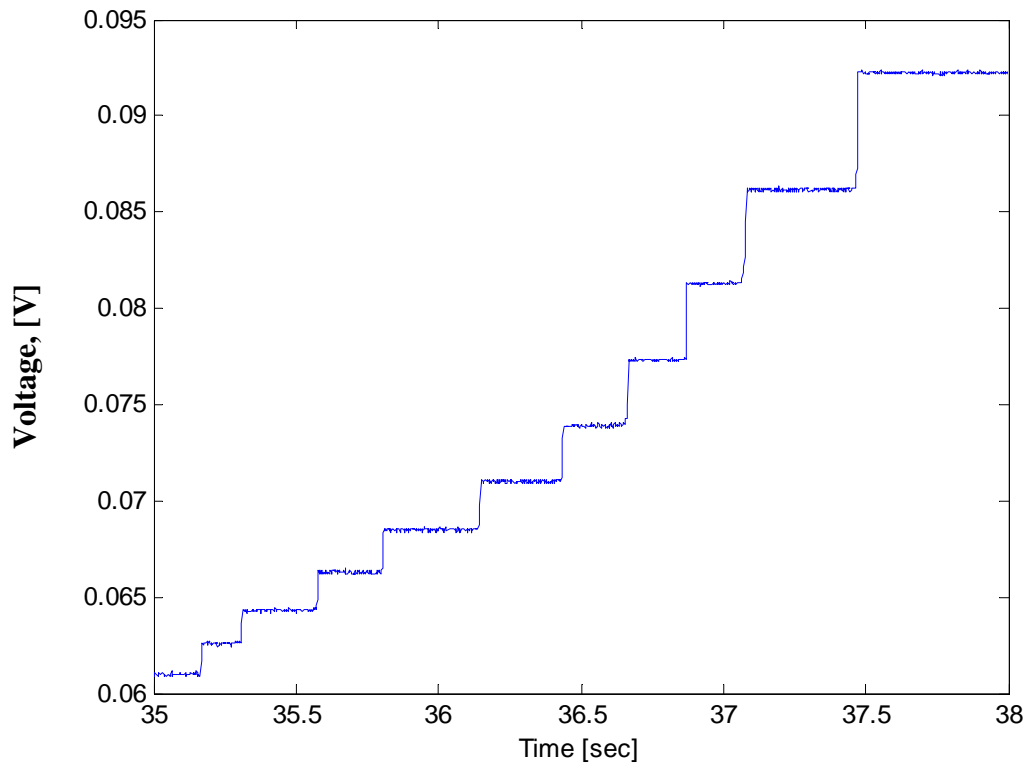
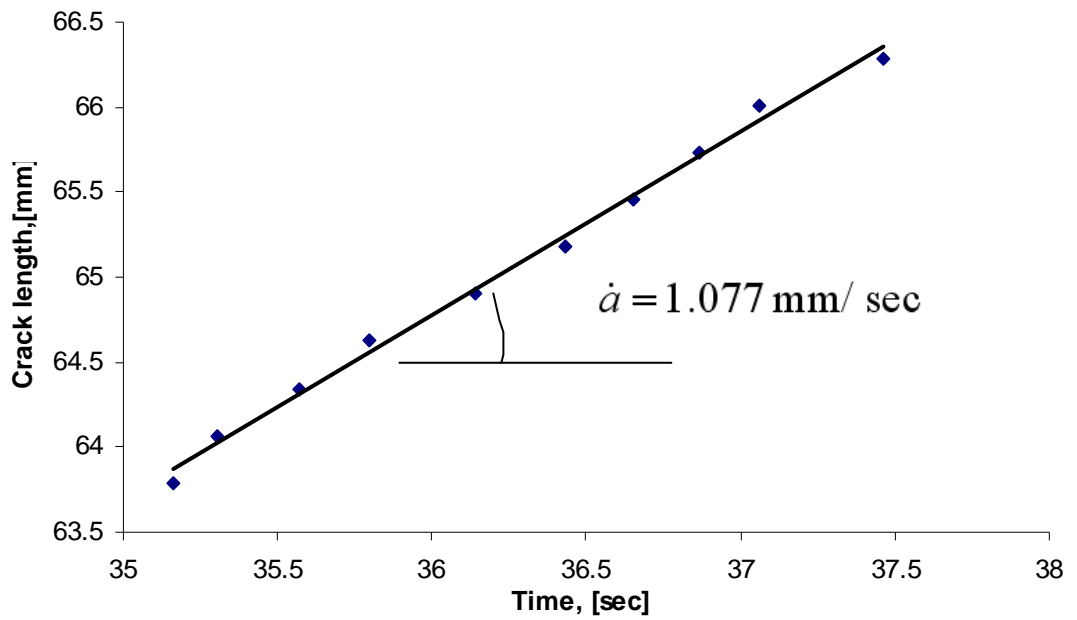


**Figure 8.2 Typical moisture content with time for T800H/3900-2 specimens.**

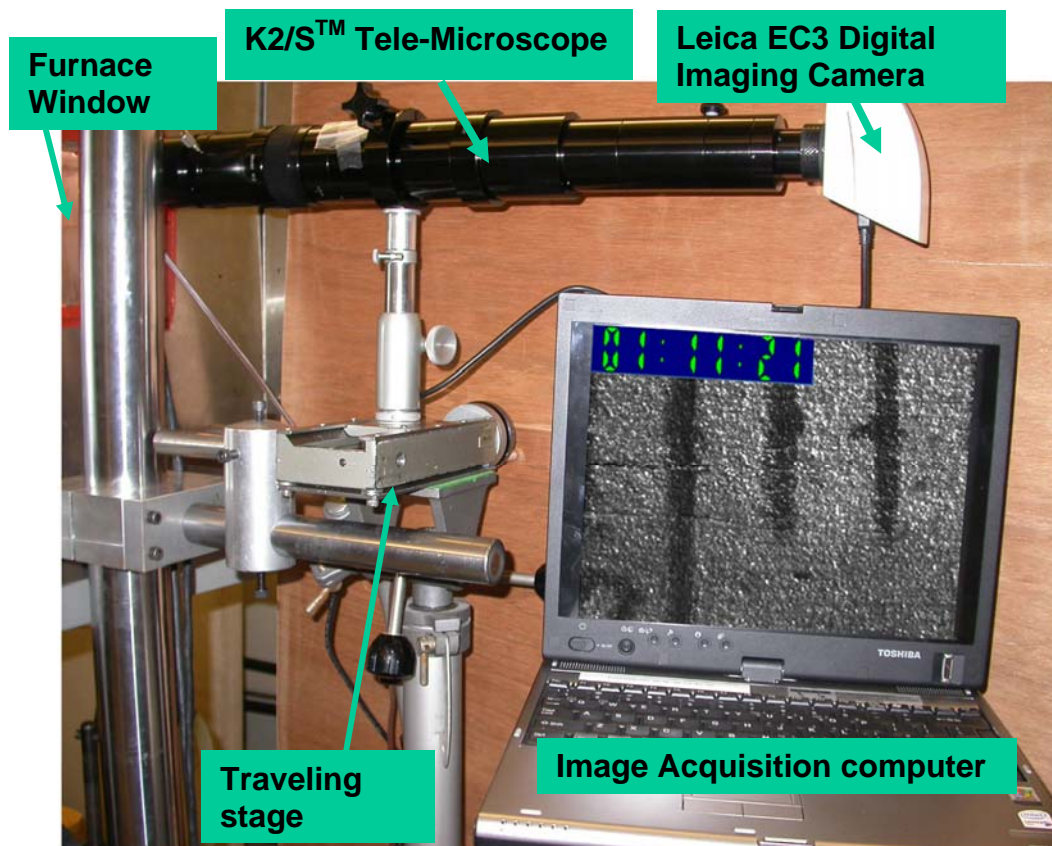


(a)

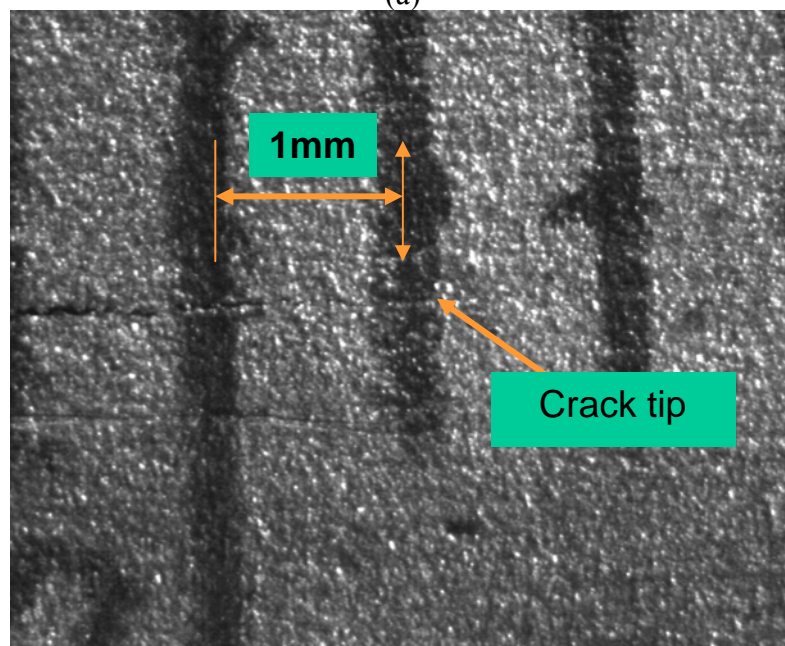


(b)

Figure 8.3 Typical output from one crack gage: (a) voltage output (b) crack speed.



(a)



(b)

Figure 8.4 Tele-Microscope System (TMS) and a sample image.

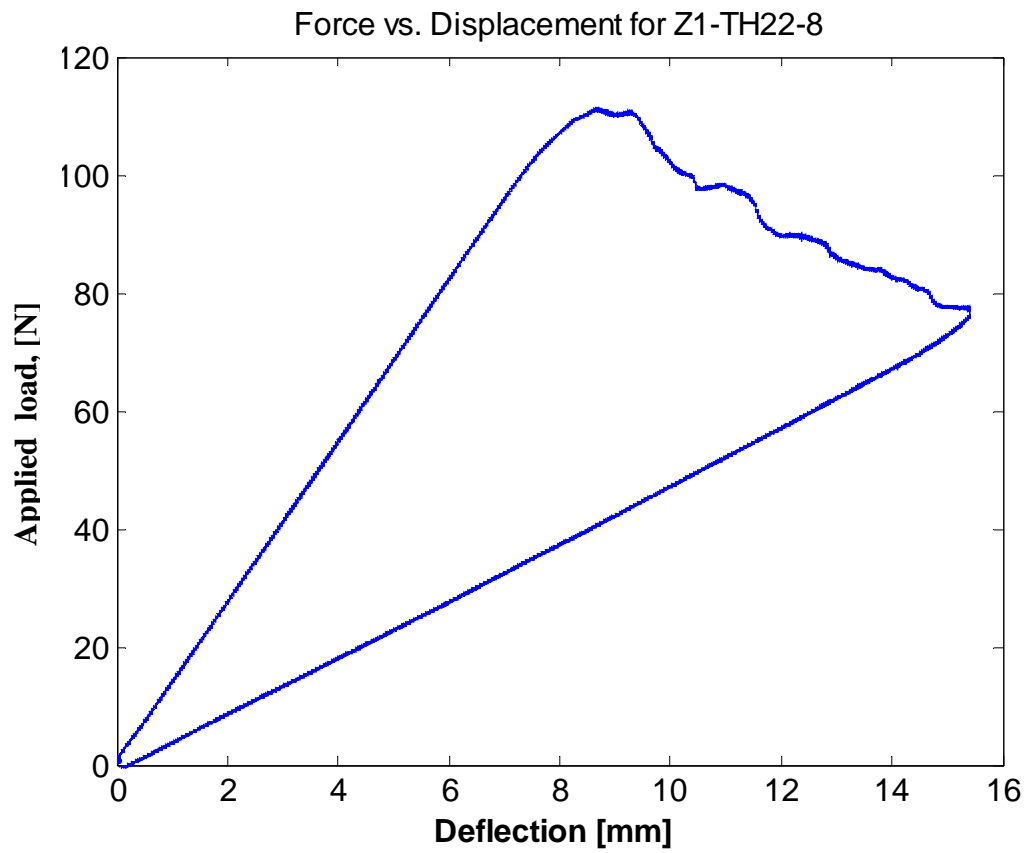


**Figure 8.5 Typical load-deflection curve of T800H/3900-2 dry DCB specimen at 98°C.**

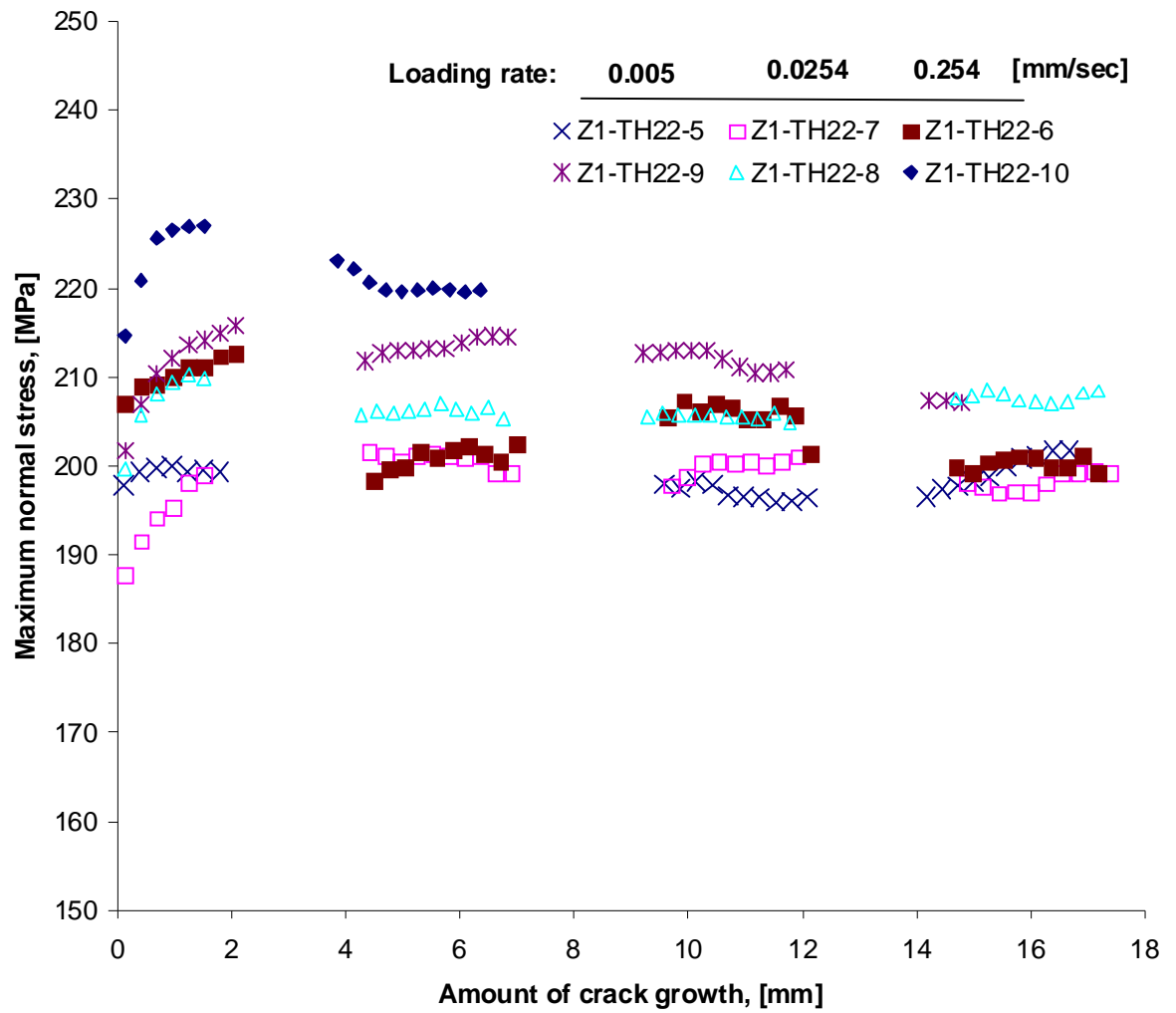


Figure 8.6 Maximum normal stresses of dry DCB specimens tested at 98°C.



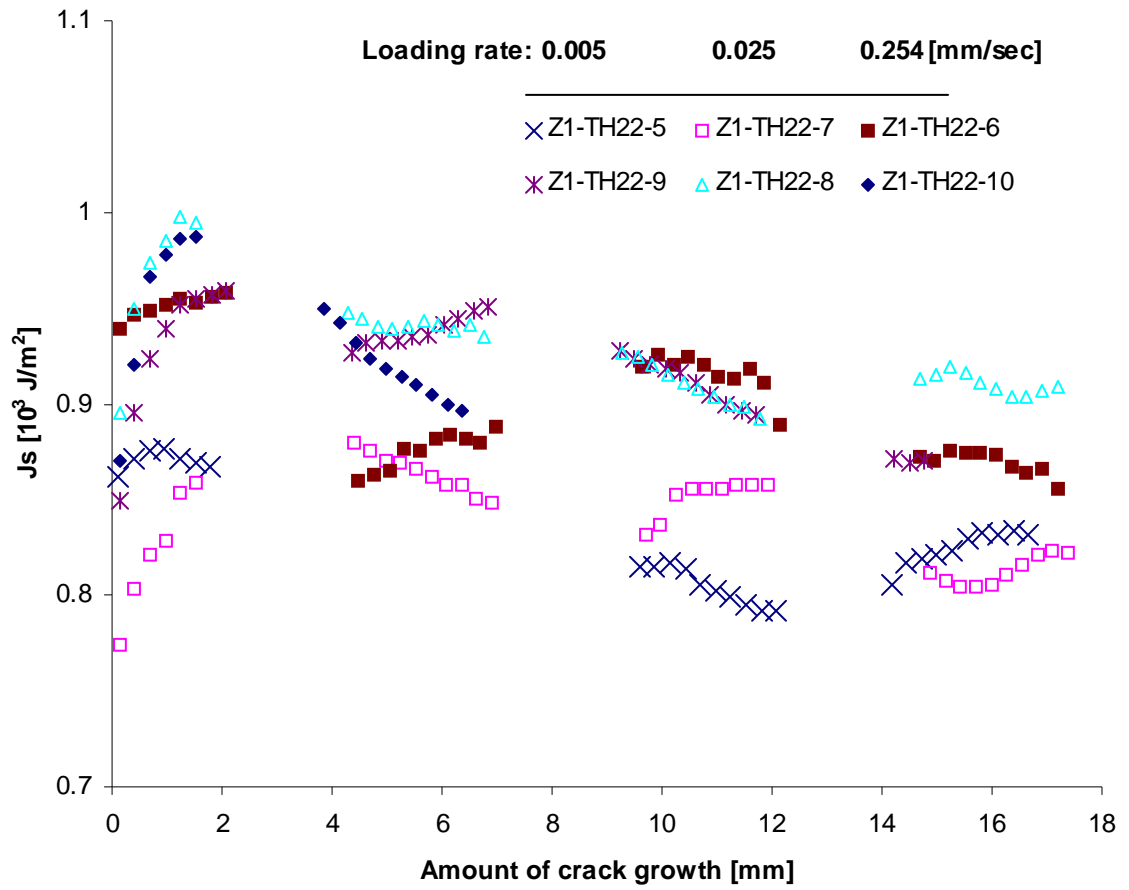


Figure 8.7  $J_s$  vs. crack growth of T800H/3900-2 dry DCB specimens at 98°C.

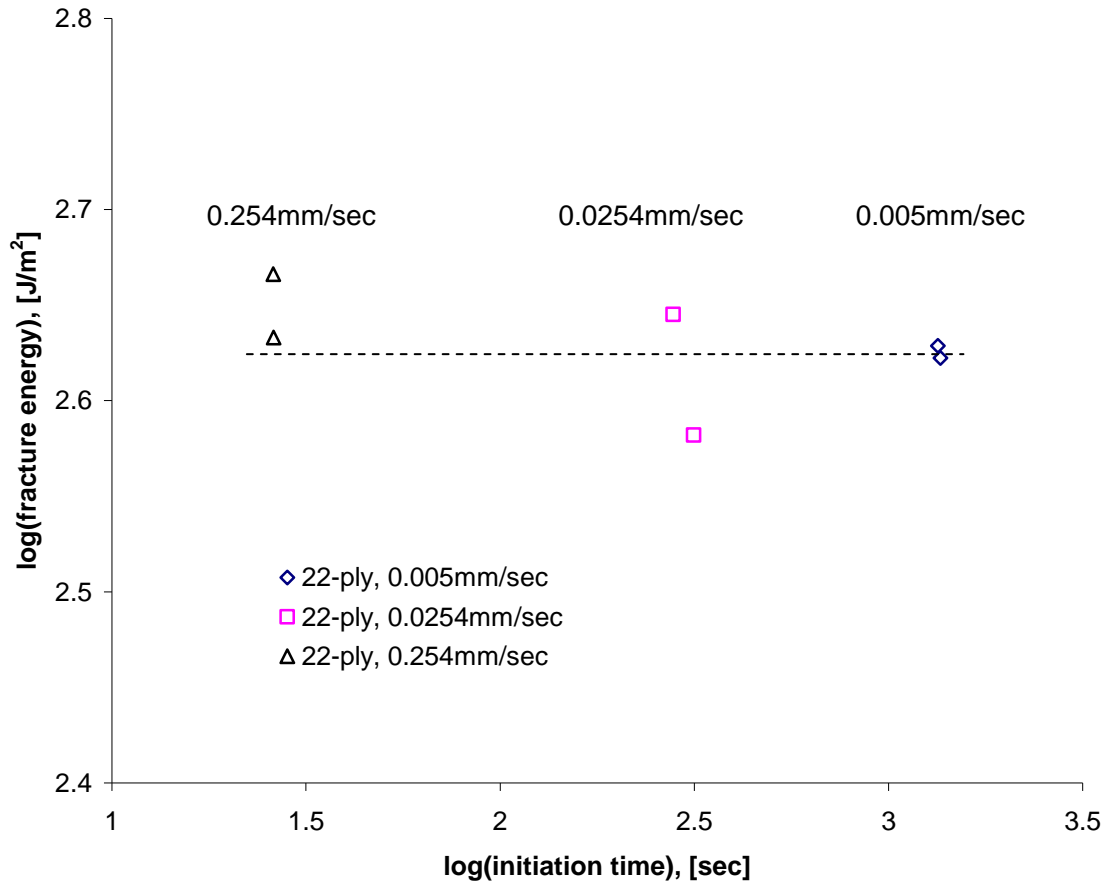


Figure 8.8 Fracture curve  $t_i(\Gamma_{II})$  of T800H/3900-2 dry DCB specimens at 98°C.

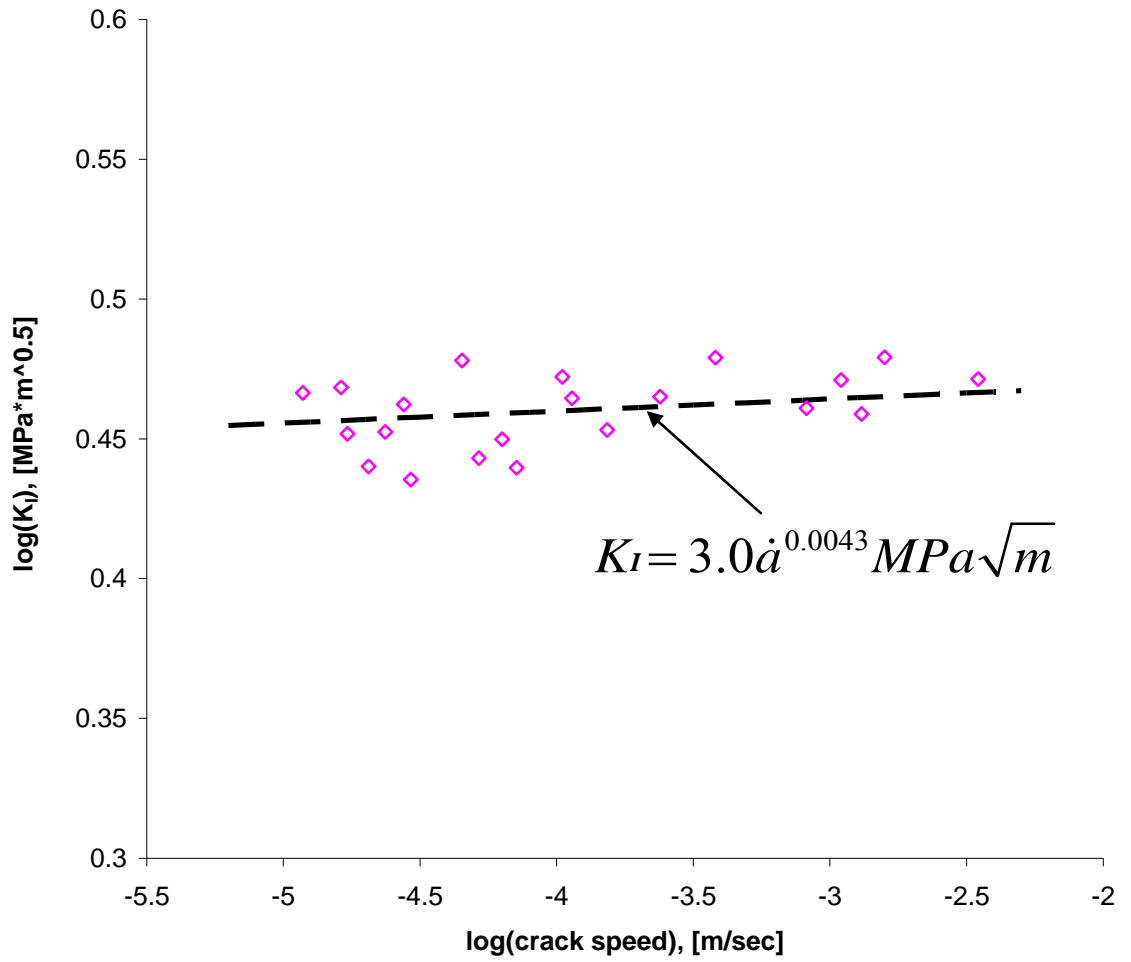


Figure 8.9 Fracture curve  $\dot{a}(K_I)$  for T800H/3900-2 dry DCB specimens at 98°C.

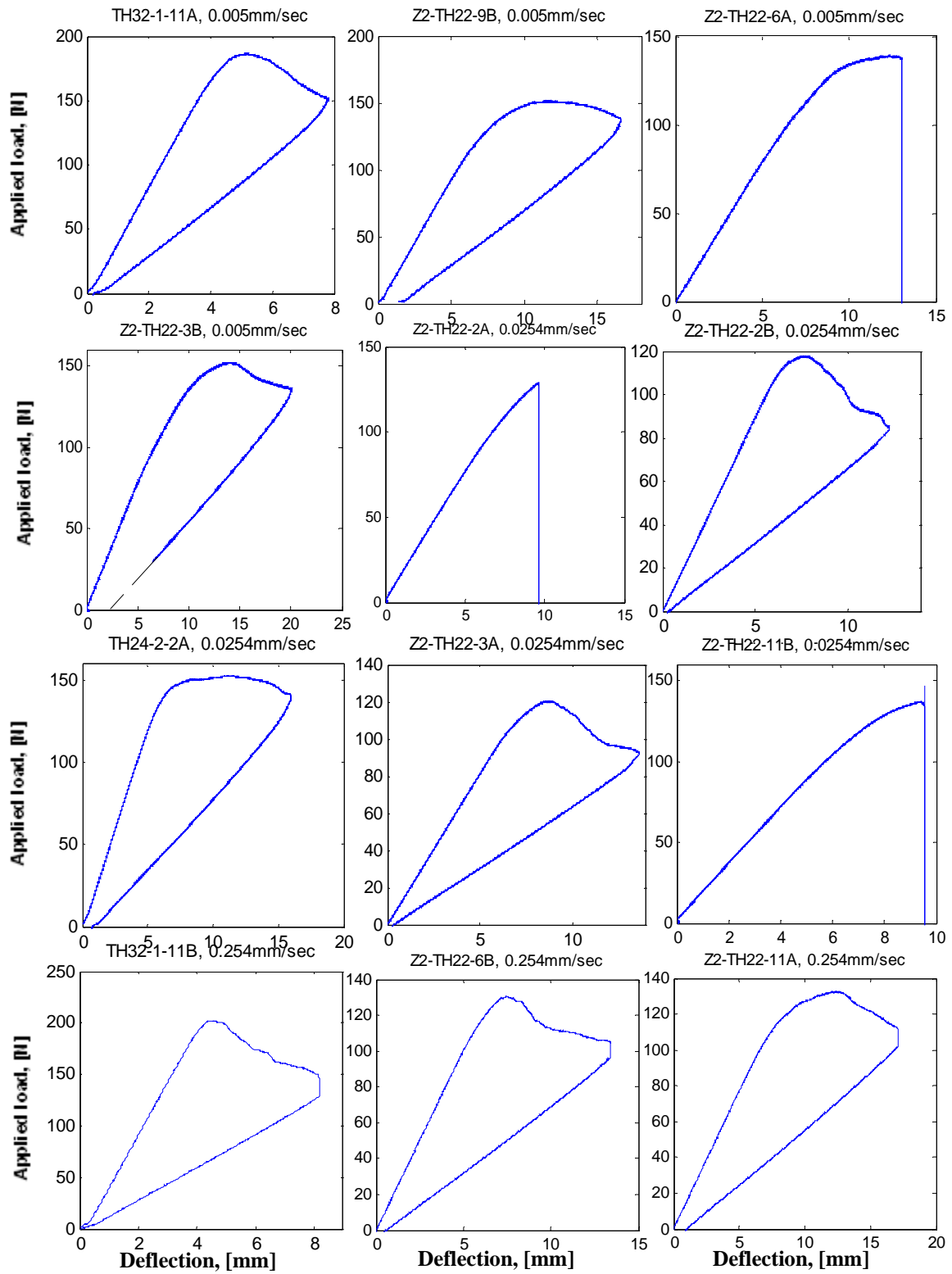
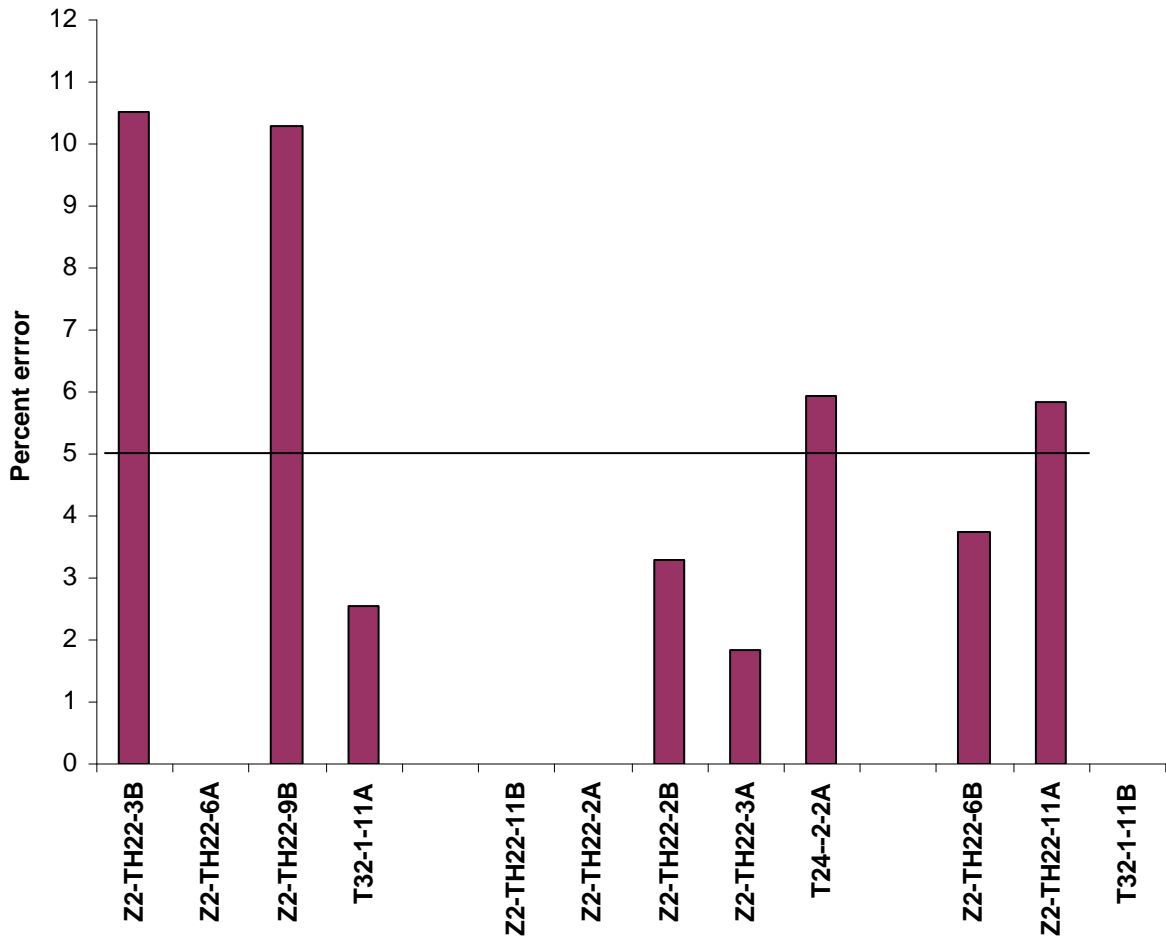


Figure 8.10 Load-deflection curves for T800H/3900-2 wet DCB specimens at 98°C.



Note: Z2-TH22-6A, Z2-TH22-11B, and Z2-TH22-2A had tab debonding problems; two 32-ply specimens have negligible residual deformation.

**Figure 8.11 Percent residual deformation to maximum deformation for T800H/3900-2 wet DCB specimens at 98°C.**

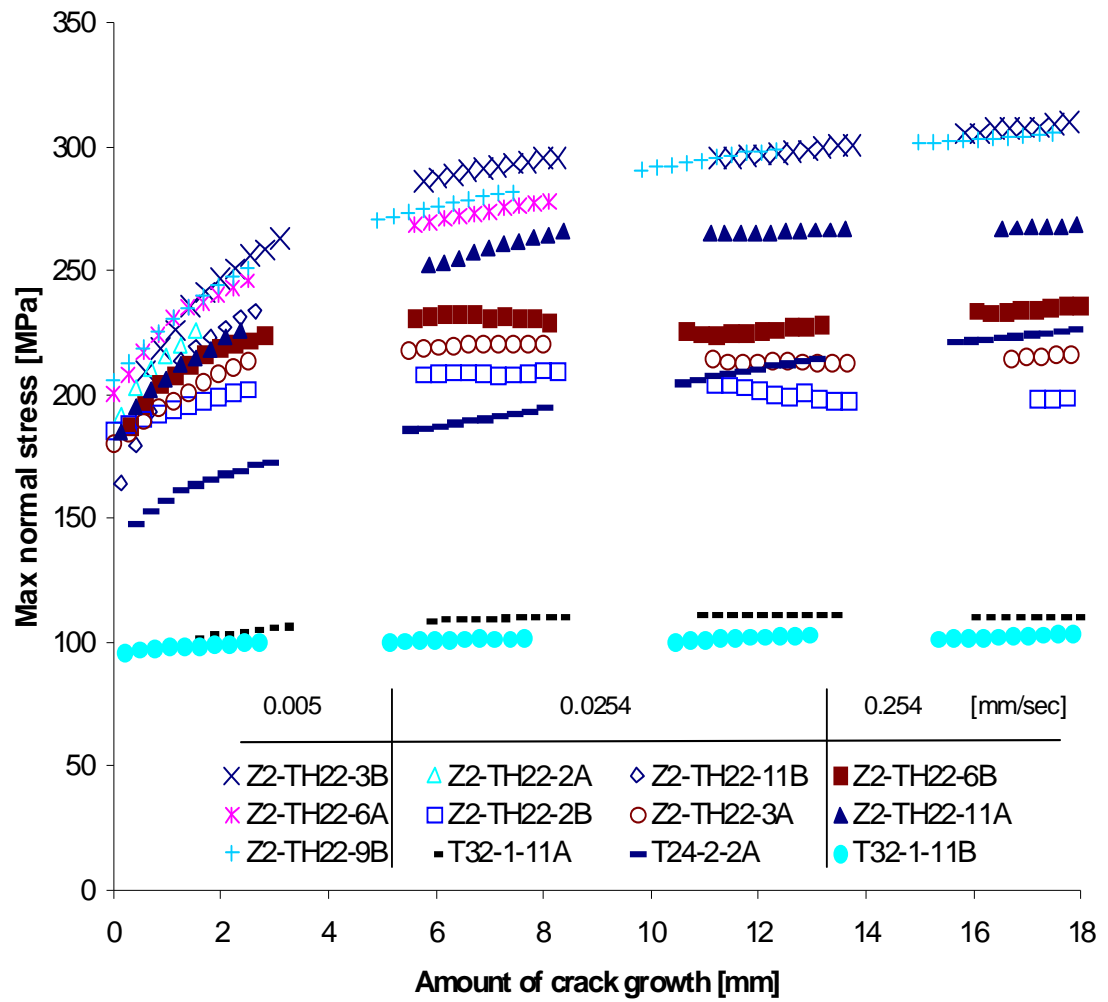


Figure 8.12 Maximum normal stresses for wet DCB specimens tested at 98°C.

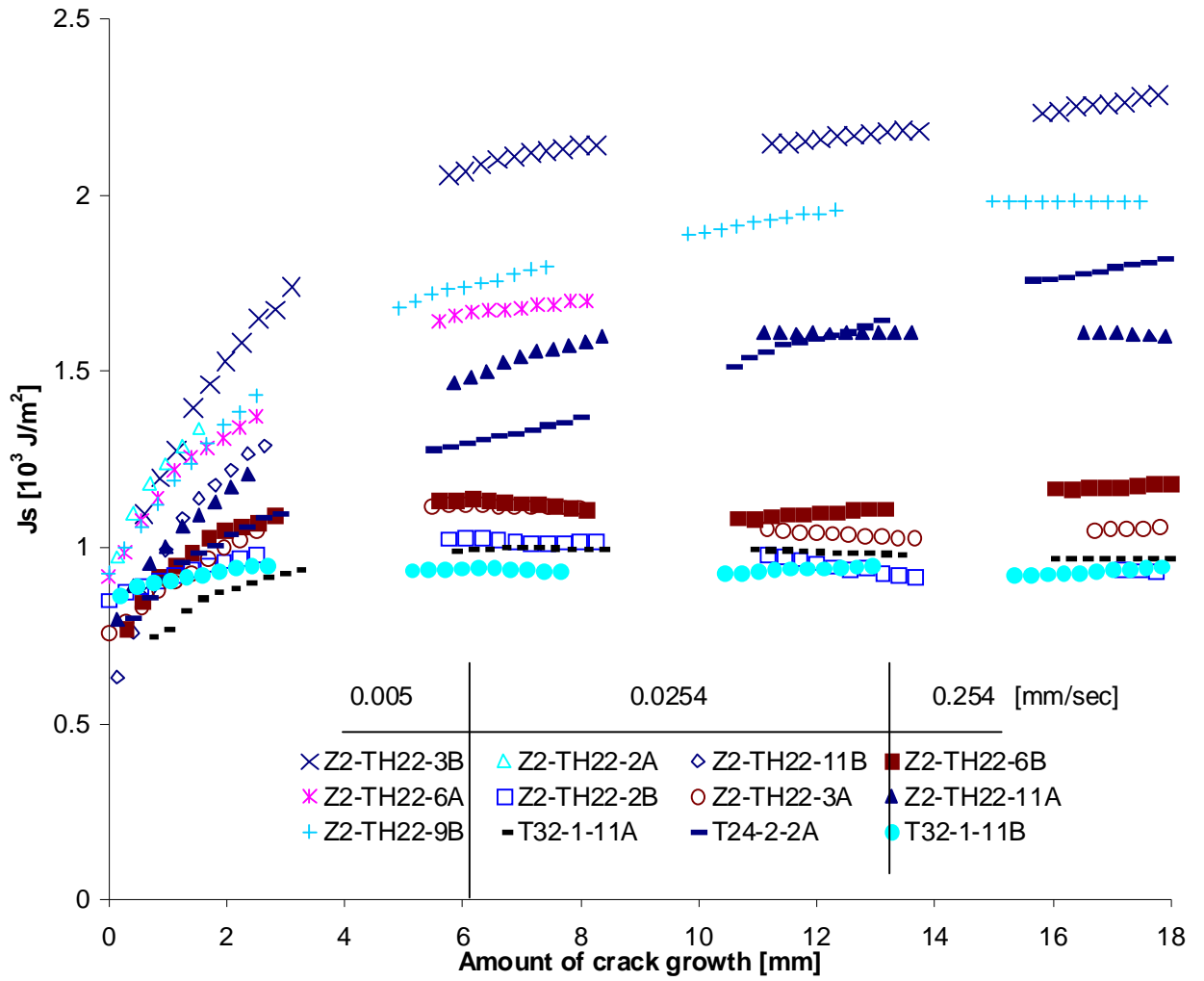


Figure 8.13  $J_s$  vs. crack growth for T800H/3900-2 wet DCB specimens at 98°C.

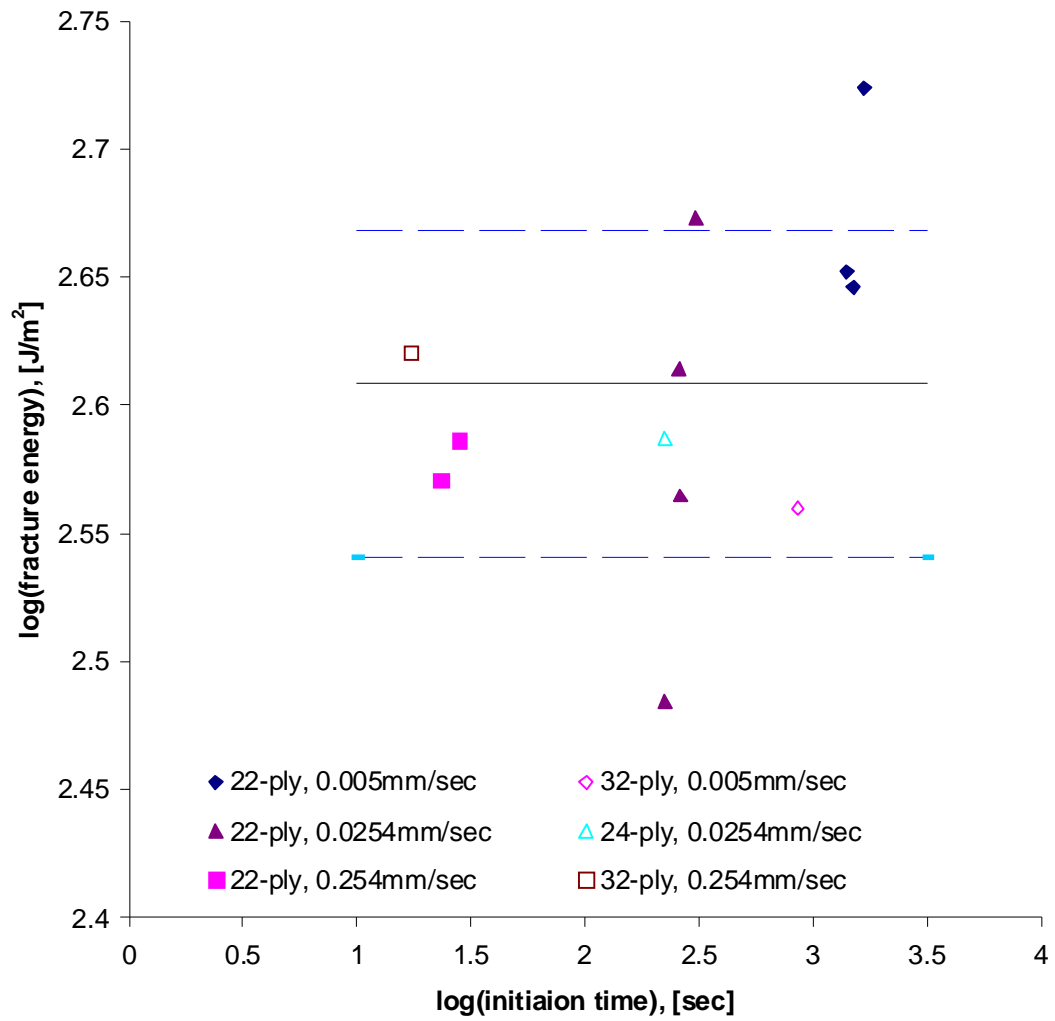


Figure 8.14 Fracture curve  $t_i(\Gamma_{II})$  for T800H/3900-2 wet DCB specimens at 98°C.



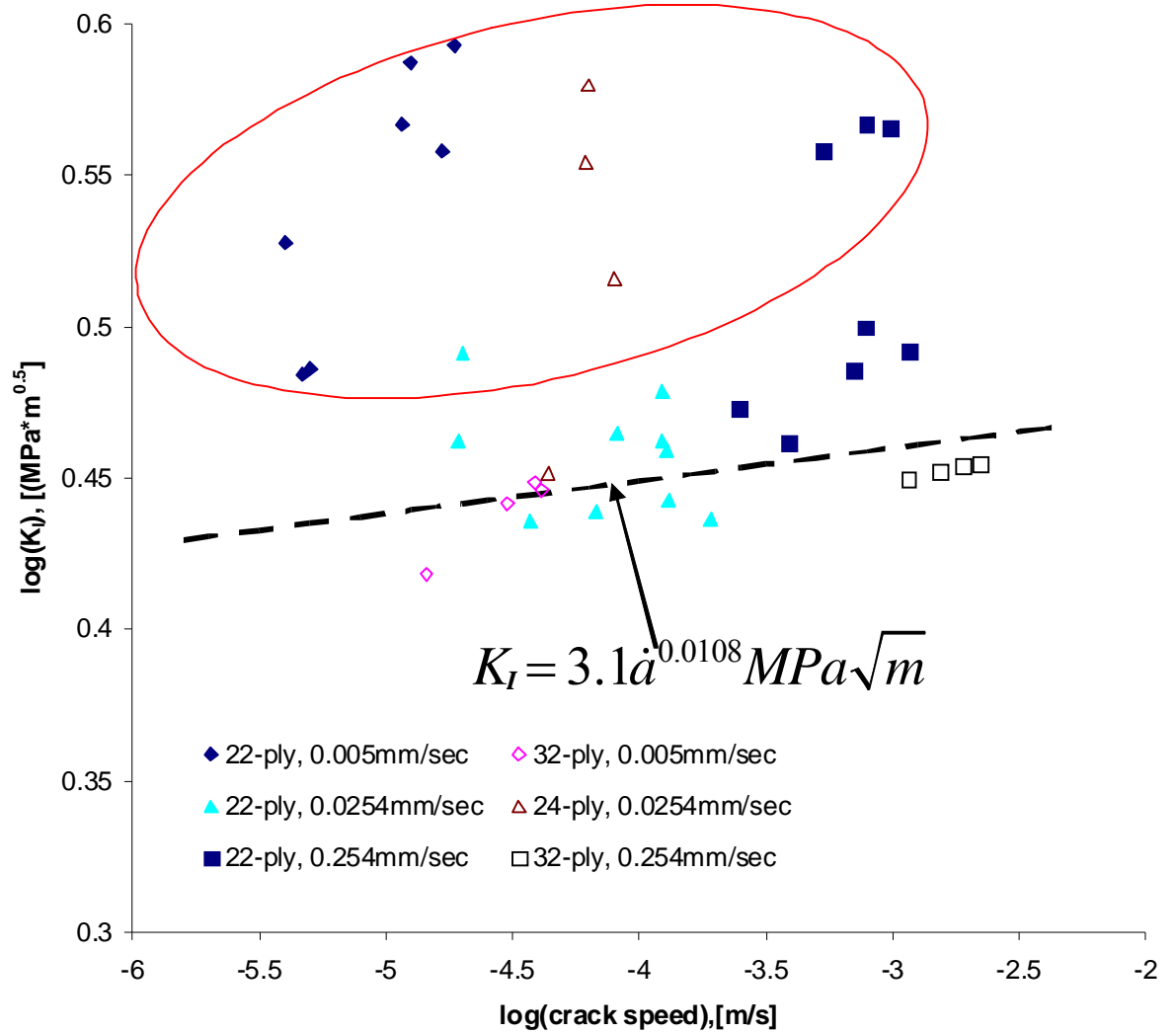


Figure 8.15 Fracture curve  $\dot{a}(K_I)$  for T800H/3900-2 wet DCB specimens at 98°C.

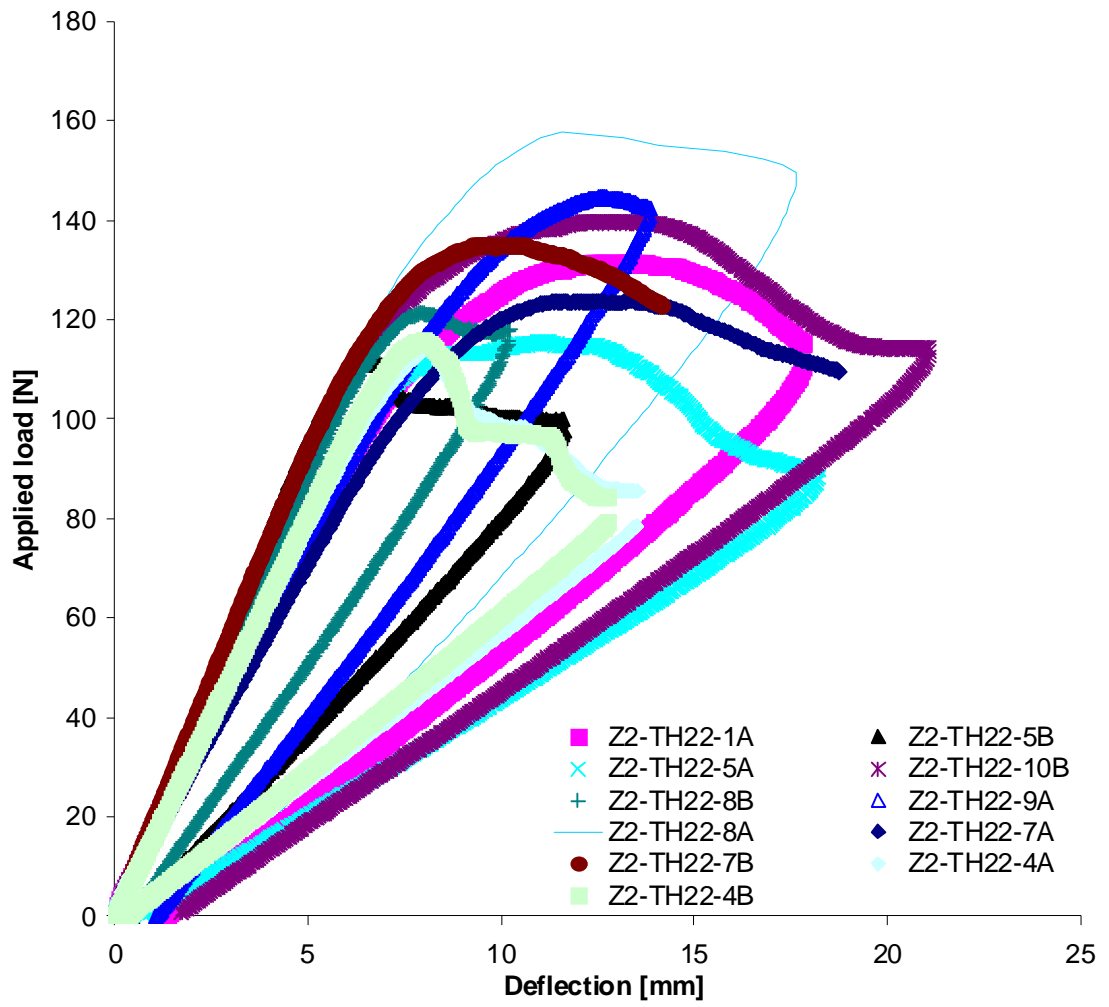
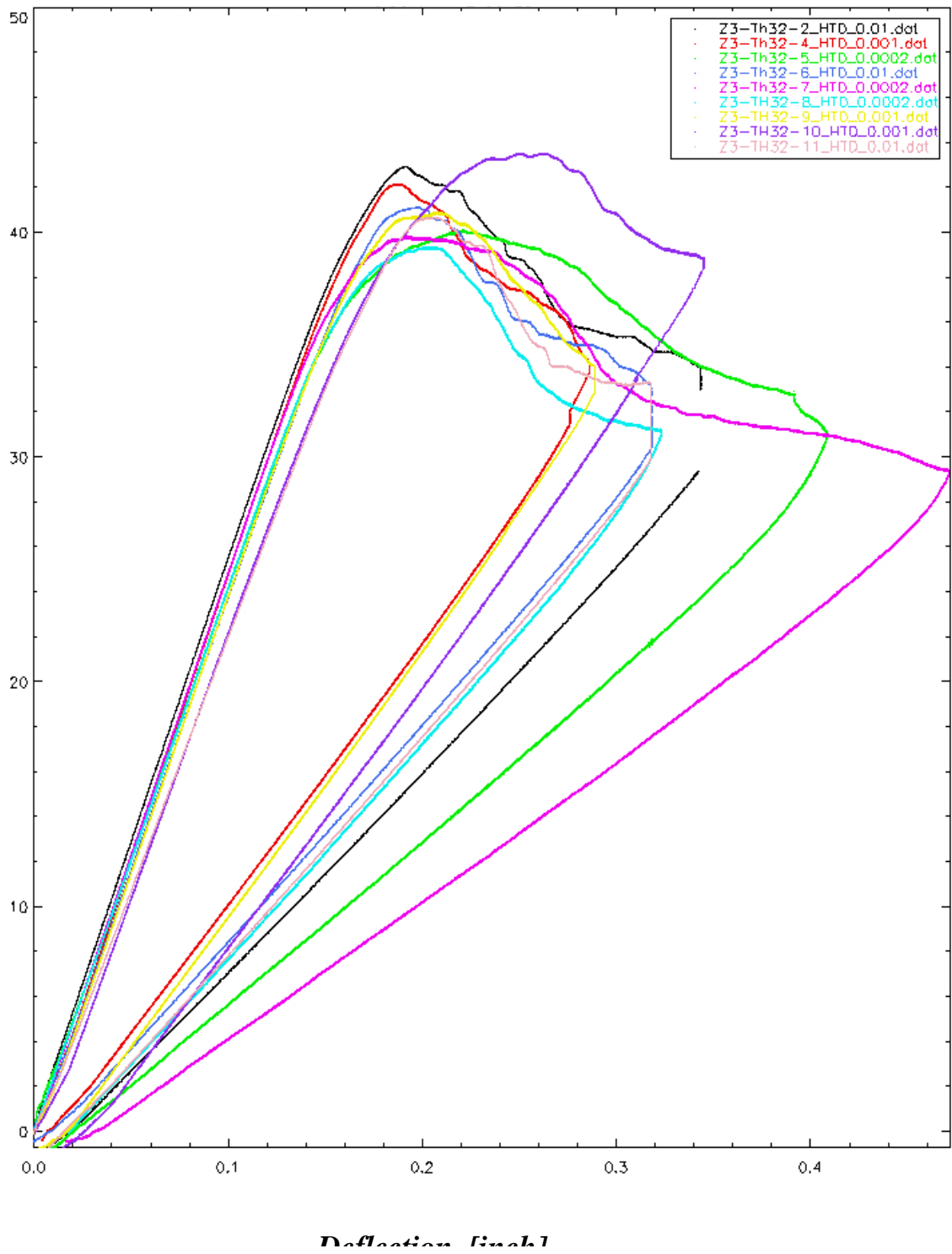
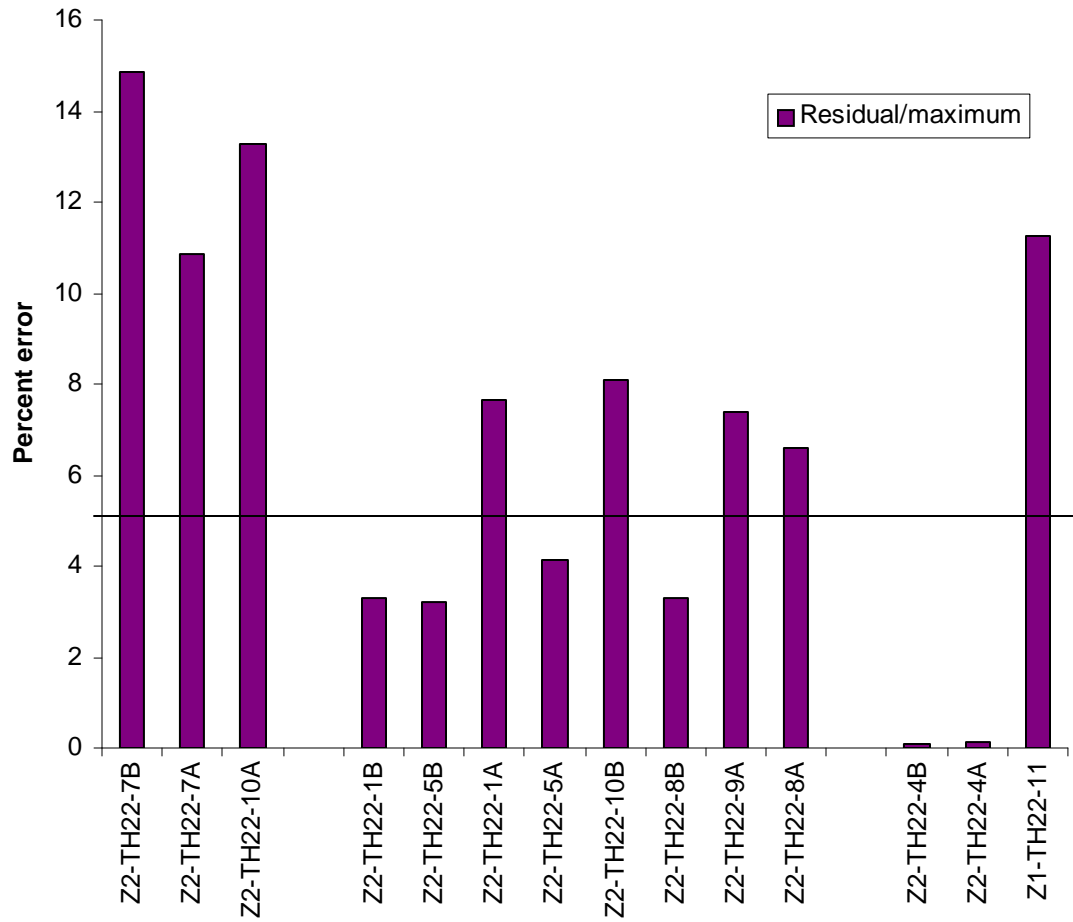


Figure 8.16 Load-deflection curves for 22-ply dry DCB specimens at 125°C.



**Figure 8.17 Load-deflection curves for 32-ply dry DCB specimens at 125°C.**



**Figure 8.18 Percent residual deformation to maximum deformation for 22-ply dry DCB specimens at 125°C.**



Note: Z3-TH32-1 and Z3-TH32-3 had tab debonding problems.

**Figure 8.19 Percent residual deformation to maximum deformation for 32-ply dry DCB specimens at 125°C.**

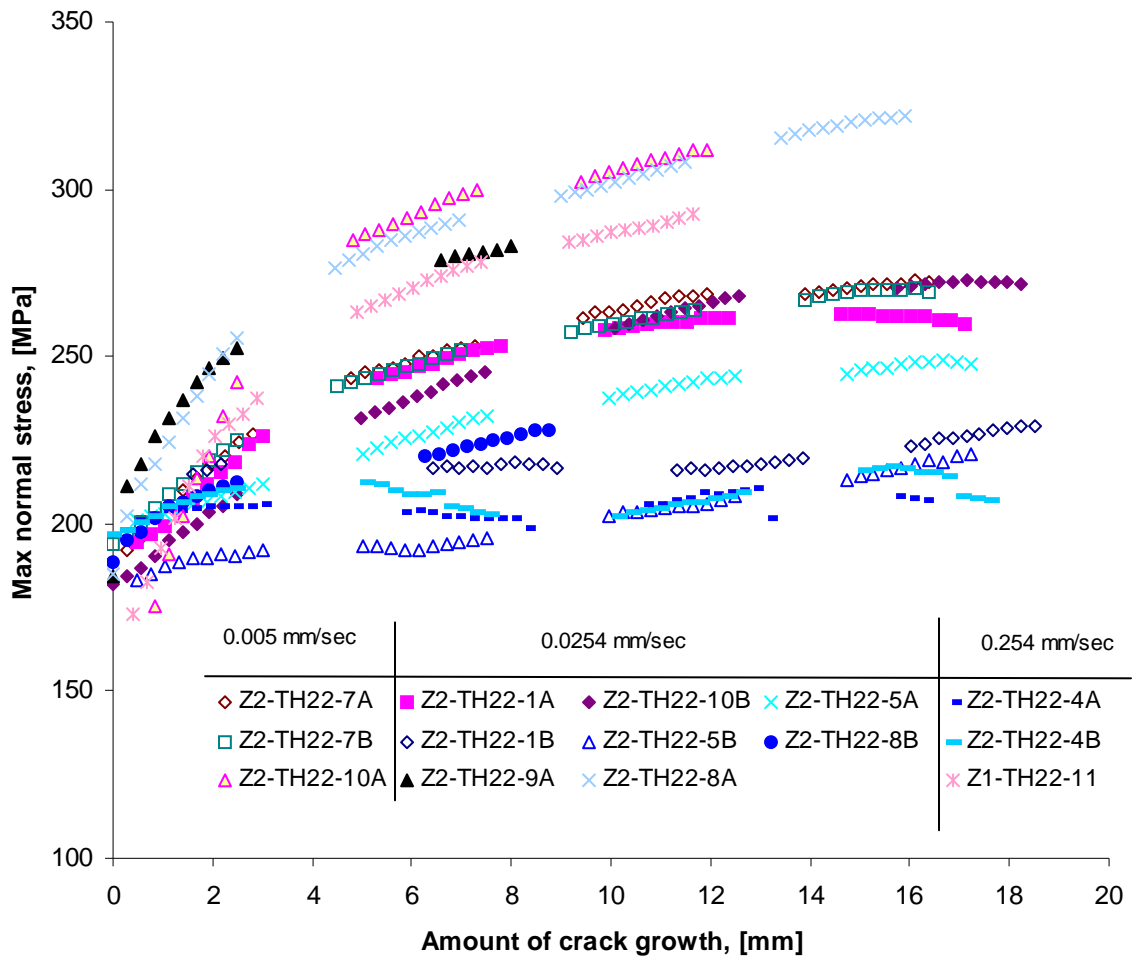


Figure 8.20 Maximum normal stresses for 22-ply dry DCB specimens tested at 125°C.

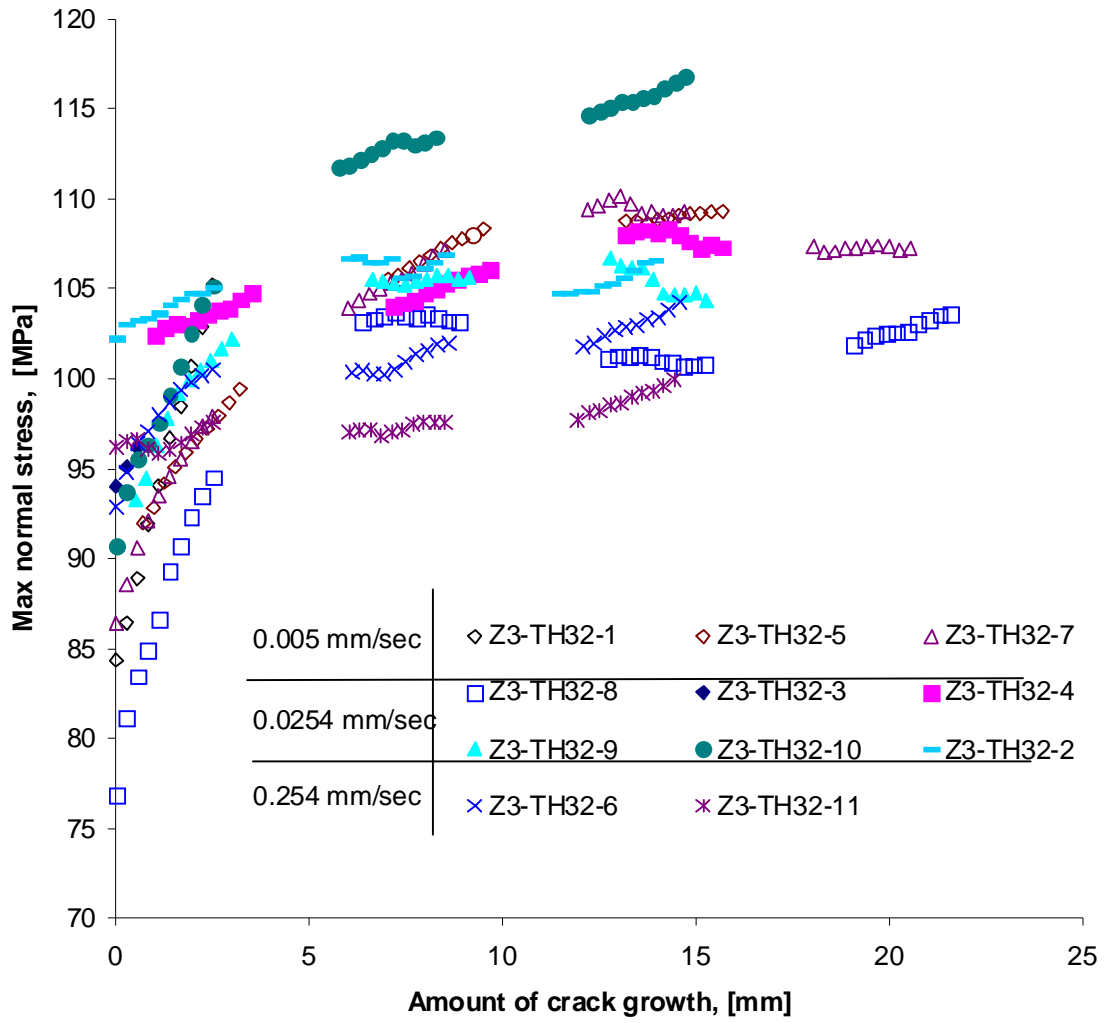


Figure 8.21 Maximum normal stresses for 32-ply dry DCB specimens tested at 125°C.

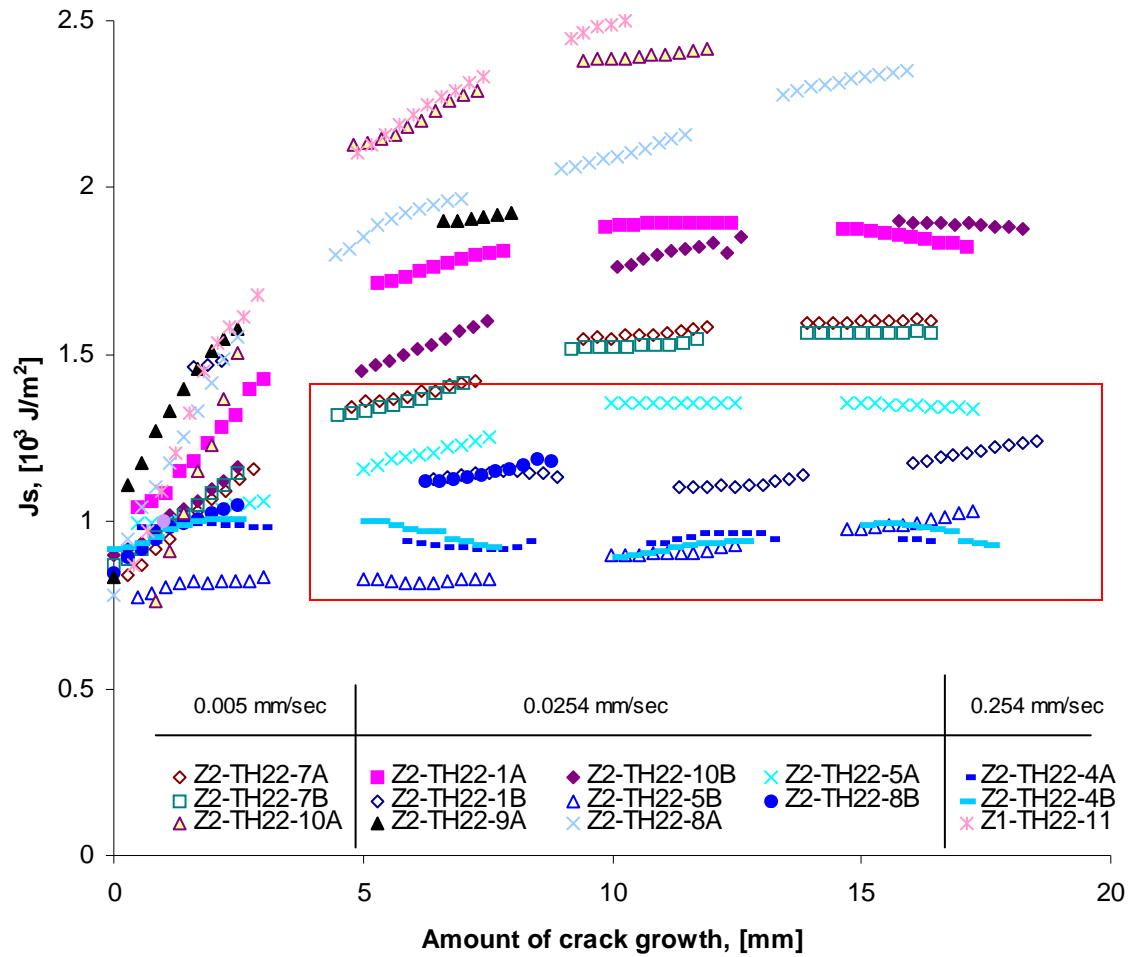
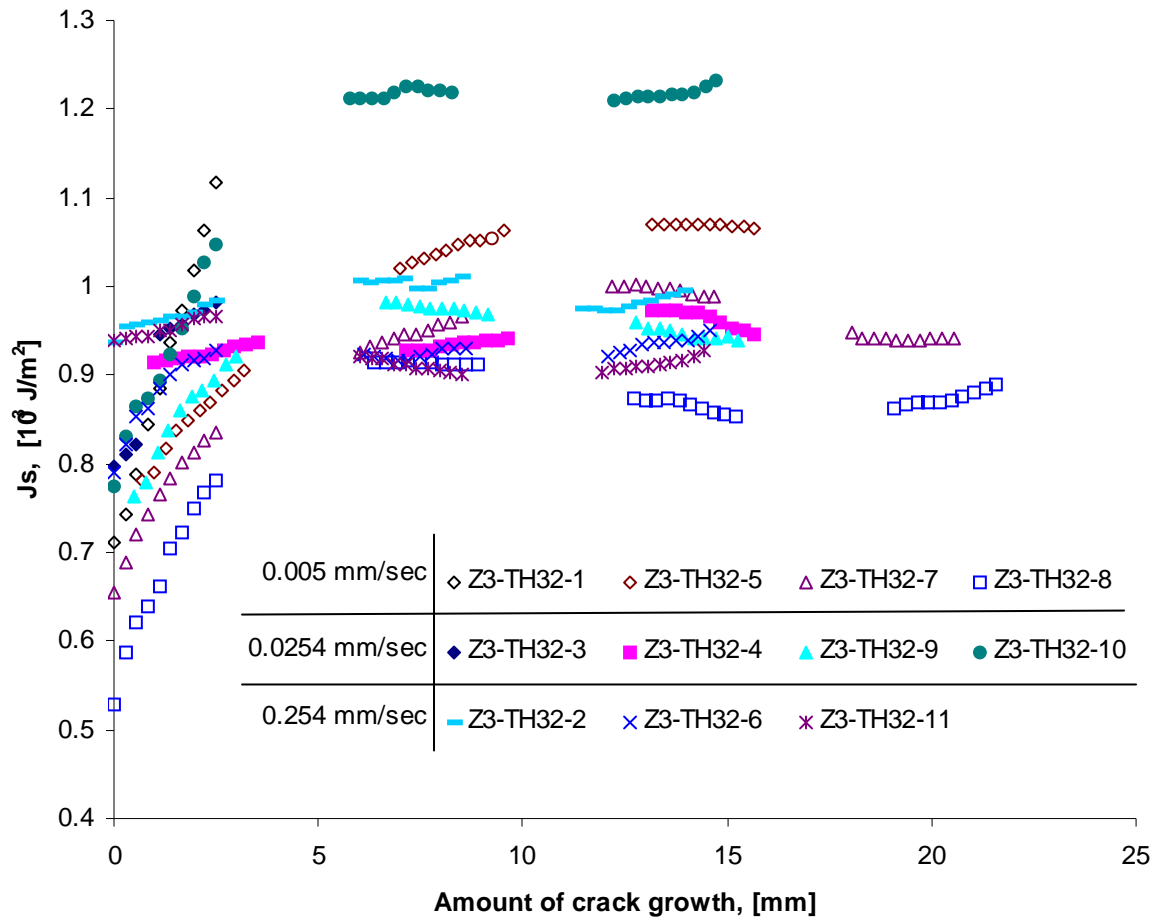


Figure 8.22  $J_s$  vs. crack growth for 22-ply dry DCB specimens at 125°C.





**Figure 8.23  $J_s$  vs. crack growth for 32-ply dry DCB specimens at 125°C.**

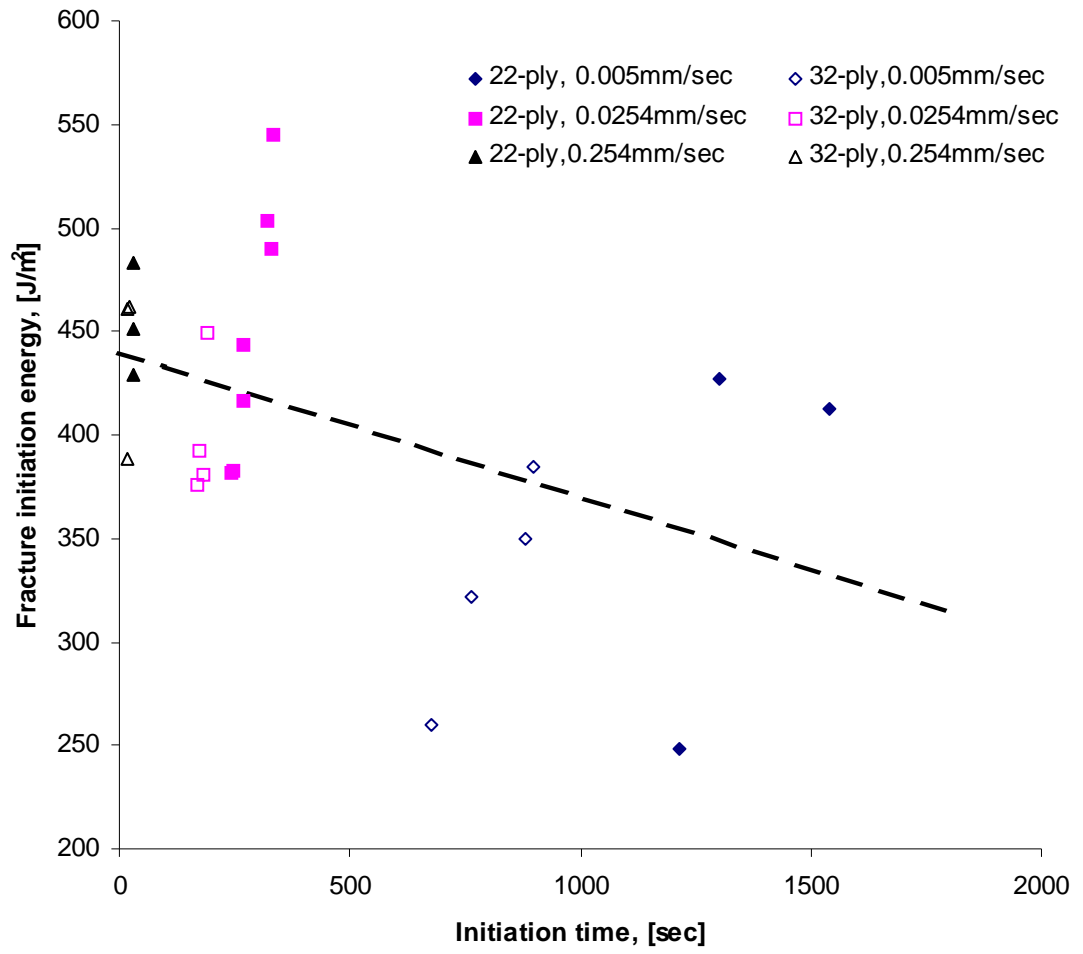


Figure 8.24 Fracture curve  $t_i(\Gamma_{II})$  for T800H/3900-2 dry DCB specimens at 125°C.

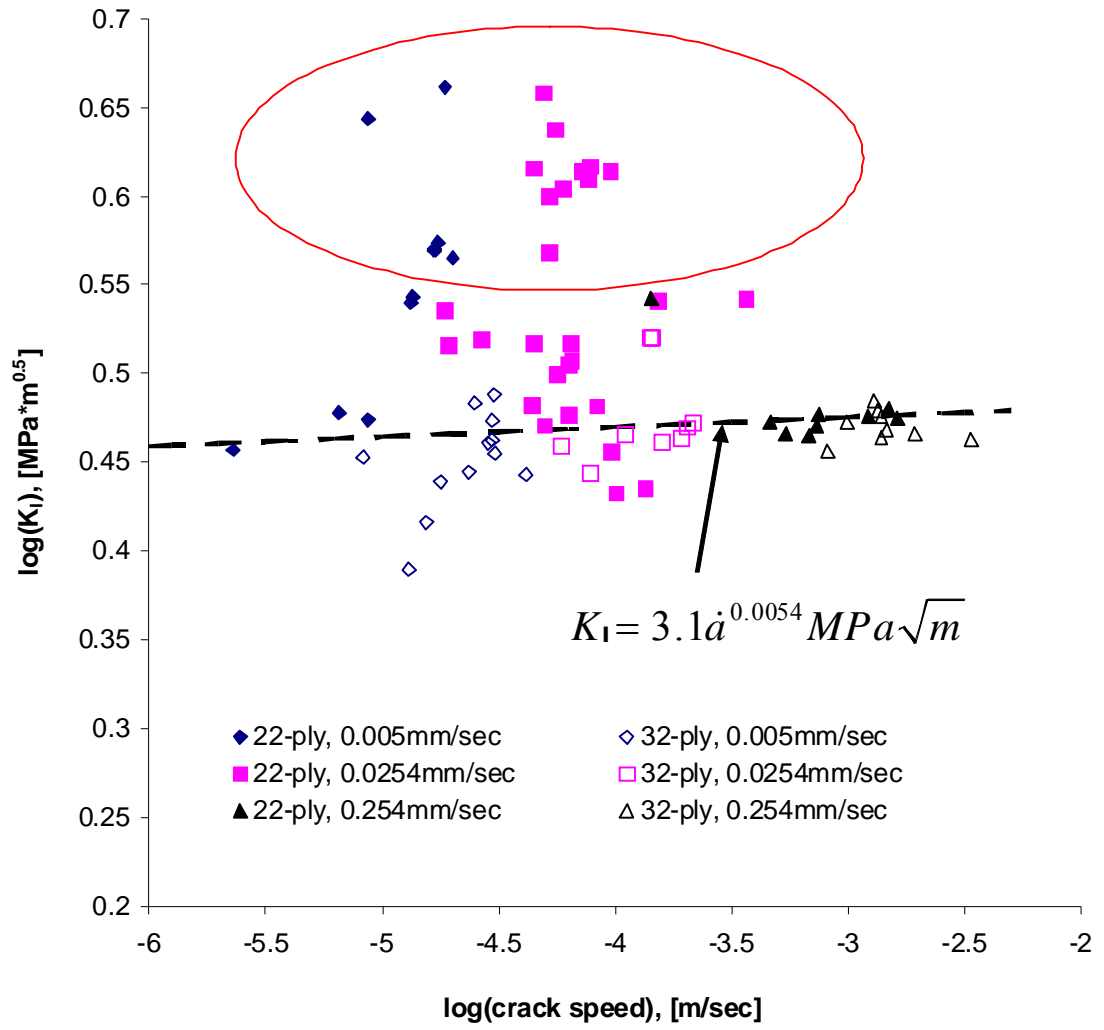
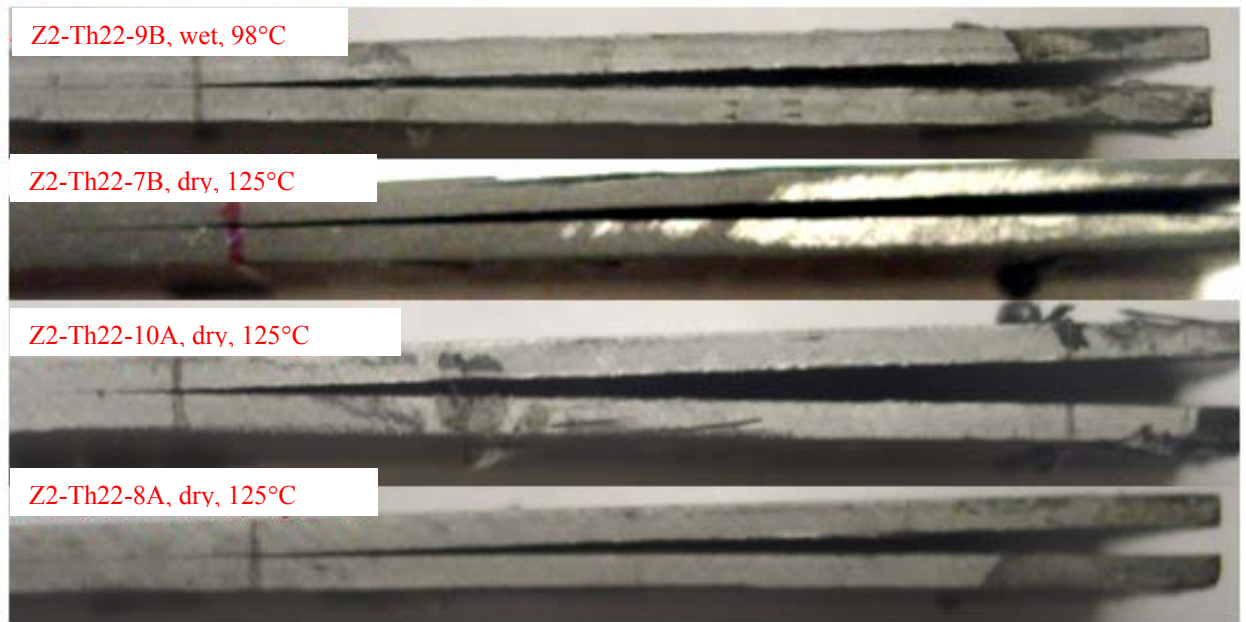
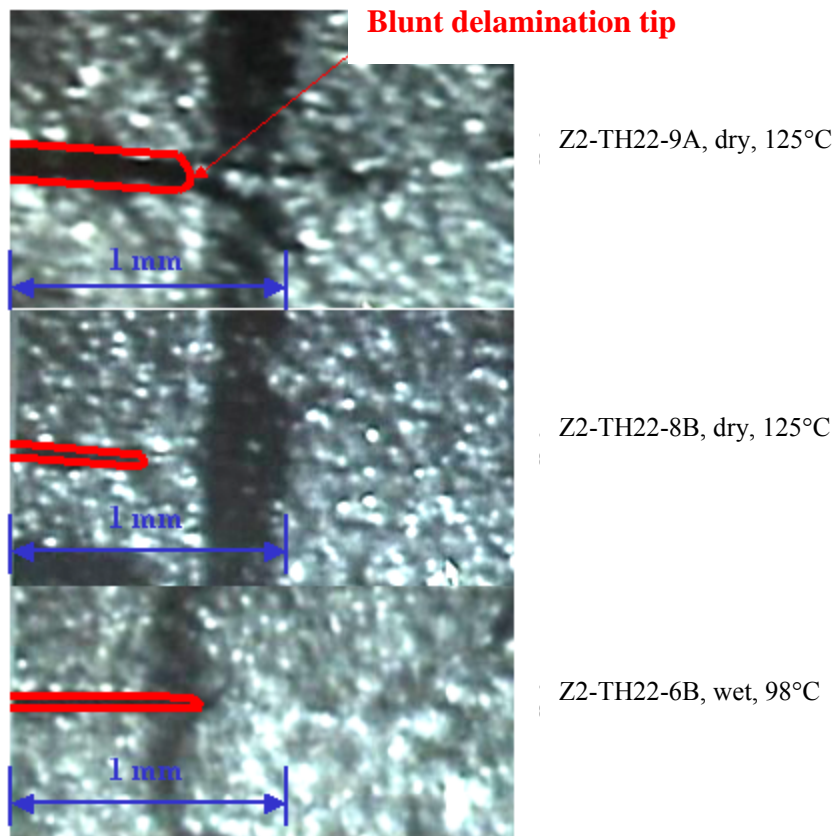


Figure 8.25 Fracture curve  $\dot{a}(K_I)$  of T800H/3900-2 dry DCB specimen at 125°C.



**Figure 8.26 Pictures of residual deformation after DCB fracture tests.**



**Figure 8.27 Example crack tip shapes from TMS images.**

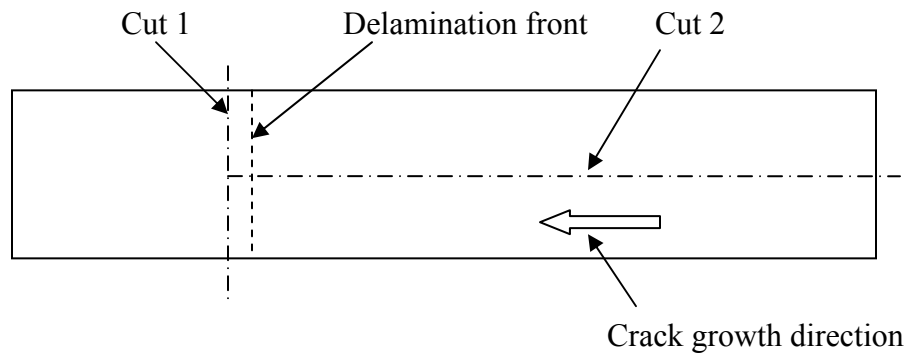
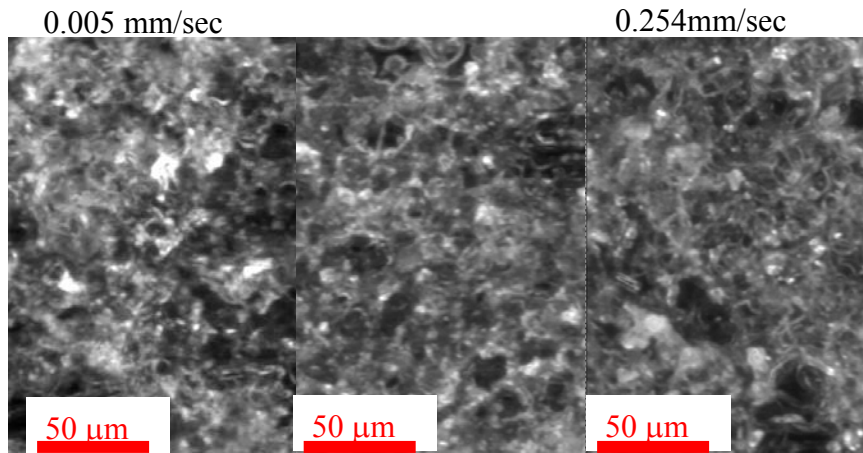
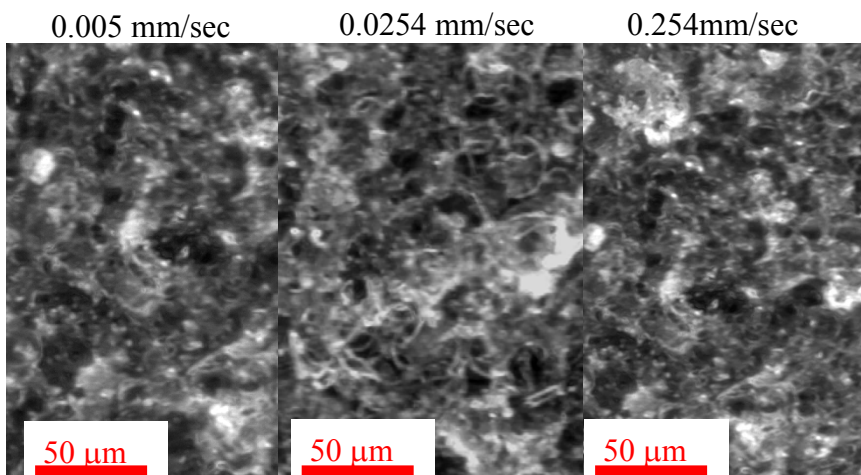


**Figure 8.28 Schematic of specimen cutting sequence.**

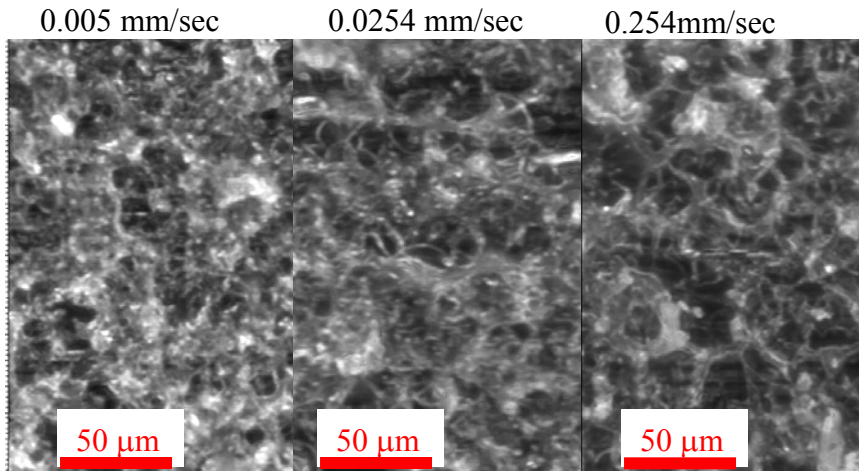


(a). Typical fracture surface next to the delamination insert for dry 22-ply specimens tested at 125°C

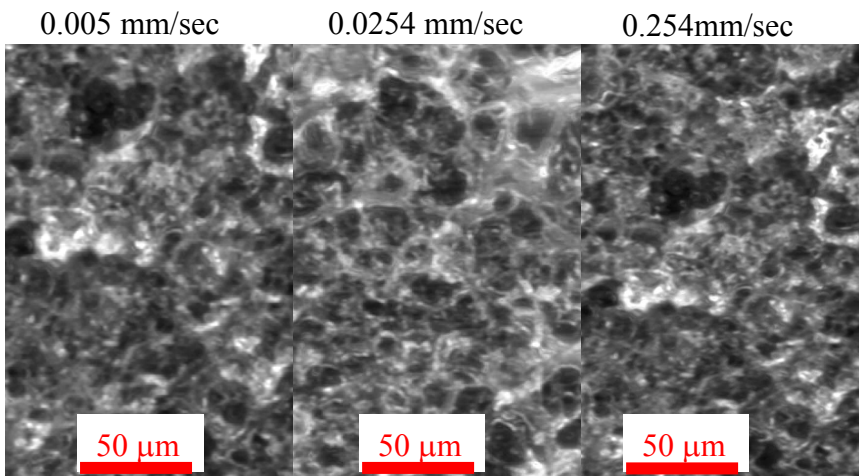


(b). Typical fracture surface next to the delamination insert for dry 32-ply specimens tested at 125°C

**Figure 8.29 Typical fracture surfaces at initiation next to the delamination insert for specimens at 125°C.**



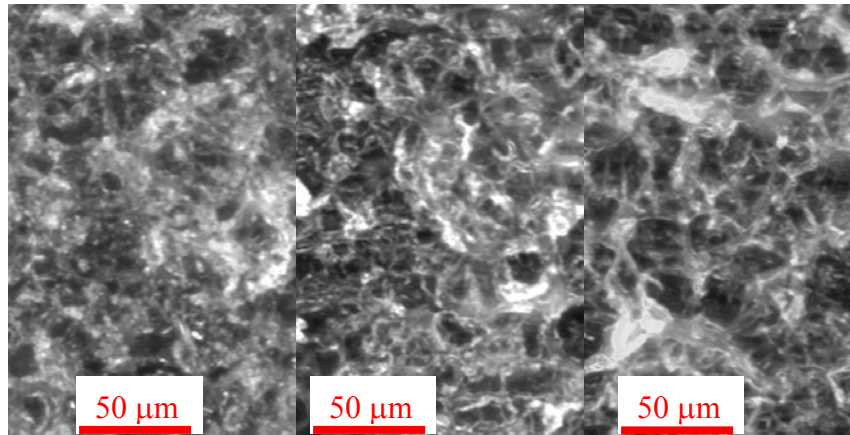
(a). Typical fracture surface during delamination propagation for dry 22-ply specimens tested at 125°C



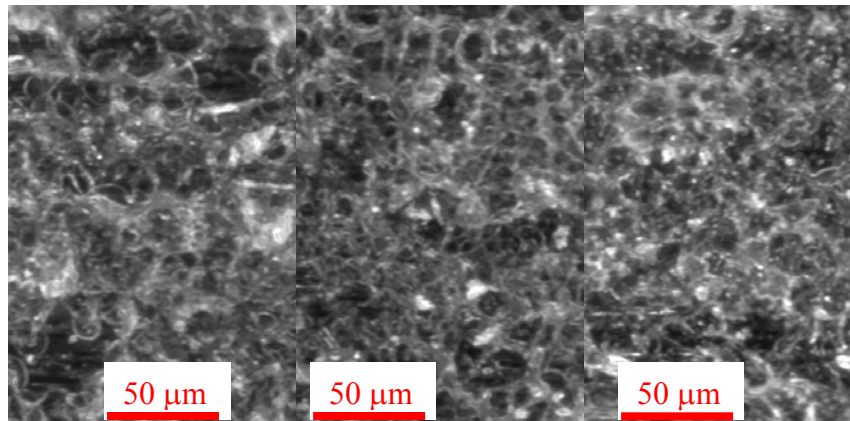
(b). Typical fracture surface during delamination propagation for dry 32-ply specimens tested at 125°C

**Figure 8.30 Typical fracture surfaces scan during propagation for specimens at 125°C.**



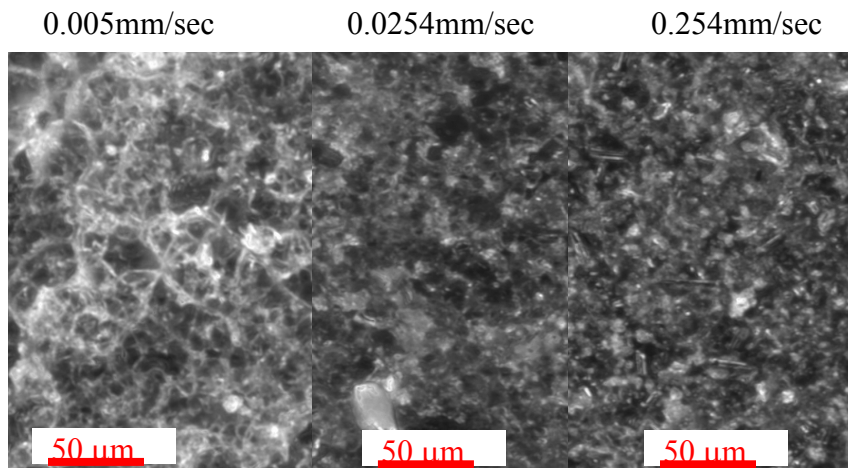


(a) Problematic dry specimens at 0.0254mm/sec and 125°C

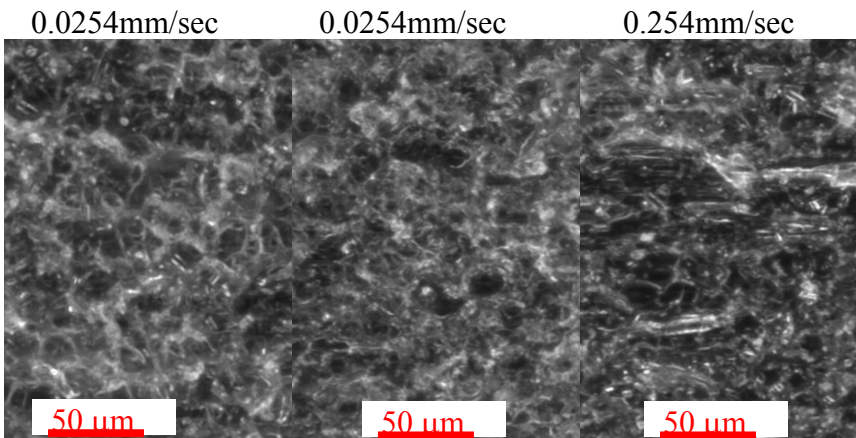


(b) Regular dry specimens at 0.0254mm/sec and 125°C

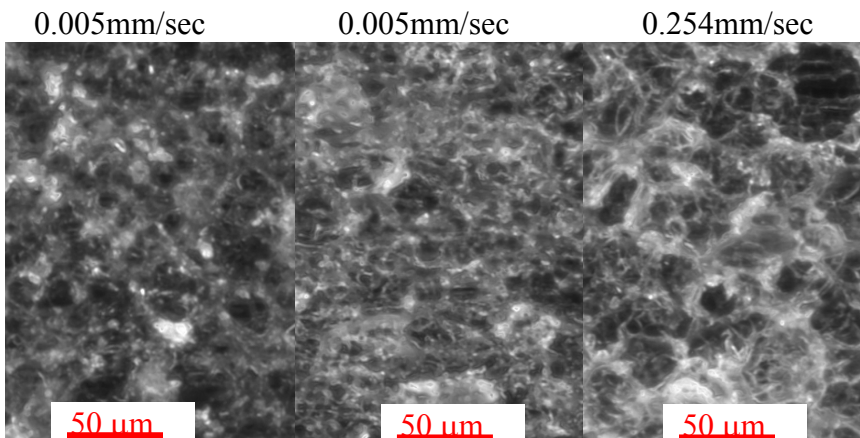
**Figure 8.31 Comparison of fracture surfaces during propagation for specimens tested at 0.0254mm/sec and 125°C.**



(a). Typical fracture surface at delamination initiation next to insert for wet 22-ply specimens tested at 98°C



(b). Typical fracture surface during delamination propagation for regular wet 22-ply specimens tested at 98°C



(c). Typical fracture surface during delamination propagation for problematic wet 22-ply specimens tested at 98°C

**Figure 8.32 Typical fracture surfaces of wet specimens at 98°C.**

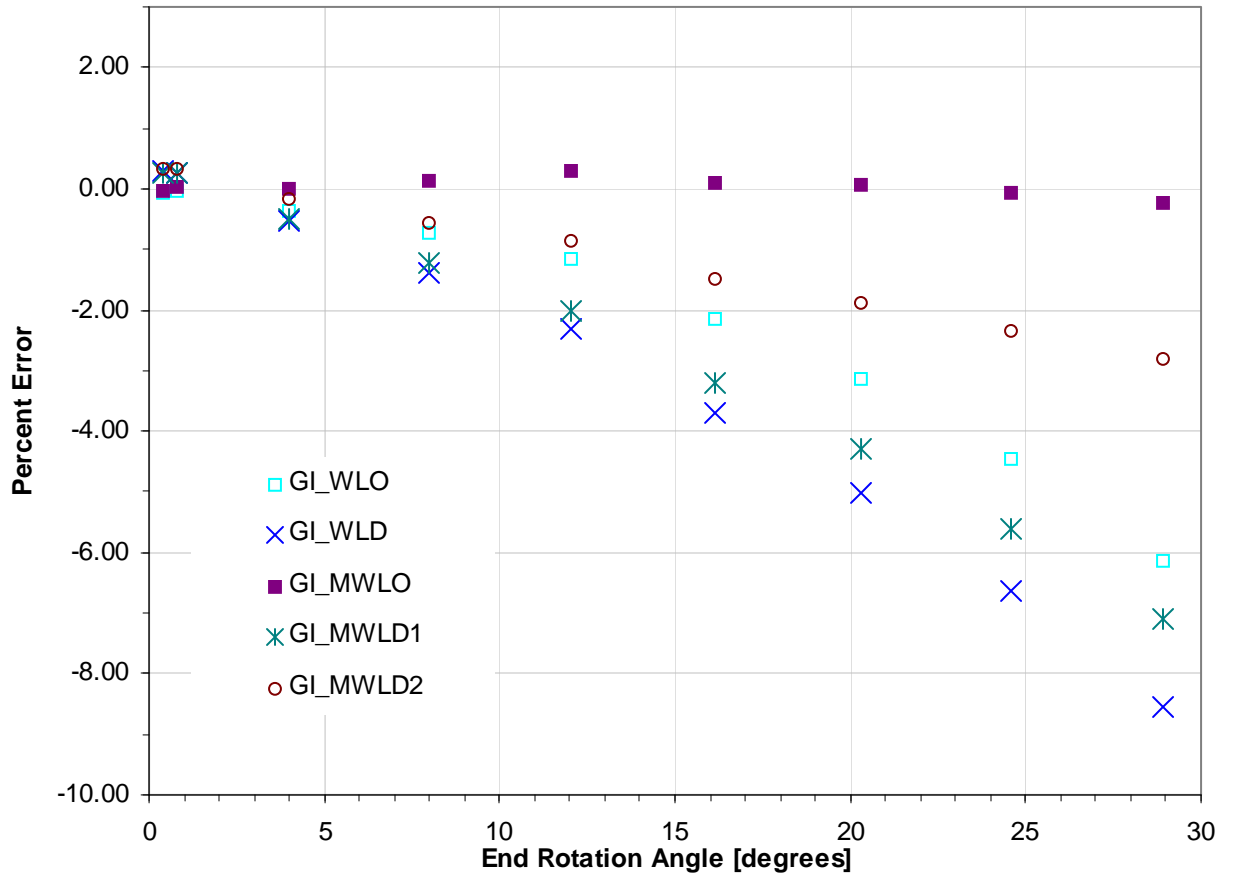


**Figure A.1 Evaluation of various data reduction methods for material 1.**

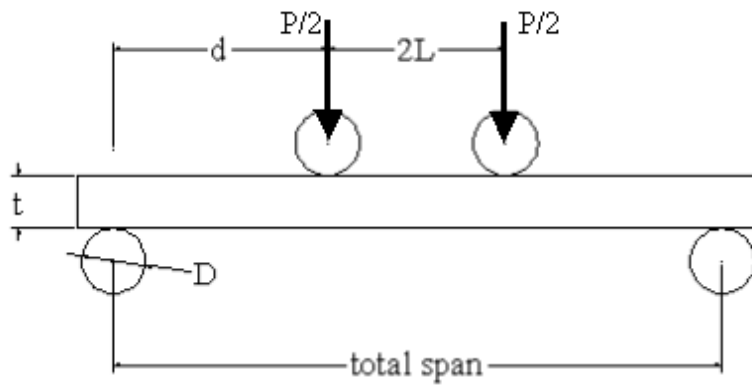


**Figure B.1. Sketch of 4-point bending test.**

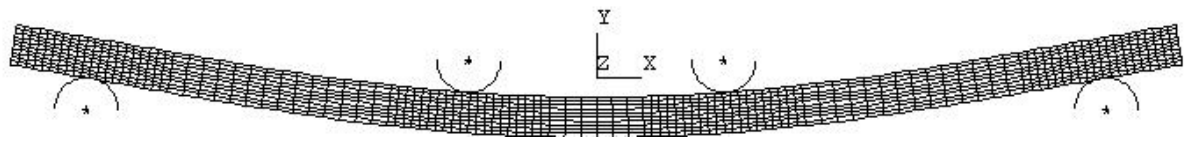


**Figure B.2. Deformed shape with FE mesh of 4-point bending specimen.**

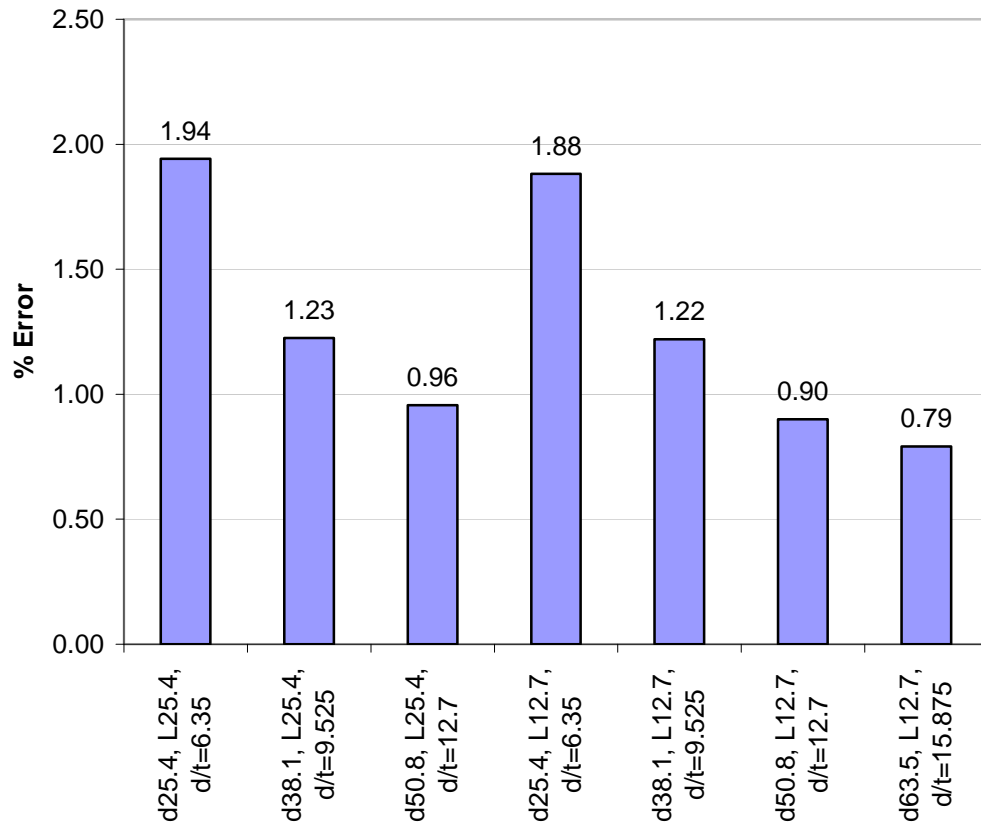


**Figure B.3. Loading span ratio effects on the accuracy of the beam theory stress.**

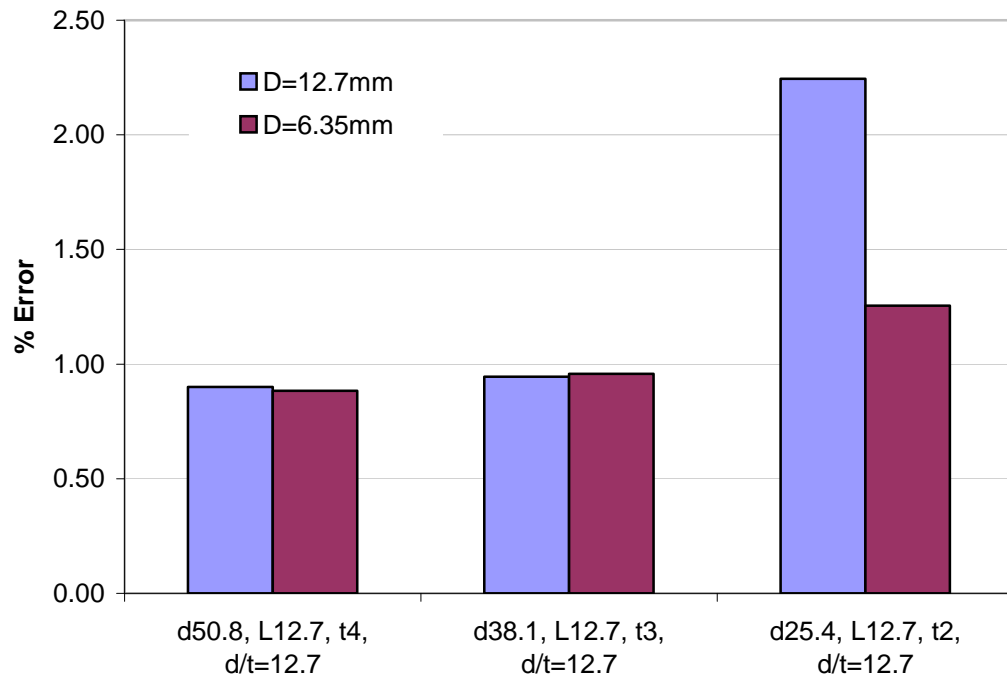
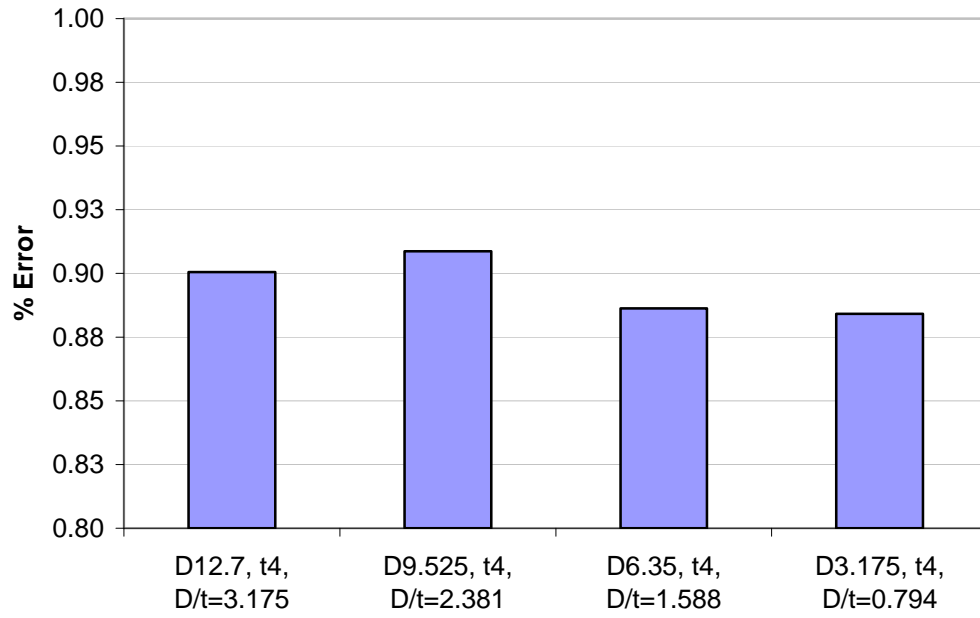
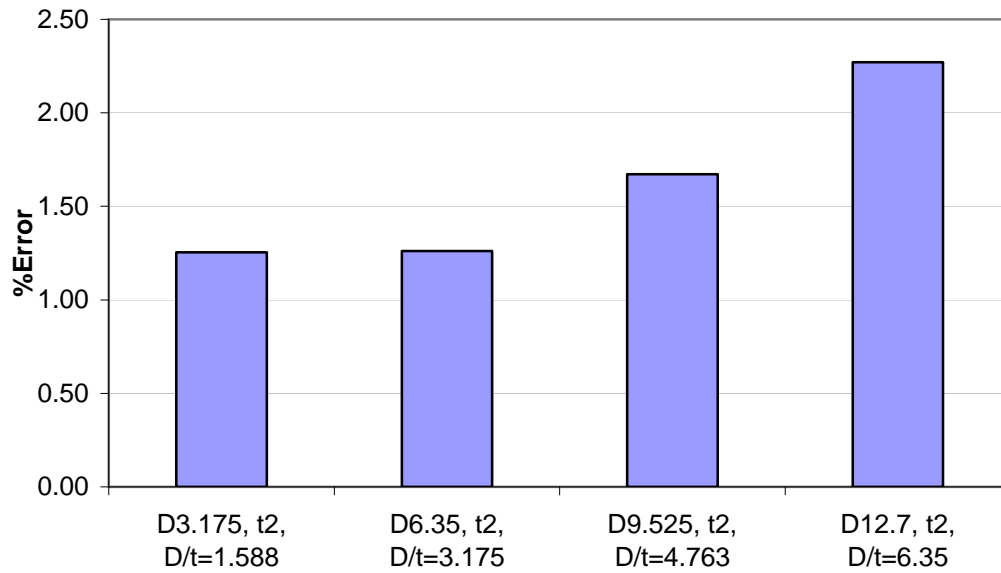


**Figure B.4. Specimen thickness effects.**



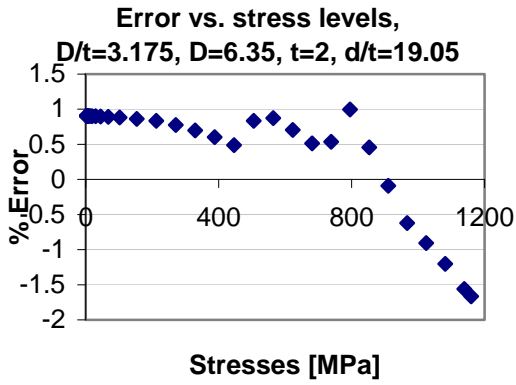
(a)



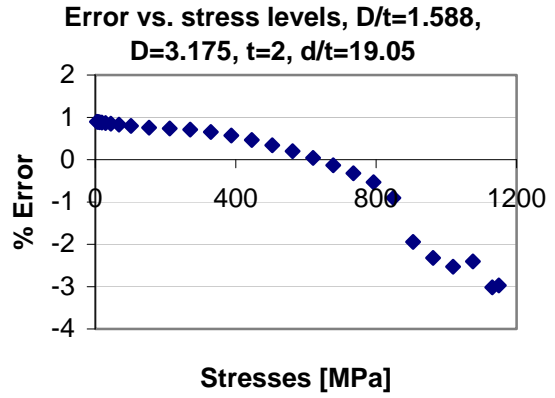
(b)

**Figure B.5. Roller diameter effects with (a) specimen thickness 4mm and (b) specimen thickness 2mm.**

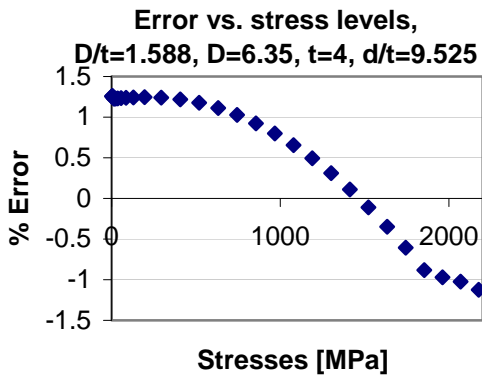




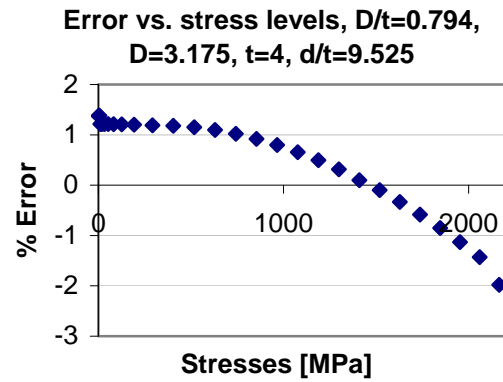
(a)



(b)



(c)



(d)

**Figure B.6. Stress level effects on prediction of stresses for various geometries.**

## VITA

NAME OF AUTHOR: Wenming Zhao

PLACE OF BIRTH: Inner Mongolia, China (PRC)

BIRTH: April, 1975

### GRADUATE AND UNDERGRADUATE SCHOOLS ATTENDED:

Clarkson University, Potsdam, New York

TongJi University, Shanghai, China

### DEGREES AWARDED:

Master of Science, Structural and Material Engineering, 2003, Clarkson  
University

Bachelor of Engineering, Structural Engineering, 1997, TongJi University

### PROFESSIONAL EXPERIENCE:

2008–now: Mechanical Engineer and Liaison, Cambric Corp

2008: Internship, GE Global Research Center

2003-2008: Research Assistant, Department of Mechanical and Aerospace  
Engineering, Syracuse University

2003: Teaching Assistant, Department of Civil and Environmental  
Engineering, Clarkson University

2001-2002: Research Assistant, Department of Civil and Environmental  
Engineering, Clarkson University

1997-2000: Engineer and project leader, Shanghai Municipal Housing Design  
Institute